

Field Emission Study on CW Superconducting Cavity

Enrico Cenni

Dissertation for doctoral course at
The Graduate University for Advanced Studies
High Energy Accelerator Research Organization (KEK)
Tsukuba
Japan

Supervisor: Professor Furuya Takaaki

Contents

Chapter I

| | | |
|-----|---|----|
| 1.1 | Introduction..... | 2 |
| 1.2 | Motivation..... | 9 |
| 1.3 | State of the Art and Original aspects | 12 |
| 1.4 | Dissertation layout | 14 |
| | Chapter references..... | 15 |

Chapter II

| | | |
|-------|---|----|
| 2.1 | Particle acceleration | 17 |
| 2.2 | Electro Magnetic field theory | 18 |
| 2.3 | RF resonator..... | 20 |
| 2.3.1 | LC circuit | 21 |
| 2.3.2 | From lumped circuit to cavity resonator | 22 |
| 2.3.3 | Forced RF resonator..... | 23 |
| 2.4 | RF cavity design..... | 26 |
| 2.5 | Figures of merit..... | 33 |
| 2.5.1 | Cavity voltage and Transit time factor..... | 34 |
| 2.5.2 | Surface resistance and Power loss | 37 |
| 2.5.3 | Q value and Geometry factor | 39 |
| 2.5.4 | Shunt impedance | 40 |
| 2.5.5 | R over Q..... | 41 |
| 2.5.6 | Peak fields..... | 41 |
| 2.5.7 | Cell to cell coupling | 43 |
| 2.6 | ERL cavity | 46 |
| 2.6.1 | ERL machine requirements..... | 46 |
| 2.7 | Field emission theory..... | 58 |
| 2.7.1 | Field emission onset..... | 60 |
| 2.8 | Cavity preparation..... | 67 |
| 2.8.1 | Bulk removal..... | 68 |

| | |
|--|----|
| 2.8.2 Degassing and Annealing | 70 |
| 2.8.3 Light removal..... | 70 |
| 2.8.4 Low temp bake out..... | 71 |
| 2.9 Vertical test measure..... | 72 |
| 2.9.1 Measured quantity..... | 72 |
| 2.9.2 Dissipated power:..... | 73 |
| 2.9.3 Resonant frequency:..... | 74 |
| 2.9.4 Decay time ($\tau_{1/2}$): | 74 |
| 2.9.5 Loaded Q (Q_L)..... | 74 |
| 2.9.6 Unloaded Q (Q_0) | 76 |
| 2.9.7 Surface resistance..... | 77 |
| Chapter references | 79 |

Chapter III

| | |
|---|-----|
| 3.1 Field emission calculation..... | 82 |
| 3.2 Electromagnetic field calculation..... | 83 |
| 3.2.1 Field flatness | 88 |
| 3.3 Particle tracking | 93 |
| 3.4 Particle tracking example..... | 98 |
| 3.4.1 Systematic approach (parameters scan) | 101 |
| 3.4.2 Generalized location-phase diagram..... | 108 |
| 3.4.3 Impact energy..... | 109 |
| 3.5 Dark current calculation..... | 112 |
| 3.5.1 Surface electric field | 112 |
| 3.5.2 Emitted current..... | 113 |
| 3.5.3 Dissipated power..... | 114 |
| 3.6 EGS5 simulation | 117 |
| 3.6.1 EGS5 example..... | 119 |
| Chapter references | 124 |

Chapter IV

| | |
|----------------------------------|-----|
| 4.1 Vertical test stand..... | 126 |
| 4.2 Low level RF system | 128 |
| 4.3 Rotating mapping system..... | 129 |
| 4.4 NaI scintillator..... | 133 |
| Chapter references..... | 137 |

Chapter V

| | |
|--|-----|
| 5.1 Vertical test data analysis..... | 139 |
| 5.1.1 Secondary electron yield..... | 140 |
| 5.2 Cavity #1 4th and 5th Vertical Test | 153 |
| 5.2.1 Vertical test schedule | 154 |
| 5.2.2 Surface resistance..... | 155 |
| 5.2.3 Dissipated power..... | 167 |
| 5.2.4 X-ray mapping | 174 |
| 5.2.5 The sharp spot..... | 176 |
| 5.2.6 The broad spot..... | 184 |
| 5.2.7 4 th and 5 th vertical test π modes summary..... | 189 |
| 5.3 Cavity #4 1 st vertical test..... | 191 |
| 5.3.1 Surface resistance..... | 192 |
| 5.3.2 Accelerating modes measures..... | 193 |
| 5.3.3 Power loss and field emission onset | 194 |
| 5.3.4 Enhancing factor from data..... | 197 |
| 5.3.5 π mode at 22MV/m transmitted power | 209 |
| 5.3.6 8/9 π mode at 23.5MV/m transmitted power | 211 |
| 5.3.7 π mode at 22MV/m incident angle..... | 213 |
| 5.3.8 8/9 π mode at 23.5MV/m incident angle..... | 215 |
| 5.4 High power test | 218 |
| 5.4.1 PIN diodes setup | 220 |
| 5.4.2 Cavities condition during last vertical test..... | 224 |
| 5.4.3 High power test schedule | 225 |

| | |
|---|-----|
| 5.4.4 Upstream cavity radiation pattern | 226 |
| 5.4.5 Upstream NaI scintillator measure | 229 |
| 5.4.6 Downstream cavity radiation pattern | 236 |
| 5.4.7 Upstream NaI scintillator measure | 239 |
| 5.4.8 High power test summary | 242 |
| 5.5 Cavities model comparison | 243 |
| 5.5.2 Danger area | 250 |
| 5.5.2 Danger length | 251 |
| Chapter references | 253 |

Chapter VI

| | |
|------------------|-----|
| Conclusion | 254 |
| Outlook | 255 |

Acknowledgments

Appendix

CHAPTER I

Introduction and Motivation

1.1 Introduction

Since their introduction, particle accelerators have become one of the most valuable instruments for both basic and applied scientific research. Thanks to them it is possible to shed light on different scientific issues from basics (like the hunt of the Higgs boson) to applied ones, from medical and biological studies, material properties analysis to investigations on ancient artifacts.

Inside each accelerator, some components enable the particles to be accelerated and can be seen as the “engine” of the accelerator machine. In synchrotron or Linac machine they are typically build as electromagnetic resonator with a specific natural frequency, hence their appellation “RF cavities”. The operating conditions have a broad range parameters as a function of the accelerator design requirements, depending on the accelerating particles (electrons, protons or heavy ions) or the machine application (i.e. light source or collider). Different configurations were extensively studied in order to exploit high energy particle for scientific investigation.

The accelerating cavities can be classified in two groups, depending on their working condition or application: one represents the cavities built with superconducting materials (typically Niobium), the other the ones built with normal conducting materials (typically Copper).

Superconducting cavities have proven to be one of the most promising technologies to accelerate particles. Indeed, superconducting cavities allow reaching an high electric field operation while keeping an electrical power consumption as low as possible. Next table shows a comparison between two pillbox cavities, one made with Niobium and operated at 2K, the other built with Copper and operating at room temperature. The model parameters are calculated through SuperFish code [1, 2].

Table 1.1 Comparison between normal conducting and superconducting pillbox cavities (*calculated with SuperFish code [1, 2]*).

| Property | Normal conducting (Cu-type) | Superconducting (Nb-type) |
|---|--------------------------------|------------------------------|
| Cavity Radius (R_{cav}) | 8.827 cm | 8.827 cm |
| Cavity Length (L) | 10 cm | 10 cm |
| ω_0 TM010 | 1301 MHz | 1301 MHz |
| Temperature | 300 K | 2 K |
| Surface resistance (R_s) | $9 \times 10^{-3} \Omega$ (Cu) | $2 \times 10^{-8} \Omega$ |
| Cavity Voltage (V_{acc}) | 100 KV | 100 KV |
| Power dissipation (P_{loss}) | 2458 W | 7 W |
| Stored Energy (U) | $7 \times 10^{-3} \text{ J}$ | $7 \times 10^{-3} \text{ J}$ |
| Transit time factor | 0.61 | 0.61 |
| Quality factor (Q_0) | 25590 | $9 \cdot 10^9$ |
| R/Q | 159 Ω | 159 Ω |
| Geometry Factor (G) | 240 Ω | 240 Ω |

Nowadays, more and more particle accelerators are designed in order to take advantage of superconducting cavities peculiarity [3]. Thus, it was decided recently to use superconducting cavities within the LHC project and the future ILC project in order to achieve high accelerating field while keeping the power consumption and the numbers of cavities (excavation costs) as low as possible [4].

Many new projects dealing with new light sources are dedicated to Energy Recovery Linac (ERL) scheme. Research teams dealing with this technology are based in United States at Cornell University, Jefferson Laboratory and Brookhaven Laboratory, in Europe at Helmholtz Center in Berlin (BERLinPro) and in Japan at KEK [5].

At KEK, the project is divided in two phases:

- the first phase is the development of a prototype device, relatively small (around 300 m circumference) that is a compact version of the ERL (c-ERL Figure 1.1) to prove, develop and test the technology required for this kind of particle accelerator,
- the second phase is the building of the actual machine that will be larger (around 3 km circumference) and will allow many user front ends in order to exploit the unique properties of the light produced by this machine (Figure 1.2).

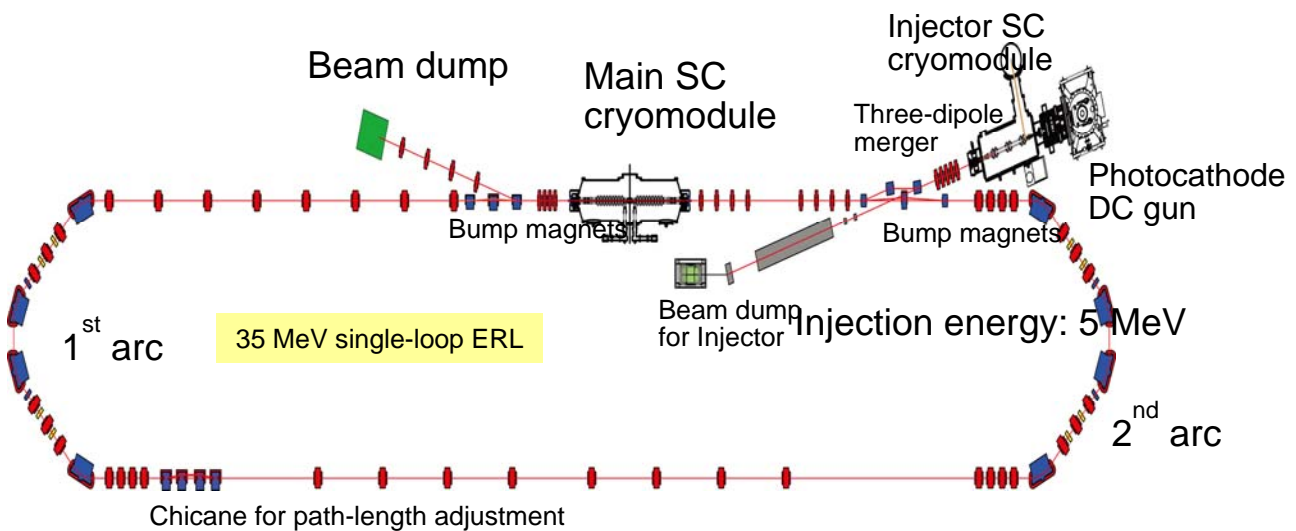


Figure 1.1 Schematic view of the c-ERL [5, 6].

As in mid-2013, the first phase is on-going and the second phase is expected to start in the next years.

In common particle accelerators light source electron bunches turn many times into the storage ring producing synchrotron light. After each turn, the *quality* of the electrons bunch degrades (emittance increases due to quantum effect) and so does the quality of the synchrotron light. One way to solve this problem could be to circulate a new bunch of electrons after every turn while the old one is damped. One of the main disadvantages of this option is that a very large amount of power will be needed to accelerate each time the fresh bunch. To tackle this problem, the idea is to recover some

energy from the dumping bunch to accelerate the new one. This was first proposed in 1965 by M. Tigner from Cornell University [7], and its proof of concept was demonstrated twenty years later (1986, Stanford University) [8]. Since then, more and more research groups have been attracted by this technology to produce light sources.

In order to take advantage from the low emittance beam produced in a Linac and to be competitive with circular synchrotron light source, it is necessary to accelerate particles up to several GeV with a beam current of several 100mA. It is straightforward to notice that in this scheme the Linac shall delivers a power of order GW to the beam, that is practically unfeasible without recovering part of the beam energy. In this framework the RF cavities shall exchange energy with the incoming and outgoing electrons continuously, in other word each cavity shall operate in continuous wave (CW) mode. The usage of a normal conducting cavity is not possible due to the large amount of heating produced and therefore a cooling system is needed. This is why the superconducting cavities are good candidates for ERL usage.

Currently at KEK, the two main light sources are Photon Factory (PF) a 2.5GeV ring and Photon Factory Advanced Ring (PF-AR) a 6.5GeV ring.

More than 30 years after their first beam and after an extensive discussion between users and accelerator physicists, it was concluded that Energy Recovery Linac (ERL) based light source would be the most suitable for their future projects.

Indeed, as already pointed out, this technology is attractive not only to users because of the high quality of the light produced in terms of brightness, coherence and high repetition rate, but also to accelerator physicists because of the technology challenges they have to face.

To achieve this, the main linac accelerating cavities are one of the essential components. Due to the stringent request imposed by the ERL specification they need to have a special design in order to

work in continuous wave (CW 100% duty factor) allowing 100mA of beam current with a good HOMs damping.

In order to prove, understand and develop the technology needed for such particle accelerators, a compact model (c-ERL) was designed (see **Errore. L'origine riferimento non è stata trovata.**1 and **Errore. L'origine riferimento non è stata trovata.**). The c-ERL is composed of different parts and thus, all the particle accelerator components can be tested and improved.

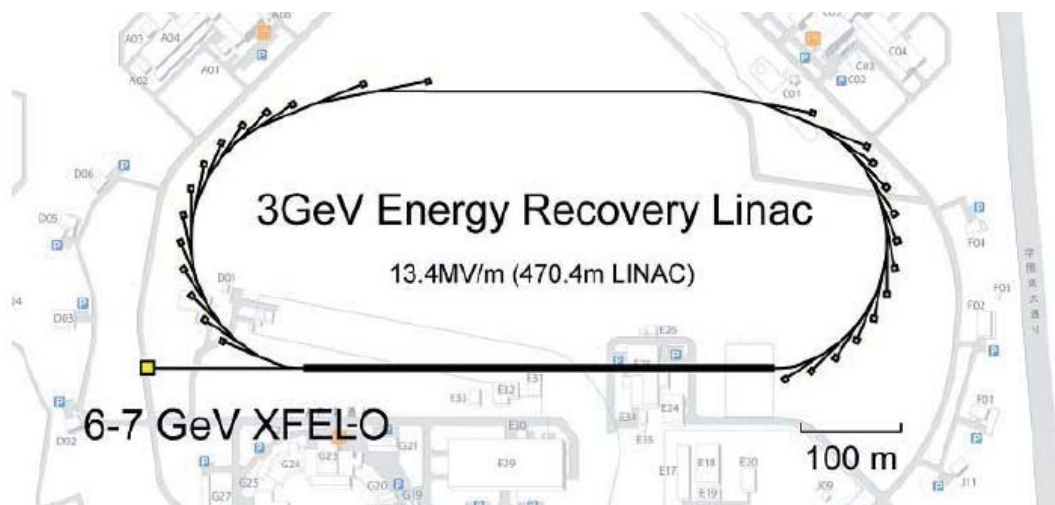


Figure 1.2 Schematic view of the ERL (From Energy Recovery Linac Preliminary Design Report) [5].

In the c-ERL, the main linac is equipped with two L-band superconducting cavities. The design of the cavities took into account all the ERL machine requirements. Thus, during the optimization of an L-band cavity, the shape was modified to allow a CW operation with 100mA current and strong HOMs damping avoiding BBU (**Errore. L'origine riferimento non è stata trovata.**) along with cavity main parameters (see Table below)[9].



Figure 1.3 KEK-ERL model 2 superconducting cavity.

Table 1.2 KEK-ERL model 2 superconducting cavity [9] (calculated with SuperFish).

| Property | KEK-ERL mod2 |
|-------------------------------------|-------------------------------------|
| Operating field | $15 \frac{MV}{m}$ |
| Operation mode | CW |
| Quality factor (Q_0) | 10^{10} |
| Cavity Length (L) | 103.77 cm ($9 \frac{\lambda}{2}$) |
| Cavity diameter | 20.66cm |
| $\omega_{0 \text{ TM010}}$ | 1300 MHz |
| Temperature | 2K |
| Surface resistance (R_s) | 26 n Ω |
| Accelerating Field (E_{acc}) | $1 \frac{MV}{m}$ |
| Power dissipation (P_{loss}) | 111 mW |
| Stored Energy (U) | 0.15 J |
| Transit time factor | 0.72 |
| Quality factor (Q_0) | 10^{10} |
| R/Q | 896 Ω |
| Geometry Factor (G) | 289 Ω |
| Iris radius | 4 cm |
| E_{pk}/E_{acc} | 3.0 |
| H_{pk}/E_{acc} | $42 \frac{Oe}{MV m^{-1}}$ |
| K_{cc} (cell to cell coupling) | 3.8% |

1.2 Motivation

Due to the cavity design requirements (Table 1.2) and CW operating condition, field emission can be a severe limiting factor for ERL cavity performance (Figure 1.6).

To address this problem, a research program is ongoing and can be divided in three broad areas:

1. **Detection**: in order to measure the field emission effects during cavity operation (x-ray production, Q-E curve slope, quenches and bursts)
2. **Simulation and calculation**: carried out by means of simulation codes and algorithm to achieve a deeper understanding of the phenomena related to field emission process, and eventually explain the experimental results
3. **Possible solutions**: once the experimental and analytical tools have proved their reliability, investigation of different cavity shapes in order to find the optimum solution with respect to field emission phenomena.

One of the main concerns while designing the cavity was the ratio between the Electric Field on the surface and the Accelerating Field. Indeed, while in the original TESLA-type cavity the maximum of this ratio ($E_{\text{peak}}/E_{\text{acc}}$) reaches 1.98 [10], in the ERL type the $E_{\text{peak}}/E_{\text{acc}}$ reaches 3.0 [9].

In a broader frame, field emission can be a limiting factor not only for CW operating machine, but also for high gradient ones operating in pulsed mode, like the International Linear Collider (ILC) [4]. As this issue applies to other systems,, there is a strong motivation to achieve a better knowledge about field emission effect inside superconducting cavities, in order to understand the complex relation between cavity geometry, operating conditions and field emission effect.

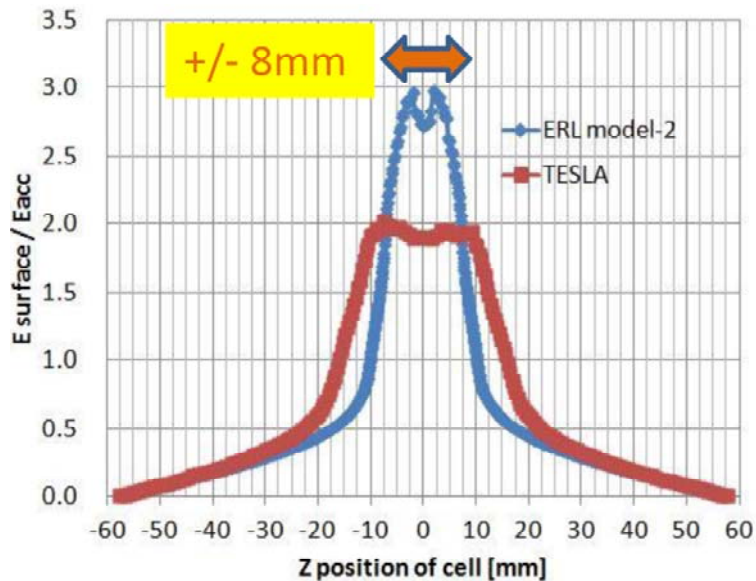


Figure 1.4 Surface electric field, comparison between TESLA shape and ERL model 2.

Due to this, field emission can be one of the major limiting factor in the cavity performance. In fact, the emitted electrons can increase the cavity loss and cryogenic load and also generate dark current, increasing the radiation dose suffered by components up-stream and down-stream with respect to the cavity.

In summary, here is a list of the different issues related to field emission:

- Quenches
- Q drop
- Cryogenic losses increase
- Dark current
- Radiation dose increase

Since the development of the first single cell cavity, a large effort has been put to detect field emitted electrons moving inside the cavity. Thus, a special system was designed in order to detect x-ray produced by electrons impacting on the cavity surface. This system consists of a set of PIN diodes [11] that are placed around the cavity surface and that can turn around it. This setup gives a detailed image (0.5° resolution) of the x-ray profile [12].

The same principle was used to design a detection system for the 9-cell structures, capable to detect x-ray during vertical tests operation (rotating mapping system). The images obtained from the sensors are like a map showing x-ray “hot spot”, allowing online and offline data analysis in order to provide valuable information on field emission events.

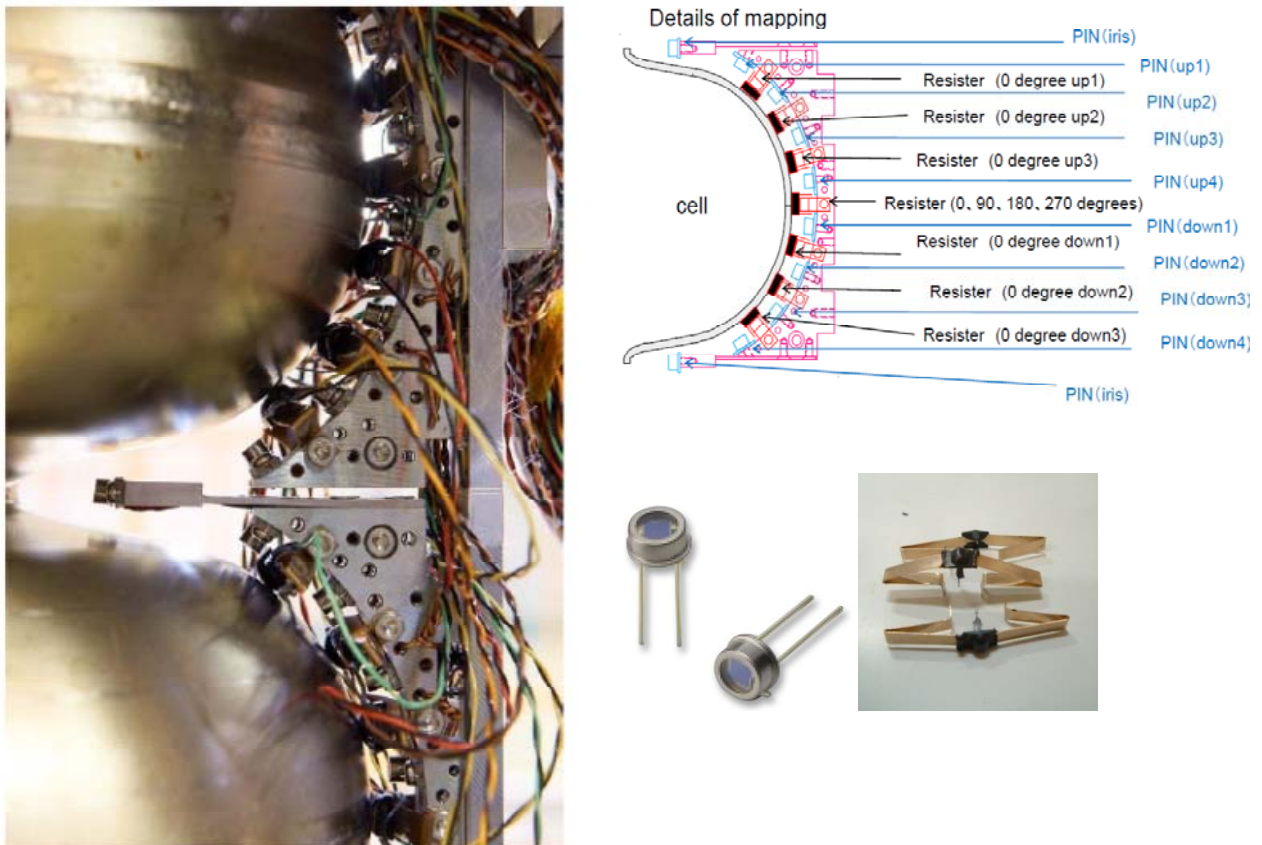


Figure 1.5 Rotating mapping system details, sensors installation around a cell (left), sensors location drawing (top right), PIN diodes and carbon resistors (bottom right).

The map, as can be seen below, shows x-ray intensity with respect to cavity meridian and longitudinal axis position.

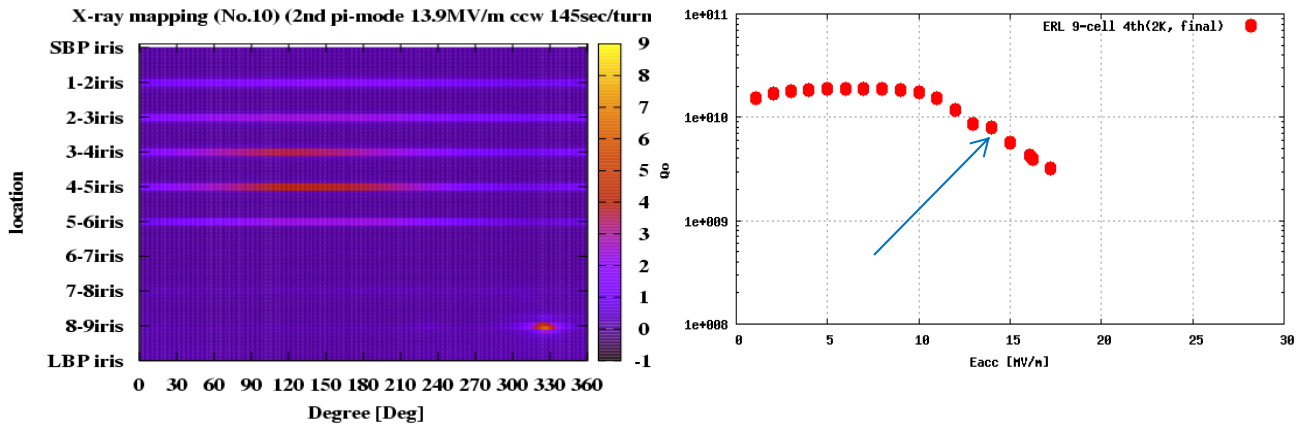


Figure 1.6 X-ray map during cavity vertical test (left), Q-E plot during the same test (right).

The x-ray map and the cavity Q-E curve taken took during a vertical test are displayed on Figure 1.6. On the Q-E curve, the arrow points to the cavity condition during the mapping).

1.3 State of the Art and Original aspects

Field emission effect is well known since the beginning of the last century and it was well explained by quantum mechanics theory in 1928 by Fowler and Nordheim [13]. Field emission was recognized as one of the limiting factor along with multipacting and quenches in the path towards high gradient in RF cavities [14].

Most studies performed about field emission in RF cavities dealt with the heat effect produced by the emitter because a typical vertical test set up was equipped with temperature sensors in order to spot quenches location [15]. With recent improvements in cavity preparation, surface defects that generate quenches will become more rare and field emission effect could be the next challenge to overcome.

Among these studies, field emission in multi-cell RF cavities is rarely studied [16, 17] and none of them investigate the x-ray produced by emitted electrons incident to the cavity surface, neither

gives a systematic approach to understand the complex relation between field emission, cavity geometry and operating conditions.

With the combination of a rotating mapping system and x-ray detector, it is possible to collect precious information about field emitted electrons. Such detailed data concerning x-ray are valuable tool in order to understand field emission behaviour inside superconducting cavities.

Aside the greater resolution and sensitivity of x-ray detection, with respect to conventional temperature mapping, x-ray detection is able to gather information from cavity region usually not accessible for temperature sensors like cavity iris. The iris, as will be shown in the dissertation, have a pivotal role for field emission in RF cavities, their geometry and local surface electric field can strongly influence the cavity performance with respect to field emission phenomena, due to this is mandatory to collect data, during cavity testing, from this region.

The data acquired during vertical tests and high power tests will be analyzed to determine the emitter properties and location. This will allow to understand the complex relation between cavity geometry, operating condition and field emission effect.

More generally, through a systematic study it will be possible to derive some general aspects about field emission with respect to different cavity geometry in order to achieve a deeper process understanding and possibly do some step towards its reduction or elimination.

1.4 Dissertation layout

The dissertation starts from the theoretical background needed to understand cavities performance, their testing and field emission quantum mechanics behavior (chapter 2). Chapter 3 is devoted to explain the analytical and experimental tools needed to investigate field emission processes and their effects on cavity performance. The experimental setup will be described in chapter 4. In chapter 5, the experimental data are analyzed by means of analytical tools developed in chapter 3. In the conclusion chapter the critical aspects of field emission effect related to cavities design and how to exploit some of them in order to reduce its impact on cavity performance will be presented.

Chapter references

1. Halbach, K. and R. Holsinger, *SUPERFISH-a computer program for evaluation of RF cavities with cylindrical symmetry*. part. Accel., 1976. **7**(LBL-5040): p. 213-222.
2. Menzel, M. and H. Stokes, *Users guide for the POISSON/SUPERFISH Group of Codes*, 1987, Los Alamos National Lab., NM (United States).
3. Podlech, H., *Superconducting versus normal conducting cavities*. arXiv preprint arXiv:1303.6552, 2013.
4. Phinney, N., N. Toge, and N. Walker, *ILC reference design report volume 3-accelerator*. 2007.
5. Nakamura, N., *Review of ERL Projects at KEK and Around the World*. TUXB02, these proceedings, 2012.
6. Sakanaka, S., et al. *Status of ERL and cERL projects in Japan*. in *Proc. Linac*. 2010.
7. Tigner, M., *A possible apparatus for electron clashing-beam experiments*. *Il Nuovo Cimento* (1955-1965), 1965. **37**(3): p. 1228-1231.
8. Smith, T., et al., *Development of the SCA/FEL for use in biomedical and materials science experiments*. *Nuclear Instruments and Methods in Physics Research Section A: Accelerators, Spectrometers, Detectors and Associated Equipment*, 1987. **259**(1): p. 1-7.
9. Umemori, K., et al. *Design of L-band superconducting cavity for the energy recovery linacs*. in *APAC*. 2007.
10. Geng, R.-L., *Review of new shapes for higher gradients*. *Physica C: Superconductivity*, 2006. **441**(1): p. 145-150.
11. HamatsuPhotonics, S1223.
<http://www.hamamatsu.com/us/en/product/category/3100/4001/4103/S1223/index.html>.
12. Sakai, H., et al., *Cavity diagnostics using rotating mapping system for 1.3 GHz ERL 9-cell superconducting cavity*. *IPAC*. **10**: p. 2950.
13. Fowler, R.H. and L. Nordheim, *Electron emission in intense electric fields*. *Proceedings of the Royal Society of London. Series A, Containing Papers of a Mathematical and Physical Character*, 1928. **119**(781): p. 173-181.
14. Ginsburg, C., *Superconducting RF R&D Towards High Gradient*. proceedings of LINAC08, Victoria, British Columbia, Canada, 2008.
15. Padamsee, H., et al., *RF Superconductivity for Accelerators*. *Physics Today*, 1999. **52**: p. 54.
16. Yunn, B.C. and R.M. Sundelin. *Field emitted electron trajectories for the CEBAF cavity*. in *Particle Accelerator Conference, 1993., Proceedings of the 1993*. 1993. IEEE.
17. Gopych, M., et al., *Study of dark current phenomena in a superconducting accelerating cavity at the S-DALINAC*. *Nuclear Instruments and Methods in Physics Research Section A: Accelerators, Spectrometers, Detectors and Associated Equipment*, 2005. **539**(3): p. 490-498.

CHAPTER II

Theory

Abstract

In this section will be discussed the theoretical background needed to understand superconductive cavity properties and their design by means of Electro-Magnetic theory. The quantum mechanical theory will be introduced in order to understand the field emission process and how it can affect the cavity performance. In the last part will be explained how during vertical test the cavity performance are inspected.

2.1 Particle acceleration

A particle immersed in an electro-magnetic field experience a force \mathbf{F} proportional to the electric and magnetic field, the Lorentz force. That can be written as:

$$\vec{\mathbf{F}} = \frac{d\vec{\mathbf{p}}}{dt} = q(\vec{\mathbf{E}} + \vec{\mathbf{v}} \times \vec{\mathbf{B}}), \quad (2.1)$$

where q is the particle charge \mathbf{E} and \mathbf{B} are the electric and magnetic field while \mathbf{v} is the particle speed. Due to the high speed reached by particle it is necessary to use the relativistic equation of motion and dynamics, in this framework the particle total energy W can be expressed as:

$$W = \sqrt{(m_0 c^2)^2 + (pc)^2} = \gamma m_0 c^2, \quad (2.2)$$

where m_0 is the particle rest mass and γ is the Lorentz factor, function of the particle speed. The first term in the sum take into account the rest mass energy while the second the particle momentum. From this it is straightforward to derive the kinetic energy expression that is the difference between the total energy and the rest mass energy

$$W_{kin} = (\gamma - 1) m_0 c^2. \quad (2.3)$$

The change in the particle energy can be expressed in differential form as [1]

$$WdW = c^2 \vec{\mathbf{p}} \cdot d\vec{\mathbf{p}} = c^2 \vec{\mathbf{p}} \cdot q(\vec{\mathbf{E}} + \vec{\mathbf{v}} \times \vec{\mathbf{B}}) dt = qc^2 \vec{\mathbf{p}} \cdot \vec{\mathbf{E}} dt \quad (2.4)$$

$$\vec{\mathbf{v}} = \frac{\vec{\mathbf{p}}}{m_0 \gamma}, \quad (2.5)$$

that leads to

$$dW = q\vec{\mathbf{v}} \cdot \vec{\mathbf{E}} dt. \quad (2.6)$$

That means that only the electric field can change the particle energy, so it is important to design a proper accelerating structure where particles can strongly interact with the electric field.

2.2 Electro Magnetic field theory

The first step in any electro-magnetic calculation shall be the introduction to the Maxwell equations, their differential form is [2]:

$$\nabla \times \vec{B} = \mu_0 \left(\epsilon_0 \frac{\partial \vec{E}}{\partial t} + \vec{J} \right), \quad \nabla \times \vec{E} = -\frac{\partial \vec{B}}{\partial t}, \quad (2.7)$$

$$\nabla \cdot \vec{B} = 0, \quad \nabla \cdot \vec{E} = \frac{\rho}{\epsilon_0}. \quad (2.8)$$

where μ_0 and ϵ_0 are the vacuum permittivity and permeability, \vec{J} is the current density and ρ is the charge density, while \vec{E} and \vec{B} are the electric and magnetic field.

A special case for the above equations can be calculated when the current density and the charge density are zero, that is considering an electromagnetic field filling a space in vacuum. In this condition the Maxwell equations can be expressed in their differential form as:

$$\nabla \times \vec{B} = \frac{1}{c^2} \frac{\partial \vec{E}}{\partial t}, \quad \nabla \times \vec{E} = -\frac{\partial \vec{B}}{\partial t}, \quad (2.9)$$

$$\nabla \cdot \vec{B} = 0, \quad \nabla \cdot \vec{E} = 0. \quad (2.10)$$

Reminding that $\nabla \times (\nabla \times \vec{F}) = \nabla(\nabla \cdot \vec{F}) - \nabla^2 \vec{F}$ the above equations lead to the Helmholtz equation

$$\frac{1}{c^2} \frac{\partial^2 \vec{E}}{\partial t^2} - \nabla^2 \vec{E} = 0, \quad (2.11)$$

the same can be written for the magnetic field

$$\frac{1}{c^2} \frac{\partial^2 \vec{B}}{\partial t^2} - \nabla^2 \vec{B} = 0. \quad (2.12)$$

Both equation can describe a sinusoidal plane wave propagating in the space at speed c .

The above equations can be written in a compact form using the D'Alembert operator defined as

$$\square \stackrel{\text{def}}{=} \frac{1}{c^2} \frac{\partial^2}{\partial t^2} - \nabla^2. \quad (2.13)$$

In this for the wave equations become simply

$$\square \vec{E} = 0 \text{ or } \square \vec{B} = 0. \quad (2.14)$$

Looking at the second Maxwell equation in its integral form

$$\oint_{\partial \Sigma} \vec{E} \cdot d\vec{l} = - \frac{d}{dt} \iint_{\Sigma} \vec{B} \cdot d\vec{\sigma}. \quad (2.15)$$

Where Σ is surface with $\partial \Sigma$ as contour, it is clear that on a closed loop without a time changing magnetic field the total electric field work is zero and so will be the change in the particle kinetic energy following a closed loop. So if a particle shall be accelerated on a closed loop a magnetic field variation in time it is needed, so that its derivative with respect to time is different from zero.

2.3 RF resonator

A good starting point to understand an RF resonator (or a so called RF cavity) could be a simple RLC circuit with equipped with a series of electrical lumped elements. A resistor R , a capacitor C and an inductance L .

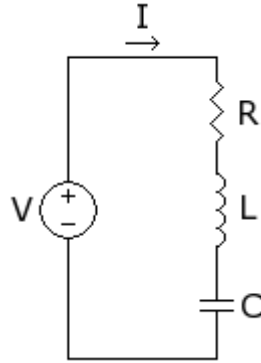


Figure 2.1 RLC circuit scheme.

The voltage drop at each circuit element can be written as

$$V_R + V_L + V_C = V(t). \quad (2.16)$$

Expanding each term we can obtain:

$$R i(t) + L \frac{di}{dt} + \frac{1}{C} \int_{-\infty}^{\tau=t} i(\tau) d\tau = V(t). \quad (2.17)$$

Differentiating both equation side and assuming a constant voltage V applied to the circuit the following differential equation for the charge Q can be obtained

$$R \frac{dQ(t)}{dt} + L \frac{d^2Q(t)}{dt^2} + \frac{1}{C} Q(t) = 0. \quad (2.18)$$

Rearranging the equation following the derivation order it becomes

$$\frac{d^2Q(t)}{dt^2} + \frac{R}{L} \frac{dQ(t)}{dt} + \frac{1}{LC} Q(t) = 0. \quad (2.19)$$

This is a well known differential equation, indeed if instead charge we define a displacement, the equation describe a harmonic damped mechanical oscillator.

$$\frac{d^2x(t)}{dt^2} + c \frac{dx(t)}{dt} + \frac{k}{m}x(t) = 0 \quad (2.20)$$

Describing the action of a spring with constant k on a mass m with a friction proportional to the speed with a constant c . The $x(t)$ coefficient define the resonant frequency $\omega_0 = \sqrt{\frac{k}{m}}$ while the coefficient in front of $\frac{dx(t)}{dt}$ describe the damping factor.

In the same way the lumped circuit represent a damped harmonic oscillator, but instead of an oscillating displacement, is the charge that change with time. The resonant frequency $\omega_0 = \frac{1}{\sqrt{LC}}$ is determined by the capacitor and the inductance, while the damping factor is proportional to the ratio between the resistance and the inductance.

2.3.1 LC circuit

Considering a circuit with a negligible resistance it behaves as a harmonic oscillator. Without a damping element, it can preserve its oscillation as long as any other perturbation appear.

The charge oscillation can be described as follow

$$\frac{d^2Q(t)}{dt^2} + \omega_0^2 Q(t) = 0. \quad (2.21)$$

It is analog to the equation describing the oscillating voltage for a RLC circuit (without a dissipative element):

$$\frac{d^2V(t)}{dt^2} + \frac{1}{RC} \frac{dV(t)}{dt} + \frac{1}{LC} V(t) = 0. \quad (2.22)$$

Equation 2.22 describes an oscillating voltage $V(t)$ instead of an oscillating charge, but the resonant frequency is still $\omega_0 = \frac{1}{\sqrt{LC}}$, indeed it depends only on capacitance and inductance.

2.3.2 From lumped circuit to cavity resonator

Lets imagine the most simple parallel LC circuit, made of one capacitor and one inductance [2], the circuit will have a resonant frequency of $\omega_0 = \frac{1}{\sqrt{LC}}$ as seen above. If we want to raise the resonant frequency, while keeping the same capacitance, the inductance shall be decreased, it can be done by reducing the number of turns in the inductance coil. Continuing this process until we just have one single wire connecting the top and bottom plates of the capacitor (Figure 2.2). To increase further the frequency it is possible to add more parallel inductance made of a single wire, connecting top and bottom plates as shown in Figure 2.2.

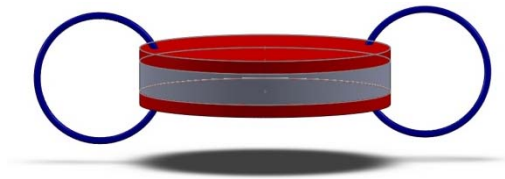


Figure 2.2 Capacitor connected with “single-loop” inductance.

If we keep adding single wire around the capacitor it is possible to create a complete enclosed resonant system (Figure 2.3).

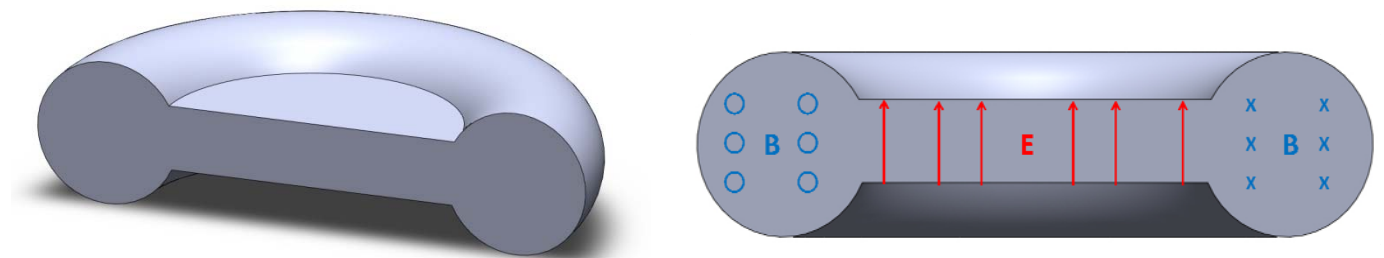


Figure 2.3 Resonator obtained from a capacitor enclosed by “single-loop” inductances.

At this point it is clear the analogy between a RLC lumped circuit and an enclosed resonator, thus it is straightforward to define the natural resonant frequency $\omega_0 = \frac{1}{\sqrt{LC}}$.

2.3.3 Forced RF resonator

If the circuit is fed with an RF voltage it is possible to calculate the circuit response with respect to the fed frequency.

The voltage equation can be written as:

$$\frac{d^2V(t)}{dt^2} + \gamma \frac{dV(t)}{dt} + \omega_0^2 V(t) = V_0 e^{j\omega t}. \quad (2.23)$$

The circuit is fed with an external RF generator that oscillate with frequency ω while the natural frequency ω_0 is $\frac{1}{\sqrt{LC}}$, and the damping factor γ takes into account any dissipative element.

The general solution of this differential equation can be describe as $V(t) = A e^{j\omega t}$, by substituting this expression in the differential equation we obtain an algebraic equation.

$$-A \omega^2 e^{j\omega t} + j\gamma A \omega e^{j\omega t} + A \omega_0^2 e^{j\omega t} = V_0 e^{j\omega t}, \quad (2.24)$$

dividing both term by $e^{j\omega t}$ we obtain

$$A = \frac{V_0}{\omega_0^2 - \omega^2 + j\gamma\omega}. \quad (2.25)$$

The circuit oscillation amplitude (A) is proportional to the applied voltage amplitude multiplied by a factor that depends on the natural frequency, the feeding frequency and the damping coefficient. This factor is a complex number and can be written in a general form as $\rho e^{j\theta}$ where ρ is the module and θ is the phase.

The square of the module (that is proportional to the electric power) can be written as

$$\rho^2 = \frac{1}{(\omega_0^2 - \omega^2)^2 + \gamma^2 \omega^2} \quad (2.26)$$

Through this it is possible to understand some general feature of the oscillating circuit:

- At low feed frequency, down to zero, the circuit response tends to be equal to $\frac{V_0}{\omega_0^2}$
- At very high frequency, much higher than the natural one, the oscillation is almost negligible and it tends to zero while the frequency increase
- At the resonance, when $\omega = \omega_0$, the maximum oscillation amplitude is equal to $\frac{V_0}{\gamma \omega}$ and not infinity as we can expect from an ideal case without any damping coefficient

Further by plotting the module of the oscillating voltage against the feeding frequency ω we obtain the curve shown in Figure 2.4.

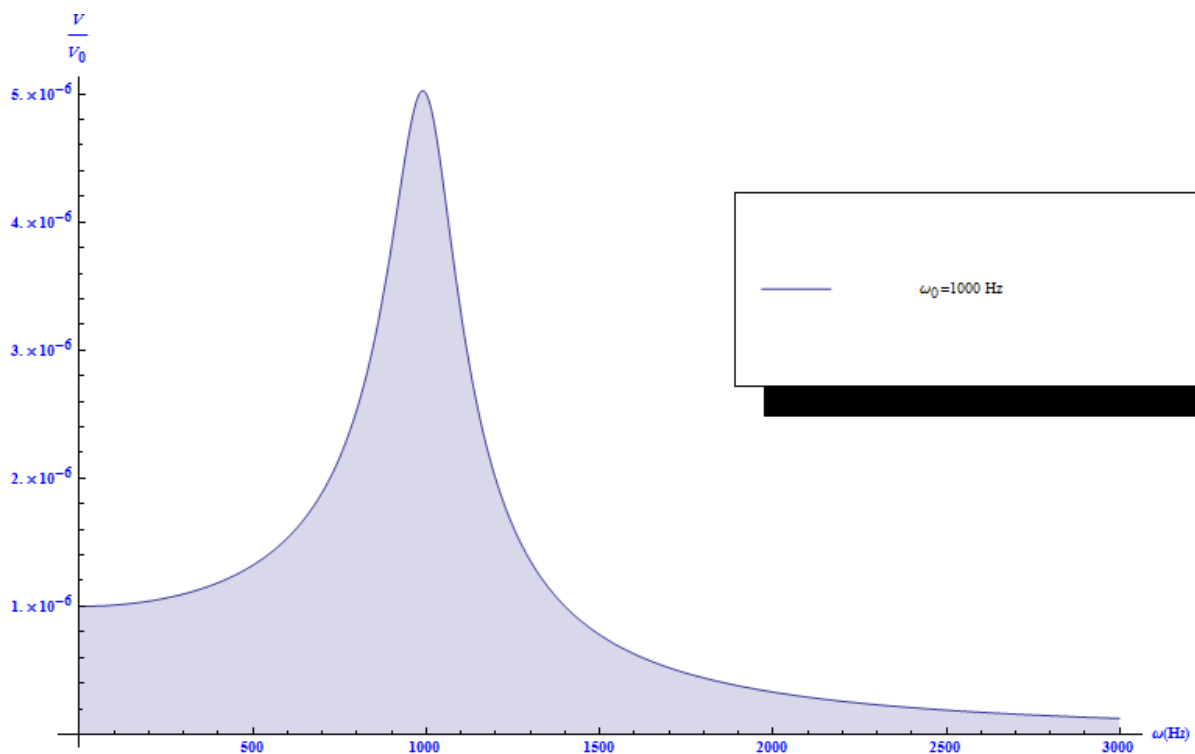


Figure 2.4 Resonance curve. Circuit voltage against the feeding frequency, the natural frequency is 1000Hz and the damping factor is 200.

The curve (Figure 2.4) describe circuit response, in terms of voltage amplitude, with respect to the feeding frequency, the calculation was carried out by using a resonant circuit with a damping coefficient equal to 200 and a natural frequency equal to 1000Hz.

To understand the implication concerning the damping coefficient it is possible to calculate an approximated expression for ρ when the feeding frequency is near the resonance [2]. In this framework it becomes

$$\rho^2 \approx \frac{1}{(\omega_0 - \omega)^2 + \gamma^2}, \quad (2.27)$$

that represent a Lorentzian function where γ is the full width at half maximum.

From this we can define two important quantities (figure of merit), the bandwidth $\Delta\omega=\gamma$ and the resonator quality factor $Q = \frac{\omega_0}{\Delta\omega}$. The first one represent the frequency interval within the voltage amplitude is reduce by half (-3db), the second one represent how much peaked is the resonance curve or, as we will see later, the ratio between the stored energy in the circuit and the dissipated power in each cycle.

To close this section we can analyze the phase part of the circuit response factor $\rho e^{j\theta}$, to determine which implication it has on the resonator response.

Briefly recalling the previous result we can write that

$$A = \frac{V_0}{\omega_0^2 - \omega^2 + j\gamma\omega} = V_0 \rho e^{j\theta}, \quad (2.28)$$

where

$$\rho = \sqrt{\frac{1}{(\omega_0^2 - \omega^2)^2 + \gamma^2\omega^2}}. \quad (2.29)$$

By some simple substitution we can obtain that

$$\operatorname{tg}(\theta) = \frac{-\gamma\omega}{\omega_0^2 - \omega^2}. \quad (2.30)$$

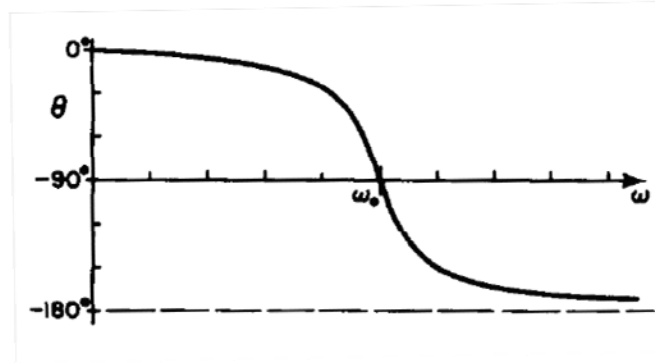


Figure 2. 5 Phase shift with respect to the driving frequency (from Feynman lectures on physics [2]) at resonance frequency the response lag 90° respect to the feeding.

As can be seen in Figure 2. 5, the $e^{j\theta}$ introduce a phase shift between the feed signal and the circuit response, at the resonance the circuit response lag the feed signal by 90° .

2.4 RF cavity design

By adding two holes on the resonator axis (Figure 2.3) allow a charged particle to enter the enclosed volume parallel to the electric field and be accelerated. This simple design is commonly called Pillbox cavity.

The resonator basic features were already described before, thus we can go further to analyze its figure of merit common to any other RF cavity design.

Aside to its conceptual simplicity the other main features are that we can solve analytically the Maxwell equations and obtain the exact profile of the electric and magnetic field stored in the cavity volume.

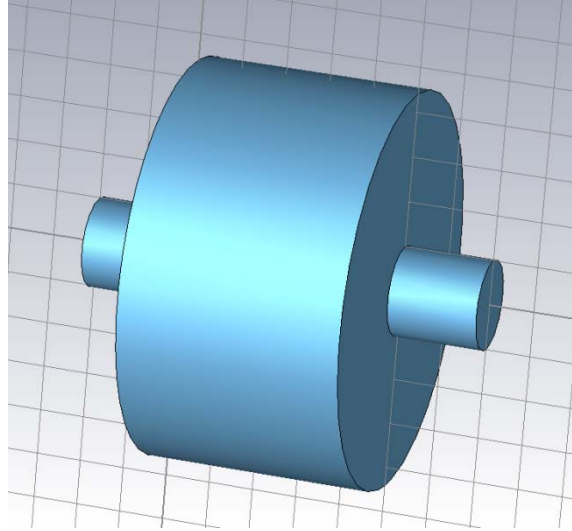


Figure 2. 6 Pillbox cavity model.

Once an electromagnetic field is confined into a defined volume it will satisfy specific boundary conditions, in particular if a conductor surface is used, thus the tangential component of the electric field and the normal component of the magnetic field shall be zero at the boundaries.

The Maxwell equation in free space state:

$$\frac{1}{c^2} \frac{\partial^2 \vec{E}}{\partial t^2} - \nabla^2 \vec{E} = 0 \text{ and } \frac{1}{c^2} \frac{\partial^2 \vec{B}}{\partial t^2} - \nabla^2 \vec{B} = 0, \quad (2.31)$$

by adding the boundary condition for a perfect conductor

$$n \times \vec{E} = 0 \text{ and } n \cdot \vec{B} = 0 \quad (2.32)$$

and expressing the gradient in cylindrical coordinates we can obtain:

$$\frac{\partial^2 \vec{E}_z}{\partial z^2} + \frac{1}{r} \frac{\partial}{\partial r} \left(r \frac{\partial \vec{E}_z}{\partial r} \right) + \frac{\omega^2}{c^2} \vec{E}_z - \frac{1}{c^2} \frac{\partial^2 \vec{E}_z}{\partial t^2} = 0. \quad (2.33)$$

Through variable separation the electric field can be written as a product between a function depending on space variable and a time varying one as

$$\vec{E}_z(r, t) = \vec{E}_z(r) \vec{E}_z(t). \quad (2.34)$$

The function of space becomes

$$\frac{\partial^2 \vec{E}_z}{\partial z^2} + \frac{1}{r} \frac{\partial}{\partial r} \left(r \frac{\partial \vec{E}_z}{\partial r} \right) + \frac{\omega^2}{c^2} \vec{E}_z = 0, \quad (2.35)$$

this equation is the Bessel differential equation, it appears anytime we have to deal with resonator with a cylindrical shape, its solutions are well known so in this case all the detailed calculation are not shown and we can jump directly to the complete solution [3-5].

Introducing these conditions and exploiting the cylindrical symmetry it is possible to express the electric field along the cavity axis (E_z Z by convention) where the particles are accelerated.

Charged particles enter the cavity at $Z=0$ and exit at $Z=L$, during their flight they will interact with the electric field defined by the following equation:

$$\vec{E}_z(r, t) = \vec{E}_0 J_0 \left(\frac{\omega r}{c} \right) e^{i\omega t}. \quad (2.36)$$

Where $J_0(\omega r/c)$ is the first kind Bessel function, for cylindrical wave it plays the same role as the cosine function for plane wave.

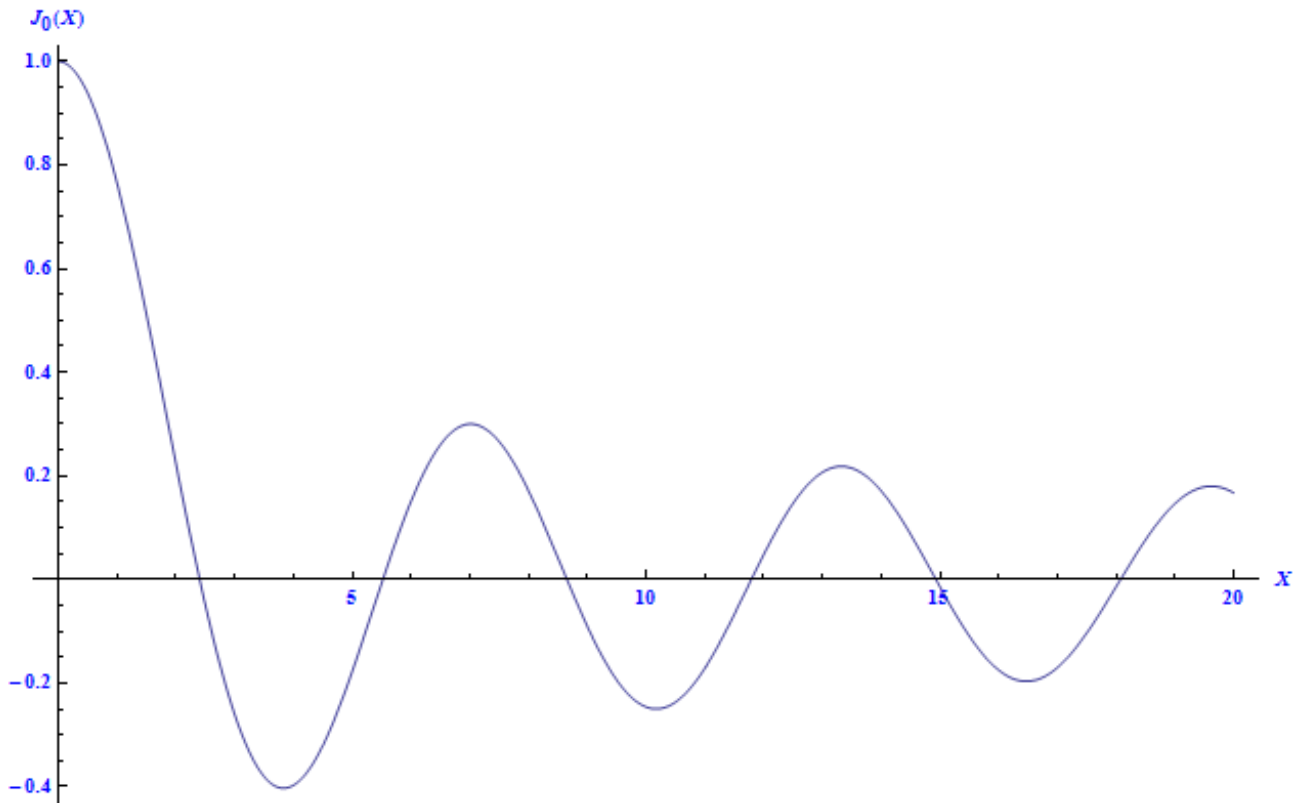


Figure 2.7 First kind Bessel function $x = \frac{\omega r}{c}$.

By recalling the boundary conditions, we know that \mathbf{E}_z shall vanish at the cavity surface so

$$\vec{\mathbf{E}}_z(\mathbf{R}_{cav}, t) = 0 \quad (2.37)$$

To fulfill this condition the J_0 function shall be zero on the cavity surface, the first zero can be found at $\frac{\omega r}{c} \approx 2.405$ [3] as can be seen in Figure 2.7.

This implies that the resonant frequency depends only on the cavity radius

$$\omega_0 \approx \frac{2.405 c}{R_{cav}}. \quad (2.38)$$

Higher resonant modes can be obtained by using other Bessel function zeros.

Each mode can be defined with respect to its symmetry, by convention it is used the direction along which the particles are accelerated (Z axis).

In this framework we can define:

- **Transverse Magnetic modes (TM):** There is no magnetic field along the propagation direction (only transverse component)
- **Transverse Electric modes (TE):** There is no electric field along the propagation direction (only transverse component)
- **Transverse Electromagnetic (TEM):** Neither electric nor magnetic field along the propagation direction
- **Hybrid:** Both electric and magnetic field are present along the propagation direction

It is straightforward, as we state in the introduction, that to accelerate a charged particle we need an electric field along its direction of flight, thus TM series is the most suitable. In cylindrical coordinates they can be listed by using three numbers, defining how many half-wavelength are present in a specific direction, they are ordered as $TM_{\phi r z}$. The first subscript refer to azimuthal coordinate, the second to the radial coordinate and the third to the longitudinal direction.

In the Figure 2. 8 is represented the electric field inside a pillbox cavity defined by parameters listed in table 2.1. It is the first resonant mode (corresponding to the first Bessel function zero) for the TM family.

Table 2.1 Pillbox cavity dimensions and natural frequency.

| Property | Value |
|---|--------------|
| Cavity Radius (R_{cav}) | 8.827 cm |
| Cavity Length (L) | 10 cm |
| ω_0 | 1304 MHz |

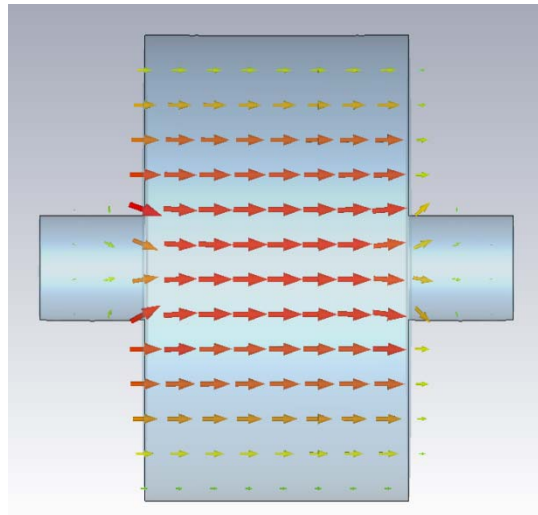


Figure 2. 8 Pillbox cavity, electric field for TM_{010} mode.

By cutting the pillbox on different plane it is possible to appreciate the dependence of the electric field (or magnetic) with respect to coordinates change. In Figure 2. 9 can be seen the electric field (lines and arrows) along with the magnetic field (circle) in the Z - R plane.

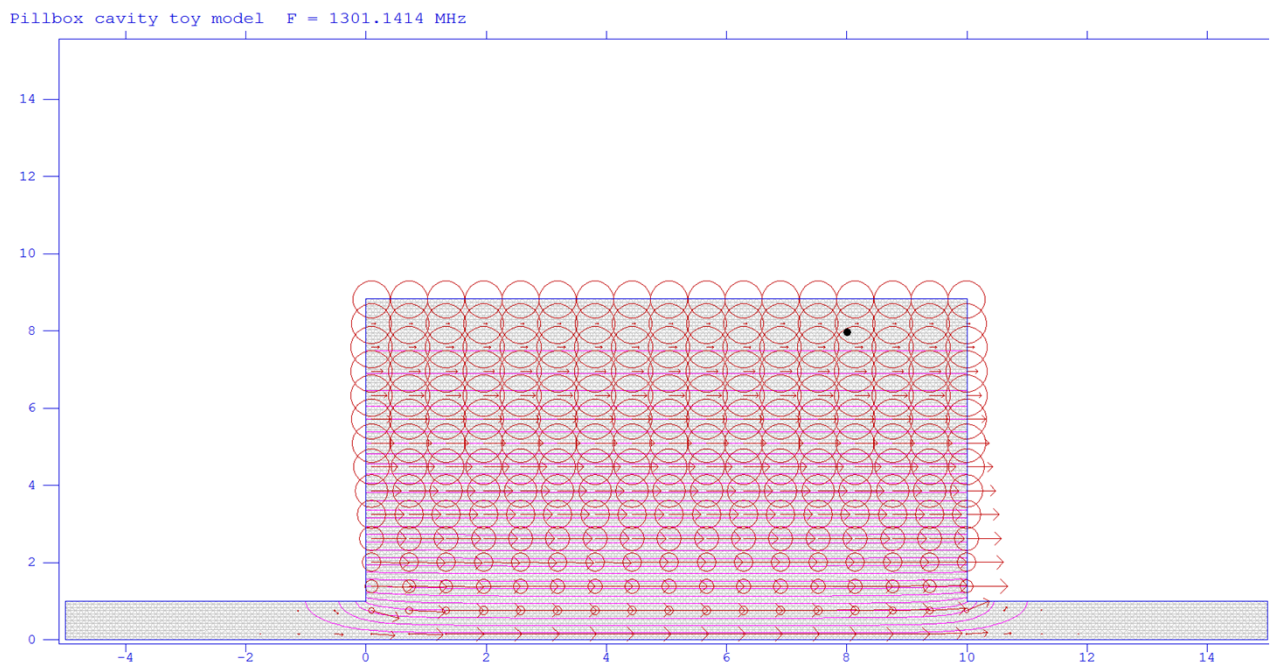


Figure 2. 9 Pillbox cavity, electric and magnetic field for TM_{010} mode.

The electric field along the Z direction is maximum in cavity center while the magnetic field is maximum near the equator wall (Figure 2. 10).

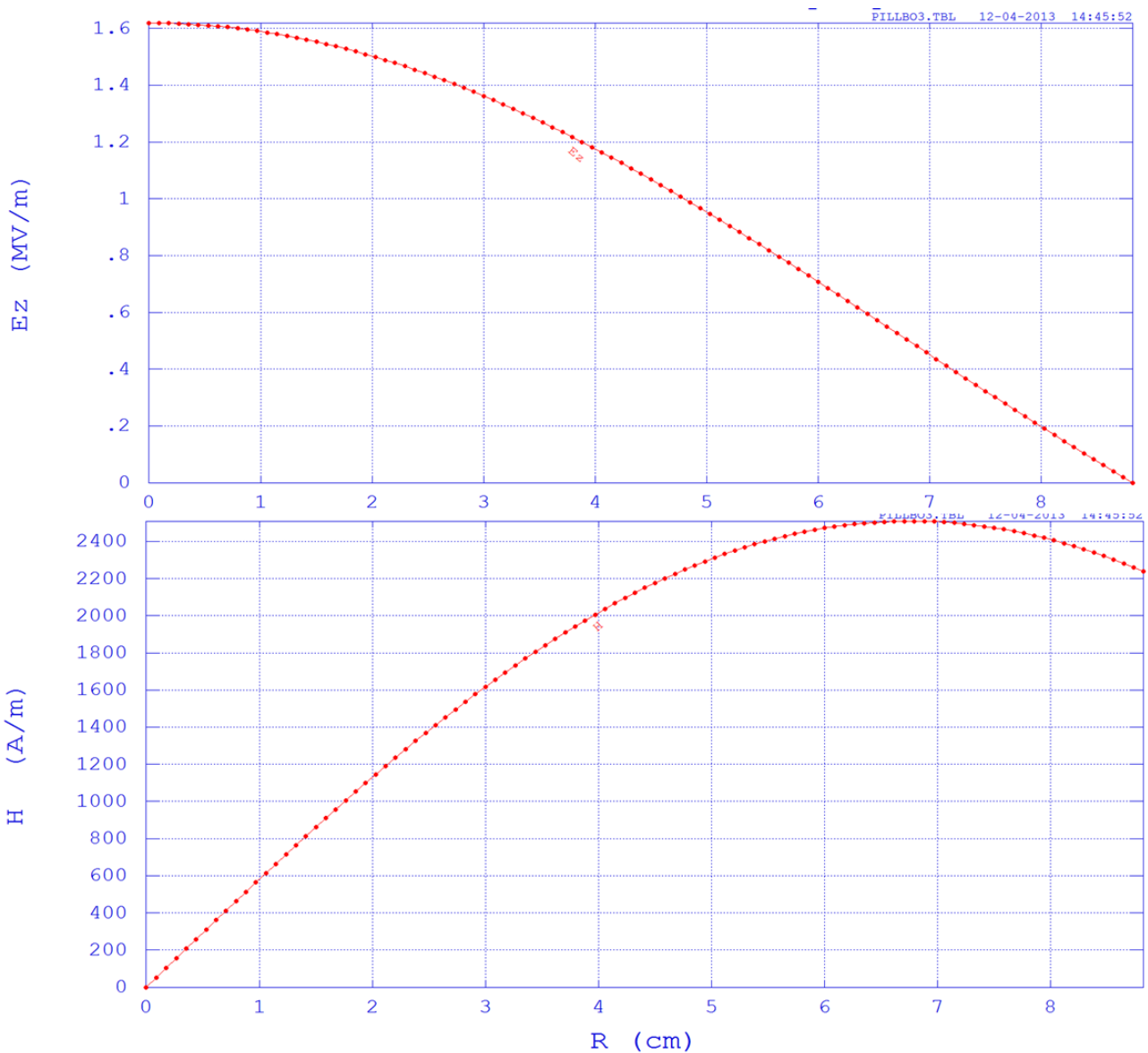


Figure 2. 10 Electric and magnetic field intensity with respect to radial coordinates for TM_{010} mode .

To accelerate charged particles it is important to have a strong electric field in their direction of motion, at the same time the magnetic field shall be minimized to avoid deflection that leads to emittance increase.

In Figure 2. 11 can be appreciated the electric field components along the cavity axis, the radial component is zero that is the electric field is pointing along the z-axis.

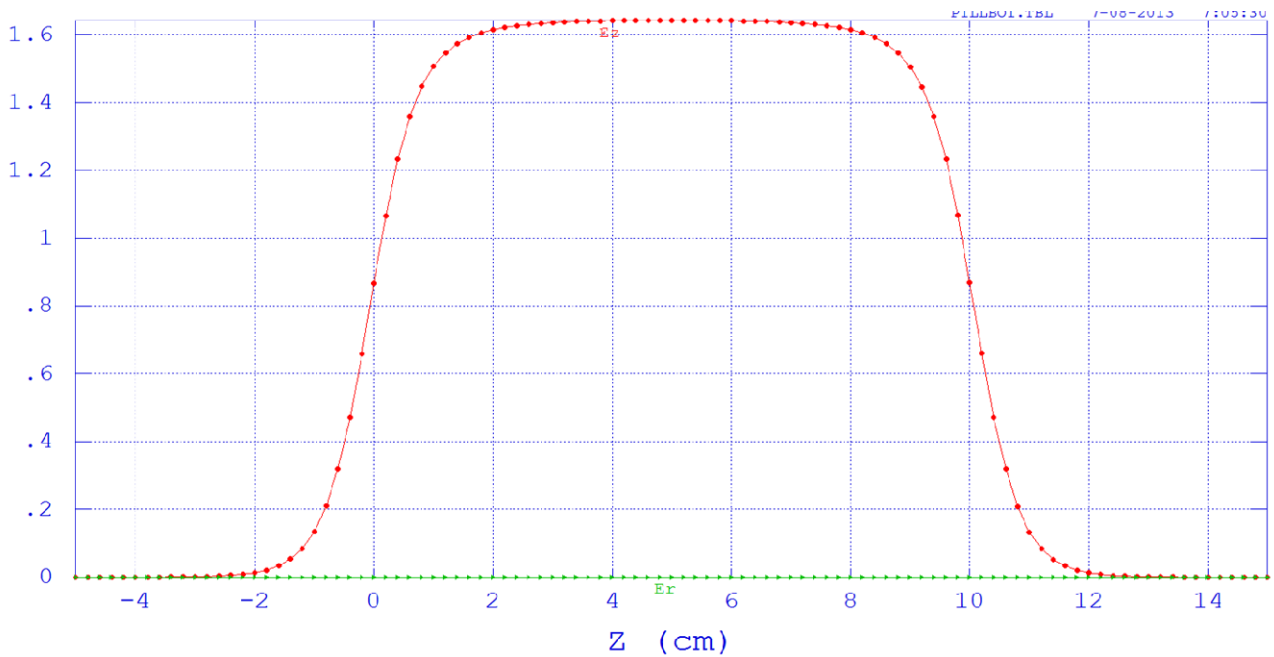


Figure 2. 11 Electric field components along the Pillbox cavity axis for TM_{010} .

From pictures above can be appreciated that TM_{010} mode is optimal for particles acceleration, electric field magnitude is maximum on cavity axis, while the radial component and the magnetic field is minimum.

2.5 Figures of merit

Now that we know the electromagnetic field pattern inside the cavity we can calculate some important quantities (figure of merit) in order to evaluate its performance also with respect to other geometries.

Through the Bessel function we have already found that the resonant frequency for the fundamental TM_{010} mode as shown in equation 2.38.

2.5.1 Cavity voltage and Transit time factor

To calculate the electric voltage inside a DC capacitor we shall simply multiply the electric field by the distance between the capacitor plates:

$$V = E \cdot d. \quad (2.39)$$

But for the RF cavity it must be taken into account that the electric field is changing while the particle is moving inside it with a speed $v = \beta c$. Thus the cavity voltage (or accelerating voltage) can be expressed as

$$V_{acc} = \int_{-\frac{L}{2}}^{\frac{L}{2}} \vec{E}_z e^{i\omega t} dz = \int_{-\frac{L}{2}}^{\frac{L}{2}} \vec{E}_z e^{i\frac{\omega z}{\beta c}} dz \quad (2.40)$$

where the time variable is substituted by

$$t = \frac{z}{\beta c}. \quad (2.41)$$

And the accelerating field E_{acc} is defined as

$$E_{acc} = \frac{V_{acc}}{L}, \quad (2.42)$$

where L is the cavity length.

Frequently it is also define the ratio between the accelerating voltage and the ideal (non-physical) voltage as a particle moving at infinite speed, it is called Transit Time Factor (TTF)[1, 4, 5].

$$TTF = \frac{\left| \int_{-\frac{L}{2}}^{\frac{L}{2}} \vec{E}_z e^{i\frac{\omega z}{\beta c}} dz \right|}{\left| \int_{-\frac{L}{2}}^{\frac{L}{2}} \vec{E}_z dz \right|} \quad (2.43)$$

By definition the transit time factor belongs to the interval [0,1]. It represents the ratio between the real energy gain and the ideal one so that:

$$W_{gain} = eV_0 TTF, \quad (2.44)$$

where eV_0 is the energy gain as the particle move at infinite speed or, from another point of view, the energy that a charged particle, with charge e , can have passing through a gap with a constant voltage V_0 . Because the transit time factor is always less than 1 that means that the energy gain will be always a fraction of the ideal case.

For the pillbox cavity the calculation is simple, in fact the transit time factor for particle moving on the cavity axis is [1]

$$TTF = \frac{\left| \int_{-\frac{L}{2}}^{\frac{L}{2}} \vec{E}_z(\mathbf{0}, z) \cos(\omega t) dz \right|}{\left| \int_{-\frac{L}{2}}^{\frac{L}{2}} \vec{E}_z(\mathbf{0}, z) dz \right|} = \frac{\left| \sin\left(\frac{\omega L}{2\beta c}\right) \right|}{\frac{\omega L}{2\beta c}} = \frac{\left| \sin\left(\frac{\pi K L}{\beta}\right) \right|}{\frac{\pi K L}{\beta}} \quad (2.45)$$

where L is the cavity length and βc is the particle speed, the image below (Figure 2. 12) shows how the transit time factor change with respect to $\frac{KL}{\beta}$ where K is defined as:

$$K = \frac{2\pi}{\lambda_{RF}} \quad (2.46)$$

related to the RF wave length.

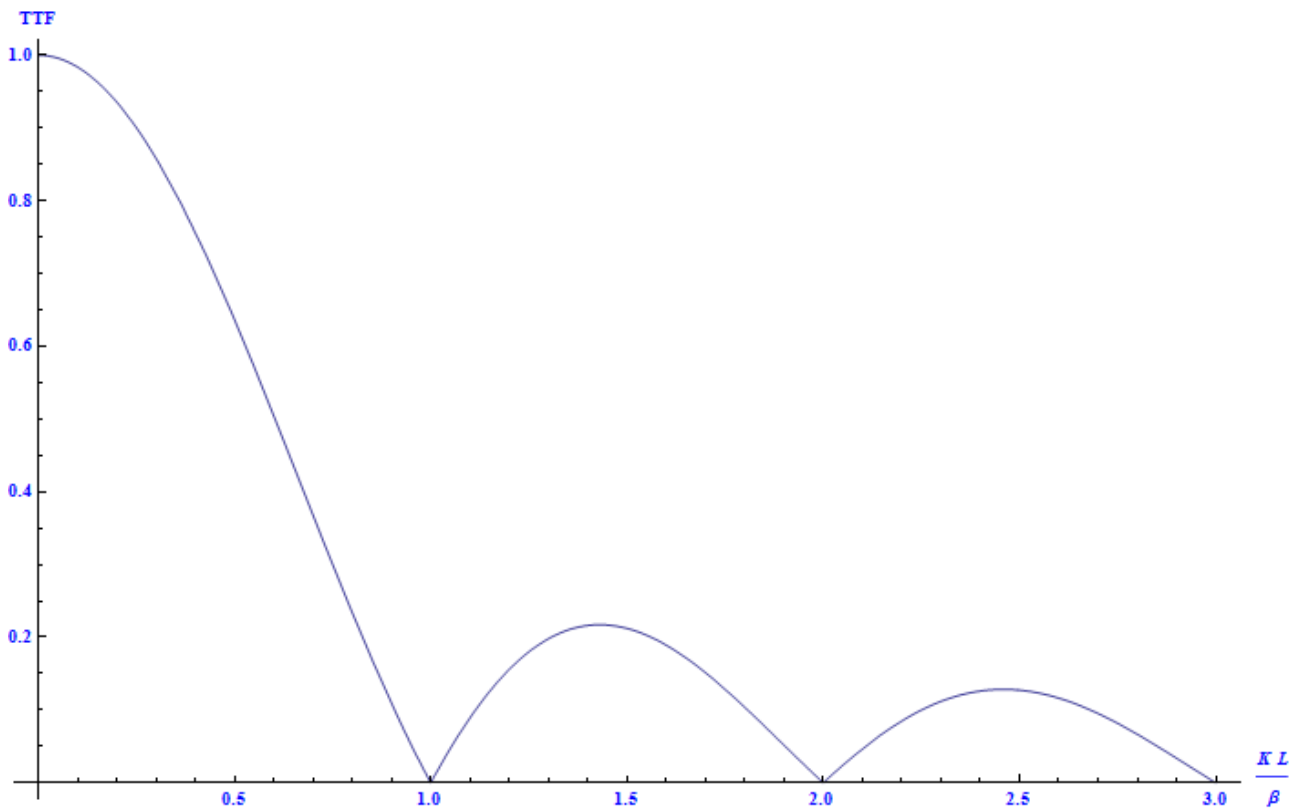


Figure 2. 12 Transit time factor for pillbox cavity.

Once the cavity frequency and particle speed is fixed than the cavity length can be optimized to maximize the transit time factor. If the cavity length has a value that $L = \frac{N\beta}{K}$, where N is an integer number, the transit time factor is equal to zero. That means that during the flight inside the cavity the particle net energy gain is also zero, i.e. this could happen if the particle is first accelerated and then decelerated or vice versa.

2.5.2 Surface resistance and Power loss

Another important quantity is the power loss in cavity walls, during the Bessel equation calculation we have considered an ideal conductor, but in reality we shall consider a finite surface resistance even for superconducting material.

The surface resistance origin for normal and superconductor come from different factors, but in both case generate power dissipation in the cavity wall. In a normal conductor the field can penetrate into the material and generate a current density

$$J(d) = J_0 e^{-\frac{d}{\delta}} \quad (2.47)$$

The distance where the current density is reduced by a factor e it is called skin depth and has a value of

$$\delta = \sqrt{\frac{2}{\omega \mu \sigma}} \quad (2.48)$$

where ω is the RF frequency, μ is the material magnetic permeability and σ is the material conductivity.

Further it is possible to define the surface resistance as

$$R_s = \frac{1}{\delta \sigma} = \sqrt{\frac{\omega \mu}{2 \sigma}} \quad (2.49)$$

commonly for copper used for RF cavities its value is in the range of milliohms.

For superconducting material the surface resistance can be divided in two part, one that depends on RF frequency and temperature can be estimated using Bardeen-Cooper-Schrieffer (BCS) theory, the

other depends on different factor such as material inclusion, hydride formation and magnetic flux pinning and is called residual resistance [5].

It can be defined as

$$\mathbf{R}_s = \mathbf{R}_{BCS} + \mathbf{R}_{res} \quad (2.50)$$

Where \mathbf{R}_{BCS} takes into account that the cooper pairs, that at DC current have zero resistance, still have a finite mass, when they are immersed into a RF field their momentum change according to the electric field leading to a small energy dissipation.

For Niobium at temperature less than 4K \mathbf{R}_{BCS} can be approximated as [6]

$$\mathbf{R}_{BCS} \approx 2 * 10^{-4} \left(\frac{\omega}{1.5 * 10^9} \right)^2 \frac{e^{-\frac{17.67}{T}}}{T}, \quad (2.51)$$

where T is the temperature and ω the cavity frequency.

Considering a Niobium cavity at 2K and 1.3GHz frequency the BCS resistance is about 10n Ω , and it drops at 1.5n Ω when the temperature is decreased to 1.6K.

The residual resistance, depending on its origin, can be the leading term in the summation and shall be evaluated case by case, typical value can span from some n Ω to tens of n Ω .

The presence of a surface resistance generate a power dissipation into the cavity walls, it can be calculated as [5]

$$\mathbf{P}_{loss} = \frac{1}{2} \mathbf{R}_s \int_S |\vec{\mathbf{H}}|^2 d\mathbf{S}, \quad (2.52)$$

where S is the cavity surface and \mathbf{H} is the magnetic field near the surface.

From the expression above it is clear that the power dissipation in a superconducting cavity is several order of magnitude less than a normal conducting. Comparing two cavities with the same geometry and filled with the same electromagnetic field inside, the power loss ratio is

$$\frac{P_{loss}^{Cu}}{P_{loss}^{Nb@2K}} = \frac{R_s^{Cu}}{R_s^{Nb@2K}} = \frac{10^{-3}}{10^{-8}} = 100,000 \quad (2.53)$$

The power loss in the normal conducting cavity is hundred thousand times bigger than for Niobium at 2K. For this reason in many application superconducting material results to be the material of choice.

It shall be made a closing remark about power dissipation, while the copper cavity exchange the excess of head load with a reservoir at ambient temperature, the superconducting cavity exchange its heat load with the cryogenic bath at 2K. In order to evaluate the real power consumption shall be taken into account also the refrigerator efficiency. It can be written as [6]

$$\eta = \frac{2K}{300K - 2K} \cdot 0.25 = 0.17\%, \quad (2.54)$$

the first term is the theoretical limit as stated in the Carnot cycle theory and 0.25 factor is the refrigerator efficiency [6]. The above results implies that to remove one watt delivered at 2K we need to supply about 600W to the refrigeration system.

2.5.3 Q value and Geometry factor

As seen before, for the resonant lumped circuit, also for the RF cavity a quality factor is defined. It represents not only the ratio between the resonant frequency and the bandwidth but also the ratio between the stored energy and the dissipated power in each cycle.

$$Q_0 = \frac{\omega_0 U}{P_{loss}}. \quad (2.55)$$

Where the stored energy is $U = \frac{\mu}{2} \int_V |\vec{H}^2| dV = \frac{\varepsilon}{2} \int_V |\vec{E}^2| dV$ and the dissipated power is $P_{loss} = \frac{1}{2} R_s \int_S |\vec{H}^2| dS$, where μ is magnetic permeability, ε is the electric permittivity and R_s is the surface resistance.

Using the above definition it is possible to define a quantity that is independent from material property the cavity geometry factor, defined as:

$$G = \frac{\omega_0 \mu \int_V |\vec{H}^2| dV}{\int_S |\vec{H}^2| dS}. \quad (2.56)$$

So the quality factor can be re-written as

$$Q_0 = \frac{G}{R_s}. \quad (2.57)$$

2.5.4 Shunt impedance

Reminding the Ohm law where the dissipated power by the resistive element is the ratio between the square of the voltage with respect to the resistance $P = \frac{V^2}{R}$, by analogy we can apply a similar definition for the RF cavity.

The shunt impedance is defined as the ratio between the square of the accelerating voltage and the dissipated power, so that

$$R_{shunt} = \frac{V_{acc}^2}{P_{loss}}. \quad (2.58)$$

It can be seen as how efficiently the cavity can sustain an accelerating voltage with respect to the dissipated power. Due to the fact that the accelerating voltage depends on the electric field line

integral, the shunt impedance is different for each cavity mode. For the accelerating mode an higher shunt impedance is preferable.

Very often it is defined with respect to the cavity length L just as

$$r_{shunt} = \frac{R_{shunt}}{L}, \quad (2.59)$$

that is the shunt impedance per unit length.

Sometime it is also defined an uncorrected shunt impedance Z that needs to be multiply by the transit time factor, as follow, to obtain the correct value

$$R_{shunt} = Z \cdot TTF^2 \quad (2.60)$$

2.5.5 R over Q

Dividing the shunt impedance by the quality factor can be evaluated how efficiently the cavity can sustain a voltage with respect to the stored energy

$$\frac{R}{Q} = \frac{V^2}{\omega_0 U}. \quad (2.61)$$

An higher “R over Q” is preferable for the accelerating mode, while for Higher Order Modes (HOMs) it should be as low as possible. While the shunt impedance depends on cavity material, the R over Q depends only on the cavity geometry.

2.5.6 Peak fields

During cavity design aside all the previous quantity it is important to consider the electromagnetic field intensity on the cavity surface. A strong surface magnetic field can lead easily to quench the

superconductor or induce a too high power dissipation for normal conducting cavity, while a strong surface electric field enhance the field emission.

Often as figure of merit are presented the ration between the peak field on the surface (magnetic and electric H_{pk} , E_{pk}) with respect to the accelerating field (E_{acc}). Different optimal solution should be considered with respect to the cavity application, just as example in the TESLA cavity the ratio $\frac{E_{pk}}{E_{acc}}$ is about 2 while $\frac{H_{pk}}{E_{acc}}$ is about $42 \frac{\text{Oe}}{\frac{\text{MV}}{\text{m}}}$ [7]. Theoretical limit for magnetic field is about 2300Oe for Nb at 1.3GHz [8] so a TESLA cavity can achieve a maximum of $54 \frac{\text{MV}}{\text{m}}$ before quenching, in practice most of the cavity quench around 1800Oe [8] limiting the accelerating field to $43 \frac{\text{MV}}{\text{m}}$.

A cavity designed for high gradient operation shall be optimize considering carefully aside all the figure of merit also the magnetic field peak on the surface in order to avoid quenches.

For ERL a great effort were put in order to damp Higher Order Modes as much as possible, specially dipole modes that can easily increase the beam emittance. For this reason cavity iris are larger than the TESLA model, leading to $\frac{E_{pk}}{E_{acc}}$ increase, reaching a value about 3 [9].

The ERL cavity design details will be shown in the next section while a summary of all the previous figures of merit will be presented at the end of this paragraph, they are calculated for two pillbox cavities, one made with Copper and one with Niobium.

Table 2.2 Cavity figure of merit compared between a normal conducting and superconducting material pillbox cavity.

| Property | Normal conducting | Superconducting |
|----------------------------------|-----------------------------|-----------------------------|
| Cavity Radius (R_{cav}) | 8.827 cm | 8.827 cm |
| Cavity Length (L) | 10 cm | 10 cm |
| ω_0 TM010 | 1301 MHz | 1301 MHz |
| Temperature | 300 K | 2 K |
| Surface resistance (R_s) | $9 \times 10^{-3} \Omega$ | $2 \times 10^{-8} \Omega$ |
| Cavity Voltage (V_{acc}) | 100 KV | 100 KV |
| Power dissipation (P_{loss}) | 2458 W | 7 W |
| Stored Energy (U) | $7 \times 10^{-3} J$ | $7 \times 10^{-3} J$ |
| Transit time factor | 0.61 | 0.61 |
| Quality factor (Q_0) | 25590 | 9×10^9 |
| R/Q | 159 Ω | 159 Ω |
| Geometry Factor (G) | 240 Ω | 240 Ω |
| E_{pk}/E_{acc} | 2.2 | 2.2 |
| H_{pk}/E_{acc} | $31.5 \frac{Oe}{MV m^{-1}}$ | $31.5 \frac{Oe}{MV m^{-1}}$ |

2.5.7 Cell to cell coupling

For multicell cavity it is important to define also another parameter, the cell to cell coupling (K_{cc}) it define how stronger each cell is coupled to the nearest neighbor. It determines the amount of electromagnetic power (Poyting vector) passing from one cell to the next one and also the spreading in the passband modes dispersion curve.

The coupling can be realized by electric or magnetic field. By opening a slot in the equator region and connecting the cells the power is transmitted by means of magnetic field, while on the iris

opening it is transmitted through electric field. Any parameters that can change electric field intensity and iris opening affect the cell to cell coupling, for cavities where the iris area is enlarged or electric field is increased the cell to cell coupling becomes bigger.

By analogy with the lumped circuit the coupling element can be represented by a capacitor connecting the resonant circuits. Each circuit is no more independent from the neighbors, a perturbation in one circuit is transmitted to all the system. More easily the coupling can be seen with a mechanical analogy, like two oscillating pendulum connected by spring, the spring constant k determines how stronger the pendulum are coupled. Looking at the two extreme case we can appreciate the coupling meaning:

- *If the spring constant is high or rigid bar connecting the bobs:* the pendulum moves as one, a perturbation in the motion of the first one is completely transmitted to the second.
- *Without a spring or a spring with negligible elastic constant:* the pendulum behave independently, a perturbation in the motion of the first one is not transmitted to the second.

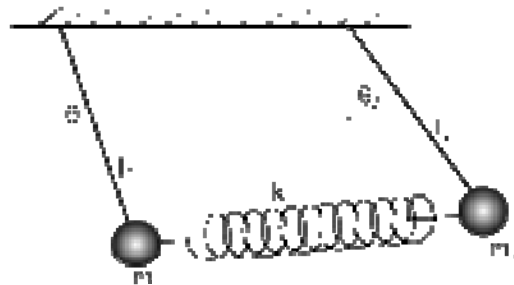


Figure 2. 13 Pendulum coupled through a spring with constant k .

A coupled resonant circuit behaves in the same way. Each cell can be seen as a resonant circuit and the electric field coupling at the iris can be represented by a capacitor (if the coupling is obtained through magnetic field the capacitor is substituted by an inductor).

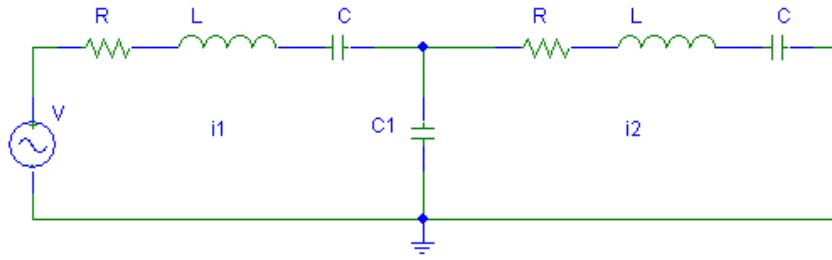


Figure 2. 14 Coupled resonant circuits, the coupling is obtained through a capacitor.

In the lumped circuit the coupling factor depends on the ratio $\frac{C}{C_1}$

In a multi cells structures the cell to cell coupling determines the spreading of frequencies in the dispersion curve, so it can be defined as [10]

$$K_{cc} = \frac{\Delta f}{\langle f \rangle} = \frac{2(f_{\pi} - f_0)}{f_{\pi} + f_0}. \quad (2.62)$$

It is the ratio between the maximum frequency spreading and the average frequency for the TM_{010} modes.

2.6 ERL cavity

In the previous paragraph we have defined the cavities figures of merit in order to “measure” the performance and compare different design solution. It is clear that depending on the particle accelerator requirement each design shall be optimized, i.e. if the machine require high gradient operation the surface peak fields (H_{pk} , E_{pk}) should be the major concern, a geometry that minimize their amplitude is preferable.

2.6.1 ERL machine requirements

The ERL synchrotron light source shall combine the good features of recent storage ring synchrotron facility and linear accelerator (Linac), to achieve this an electron beam of 100mA shall be accelerated to several GeV while preserving a small beam emittance, typical for a Linac. ERL machine promise to produce synchrotron light with high brilliance and long pulse duration outmatching storage rings technology.

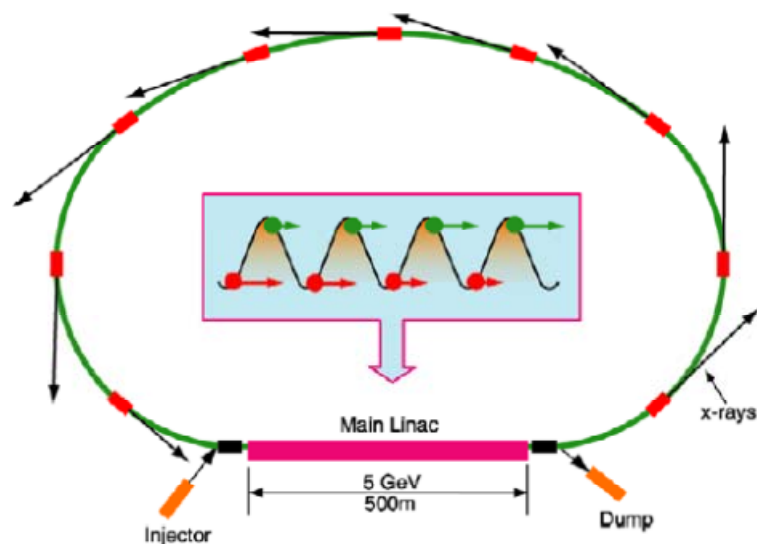


Figure 2. 15 5GeV ERL machine, green dots represent the accelerating beam and red dots represent the decelerating beam [11].

To be able to accelerate 100mA beam to several GeV energy, without any energy recovery, would be necessary to deliver several GW of power making this scheme practically unreachable, only by recovering part of the beam energy this kind of machine can be operated.

The energy is continuously exchange from damped beam to RF field and back to the new accelerated beam, because the cavities shall be always filled with electromagnetic field that means they shall operate in continuous wave (CW) mode.

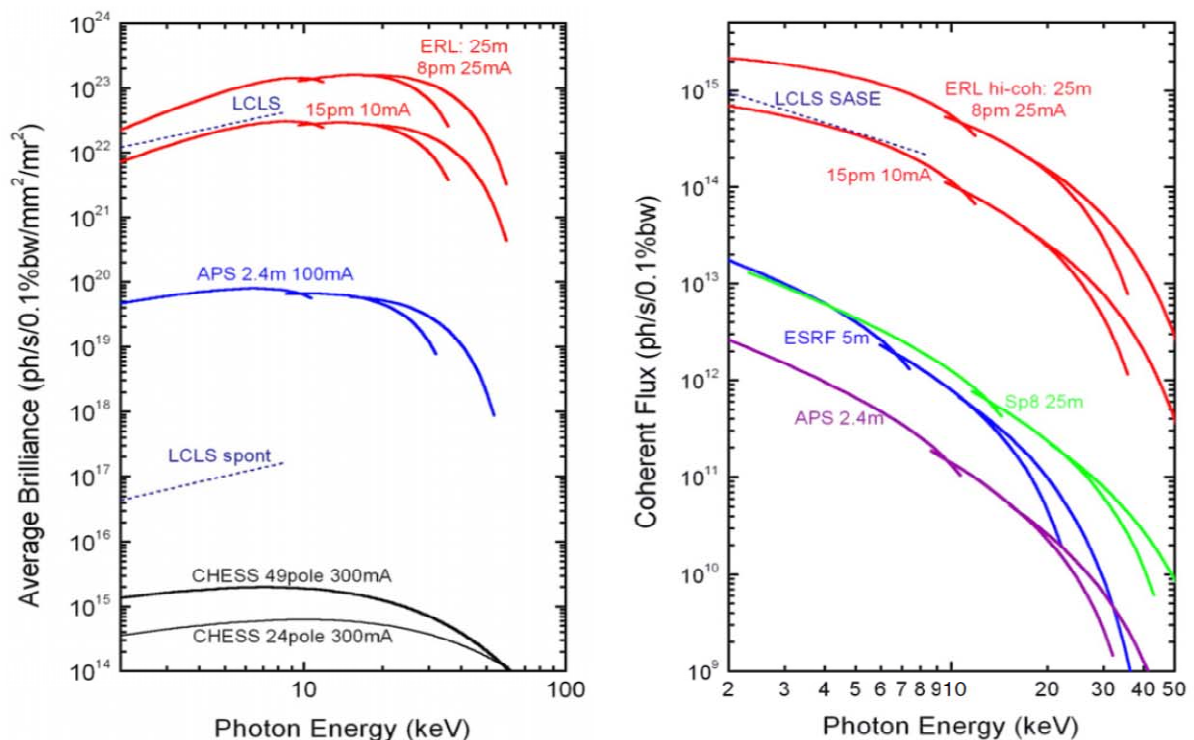


Figure 2. 16 Average brilliance and coherent flux for CHES, LCLS, APS, ESRF and ERL machine [11].

For normal conducting cavities continuous wave mode operation are very demanding, in terms of cooling power consumption, so a superconducting cavity is preferred for this working condition.

For ERL cavities one of the major concern are the High Order Modes excitation and trapping inside the cavity, because they can lead to a beam break up or just increase the beam emittance by “kicking” the particle away from the axis.

Typically the requirement concerning the HOMs for an ERL machine are [12]:

Table 2.2 HOM requirements for ERL machine.

| Mode | Requirement | Note |
|------------|--|--------------------------------------|
| Dipole | $\left(\frac{R}{Q}\right)\frac{Q}{f} < 1.4 \times 10^5 \left[\frac{\Omega}{cm^2 GHz} \right]$ | <i>BBU instabilities</i> |
| Quadrupole | $\left(\frac{R}{Q}\right)\frac{Q}{f} < 4 \times 10^6 \left[\frac{\Omega}{cm^4 GHz} \right]$ | <i>Quadrupole BBU instabilities</i> |
| Monopole | $\left(\frac{R}{Q}\right)Q < 2500 [\Omega]$ | <i>Heat load (100W at resonance)</i> |

Laboratories involved into ERL machine design found different optimal solution to address this problem, leading to different cavity design. In KEK was chosen a 9 cells L-band cavity, while other laboratories prefer a 7 cells model. The 9 cells cavity increase the accelerating mode shunt impedance and the overall machine packing factor reducing the costs, but can be more sensitive to HOM trapping with respect to shorter models (like 7 cells). During design a 7 cell model was analyzed, a reduction by half of the HOM impedances was obtained but also 20% reduction for the accelerating mode Shunt impedance, due to this reason the 9 cells designed was preferred [9].

To improve the HOMs damping many cavity parameter were checked leading to an optimal solution involving larger iris diameter, larger and asymmetric beam pipes with an eccentric flute on one side, the HOMs are then damped on a Ferrite ring located at both end (Figure 2. 17).

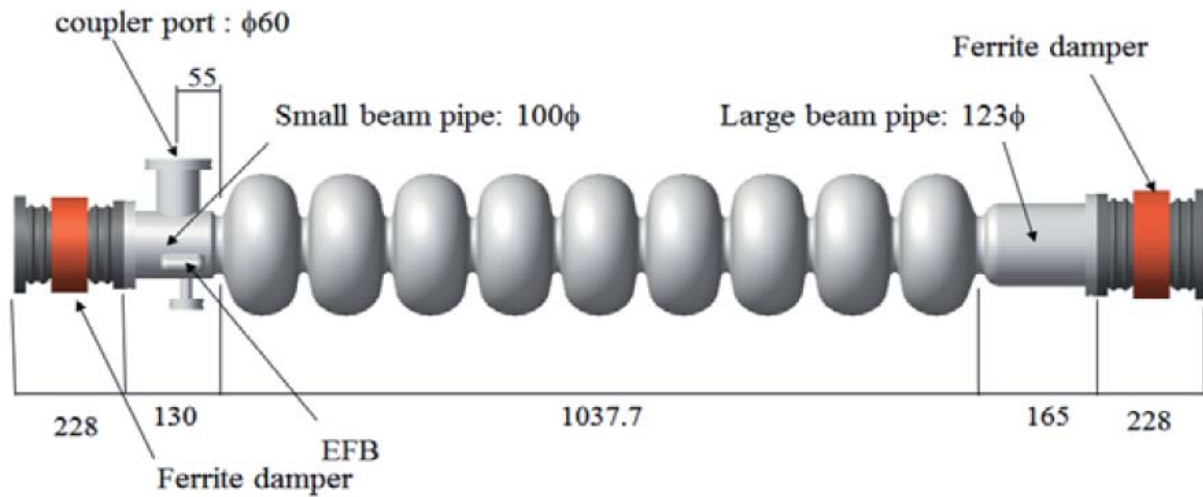


Figure 2. 17 KEK-ERL cavity with Ferrite HOM absorber (orange) [9].

In the KEK-ERL machine the main linac cavity shall operate in continuous mode while keeping an accelerating field of $15 \frac{MV}{m}$ with a quality factor $Q_0=10^{10}$ and resonant frequency for the TM_{010} mode of 1.3GHz.

The final optimized design consist of 9 elliptical shape cells, where the 7 central cells have the same geometry while the 2 end cells are slightly different in order to compensate the presence of the beam pipes. A list of geometry parameter can be found in the next figure and table.

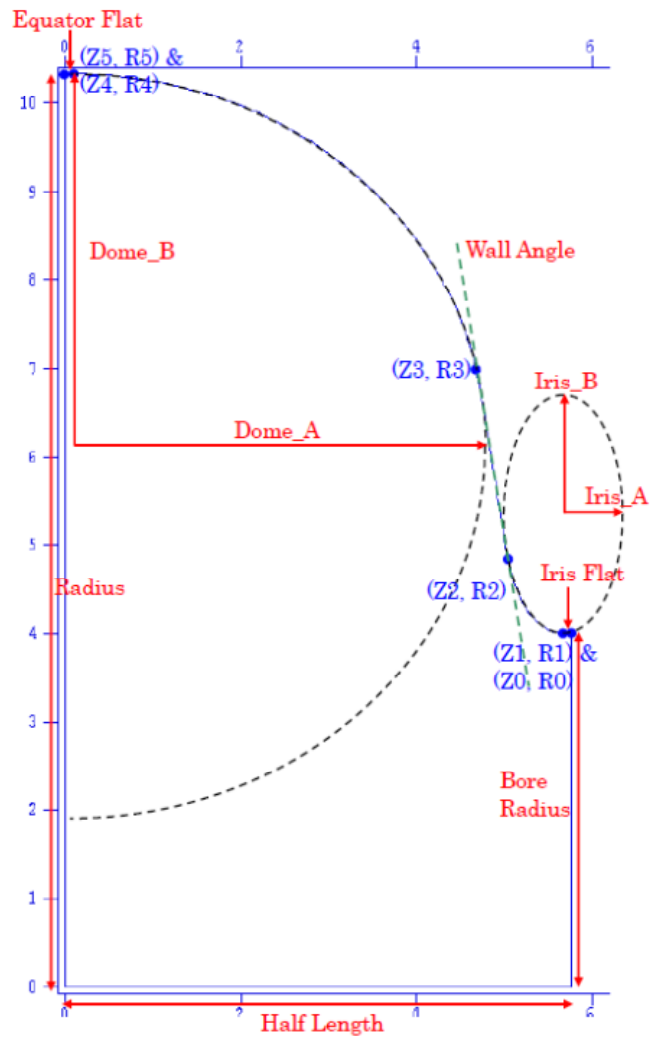


Figure 2. 18 KEK-ERL model 2 half cell schematic.

Table 2.3 KEK-ERL cavity geometry expressed in millimeter.

| Parameters | Left end cell | Central cells | Right end cell |
|------------------------|---------------|---------------|----------------|
| Half length | 57.674 | 57.652 | 57.675 |
| Radius | 103.3 | 103.3 | 103.3 |
| Bore radius | 42.0 | 40.0 | 42.0 |
| Dome A | 41.0 | 46.83 | 42.0 |
| Dome B | 41.0 | 42.0 | 42.0 |
| Equator flat | 1.0 | 1.0 | 1.0 |
| Iris A | 9.650 | 6.705 | 7.850 |
| Iris B | 9.650 | 13.409 | 7.850 |
| Iris flat | 1.0 | 1.0 | 1.0 |
| Wall angle | 15.85° | 9.22° | 17.09° |
| Small beam pipe radius | 50.0 | // | // |
| Large beam pipe radius | // | // | 61.5 |

The cavity figure of merit, are listed in Table 2.4 and compared to other design, like the baseline cavity for ILC and Low Loss cavity designed at JLAB. The calculation needed to compare the different geometries are done by means of finite element code (SuperFish [13, 14]). It can solve Maxwell equation for axial symmetry geometry and derive all the relevant quantity to evaluate cavity performance.

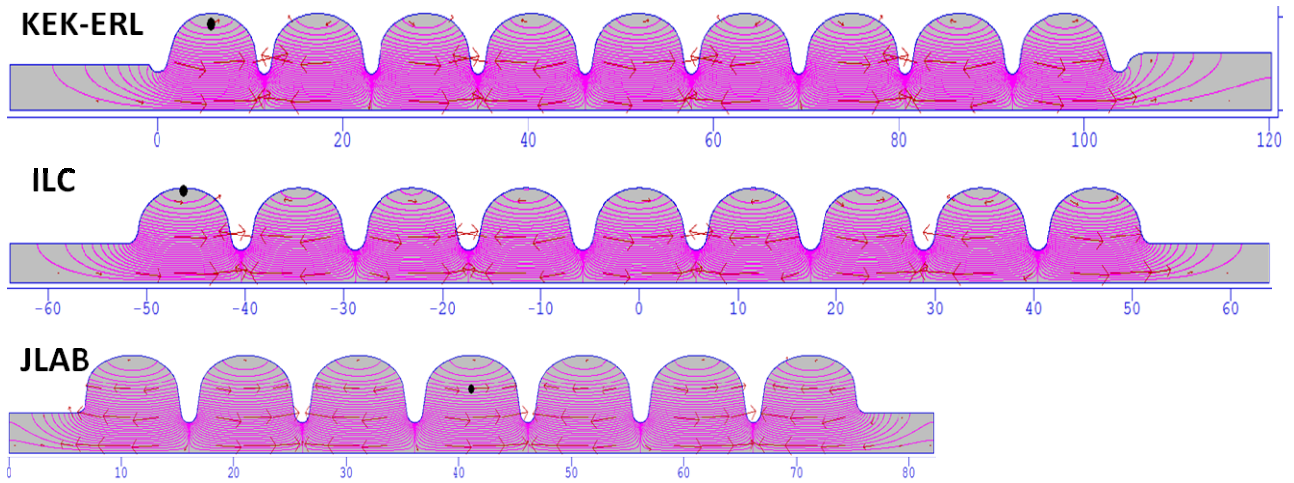


Figure 2. 19 From top to bottom, ERL mod2 cavity, ILC baseline cavity and JLAB low loss cavity. Electric field for π -mode are shown with contour and arrows.

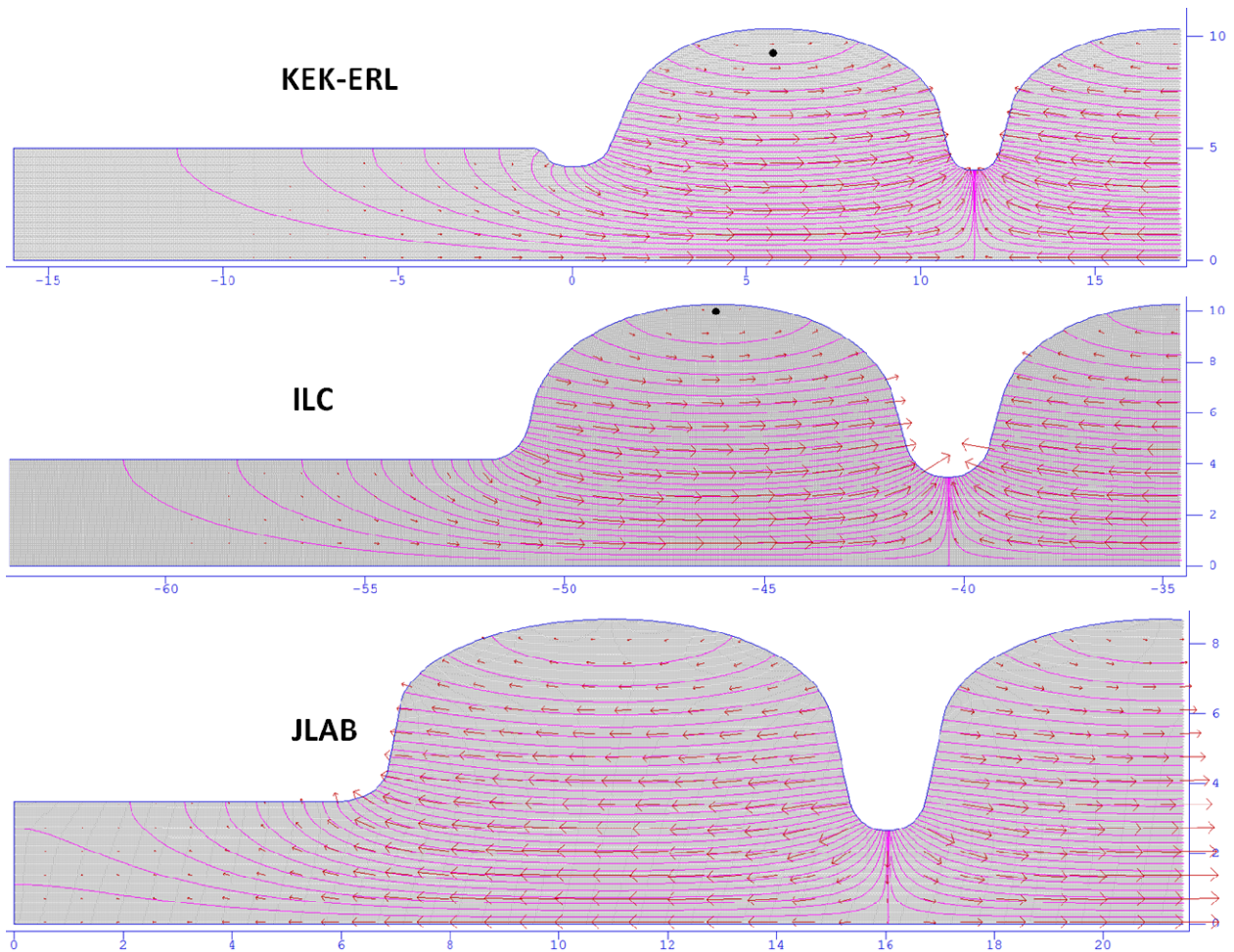


Figure 2. 20 Cavities left beam pipe and end cells.

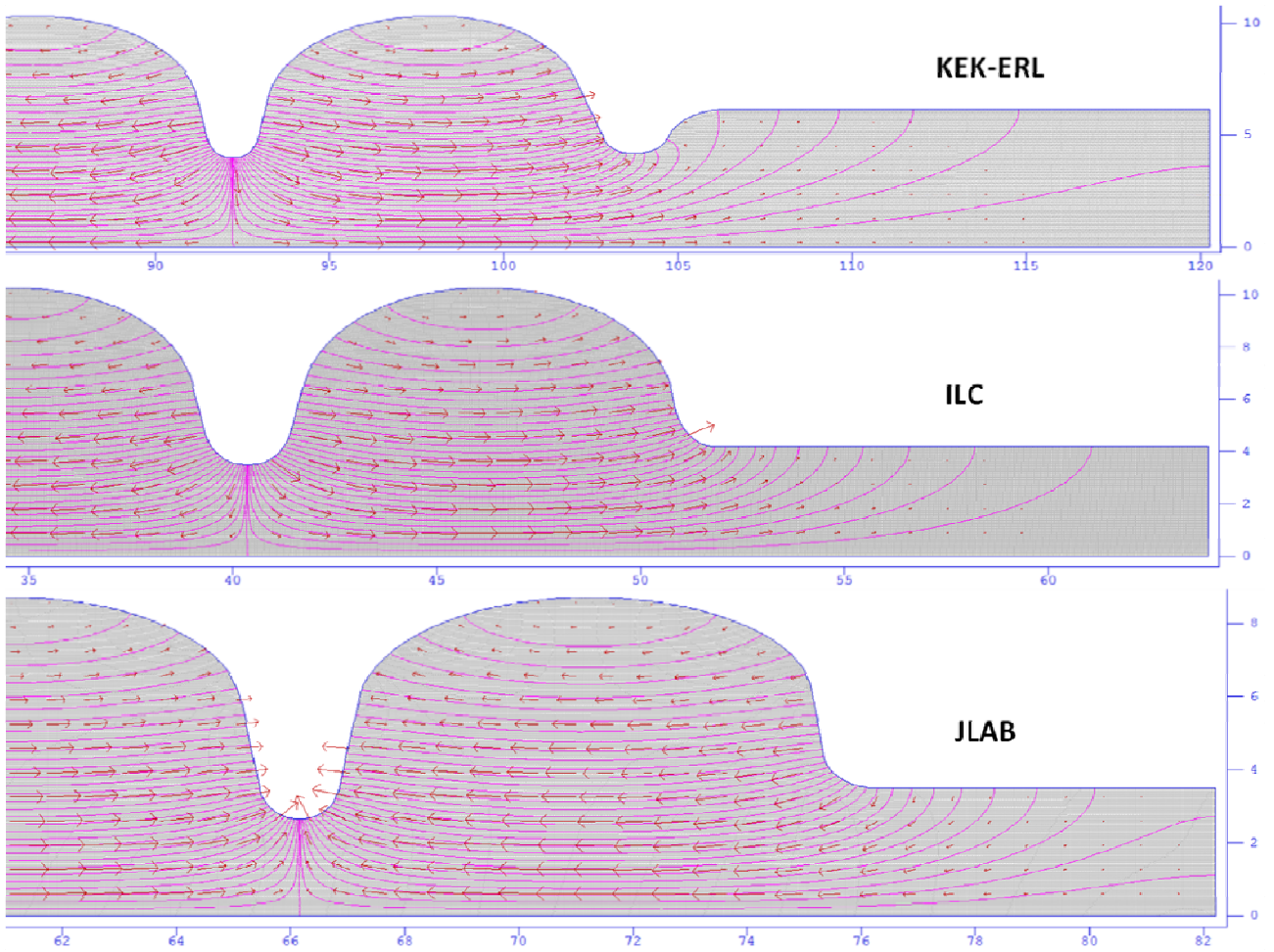


Figure 2. 21 Cavities right beam pipe and end cells.

Table 2.4 Comparison between different cavity design (ERL mod2, ILC baseline and JLAB low loss)

| Property | KEK-ERL mod2 | ILC | JLAB-LL |
|-------------------------------------|-------------------------------------|-------------------------------------|------------------------------------|
| Operating field | $15 \frac{MV}{m}$ | $35 \frac{MV}{m}$ | $12 \frac{MV}{m}$ |
| Operation mode | CW | Pulsed (1%) | CW |
| Cavity Length (L) | 103.77 cm ($9 \frac{\lambda}{2}$) | 103.77 cm ($9 \frac{\lambda}{2}$) | 70.18 cm ($7 \frac{\lambda}{2}$) |
| Cavity diameter | 20.66cm | 20.66cm | 17.4cm |
| ω_0 TM010 | 1300 MHz | 1300 MHz | 1495 MHz |
| Temperature | 2K | 2K | 2K |
| Surface resistance (R_s) | 26 n Ω | 26 n Ω | 22 n Ω |
| Accelerating Field (E_{acc}) | $1 \frac{MV}{m}$ | $1 \frac{MV}{m}$ | $1 \frac{MV}{m}$ |
| Power dissipation (P_{loss}) | 111 mW | 102 mW | 49 mW |
| Stored Energy (U) | 0.15 J | 0.13 J | 0.06 J |
| Transit time factor | 0.72 | 0.72 | 0.67 |
| Quality factor (Q_0) | 10^{10} | 10^{10} | $1.2 \cdot 10^{10}$ |
| R/Q | 896 Ω | 1018 Ω | 785 Ω |
| Geometry Factor (G) | 289 Ω | 277 Ω | 281 Ω |
| Iris radius | 4 cm | 3.5 cm | 2.65 cm |
| E_{pk}/E_{acc} | 3.0 | 2.0 | 2.3 |
| H_{pk}/E_{acc} | $42 \frac{Oe}{MV m^{-1}}$ | $42 \frac{Oe}{MV m^{-1}}$ | $40 \frac{Oe}{MV m^{-1}}$ |
| K_{cc} (cell to cell coupling) | 3.8% | 1.87% | 1.49% |

For the ERL cavity the optimization was mainly focused on the reduction of dipole modes HOM impedance, to avoid monopole HOM around multiple of 2.6GHz while keeping the accelerating mode R over Q as high as possible.

The first issue was addressed by enlarging the iris radius up to 40mm and with larger beam pipes, by doing this the HOMs impedance was significantly decreased while the accelerating mode impedance sustained a small decreasing [9].

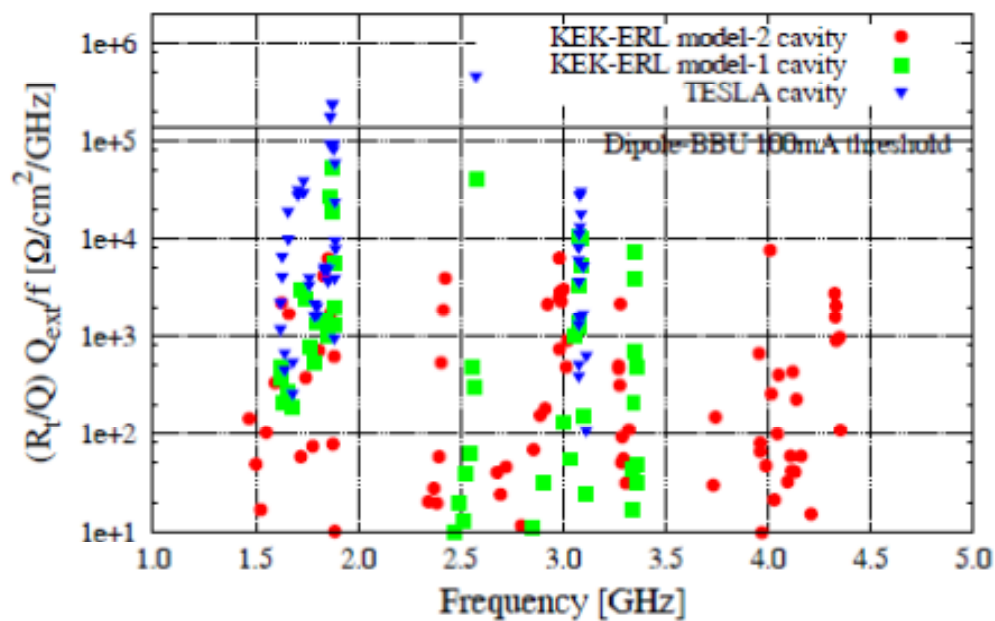


Figure 2. 22 Comparison between dipole HOM spectrum for TESLA cavity, ERL model 1 cavity (same as TESLA but with larger beam pipe) and final ERL model 2 cavity [9].

The second issue was solved by choosing carefully the cell diameter, the requirement was to keep the monopole HOMs frequency away from multiple of 2.6GHz at least by 40MHz, in order to take into account the fabrication precision, the choose diameter was 206.6mm.

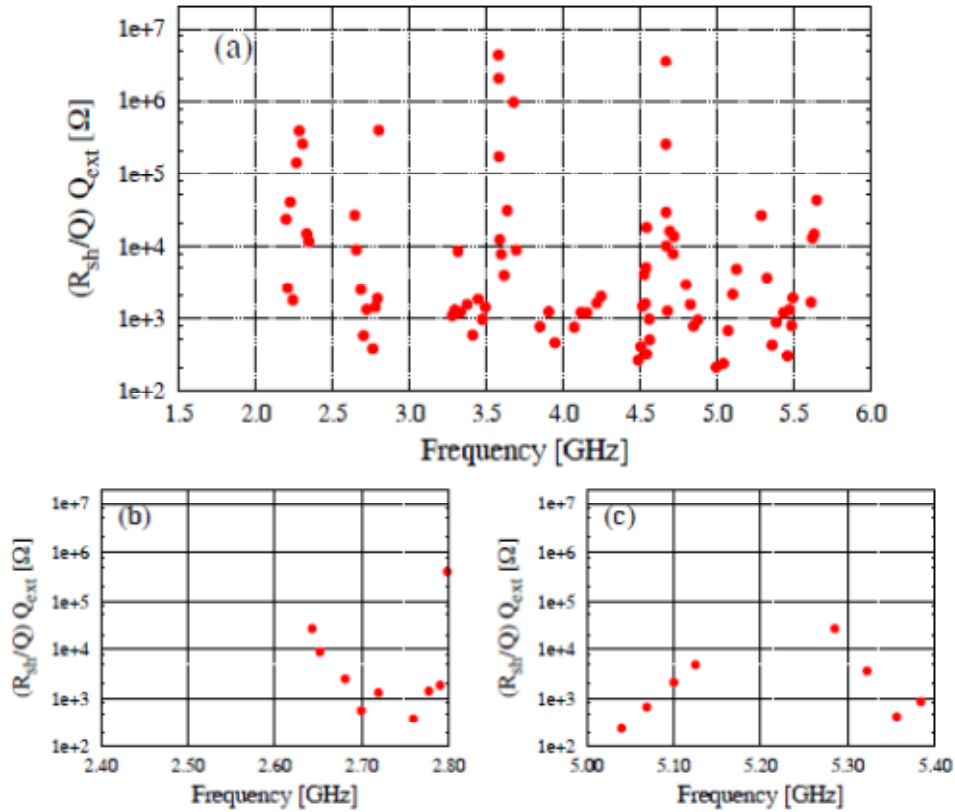


Figure 2. 23 Spectrum of Monopole HOMs around 2.6GHz and 5.2GHz [9].

The beam pipe diameter was selected in order to damp more efficiently TE_{111} and TM_{011} mode, the choice was 100mm for the small beam pipe (SBP) and 123mm for the large beam pipe (LBP). Ferrite absorber are installed at the end of the beam pipes instead of loop type absorber in order to avoid heating at CW operation [15].

A last note shall be written about eccentric fluted pipe, they were design as mode transformer, in order to convert quadrupoles modes (with a notorious high cut-off frequency) into dipole modes to obtain a more efficient damping [9].

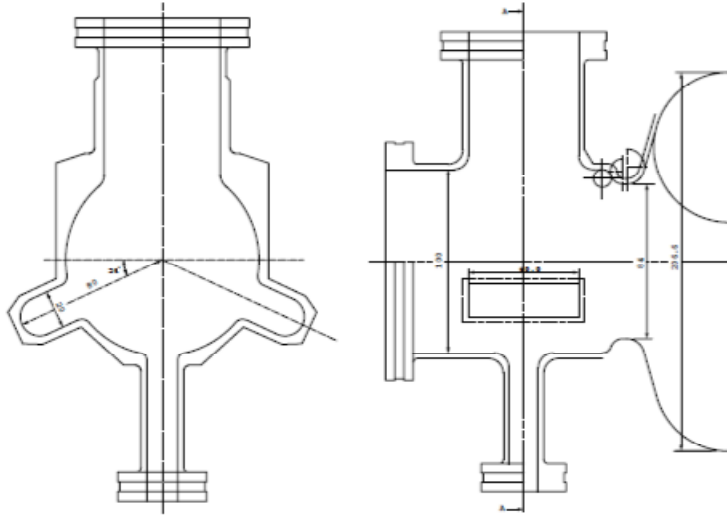


Figure 2. 24 Eccentric fluted pipe schematic drawings [9].

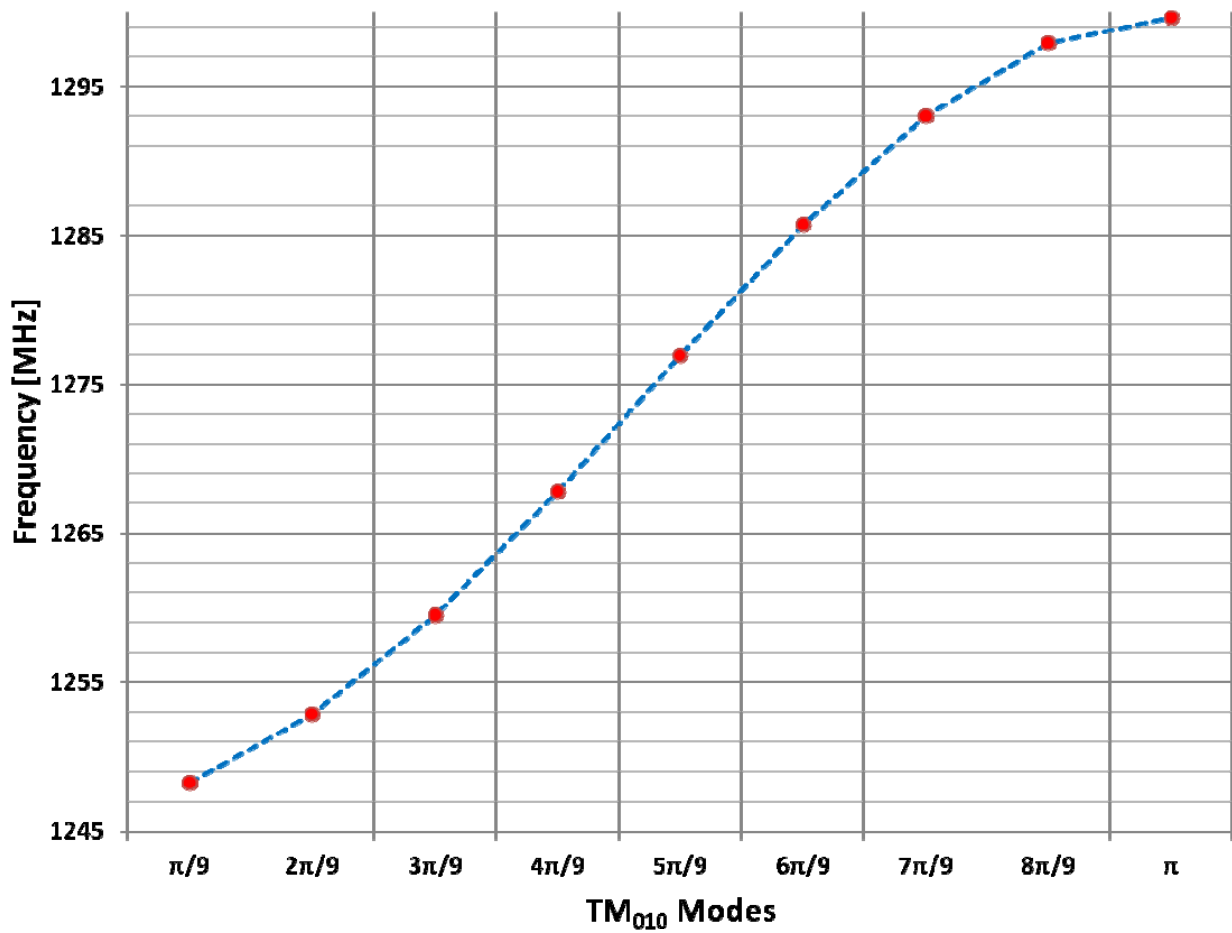


Figure 2. 25 Dispersion curve calculated by numerical code (SuperFish).

2.7 Field emission theory

The main features of the electron emission from cold metal in intense field was firstly calculated by Schottky in 1923 [16]. Later in 1928 Fowler and Nordheim faced the problem [17] using a semi-classical approach, as used by Sommerfeld to calculate the behavior of electrons in metal and hydrogen atom energy levels.

Nordheim calculated exactly the reflection and transmission coefficients for electrons with a given energy W incident on a surface with a sudden increase of potential energy (potential barrier step).

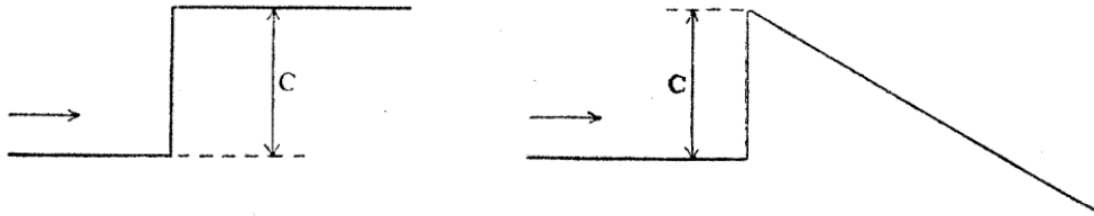


Figure 2. 26 Step potential with (right) and without (left) electric field on the metal surface.

The problem can be solved in one-dimension, assuming a potential energy step C and electron kinetic energy W . The barrier is located at $x=0$ coordinate (Figure 2. 26), the left represent a case without external electric field while the right one represent a triangular step assuming an external electric field E . The Schrödinger's equations for the triangular step are

$$\frac{d^2\varphi}{dx^2} + k^2(W - C + Ex)\varphi = 0 \quad (x > 0), \quad (2.63)$$

$$\frac{d^2\varphi}{dx^2} + k^2W\varphi = 0 \quad (x < 0). \quad (2.64)$$

Where

$$k^2 = \frac{8\pi^2m}{h^2} \quad (2.65)$$

For sake of simplicity we neglect here the influence of the image charge on rounding the step corner, while still be able to appreciate all the theoretical implication derived by Fowler and Nordheim calculation.

Fowler and Nordheim divided their calculation in two steps, first they derived the transmission coefficient $D(W)$, second by multiplying this coefficients by the number of electrons $N(W)$ impinging on the step barrier they were able to calculate the emission current.

Solving the Schrödinger's differential equation the solution for $D(W)$ is:

$$D(W) = \frac{4[W(C - W)]^{0.5}}{C} e^{\frac{-4k(C-W)^{1.5}}{3E}}. \quad (2.66)$$

While using the Sommerfeld theory $N(W)$ is:

$$N(W) = \frac{4\pi m k T}{h^3} L\left(\frac{W - \mu}{k T}\right). \quad (2.67)$$

Where

$$L(X) = \int_0^{\infty} \frac{dy}{e^{X+y} + 1} \quad (2.68)$$

and μ the parameter for electron distribution used in Fermi-Dirac statistics, k is the Boltzmann constant, T is the surface temperature, m the electron mass and h the Planck's constant.

Considering the parameter values useful in practical cases Fowler and Nordheim obtained an expression for the emission current.

$$I = 6.2 * 10^{-6} \frac{\mu^{0.5}}{(\chi + \mu)\chi^{0.5}} E^2 e^{-2.1*10^8 \frac{\chi^{1.5}}{E}} \quad (2.69)$$

Where E is the electric field in V/cm and $\chi=C-\mu$ is the work function in Volts. The expression above is strictly calculated for $T=0$, but it is still applicable when the ratio between μ and kT is big i.e. at 2K this ratio for a Niobium surface is about 25000 and the formula represent a good approximation.

Fowler and Nordheim noticed a discrepancy comparing the theoretical result with experimental data, in fact their model predict a measurable emission current when the electric field is bigger than 10^9 V/m while experiments showed emission already at 10^8 V/m or even less. The reason for this discrepancy was found to lay in the sensitivity of the electric field amplitude to micro surface features, like protrusion, that locally can strongly enhance the electric field [18, 19].

Using a more compact expression the emitted current from a micro features on the surface can be written taking into account also the field enhancing factor β [18-20]

$$I = S \frac{A\beta^2 E^2}{\Phi} e^{-B \frac{\Phi^{1.5}}{\beta E}} \quad (2.70)$$

Where

$$A = 1.54 * 10^{-6} [\text{A eV V}^{-2}] \text{ and } B = 6.83 * 10^9 [\text{eV}^{-1.5} \text{ V m}^{-1}]$$

The current I is expressed in Ampere, the electric field E is in V/m, the working function Φ in eV and S is the emission area in m^2 [5].

From the above expression it is possible to understand qualitatively the field emission behavior, which parameters influence it and the relative current intensity with respect to different cavity conditions.

2.7.1 Field emission onset

It is straightforward to notice that the emitted electron current has a strong dependency on the local electric field intensity, any surface defect that can enhance the electric field shall be considered

carefully. Fowler, Nordheim and later Latham and Xu [20] determined a threshold for the local electric field in order to emit a measurable current, the value is about $\sim 3 \times 10^9$ V/m (3000 MV/m), using this value it is possible to check where to expect field emission assuming different enhancing factor and different cavity condition.

The picture below shows the electric field on the surface near c-ERL mod2 cell iris calculated with SuperFish. The zero is located on the iris and the total distance is 4 centimeter along the cavity Z axis near the iris region. The three curves show the amplitude of the surface electric field when the E_{acc} is 15MV/m assuming an enhancing factor of 50, 65 and 100.

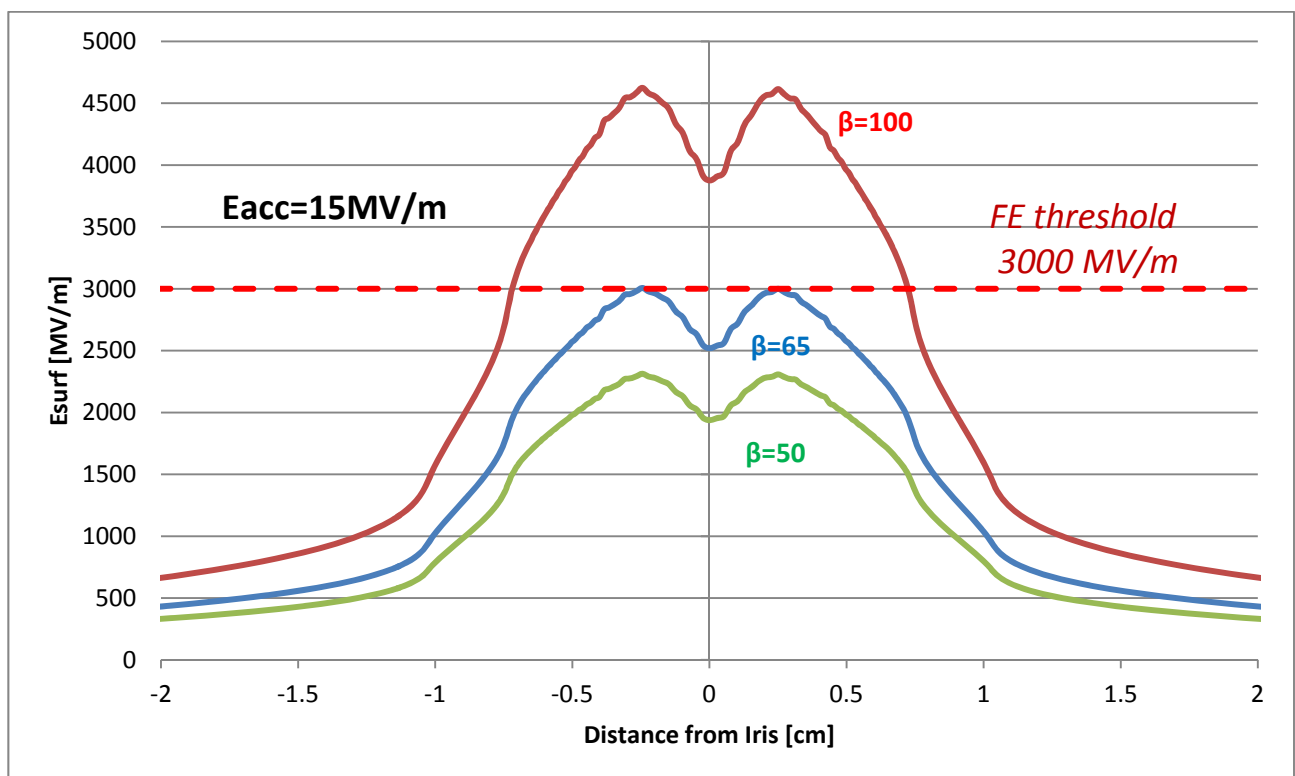


Figure 2.27 Electric surface field for KEK ERL model 2 cavity with different enhancing factors, $E_{acc}=15\text{MV/m}$.

The part of curves above the field emission threshold represent a region near the iris where the emission can occur, in this condition it can be seen that emitters with beta less than 65 cant emit any current no matter where they are located inside the cavity. Just with this simple picture can be clearly understood the paramount importance of the ratio between the peak field on the surface and

the accelerating field (E_{acc}). It is also clear that is relevant to reduce the number of emitters located on the surface, so it is mandatory to have a strong clean room operation practice.

In the next picture can be appreciated the difference between the Mod2 c-ERL cavity with an E_{peak}/E_{acc} of about 3, the Tesla-type cavity designed for the ILC project where the ratio is about 2.0 and the JLAB Low Loss cavity where the ratio is about 2.3.

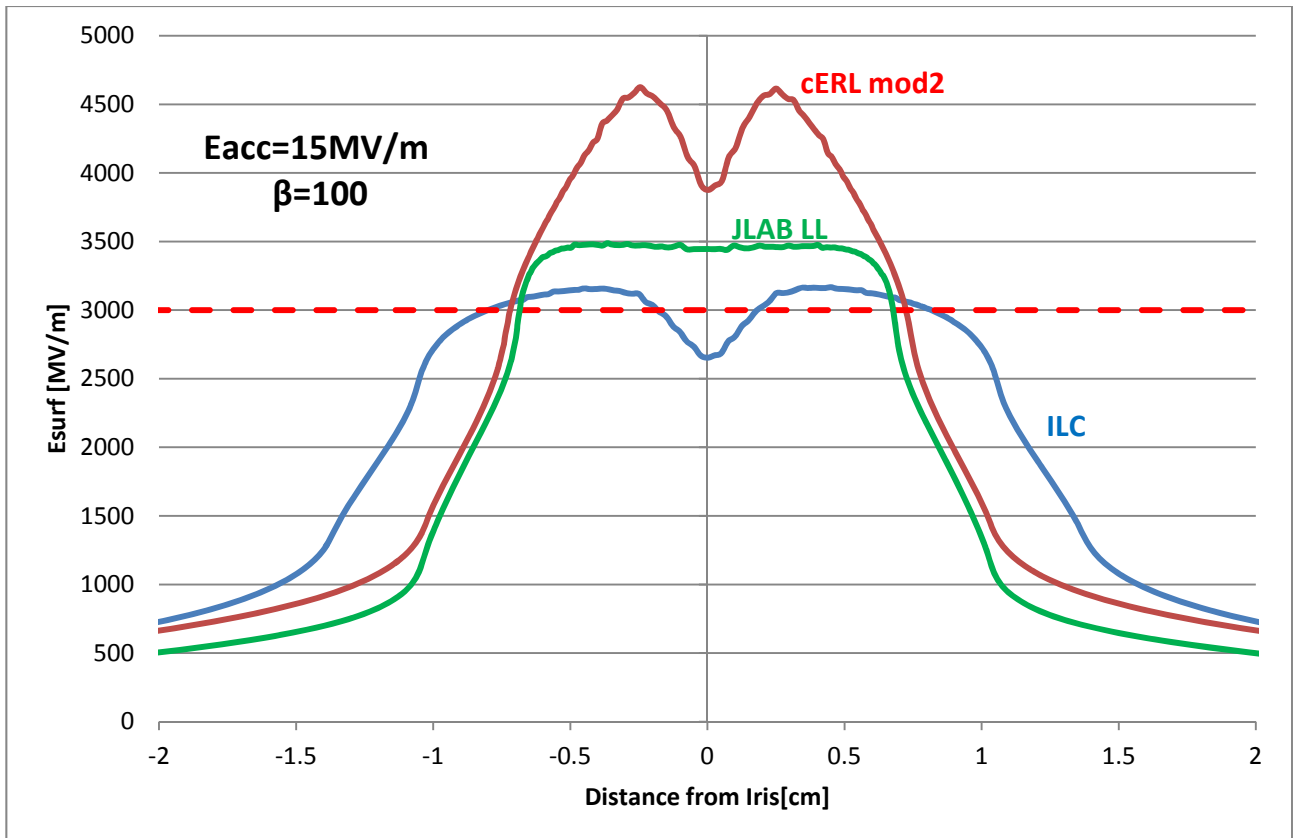


Figure 2.28 Electric surface field with enhancing factor $\beta=100$, respect to different cavity shapes, $E_{acc}=15\text{MV/m}$.

As the previous image the dashed red line indicate the field emission threshold, in the cavities the $E_{acc}=15\text{MV/m}$ and the enhancing factor is 100. While the emission region doesn't change significantly between the three cavities, as shown in table 2.5, we can expect that the emitted current will be greatly changed, due to the exponential dependency on the surface field.

Table 2.5 Comparison between different cavity geometry with respect to field emission

| <i>Cavity model</i> | <i>E_{peak}/E_{acc}</i> | <i>Emission region [cm]</i> | <i>MAX Emitted current [nA]*</i> | <i>E_{acc} field emission onset [MV/m]</i> |
|---------------------|---|---------------------------------|--------------------------------------|--|
| ERL mod2 | 3 | 1.48 | 961.5 | 10 |
| ILC | 2.2 | 1.24 | 1.4 | 13.6 |
| JLAB LL | 2.3 | 1.36 | 12.2 | 13 |

*The emitted current is calculated assuming $E_{acc}=15\text{MV/m}$, an emitter with $\beta=100$ and emission area of 10^{-13}m^2 [21]

In the same framework it is possible to calculate the expected onset for field emission, in the table above is shown an example using emitter with $\beta=100$ [18, 19, 22, 23], shall be noticed that the emission could be triggered at lower accelerating field if β is bigger than 100.

The Fowler-Nordheim formula depends also on the metal working function, it is straightforward that any surface treatment or contaminants that reduce the working function can increase the field emitted current.

The equation define the emitted current with respect to local electric field, surface property and emitter geometry, the last parameters are defined as field enhancing factor (β) and emitter area (S). While the second one is basically a scaling factor, the first determines the current rate of rise with respect to electric field and at RF regime determines the current “bell curve” width. By writing the current with the explicit dependence respect to phase (the electromagnetic field change as a sine function) the emitted current density can be plotted with respect to RF phase (θ).

$$J = \frac{I}{S} = \frac{A(\beta E \sin(\theta))^2}{\Phi} e^{-B \frac{\Phi^{1.5}}{\beta E \sin(\theta)}} \quad (2.71)$$

And the current density graph is

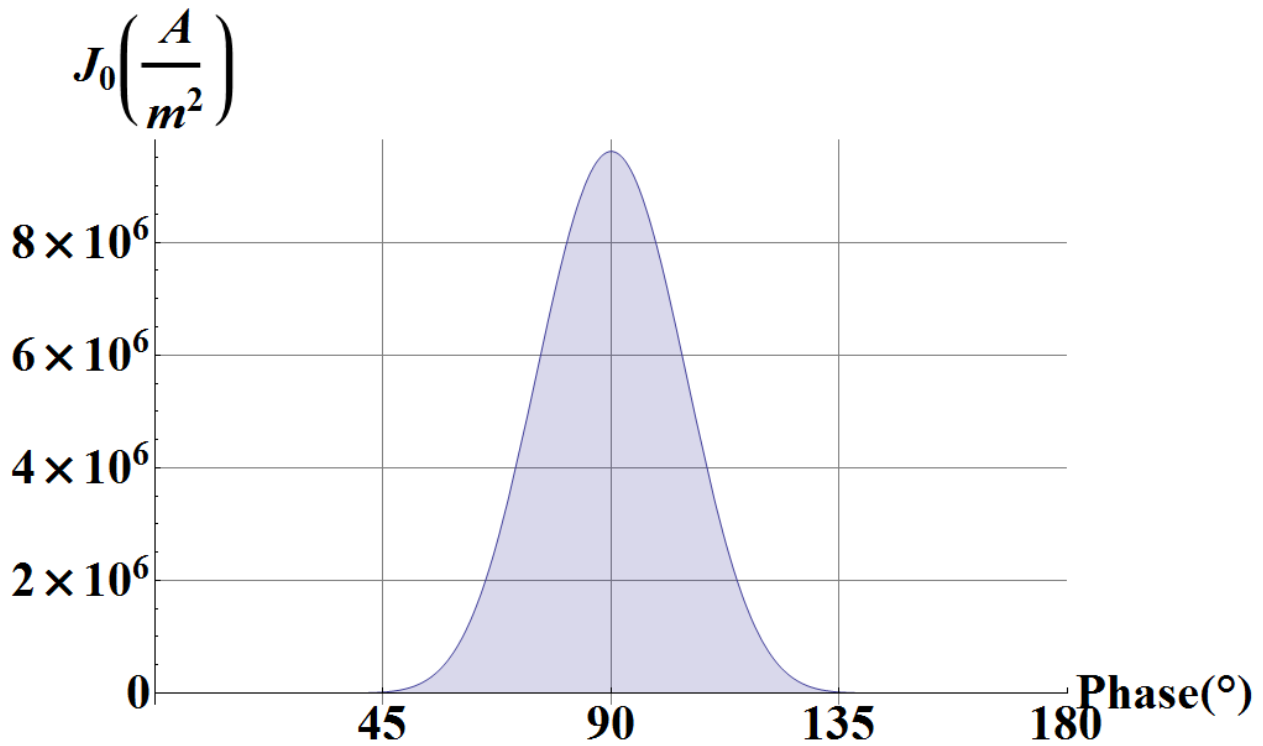


Figure 2.29 Emitted current density with respect to RF phase.

As a first approximation we can think about it as a Gaussian curve where

$$I \sim e^{-\frac{x^2}{2\sigma^2}} \quad (2.72)$$

By defining

$$x^2 = \frac{1}{\sin(\theta)} \quad (2.73)$$

$$\sigma = \sqrt{\frac{\beta E}{2B\Phi^{1.5}}} \quad (2.74)$$

Thus the full width at half mean will increase by increasing β or the local field, we can better understand this by plotting the emitted current density with respect to different enhancing factor, to

do this we need to use a logarithmic scale for the current due to fast rising with respect to the enhancing factor.

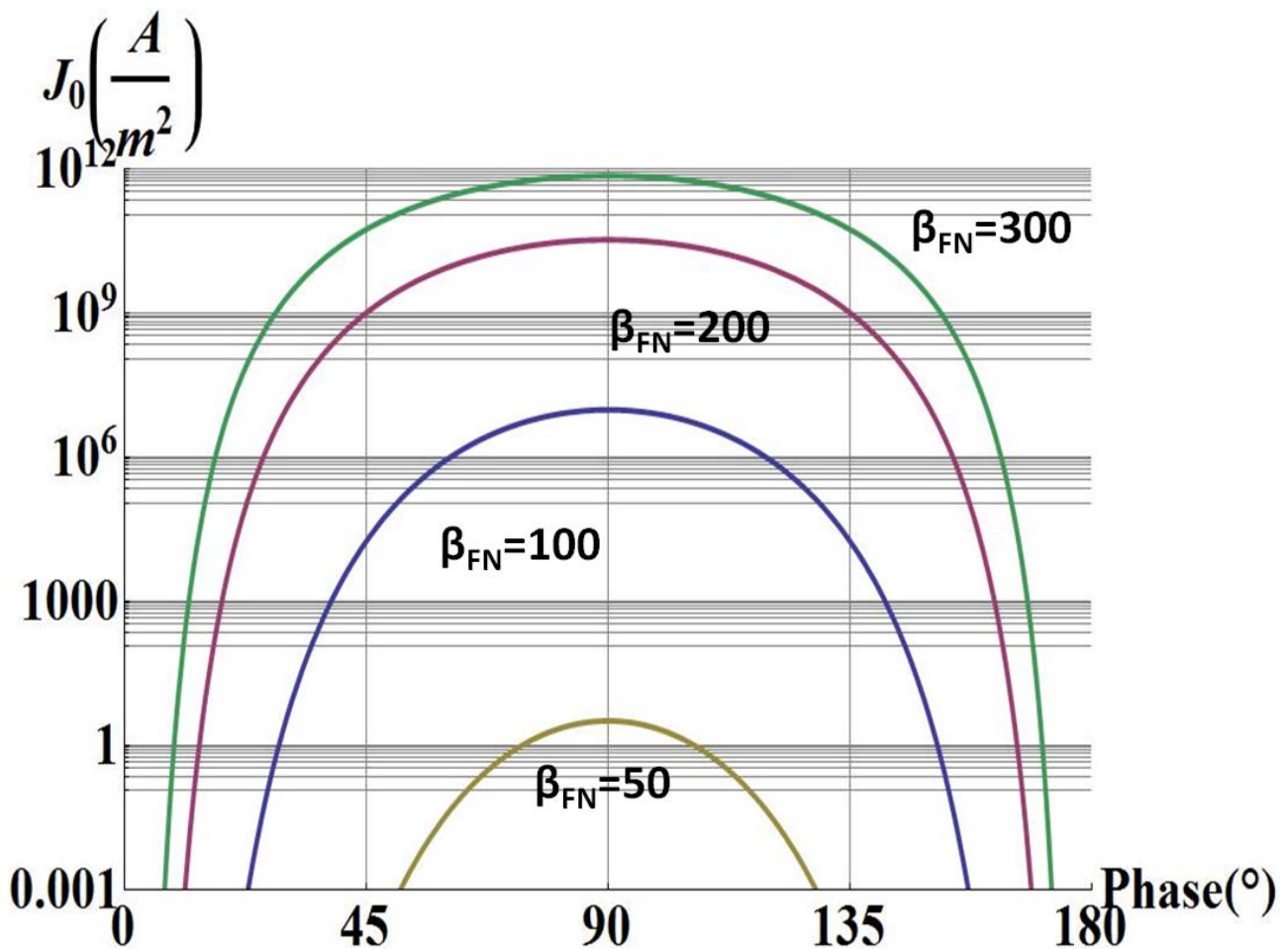


Figure 2.30 Emitted current density with respect to RF phase with different enhancing factor.

In the picture above it is possible to appreciate how fast the peak current increase with respect to beta and at the same time how the curve width increase (σ), it is clear by looking at lower part of the graph (current equal to 0.001 A/m²), the phase interval, where the emission is confined, increases with the enhancing factor.

Finally in Figure 2. 31 is presented the current dependency on the surface field with different enhancing factor.

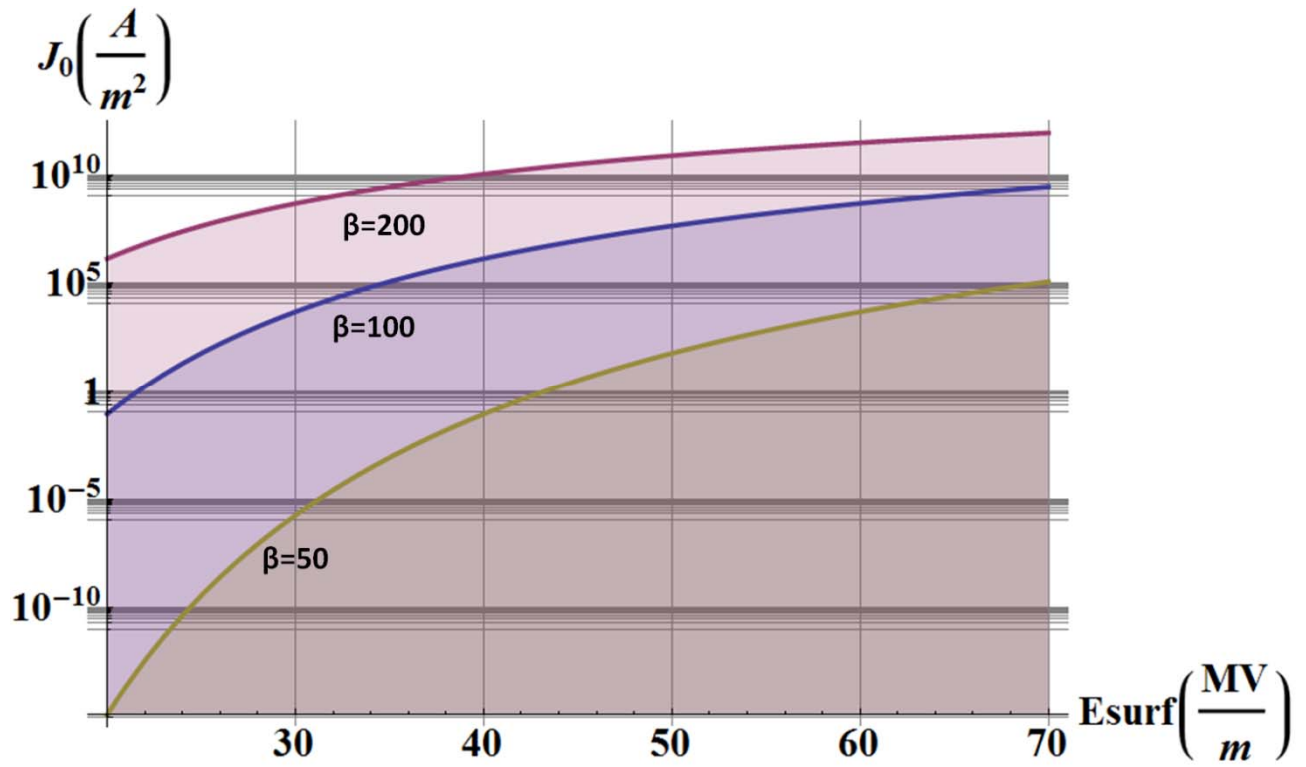


Figure 2. 31 Emitted current density with respect to electric field on the surface at different enhancing factors.

2.8 Cavity preparation

After the design the most important step is the cavity performance measure, to verify if the expected cavity features are fulfilled. Before the measure at cryogenic temperature the cavity shall pass different steps, like tuning, annealing, surface polishing and vacuum baking.

Different laboratories have developed different recipes in order to achieve better performance, they differ in surface treatment, baking temperature and process timing but all of them have common steps, like can be seen in the table below.

Table 2.6 Cavity preparation recipes [24]

| Cavity model | Bulk removal | Degassing and annealing | Light removal | 120°C Baking |
|---------------------|---------------------|--------------------------------|----------------------|---------------------|
| KEK-ERL | EP | 800°C | EP | 48hours |
| ILC | EP | 800°C | EP | 48hours |
| JLAB | BCP | 600°C | EP | 24hours |
| XFEL | EP | 800°C | BCP | 48hours |
| Cornell ERL | BCP | 650°C | BCP | 48hours |

2.8.1 Bulk removal

Usually a layer of 100 μ m or more is removed during this phase by means of Buffered Chemical Polishing (BCP) or Electro Polishing (EP) [25]. The first method consist of acid solution HF(48%), HNO₃(65%) and H₃PO₄(85%) with ration 1:1:2, cooled at 5°C and fluxed with a closed loop inside the cavity. In the second one the acid solution consist of H₂SO₄ (96%) and HF(40%) in volume ratio 9:1, kept at 35°C while a current density between 50 and 30 $\frac{mA}{cm^2}$ is used to remove Niobium layers. Keeping the voltage as low as possible and temperature around 30°C reduce particulate contamination specially sulfat formation [26, 27].

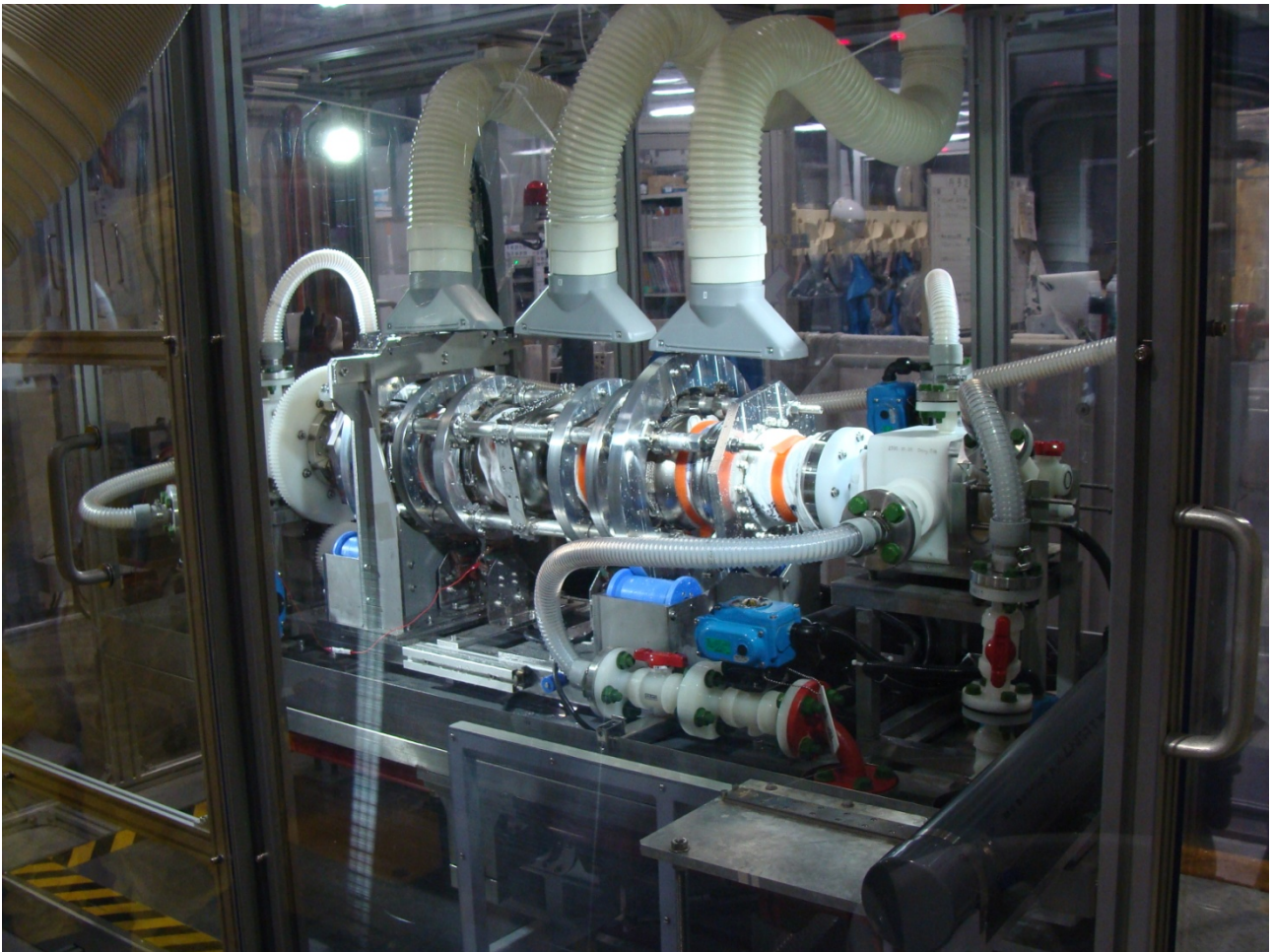


Figure 2. 32 Electropolishing system for multi-cell cavities.



Figure 2. 33 Electropolishing system control panel.

After the chemical process the cavity is washed with ultrasonic bath followed by high pressure water rinsing (100bar), ultrapure water is used to avoid contamination.

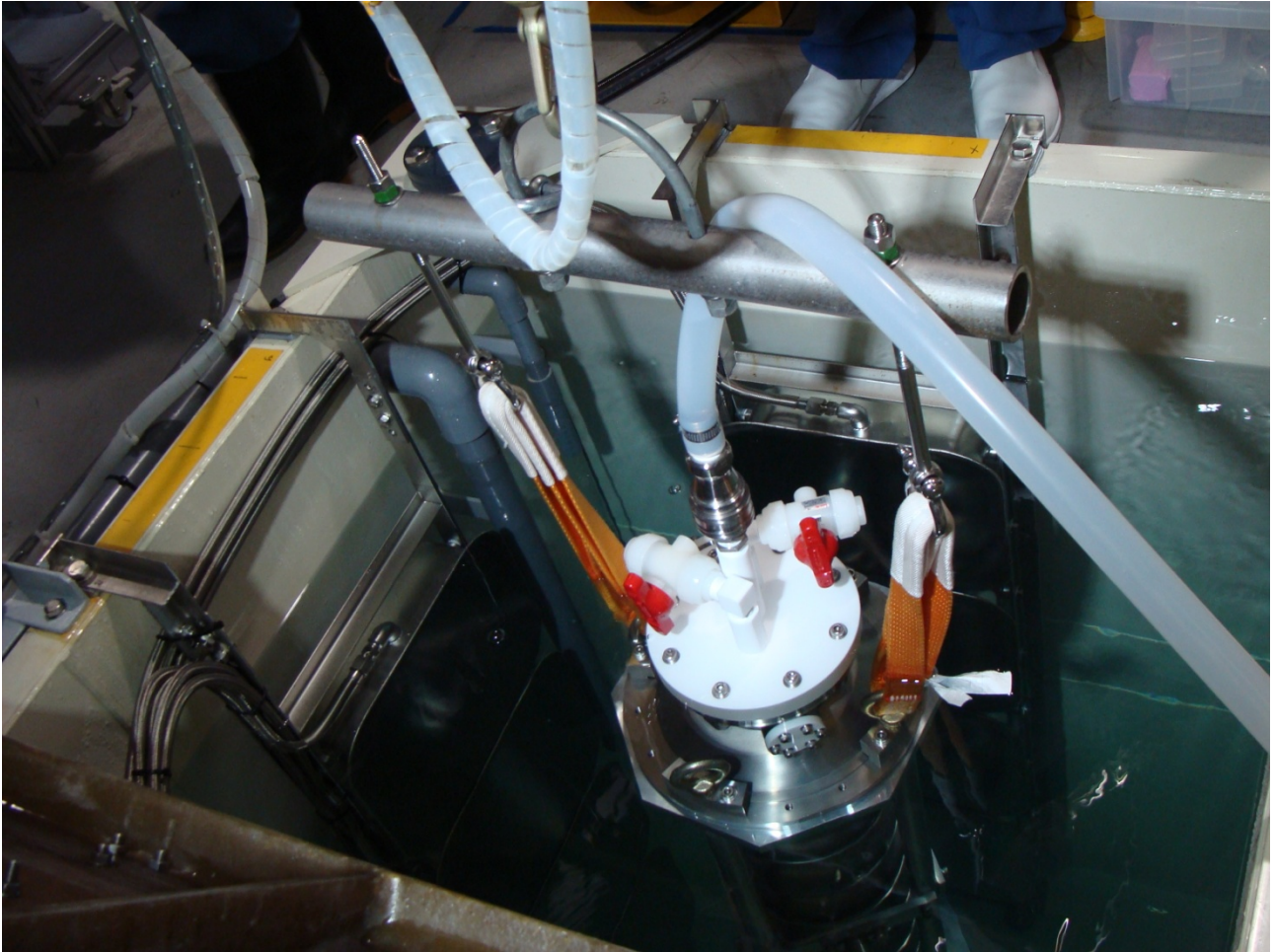


Figure 2. 34 Cavity immersed in the ultrasonic cleaning system.

2.8.2 Degassing and Annealing

During this step the cavity is put into a UHV furnace and heated to allow hydrogen and oxygen outgassing and mechanical stress relieving. Usually after this phase another tuning is needed, mainly because the relieved mechanical stress can alter the cavity geometry but also due to amount of material removed during the first polishing.

2.8.3 Light removal

In this phase is removed about 20 to 50 μm of Niobium, in order to reduce any possible surface asperity, contaminants and promote a uniform oxide layer. The chemicals solution used at this step are usually the same as the previous one, followed by the same ultra pure water rinsing. The cavity is then dried inside a class 100 (or better) clean room.

2.8.4 Low temp bake out

Once all the ancillary systems are installed on the cavity (in the clean room), it is evacuated by dry pumping system (no oil bearings shall be used) and heated at 120°C for 24-48 hours [28], this temperature and timing has proven to be the more efficient to obtain better cavity performance [29].



Figure 2. 35 Cavity during baking with heating jacket.

2.9 Vertical test measure

After all the above treatment the cavity is immersed into a cryogenic vessel and cooled to the operating temperature (typically below 2K). The vessel is shielded by the earth magnetic field through a magnetic shield and filled by liquid helium, the temperature is then decreased by evacuating the volume above the liquid by means of roots pumps.

2.9.1 Measured quantity

Once the cavity is cooled resonant mode are excited by means of RF system connected to the cavity, the last part of it (input coupler) is designed to couple with the cavity electromagnetic field, typically by coupling with the electric field it can transfer power from the RF system to the cavity.

Another coupler is used at the opposite end of the cavity it is used to measure the amount of power transmitted through the cavity. Usually the input coupler can be moved in order to find the optimum coupling position while the transmitted power probe is usually fixed.

During the test it is possible to measure a set of quantity in order to derive the cavity figures of merit. Aside that data (as will be described in the next chapter) information coming from x-ray detector and temperature sensors can be collected.

Measuring the dissipated power, the decay time, the resonance frequency and combining this information with the ones derived from simulation the overall cavity performance can be estimated.

In the image below (Figure 2. 36) can be found a block diagram for the RF system used for vertical test at Superconducting Test Facility (STF) in KEK.

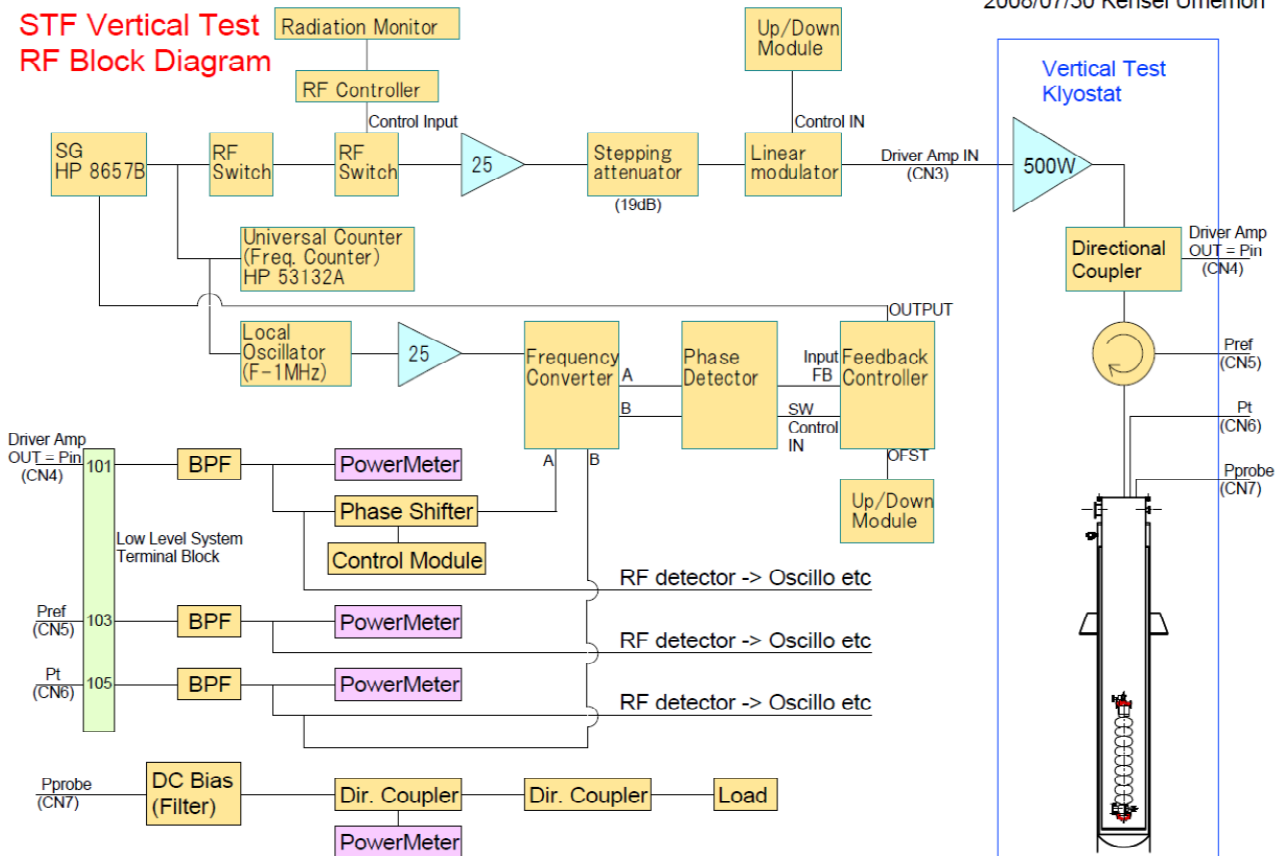


Figure 2. 36 RF system block diagram for vertical test stand installed at STF in KEK.

2.9.2 Dissipated power:

Using energy conservation we can write

$$P_{in} = P_{ref} + P_t + P_{pick} + P_{loss}, \quad (2.75)$$

where P_{in} is the input power, P_{ref} is the reflected power, P_t is the transmitted power, P_{pick} is the power collected at the pick-up probe and P_{loss} is the power dissipated by the cavity during operation.

After measuring the cable correction coefficients the only unknown in the equation above is power dissipated in the cavity (P_{loss}) so that

$$P_{loss} = P_{in} - P_{ref} - P_t - P_{pick}, \quad (2.76)$$

2.9.3 Resonant frequency:

The passband mode frequencies are measured by means of Time Domain Reflectometer (TDR), this information are then used to excite different mode during the test.

2.9.4 Decay time ($\tau_{1/2}$):

By measuring the time needed for the power to decay to half of its initial value after the input power is switched off, typically is in the order of magnitude of hundreds of milliseconds.

From the measured quantity listed above the cavity figure of merit is derived during operation.

2.9.5 Loaded Q (Q_L)

Once the RF feeding is switched off the energy contained in the cavity decay with a rate proportional to the leaking power through probes and coupler, thus can be written

$$\frac{dU}{dt} = -(P_t + P_{pick} + P_{loss}) = -P_{load}, \quad (2.77)$$

We can define a quality factor as

$$Q_L = \frac{\omega U}{P_{load}}. \quad (2.78)$$

Where the definition is similar to the unloaded Q, but considering the total leaking power and not only the P_{loss} .

By substituting the above expression in the differential equation, we can obtain

$$\frac{dU}{dt} = -\frac{\omega U}{Q_L}, \quad (2.79)$$

That has a well known solution

$$U(t) = U_0 e^{-\frac{\omega t}{Q_L}} \quad (2.80)$$

Where U_0 is the stored energy at $t=0$, thus the energy in the cavity decay exponentially with a time constant

$$\tau_L = \frac{Q_L}{\omega} \quad (2.81)$$

By measuring the decay time we can calculate the loaded quality factor.

In the same way it is possible to define a quality factor for each power leakage term, as the ratio between the stored energy and the dissipated power. So that

$$Q_{ext} = \frac{\omega U}{P_{ref}} \quad (2.82)$$

And

$$Q_t = \frac{\omega U}{P_t} \quad (2.83)$$

Where the first refer to the power dissipated (reflected) through the coupler and the latter refer to the power transmitted.

Recalling the energy conservation for the undriven cavity

$$P_{load} = P_{loss} + P_{ref} + P_t + P_{pick} \quad (2.84)$$

And dividing by the stored energy multiplied by the resonant frequency

$$\frac{P_{load}}{\omega U} = \frac{P_{loss} + P_{ref} + P_t + P_{pick}}{\omega U} \quad (2.85)$$

We obtain

$$\frac{1}{Q_L} = \frac{1}{Q_0} + \frac{1}{Q_{ext}} + \frac{1}{Q_t} + \frac{1}{Q_{pick}} \quad (2.86)$$

By defining the coupling parameters as

$$\beta_{ext} = \frac{Q_0}{Q_{ext}} = \frac{P_{ref}}{P_{loss}}, \quad (2.87)$$

$$\beta_t = \frac{Q_0}{Q_t} = \frac{P_t}{P_{loss}}, \quad (2.88)$$

$$\beta_{pick} = \frac{Q_0}{Q_t} = \frac{P_{pick}}{P_{loss}}, \quad (2.89)$$

so that

$$\frac{1}{Q_L} = \frac{1}{Q_0} (1 + \beta_{ext} + \beta_t + \beta_{pick}). \quad (2.90)$$

2.9.6 Unloaded Q (Q_0)

It is possible to derive the unloaded Q (Q_0) by measuring the loaded Q and the coupling parameters (measuring the power at each port).

$$Q_0 = Q_L (1 + \beta_{ext} + \beta_t + \beta_{pick}) \quad (2.91)$$

Where

$$Q_L = \frac{2\pi\omega\tau_{L1/2}}{\ln(2)} \quad (2.92)$$

Where ω is the resonant frequency and $\tau_{L1/2}$ is the measured decay time.

By measuring the reflected and the input power feed from the RF system can be defined

$$\beta^* = \frac{1 + \sqrt{\frac{P_{ref}}{P_{in}}}}{1 - \sqrt{\frac{P_{ref}}{P_{in}}}} \text{ for overcoupling} \quad \beta^* = \frac{1 - \sqrt{\frac{P_{ref}}{P_{in}}}}{1 + \sqrt{\frac{P_{ref}}{P_{in}}}} \text{ for undercoupling} \quad (2.93)$$

They represent the coupling strength parameters. By defining β_{in} as

$$\beta_{in} = \beta^* (1 + \beta_t + \beta_{pick}). \quad (2.94)$$

So that

$$Q_0 = Q_L (1 + \beta_{in} + \beta_t + \beta_{pick}). \quad (2.95)$$

At the same time the accelerating field can be calculated as

$$E_{acc} = Z \sqrt{P_t Q_t}, \quad (2.96)$$

where Z is the cavity impedance.

Different accelerating voltage can be associated to Q_0 values, by plotting the corresponding quantity it is possible to evaluate the cavity behaviour at different operating condition and determine any unpredicted issue, like field emission, multipacting or quenches.

2.9.7 Surface resistance

A last important quantity that can be derived during cavity test is the surface resistance. By recalling the relation between the quality factor and the geometry factor, the surface resistance can be defined as

$$R_s = \frac{G}{Q_0} \quad (2.97)$$

Where G is obtained from numerical calculation and Q_0 is derived from measured data. The Niobium residual resistance can be calculated by fitting the surface resistance against the cavity temperature as shown in the image below.

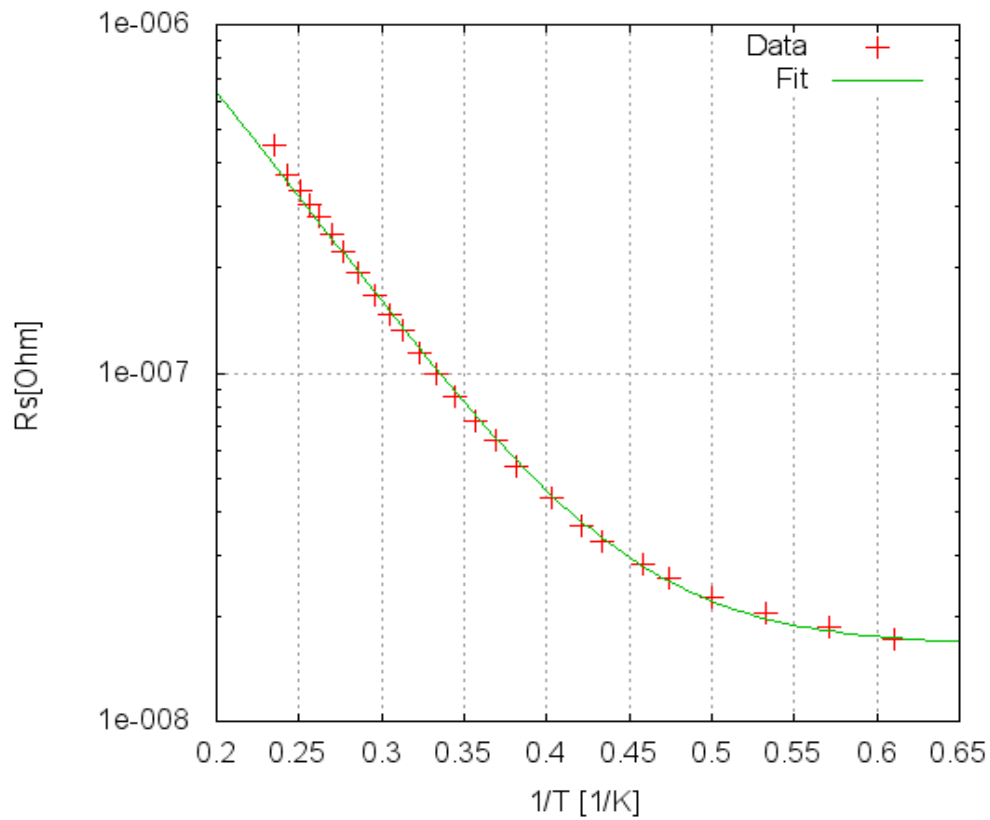


Figure 2. 37 Surface resistance with respect to cavity temperature, the obtained residual resistance is 16nΩ.

Chapter references

1. Jensen, E., *RF cavity design*. CERN Accelerator school (CAS), 2011.
2. Feynman, R., R. Leighton, and M. Sands, *The Feynman Lectures on Physics, Vol II*, 1964, Addison-Wesley.
3. Abramowitz, M. and I.A. Stegun, *Handbook of Mathematical Functions: With Formulas, Graphs, and Mathematical Tables. Vol. 55*. 1964: DoverPublications. com.
4. Wiedemann, H., *Particle accelerator physics2007: Springer London, Limited*.
5. Padamsee, H., et al., *RF Superconductivity for Accelerators. Physics Today*, 1999. **52**: p. 54.
6. Podlech, H., *Superconducting versus normal conducting cavities. arXiv preprint arXiv:1303.6552*, 2013.
7. Geng, R.-L., *Review of new shapes for higher gradients. Physica C: Superconductivity*, 2006. **441(1)**: p. 145-150.
8. Geng, R., et al. *Testing the first 1300 MHz reentrant cavity. in Proceedings of the Workshop of Pushing the Limits of RF Superconductivity*, Argonne National Laboratory. 2004.
9. Umemori, K., et al. *Design of L-band superconducting cavity for the energy recovery linacs. in APAC*. 2007.
10. Zu, D. and J. Chen, *Design study on a superconducting multicell RF accelerating cavity for use in a linear collider. Nuclear Science, IEEE Transactions on*, 1998. **45(1)**: p. 114-118.
11. Bilderback, D.H., P. Elleaume, and E. Weckert, *Review of third and next generation synchrotron light sources. Journal of Physics B: Atomic, molecular and optical physics*, 2005. **38(9)**: p. S773.
12. Liepe, M., *Conceptual layout of the cavity string of the Cornell ERL main linac cryomodule. power [MW]*, 2003. **2(4)**: p. 6.
13. Halbach, K. and R. Holsinger, *SUPERFISH-a computer program for evaluation of RF cavities with cylindrical symmetry. part. Accel.*, 1976. **7(LBL-5040)**: p. 213-222.
14. Menzel, M. and H. Stokes, *Users guide for the POISSON/SUPERFISH Group of Codes*, 1987, Los Alamos National Lab., NM (United States).
15. Kneisel, P., et al. *Testing of HOM coupler designs on a single cell niobium cavity. in Particle Accelerator Conference, 2005. PAC 2005. Proceedings of the. 2005. IEEE*.
16. Schottky, W., *Cold and hot electron discharge. Z. Phys*, 1923. **14**: p. 63.
17. Fowler, R.H. and L. Nordheim, *Electron emission in intense electric fields. Proceedings of the Royal Society of London. Series A, Containing Papers of a Mathematical and Physical Character*, 1928. **119(781)**: p. 173-181.
18. Knobloch, J., *Field emission and thermal breakdown in superconducting niobium cavities for accelerators. Applied Superconductivity, IEEE Transactions on*, 1999. **9(2)**: p. 1016-1022.
19. Jimenez, M., et al., *Electron field emission from large-area cathodes: evidence for the projection model. Journal of Physics D: Applied Physics*, 1994. **27(5)**: p. 1038.
20. Latham, R.V., *High voltage vacuum insulation: basic concepts and technological practice1995: Academic Press*.

21. Wiener, J. and H. Padamsee, *Improvements in Field Emission: A Statistical Model for Electropolished Baked Cavities*.
22. Wiener, J. and H. Padamsee, *Thermal and statistical models for quench in superconducting cavities*. TTC-Report, 2008. **8**: p. 2008.
23. Xu, N., et al., *Theoretical study of the threshold field for field electron emission from amorphous diamond thin films*. *Journal of Vacuum Science & Technology B: Microelectronics and Nanometer Structures*, 2001. **19**(3): p. 1059-1063.
24. Furuta, F., *High Q R&D at Cornell*. TTC topical-meeting on CW SRF 2013, 2013.
25. Aguilar-Saavedra, J., *TESLA TDR Part 3: "Physics at an e^+e^- Linear Collider"*. arXiv preprint hep-ph/0106315.
26. Éozénou, F., et al., *LOW-VOLTAGE ELECTRO-POLISHING OF SRF CAVITIES*.
27. Aspart, A., F. Eozenou, and C. Antoine, *Aluminum and sulfur impurities in electropolishing baths*. *Physica C: Superconductivity*, 2006. **441**(1): p. 249-253.
28. Safa, H. *High field behavior of scrf cavities*. in *Proceedings of the 10th Workshop on RF Superconductivity*. 2001.
29. Ciovati, G., *Effect of low-temperature baking on the radio-frequency properties of niobium superconducting cavities for particle accelerators*. *Journal of applied physics*, 2004. **96**(3): p. 1591-1600.

CHAPTER III

Simulation

Abstract

In this section, the main tools used to make calculation will be introduced. The first step is to calculate electro-magnetic field inside the resonant structure, then these information are used to simulate the electron trajectories with respect to their starting location, RF phase and field amplitude. During the post processing, all the above information are gathered in order to obtain a “picture” on the field emission effects, spanning from impact location to energy deposition in the cavity surface. In the last calculation step, a Montecarlo code (EGS5) is used in order to take into account the interaction between high energetic electrons and cavity material or sensors, this suite of Fortran routine allows some degree of freedom to analyze specific particle-material interaction.

3.1 Field emission calculation

To calculate systematically the effect of field emitted electrons in the cavity we shall follow different steps:

- 1- Calculate the electromagnetic field for each mode we want to analyze, typically passband modes (TM₀₁₀ group).
- 2- It is necessary to account for the amount of current emitted with respect to different operating conditions (accelerating field, excited mode, RF phase during emission) and different locations on the cavity surface.
- 3- Compute by means of tracking algorithm electron trajectories and determination of their impact location, impact angle and impact energy with respect to different starting positions and starting RF phases.
- 4- Estimation of the interaction between the electrons hitting the cavity surface and the cavity material in order to calculate the amount of power delivered to the cavity and the portion that can be transmitted outside (and then measured).

Through the steps listed above it is possible to follow electrons from the moment they leave the emitter until they hit the Niobium surface, creating a particle shower that interact with the sensors located outside the cavity.

3.2 Electromagnetic field calculation

The cavity figures of merit importance were discussed in the previous chapter, their evaluation allows to optimize a specific design in respect to accelerator requirements. Since only simple accelerating structures can be solved analytically, we should use computer codes in order to solve numerically the Maxwell equations and derive cavity performance.

Today many codes are available and it is possible to choose the best one for the problem that needs to be solved. The user shall input the cavity geometry, boundary conditions, material properties, and the code can usually calculate, aside resonant frequencies and electromagnetic field, other figures of merit like quality factor, shunt impedance, R over Q and much more.

Some codes can exploit the cavity symmetry in order to simplify the calculation and shorten the calculation time.

SuperFish [1] is the main code used in this dissertation to calculate electromagnetic field profile and cavity performance. The code is mainly developed by Los Alamos Accelerator Code Group (LAACG), it use triangular mesh to map the cavity volume and solve Maxwell equations through finite difference. The input geometry shall have an axial symmetry so that the equations are solved into 2 dimensions.

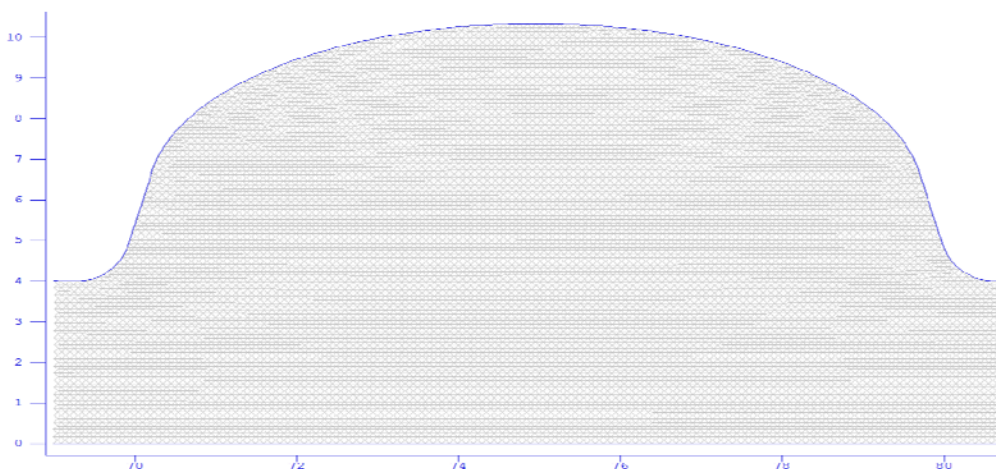


Figure 3. 1 Cavity central cell with mesh as obtained with SuperFish code.

It approximates the function differential by Taylor expansion as follow:

The differential for the function f is defined as:

$$f'(x) = \lim_{h \rightarrow 0} \frac{f(x+h) - f(x)}{h}, \quad (3.1)$$

so that

$$f(x+h) \approx f(x) + f'(x)h. \quad (3.2)$$

By expanding at higher order $f(x+h)$, it can be approximated even better [2]

$$f(x+h) \approx f(x) + f'(x)h + f''(x)\frac{h^2}{2} + \dots \quad (3.3)$$

where h is the increment between two neighbor mesh points. Among different methods to approximate the differential operator, the central difference [2] approximation has proven to be the more accurate, in this approximation we can write the differential as follow

$$f'(x) \approx \frac{f(x+h) - f(x-h)}{2h} \quad (3.4)$$

$$f''(x) \approx \frac{f(x+h) + f(x-h) - 2f(x)}{(2h)^2} \quad (3.5)$$

where $x+h$ is the mesh point next to the one we would like to calculate the differential and $x-h$ is the previous one. Through this approximation, we can calculate the differential values by knowing the function values at each mesh point.

The above method is used by Superfish to solve the differential equations in the cavity volume and calculate all the relevant quantities. In the next pictures some results from the Superfish calculation will be shown while the used code is presented in the appendix.

We can start our calculation by evaluating the resonant frequency for the accelerating mode and pass band modes, the total number of modes are determined by the number of cells. Because the ERL cavity has 9 cells, we expect to obtain 9 resonant TM_{010} modes, the way they are spread out in the frequency domain is called dispersion curve, it relates the wave number and frequency.

By design requirement, the cavity shall have a fundamental frequency for the accelerating mode around 1.3GHz, other modes will have lower one. In the table below can be seen the calculation results for the TM_{010} passband modes followed by the dispersion curve [3].

Table 3.1 Passband frequency calculated by SuperFish.

| Mode | Frequency [MHz] |
|----------|-------------------------|
| $\pi/9$ | 1252.3344 |
| $2\pi/9$ | 1256.3474 |
| $3\pi/9$ | 1262.584 |
| $4\pi/9$ | 1270.38 |
| $5\pi/9$ | 1278.8699 |
| $6\pi/9$ | 1287.0386 |
| $7\pi/9$ | 1293.8459 |
| $8\pi/9$ | 1298.3631 |
| π | <u>1299.9359</u> |

In the next picture the dispersion curve will be shown for the passband mode listed above.

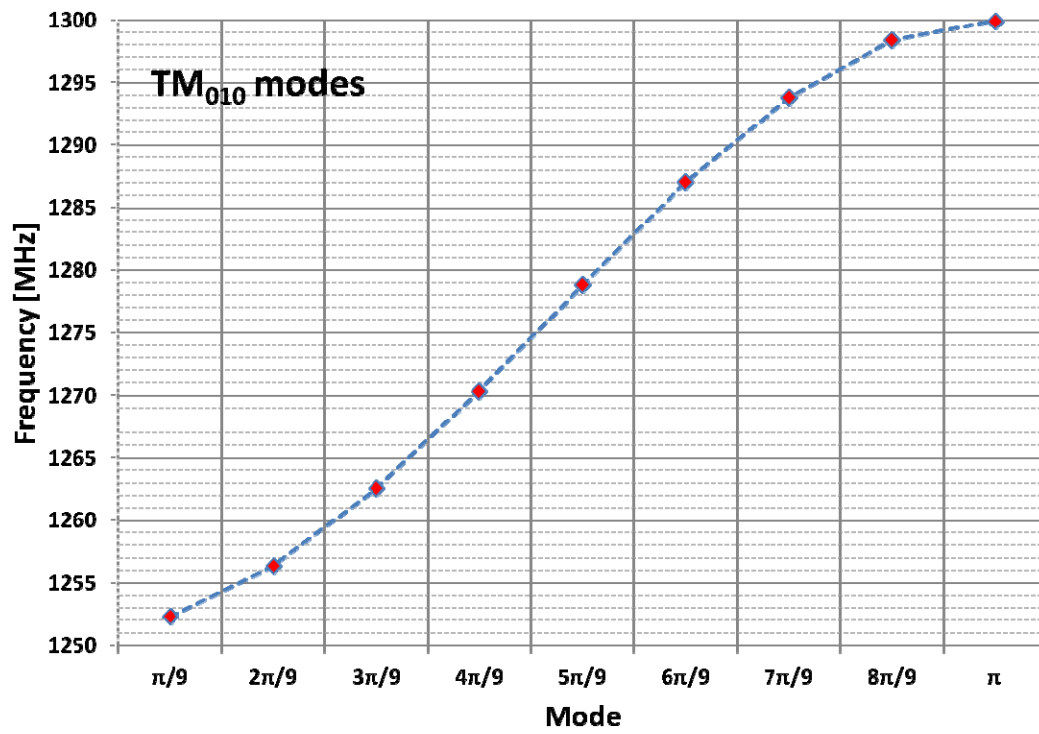


Figure 3. 2 Dispersion curve from SuperFish calculation.

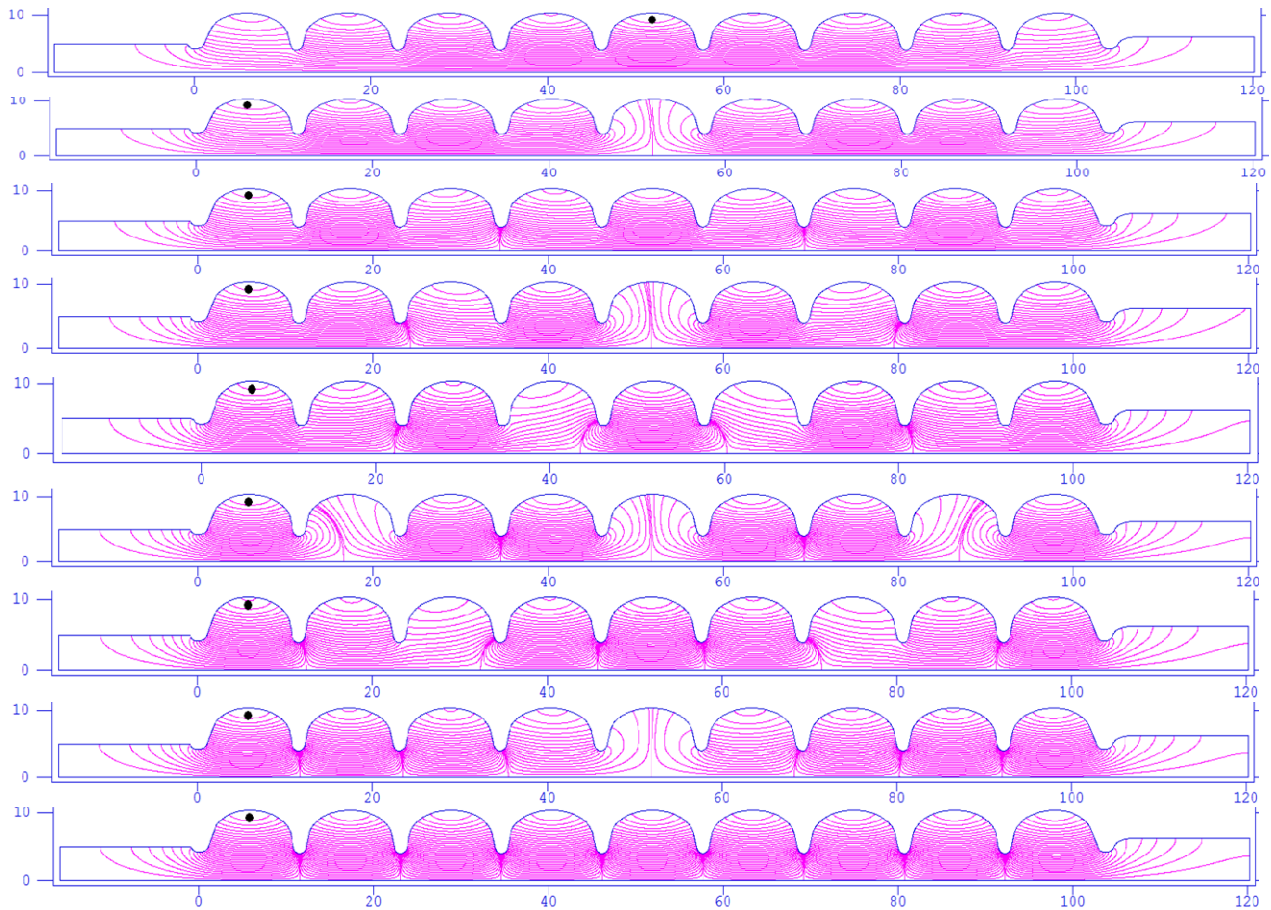


Figure 3. 3 Electric field 2D plot, from top to bottom $\pi/9$, $2\pi/9$, $3\pi/9$, $4\pi/9$, $5\pi/9$, $6\pi/9$, $7\pi/9$, $8\pi/9$ and π mode [3].

Once the 2D electromagnetic fields are calculated, it is possible to derive the magnitude of electric and magnetic fields on Niobium surface and the accelerating field on cavity axis. The former determines the field emitted current while the latter is responsible to accelerate electrons along the cavity axis.

During the design phase, it is a good practice to minimize (E_{pk}/E_{acc}) due to the dependence of field emission on the surface electric field (at the emitter location). On the other hand, how the electrons fly in the cavity shall also be considered. To calculate the power dissipated through field emission, it is necessary to know the emitted current and the electrons energy gain, both quantities depend on different cavity geometry parameters.

3.2.1 Field flatness

To obtain the most efficient energy gain for the accelerating mode it is important that the electric field is uniform from cell to cell, to define the field uniformity it is possible to introduce a new parameter called field flatness defined as [4].

$$FF = \left(1 - \frac{E_{max} - E_{min}}{\langle E \rangle} \right) \% \quad (3.6)$$

that is the difference between the maximum and minimum field amplitude divided by the average accelerating field calculated on cavity axis. In the picture below is shown the calculated field along cavity axis (Z-direction).

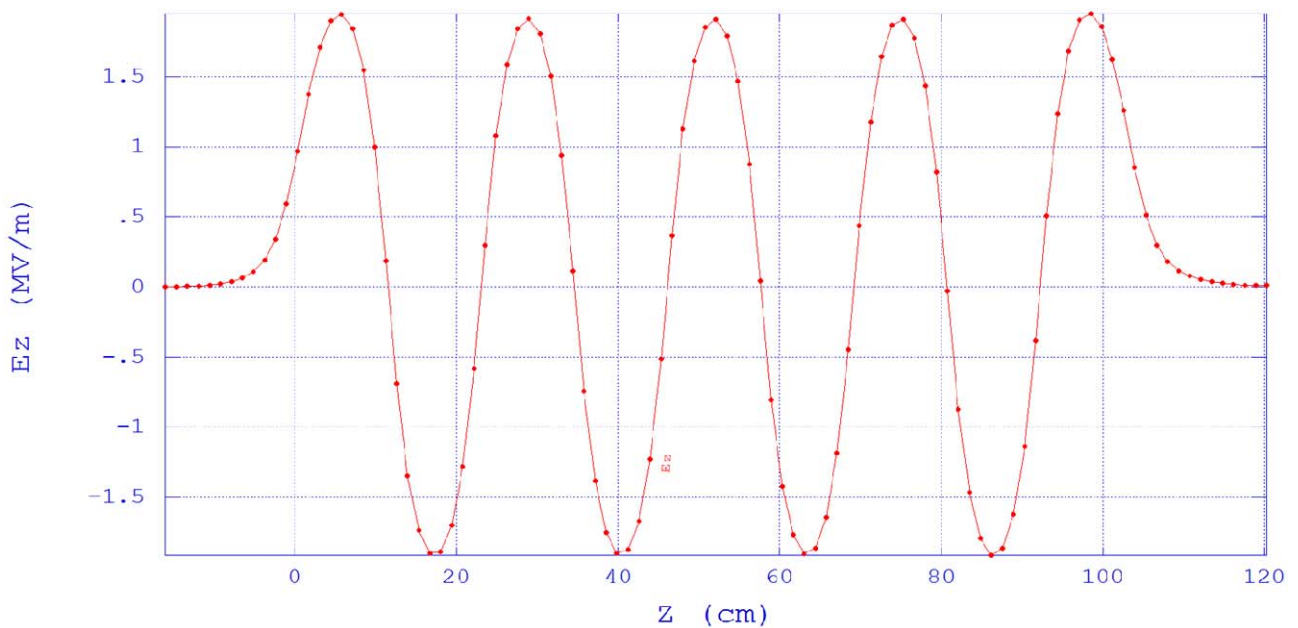


Figure 3. 4 Electric field along cavity axis for $TM_{010} \pi$ mode [3].

To see more clearly the field uniformity it is better to plot the E_z module as shown in the picture below.

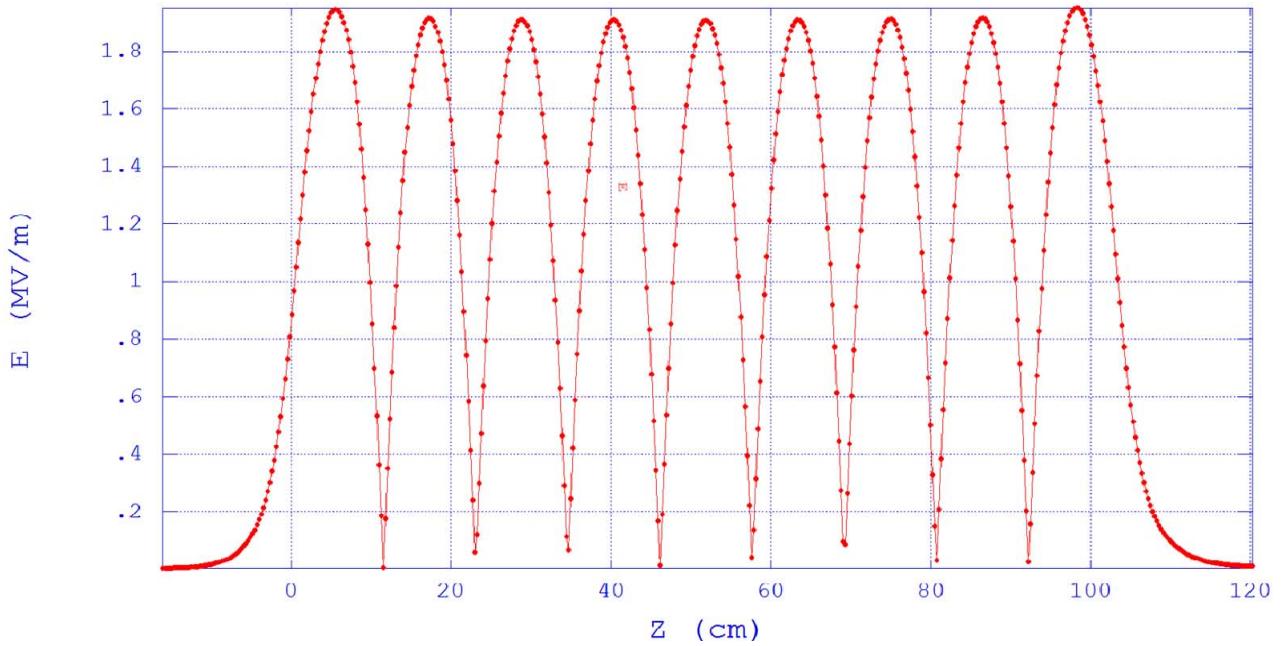


Figure 3. 5 Electric field amplitude along cavity axis for TM_{010} π mode [3].

From the calculation above we can determine the field flatness for this particular cavity geometry (as described in the previous chapter) excited to TM_{010} π mode and with $E_{acc}=1MV/m$. The maximum field is around 1.95 MV/m, the minimum peak is around 1.905 MV/m while the average is 1.92 MV/m, from this we can determine that the field flatness is about 97%.

In the next images the calculation results for the surface electric and magnetic field for the π mode will be shown, while the other passband modes will be listed in the appendix section.

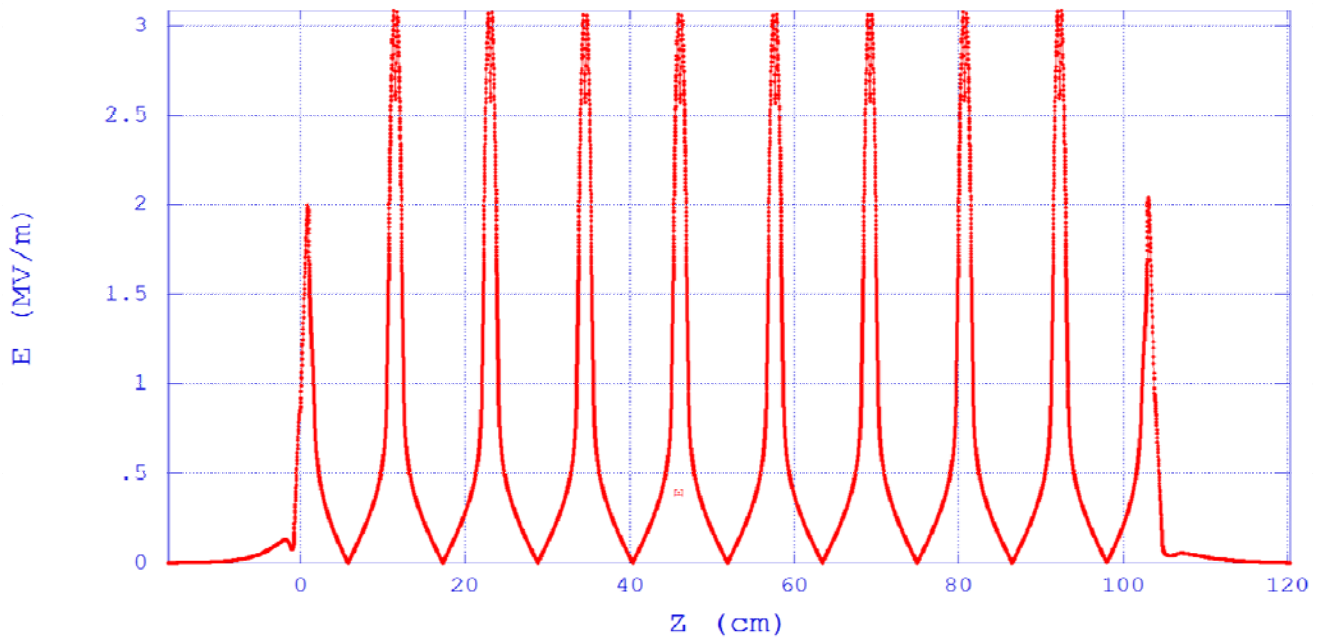


Figure 3. 6 Electric field on the surface for TM_{010} π mode and $E_{acc}=1MV/m$, with respect to Z coordinate [3].

In the next picture an enlarged view of the region around the iris between the first and second cell will be shown, in order to appreciate the field profile on the surface where it is more intense.

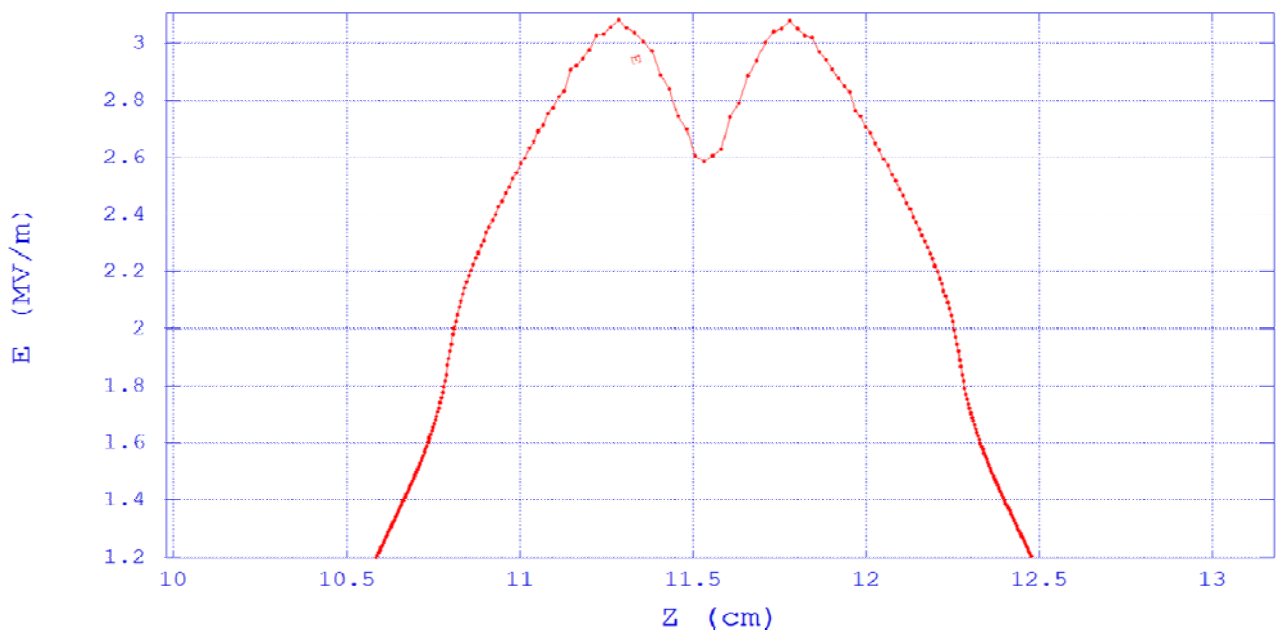


Figure 3. 7 Electric field on the surface for TM_{010} π mode and $E_{acc}=1MV/m$, with respect to Z coordinate near the iris between first and second cell.

The surface electric field and cavity geometry, as will be shown later in the dissertation, play a pivotal role for field emission process in multi cell RF cavity.

Through the numerical calculation, it is possible to calculate all the relevant quantities to characterize cavity performance such as surface magnetic field, geometric factor or impedance. They can be evaluated during design in order to obtain the optimum design with respect to the cavity application. Figure 3. 8 shows the magnetic field on the surface, its value allows to calculate the dissipated power due to the surface resistance.

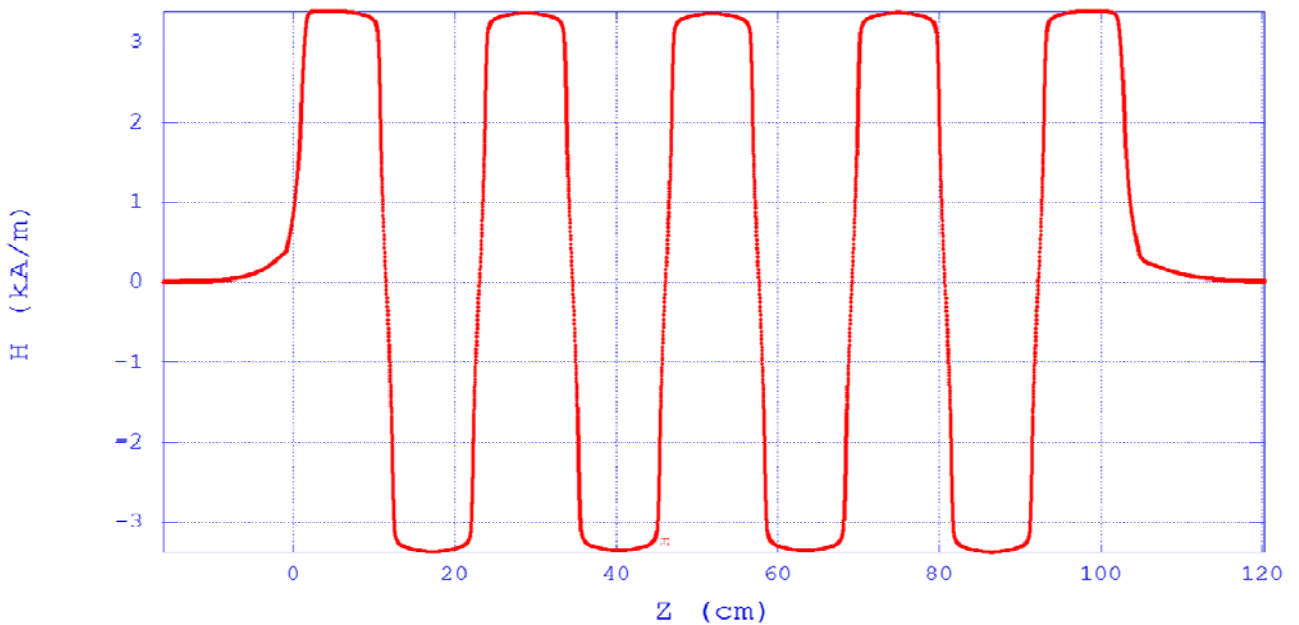


Figure 3. 8 Magnetic field on the surface for TM_{010} π mode and $E_{acc}=1MV/m$, with respect to Z coordinate [3].

Recalling that the power dissipated on cavity surface is

$$P_{loss} = \frac{1}{2} R_s \int_S |\vec{H}|^2 dS. \quad (3.7)$$

By reducing the intensity of the magnetic field, in particular with respect to the E_{acc} , it is possible to obtain a more efficient cavity design, moreover the Niobium can withstand only 2300Oe [5, 6] (practically 1700Oe up to now) before quenching. If no other issues are present, the ultimate

accelerating field is determined by the magnetic field intensity on the surface. For ERL cavity the ratio between the magnetic field peak and accelerating field is $42 \frac{\text{Oe}}{\text{MV m}^{-1}}$ [7] thus the cavity can reach at best an accelerating field of 54MV/m before quenching.

The table below summarizes the figures of merit calculated with SuperFish for ERL model 2 cavity.

Table 3.2 Calculated quantities with SuperFish for ERL cavity model.

| Property | KEK-ERL mod2 |
|----------------------------------|---|
| $\omega_{0 \text{ TM010}}$ | 1300 MHz |
| Surface resistance (R_s) | 26 n Ω @2K |
| Accelerating Field (E_{acc}) | 1 $\frac{\text{MV}}{\text{m}}$ |
| Power dissipation (P_{loss}) | 111 mW |
| Stored Energy (U) | 0.15 J |
| Transit time factor | 0.72 |
| Quality factor (Q_0) | 10^{10} |
| R/Q | 896 Ω |
| Geometry Factor (G) | 289 Ω |
| E_{pk}/E_{acc} | 3.0 |
| H_{pk}/E_{acc} | $42 \frac{\text{Oe}}{\text{MV m}^{-1}}$ |
| K_{cc} (cell to cell coupling) | 3.8% |

3.3 Particle tracking

The particle tracking is performed using FishPact code [8], electrons are generated on cavity surface, at different RF phases, with 2eV kinetic energy and tracked by means of relativistic momentum equations and Lorentz force using the electromagnetic field calculated with SuperFish.

The field is varied with a sine function oscillating at the resonant frequency, and the particle tracked at discrete time step (5ps) until it reaches the cavity surface. Along the electrons trajectory, the electromagnetic field changes with respect to time and position. At each simulation step, the electromagnetic field vectors are calculated by interpolation using SuperFish mesh points (space) and sinusoidal oscillation (time).

$$\vec{E}(\mathbf{Z}, \mathbf{R}) = \vec{E}_0(\mathbf{Z}, \mathbf{R}) \sin(\omega t), \quad (3.8)$$

$$\vec{B}(\mathbf{Z}, \mathbf{R}) = \vec{B}_0(\mathbf{Z}, \mathbf{R}) \sin\left(\omega t + \frac{\pi}{2}\right), \quad (3.9)$$

where \mathbf{Z} and \mathbf{R} are the longitudinal and radial coordinates inside the cavity, ω is the resonant frequency and t the time. The product ωt define the RF phase.

At each time step, the electrons interact with the electromagnetic field through Lorentz force, due to the field symmetry the electrons can move only on one plane corresponding to two different cavity meridians with 180° distance.

As shown before the accelerating mode is TM_{010} that is the magnetic field is perpendicular to the electrons plane of motion as shown below.

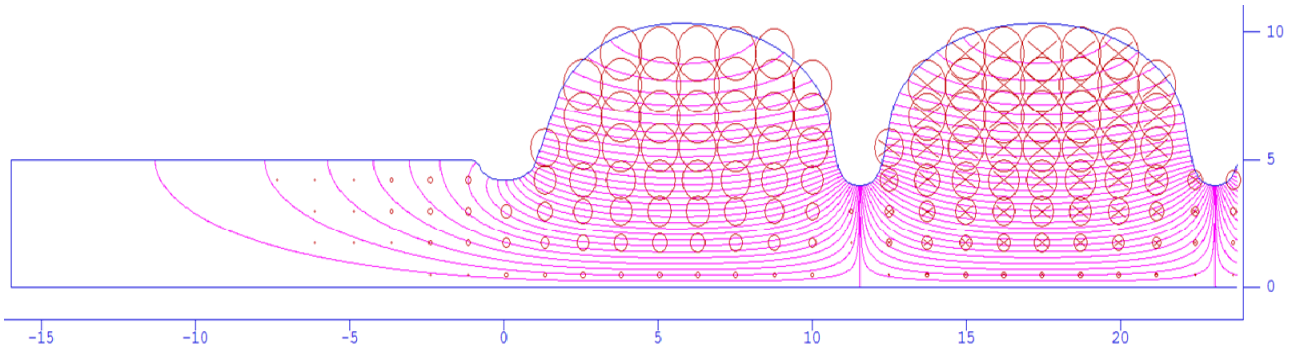


Figure 3. 9 Electric field (lines) and magnetic field (circle) in the first two cells for TM_{010} π mode.

The empty circle represents the magnetic field exiting from the paper plane, the circle with cross inside represent the magnetic field lines entering the paper plane.

The electrons dynamics is determined by the Lorentz force

$$\vec{F} = \frac{d\vec{p}}{dt} = q \left[\vec{E}(\mathbf{Z}, \mathbf{R}) + \vec{v} \times \vec{B}(\mathbf{Z}, \mathbf{R}) \right], \quad (3.10)$$

The algorithm to calculate the electron trajectory can be summarized as described in Figure 3. 10.

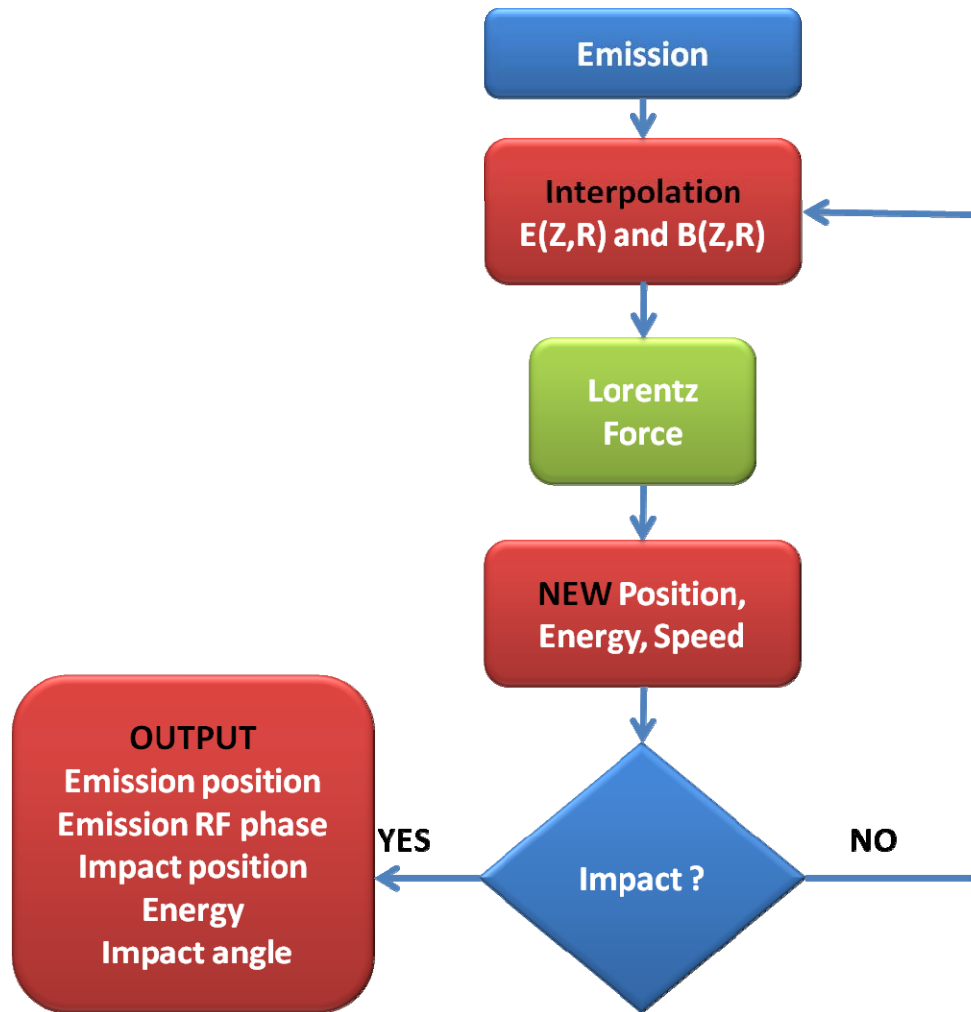


Figure 3. 10 Particle tracking code block diagram.

Once the electron hit the cavity surface, different quantities are recorded such as, impact location, impact energy, starting emitting phase and impact angle. All these information will be used during the post-processing to analyze the field emission effect on cavity performance.

After the emission, the electron starts to interact with the electromagnetic field, knowing the field vector at each position and the time interval the code calculate the momentum increment in each direction by means of 4th order Runge-Kutta method [2].

The momentum increment is

$$d\vec{p} = q[\vec{E}(Z, R) + \vec{v} \times \vec{B}(Z, R)] dt, \quad (3.11)$$

Then the new momentum can be calculated using the Runge-Kutta method as follow

$$d\vec{p} = \vec{p}' = \vec{f}(t, \vec{p}(t)) \quad (3.12)$$

where the function \vec{f} express the Lorentz force at time t .

The momentum at time interval t_{n+1} can be written as

$$\vec{p}(t_{n+1}) = \vec{p}(t_n) + (\mathbf{K}_1 + 2\mathbf{K}_2 + 2\mathbf{K}_3 + \mathbf{K}_4) \frac{dt}{6} + \mathcal{O}(dt^5), \quad (3.13)$$

where \mathcal{O} is the Landau symbol and the \mathbf{K} addendum are defined as follow:

$$\mathbf{K}_1 = \vec{f}(t, \vec{p}_n), \quad (3.14)$$

$$\mathbf{K}_2 = \vec{f}\left(\frac{t+dt}{2}, \vec{p}_n + \frac{1}{2}\mathbf{K}_1\right), \quad (3.15)$$

$$\mathbf{K}_3 = \vec{f}\left(\frac{t+dt}{2}, \vec{p}_n + \frac{1}{2}\mathbf{K}_2\right), \quad (3.16)$$

$$\mathbf{K}_4 = \vec{f}(t+dt, \vec{p}_n + \mathbf{K}_3), \quad (3.17)$$

dt is fixed to be 5ps, $\vec{p}(t_{n+1})=\vec{p}_{n+1}$ and $\vec{p}(t_n)=\vec{p}_n$ [2], the portion of code used for this calculation will be enclosed in the appendix section.

Once the momentum equation is solved the particle energy can be obtained as

$$E = \sqrt{\vec{p}^2 c^2 + m_0^2 c^4} = \gamma m_0 c^2, \quad (3.18)$$

where m_0 is the electron rest mass, c is the speed of light and γ is the Lorentz factor.

The electron speed and kinetic energy is calculated from the Lorentz factor as follow:

$$v = c \sqrt{1 - \frac{1}{\gamma^2}} \quad \text{and} \quad K.E. = (\gamma - 1) m_0 c^2 \quad (3.19)$$

Finally the new position is determined by

$$s(\mathbf{Z}, \mathbf{R}) = s_0 + \mathbf{v}dt. \quad (3.20)$$

The process described above will be repeated until the particle hit the cavity surface, at that point the data are recorded to be analyzed in the post-processing phase.

In the next two tables the input parameters used to run the simulation and the output results used for the post-processing are summarized.

Table 3.3 Particle tracking code input parameters.

| INPUT parameter | Description | Typical value |
|-------------------------|--|-------------------|
| Cavity shape | Axial symmetry | ERL-mod2 |
| E_{acc} | Accelerating field | $15 \frac{MV}{m}$ |
| Emitter position | (Z,R) in cylindrical coordinates | Around Iris |
| Emission RF phase | RF field phase during electron emission | 0-180 |
| Emission kinetic energy | Electrons kinetic energy after tunneling | 2eV |

Table 3.4 Particle tracking code output parameters.

| Simulation OUTPUT | Description | Typical value |
|-----------------------|--|---|
| Impact location | (Z,R) in cylindrical coordinates | Cavity surface |
| Impact kinetic energy | Electrons kinetic energy at the cavity surface | 1-15MeV |
| Impact angle | Angle with respect to the cavity surface | 0°-90° 90° is perpendicular to the surface |
| Emission RF phase | RF field phase during electron emission | 0-180 |

The emitter location and RF phase determines the emitted current density while other quantities address the interaction between electrons and cavity field. The data will be used in the next paragraph to calculate the particle shower once the electrons hit the cavity surface.

3.4 Particle tracking example

Finally, a calculation example will be presented to show how the simulation is performed. The KEK-ERL cavity model 2 operating at π mode with $E_{acc}=13.9\text{MV/m}$, where the emitter is located on the iris between 8th and 9th cell will be used.

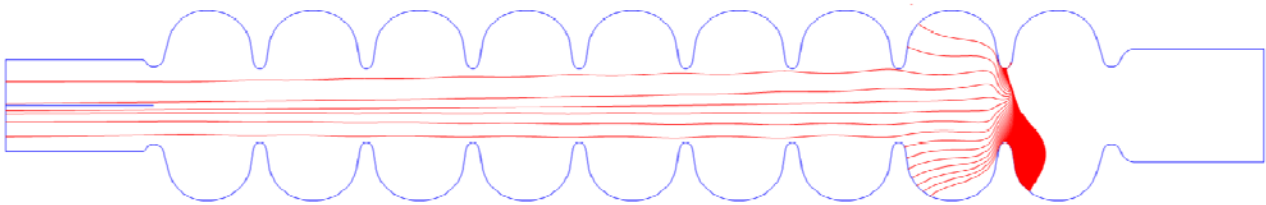


Figure 3.11 Electron trajectories, each trajectory start at different RF phase during electron emission, the emitter is located between the 8th and 9th cell (upper part).

Figure 3.11 and Figure 3.12 depict electrons trajectory that depart from the surface at different RF phase. The electrons kinematics strongly depend on cavity condition , RF phase and emitter location.

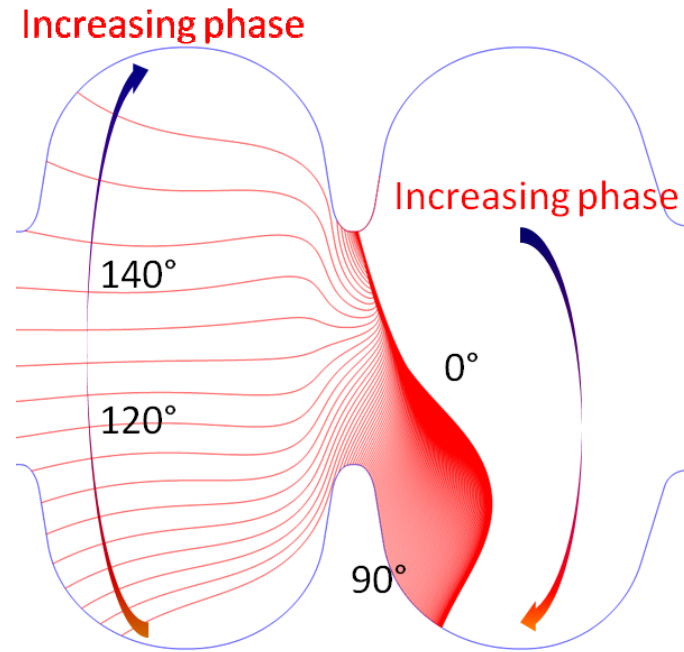


Figure 3.12 Electron trajectories, each trajectory start at different RF phase, from 0° to 180° the phase increase clockwise.

To better understand the electron behavior inside the cavity we can start by analyzing just one trajectory. In the figure below is shown a trajectory for an electron starting from 8-9 iris at 135° RF phase (the phase is varied with a sine function).

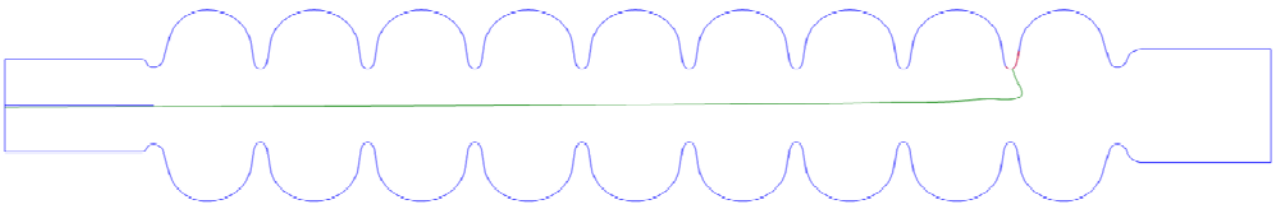


Figure 3. 13 Electron trajectory starting from 8-9 Iris at 135° RF phase.

As can be seen, the electron flies near the cavity axis, hitting the left end almost perpendicularly to the flange surface.

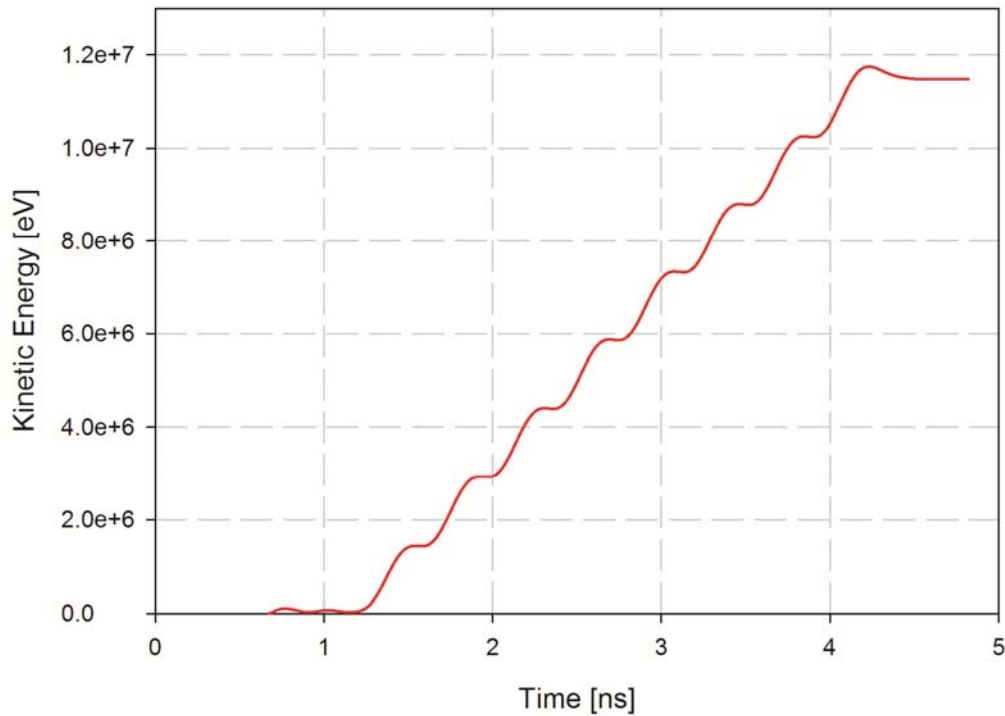


Figure 3. 14 Electron kinetic energy during the time of flight inside the cavity.

The cavity is designed for $\beta=1$ particles, but when the field emitted electrons are injected into the cavity they have a lower β . Depending on the accelerating field the electrons can reach relativistic speed after some RF cycle, so their energy gain can be less than expected for $\beta=1$ particles.

The kinetic energy does not increase smoothly, as can be seen in Figure 3. 14, but after an initial gain it decreases because the electric field has changed direction while the electron is flying in the same cell. Depending on the emission phase and accelerating field this effect can be more or less intense, while the electrons enter a cell they are initially accelerated but before they can exit the cell the electric field has already changed its versus leading to a deceleration.

In the picture below is shown the electron kinetic energy with respect to the position inside the cavity (Z axis), highlighting the cells location.

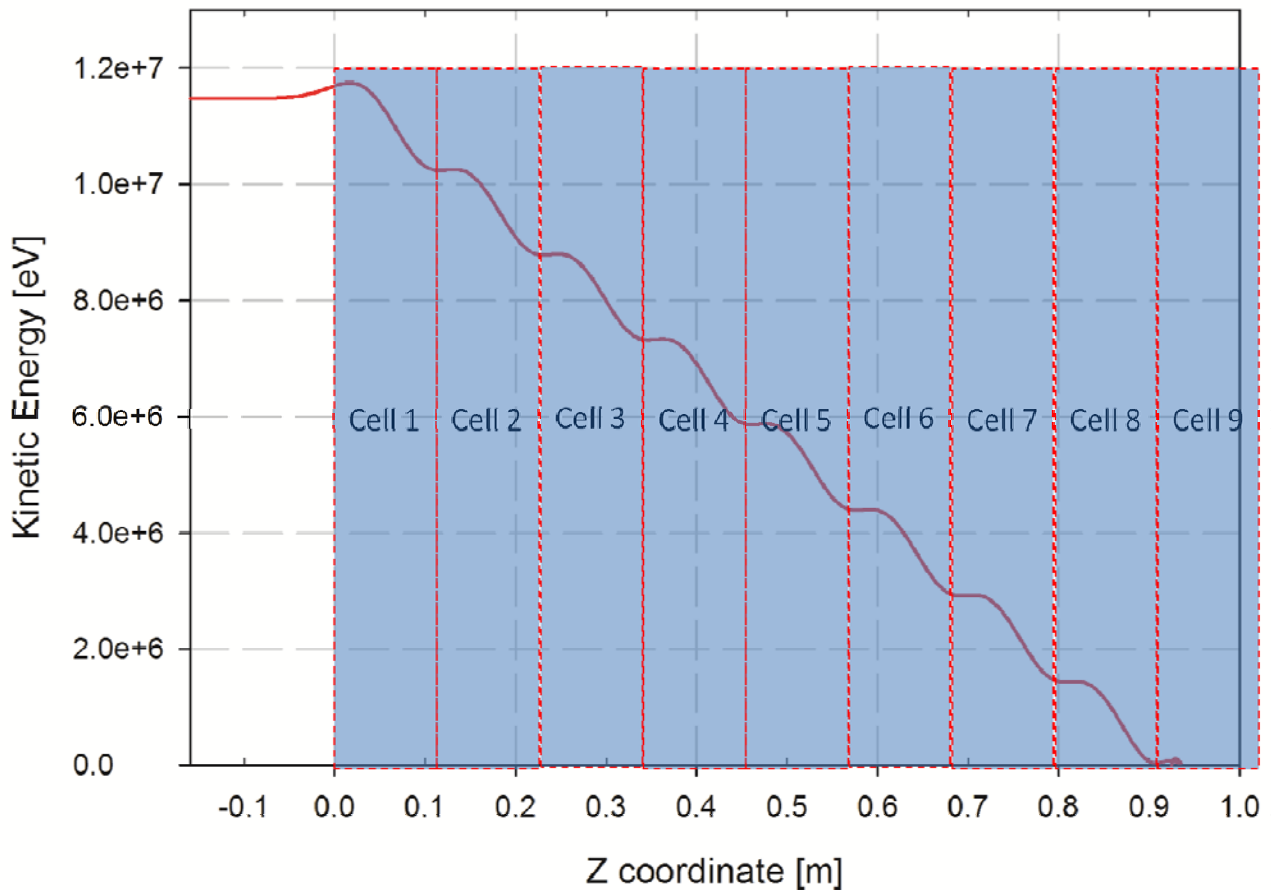


Figure 3. 15 Electron kinetic energy with respect to position inside the cavity, each cell location is highlighted, the electrons move from 9th cell to the 1st (right to left).

The electrons reach 11.5MeV passing through 8 cells and land on the flange at the small beam pipe side (SBP).

3.4.1 Systematic approach (parameters scan)

It is important to study the interaction between emitted electrons and cavity field by scanning the parameters space, such as emitter location, initial RF phase and accelerating field. This kind of systematic approach lead to an insight in the field emission process.

First, we consider to operate the cavity at its working condition TM_{010} π mode with $E_{acc}=15MV/m$ and cover the region near the 1st and 2nd cell iris with emitters spaced by 0.5mm along the cavity surface (Figure 3. 16).

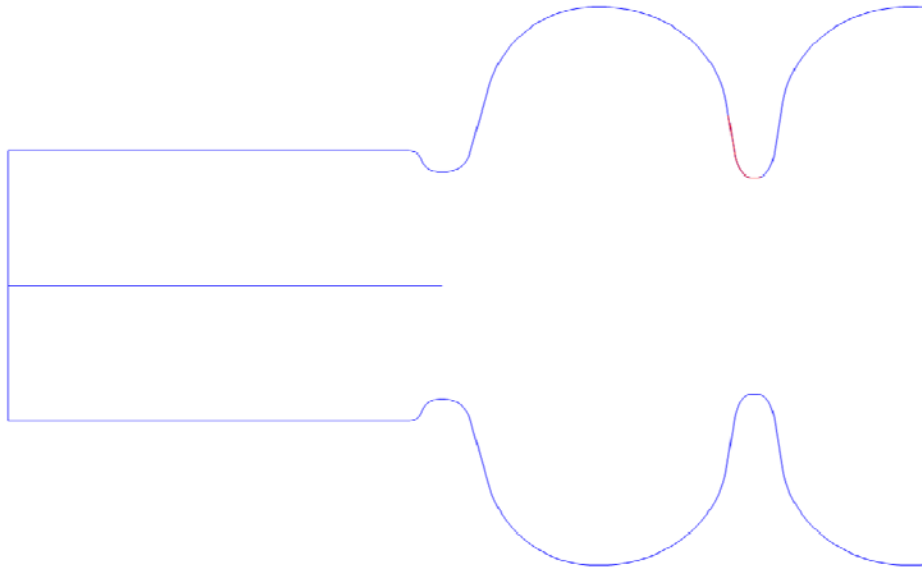


Figure 3. 16 Region where emitters are located (red line).

Then we can calculate in which operating condition electrons can escape from the cavity, either from small beam pipe (SBP) or large beam pipe (LBP). In this case the SBP is located near to the emission region so that electrons shall fly directly to the exit, on the other hand the LBP is located on the far end of the cavity, to reach that location electron trajectory shall bend to fly along the cavity axis (as shown in the previous example).

By exciting the cavity to π mode with an $E_{acc}=15\text{MV/m}$ and scanning all the emitters location at any RF phase we can obtain the plot shown in Figure 3.17. The black dots represent trajectories that can escape from LBP side while the red ones represent trajectories escaping from SBP side.

We can clearly identify two regions:

- Escaping from SBP: limited from 0° to 90° RF phase and from 4.5mm to 8.5mm away from the iris (Figure 3.18).
- Escaping from LBP: limited from 90° to 140° RF phase and from 0.5mm to 4.5mm away from the iris (Figure 3.18).

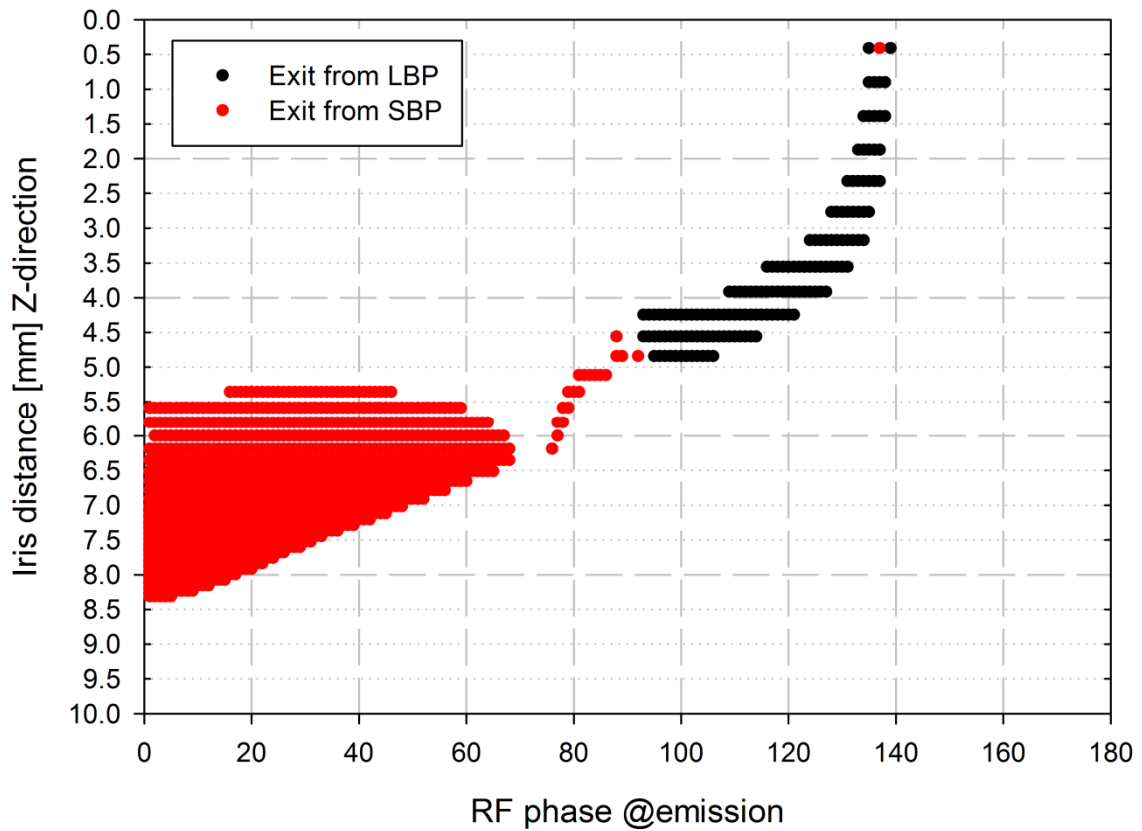


Figure 3.17 Escaping location with respect to emitter location (Z coordinate) and emission RF phase at 15MV/m π mode.

The emitter locations for each region are highlighted in the pictures below, just as a reminder the LBP is located on the right while the SBP is located on the left with respect to the pictures.

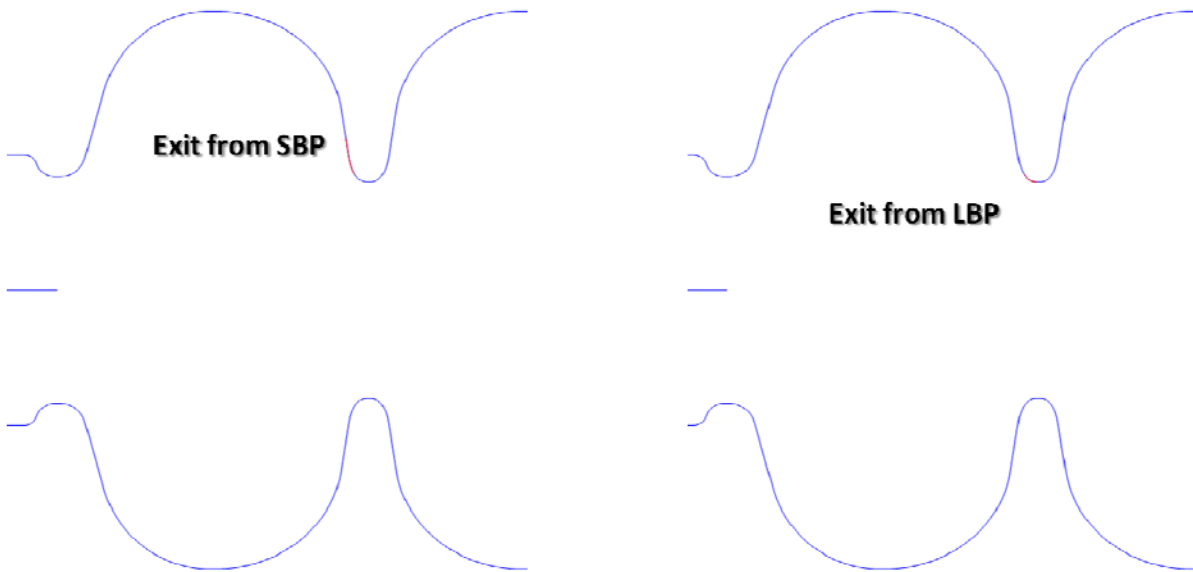


Figure 3.18 Regions located in the 1st cell that allows electrons to exit from SBP (left) or LBP (right).

Due to the field symmetry, the same emitter region can be found on each iris. In Figure 3.17 the SBP region (red dots) appears shorter with respect to the LBP region (black dots) this is due to the projection on the Z axis. To evaluate their length with the correct proportion it is better to use a coordinate that follow the cavity surface (S).

In Figure 3.19 is shown the same graph as Figure 3.17 by substituting the Z coordinate with S coordinate.

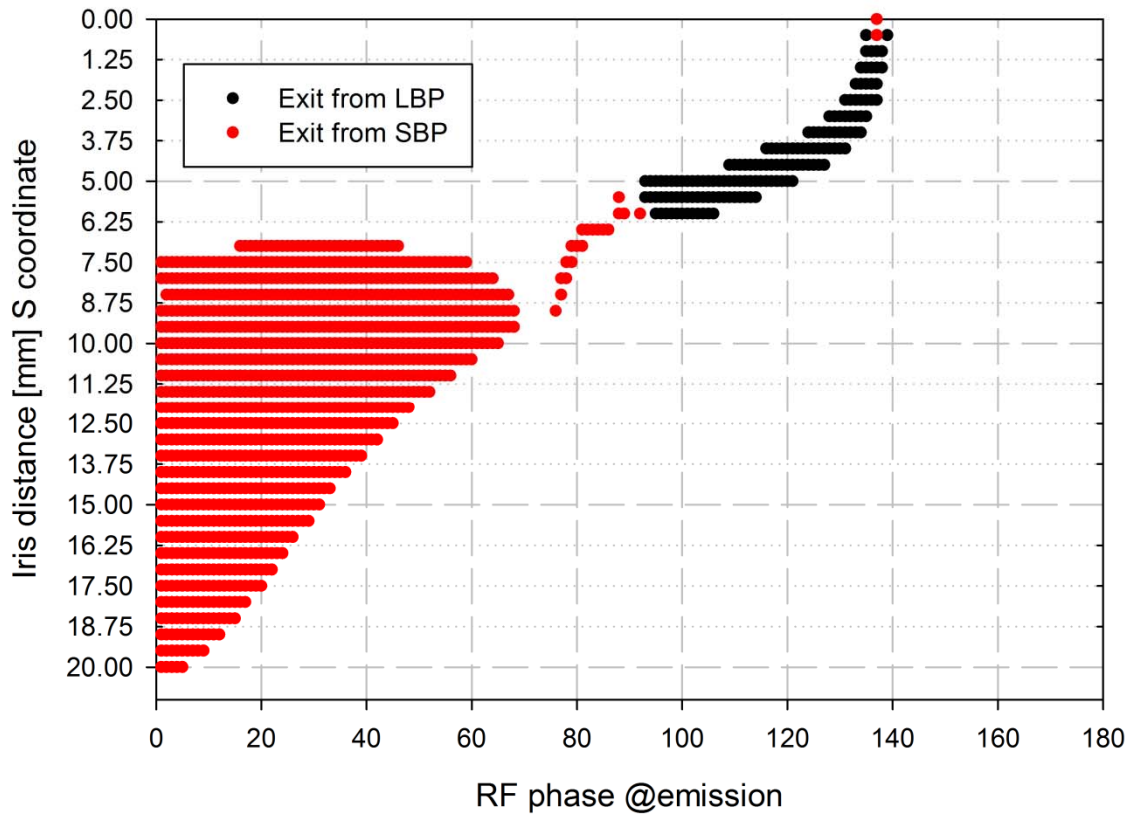


Figure 3.19 Escaping location with respect to emitter location (S-coordinate) and emission RF phase at 15MV/m π mode.

The two region are still clearly visible and with the correct proportion. Plotting all the landing locations to further understand how the electrons fly inside the cavity. That is by filling up all the missing trajectories corresponding to the blank spaces in the above plot. The result of this process is shown in Figure 3.20.

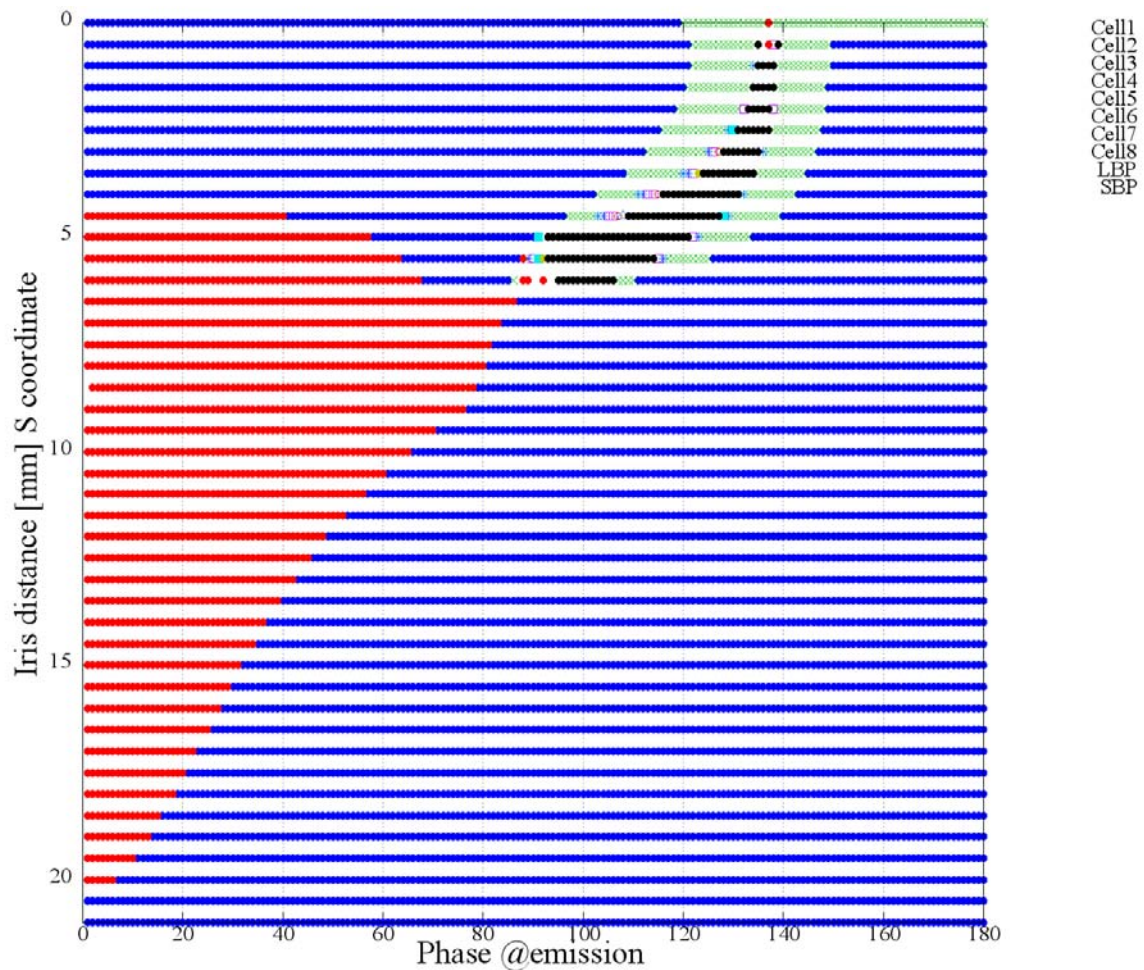


Figure 3.20 Landing location with respect to emitter location (S-coordinate) and emission RF phase at 15MV/m π mode, emitters are located on iris between cell 1 and cell 2.

Mainly the electrons remain in the first cell (blue dots), but there are region (in location-phase space) that electrons reach SBP, LBP or second cell only. It is interesting to notice that all the trajectories that can fly along the cavity are located in the top-right part of the plot, part of them can pass through the whole cavity reaching the LBP while others hit the cavity surface before exiting.

The same behavior can be expected from all iris (due to the field symmetry) with the only difference that by moving the emission region more inside the cavity the portion of electron reaching the SBP will be reduced while the ones reaching the LBP increased (due to the impacts on the inner surface). This effect is clearly visible when the emission area is located between 4th and 5th cell (Figure 3.21).

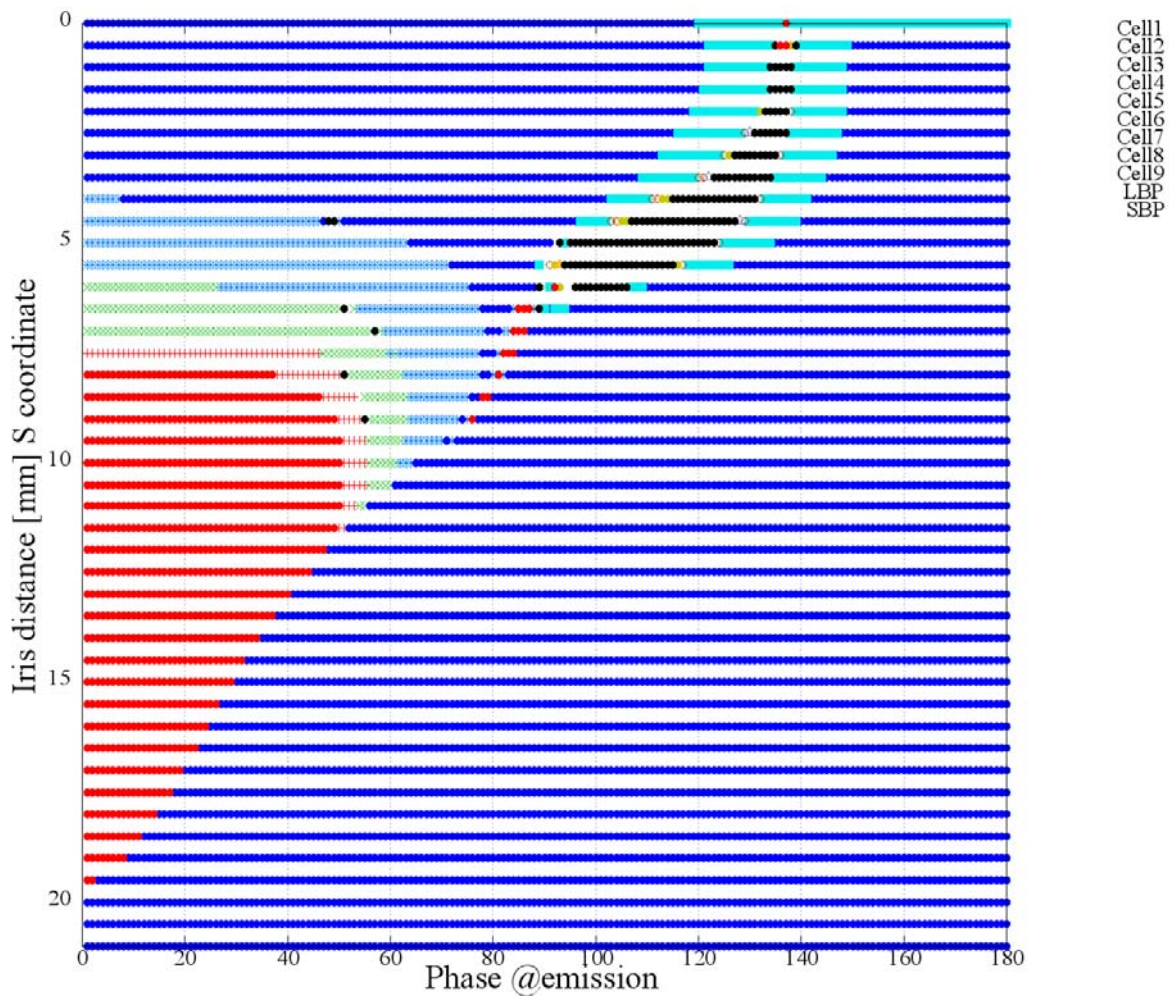


Figure 3.21 Landing location with respect to emitter location (S-coordinate) and emission RF phase at 15MV/m π mode, emitters are located on iris between cell 4 and cell 5.

To make easier the comparison with the previous figure, the electron landing inside the 4th cell is depicted in blue as in the previous plot was 1st cell, these are the cells where the emission area belong. As expected, the region that before produced emission towards SBP is now divided in different bands corresponding to cells on the path to the SBP.

3.4.2 Generalized location-phase diagram

In the next pictures a set of trajectories representative of the above regions will be represented.

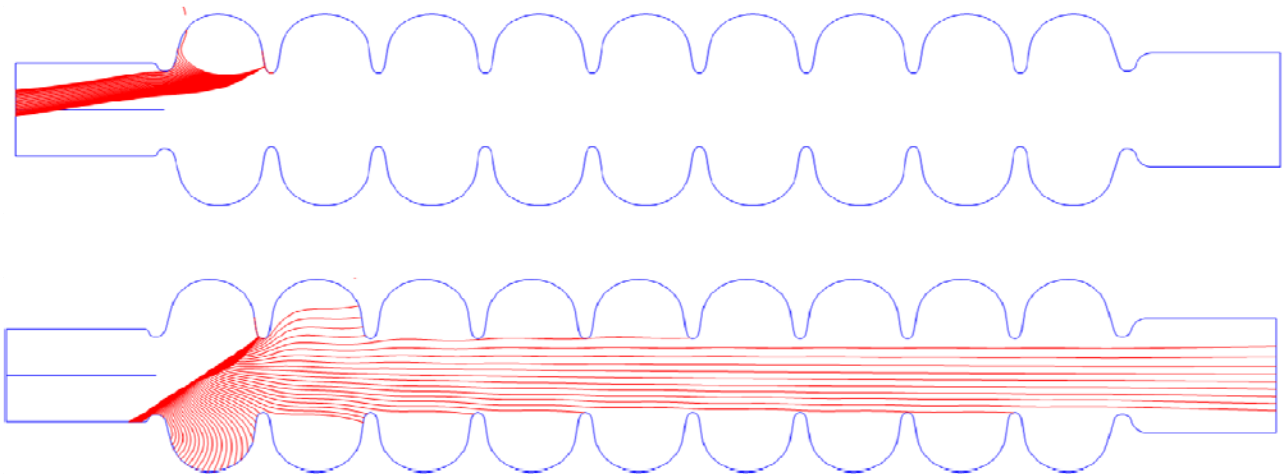


Figure 3.22 Electrons trajectory at different RF phase during emission at 15MV/m π mode, emitters are located on iris between cell 1 and cell 2.

In the first picture, the trajectories mainly proceed directly towards the SBP or they land inside the cell, while in the second case they invert their motion to proceed towards the LBP, during their flight they can land in the emitting cell or hit other iris while reaching the LBP. For simplicity let call the first case “Direct trajectory” and the latter “Inverted trajectory”.

To summarize the lessons learned from the above calculations, we can say that on each iris there are region in location-phase space where “direct trajectories” are produced and region where “inverted trajectories” are generated. The two regions produce trajectories that move in opposite direction (in the case shown above the direct proceed to the SBP and the inverted proceed to the LBP).

In Figure 3.23 a generalized diagram is shown that can be applied to any iris, while the cavity is operating at 15MV/m π mode.

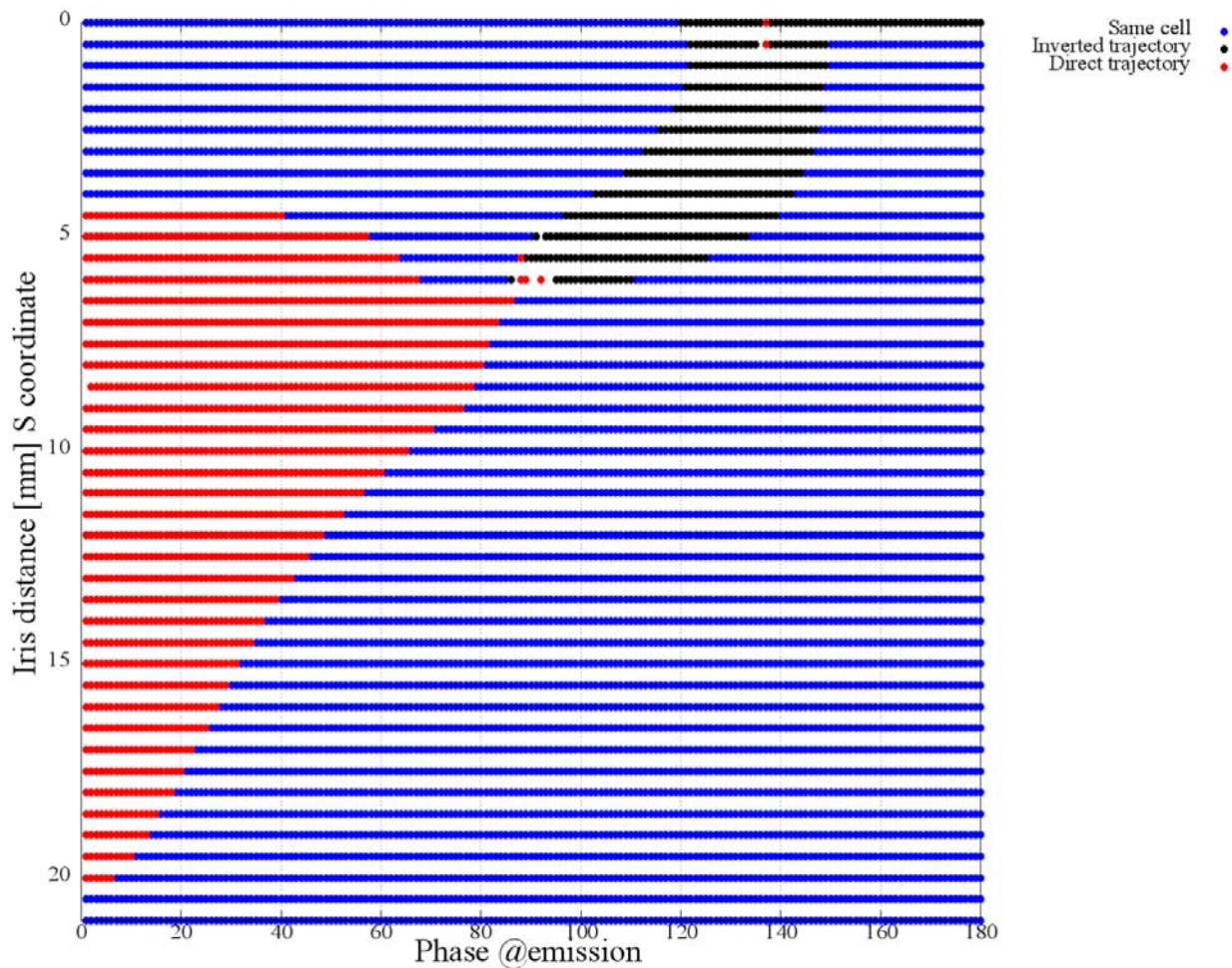


Figure 3.23 Flying direction with respect to emitter location (S-coordinate) and emission RF phase at 15MV/m π mode, the plot is generalized for any iris.

3.4.3 Impact energy

The electron impact energy can be investigated in the same way that has been done for the landing locations. It is an important quantity in the path to understand which emission region can affect the cavity performance.

In figure 3.24 a contour plot representing the impact energy in eV in the location-phase space is shown, the emitter location is always expressed as the distance from the iris in the S coordinate. The emission region is located between the 1st and 2nd cells, the cavity is excited at π mode with $E_{acc}=15\text{MV/m}$.

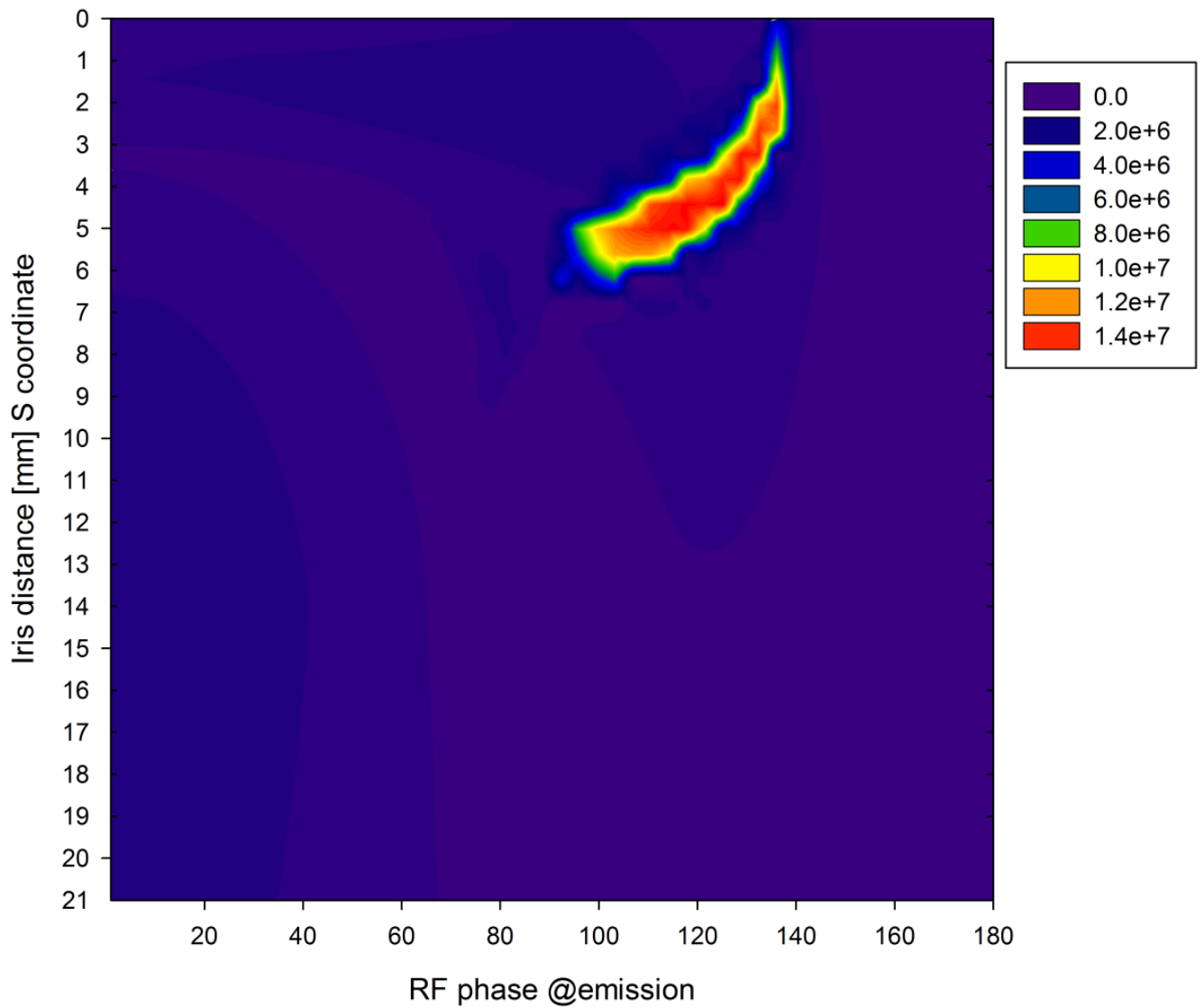


Figure 3.24 Impact energy with respect to emitter location (S-coordinate) and emission RF phase at 15MV/m π mode, emission region is between 1st and 2nd cell.

The trajectories that flight along the cavity axis (to the LBP) are clearly visible, they gain more kinetic energy with respect to others. By doing the same calculation with the emission area located between the 4th and 5th cells it will be more visible the trajectories reaching the SBP.

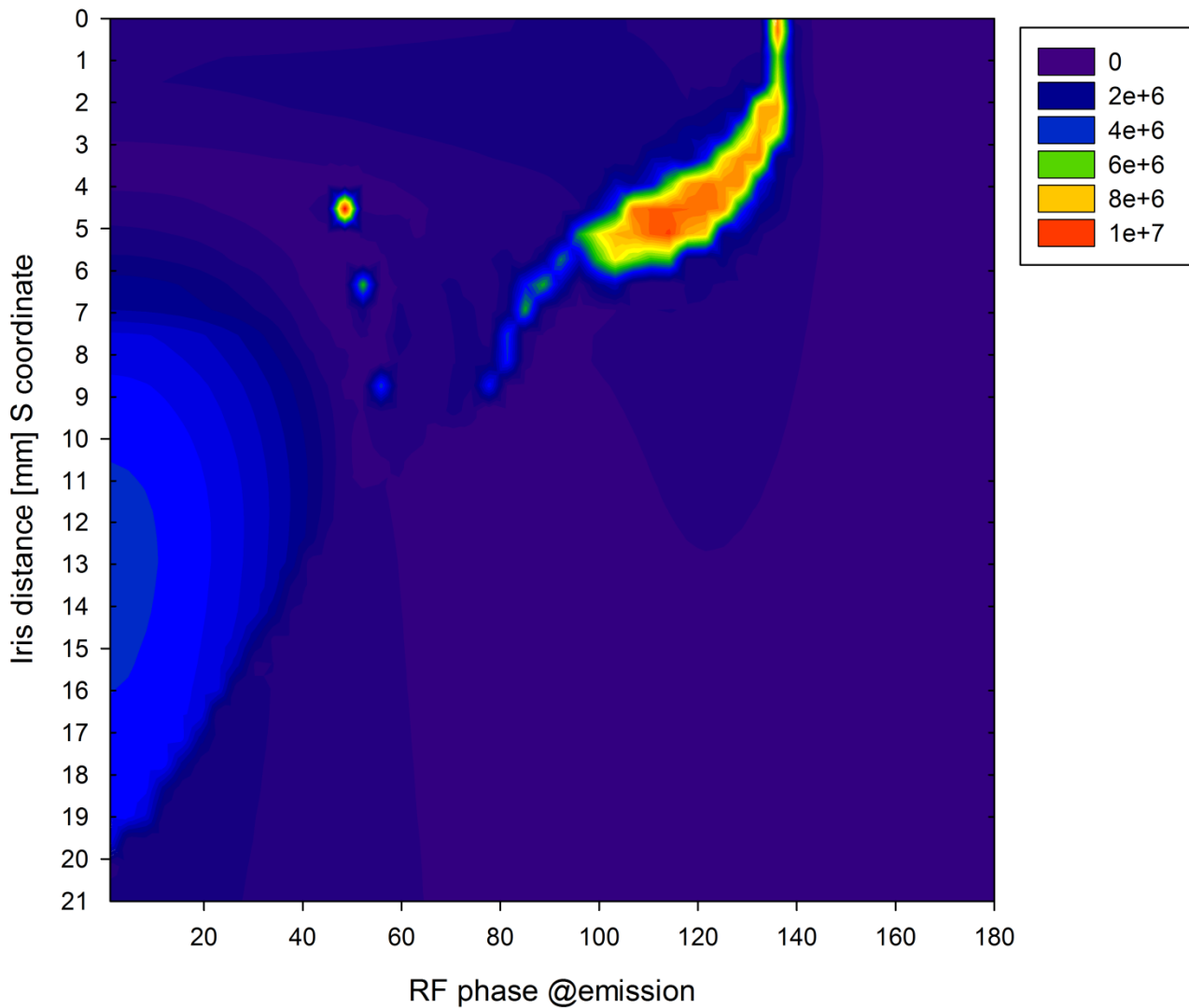


Figure 3.25 Impact energy with respect to emitter location (S-coordinate) and emission RF phase at 15MV/m π mode, emission region is between 4th and 5th cell.

The high energy region has similar shape as in the previous case, the difference is in the kinetic energy value, in the first case the electrons that land in the LBP reach 14MeV while in the second case is just 10MeV.

From this two examples, it start sto be clear which region produce electron that can reach higher kinetic energy, the power dissipated through field emission can be calculated by combining this information with the emitted current. This will be discussed in the next paragraph.

3.5 Dark current calculation

To calculate the emitted current from each region it is necessary to know the surface electric field in respect to the RF phase along with the emitter geometry and composition.

Recalling the Fowler-Nordheim equation for a sine varying RF field we can write the emitted current as

$$I = Area_{emitter} \frac{A(\beta E_{surf} \sin(\theta))^2}{\varphi} e^{-B \frac{\varphi^{1.5}}{\beta E_{surf} \sin(\theta)}}, \quad (3.21)$$

where A and B are constants, $Area_{emitter}$ is the emitter surface, θ is the RF phase, φ is the material working function and β is the field enhancing factor.

From equation 3.21 we can see the dependency on emitted current with respect to the surface electric field and RF phase along with the emitter geometry.

3.5.1 Surface electric field

First we need to calculate the electric field amplitude on the surface with respect to the RF phase and emitter location. The data are gathered from SuperFish results assuming an electric field varying as a sine function. Figure 3.26 shows the field amplitude near the cavity iris.

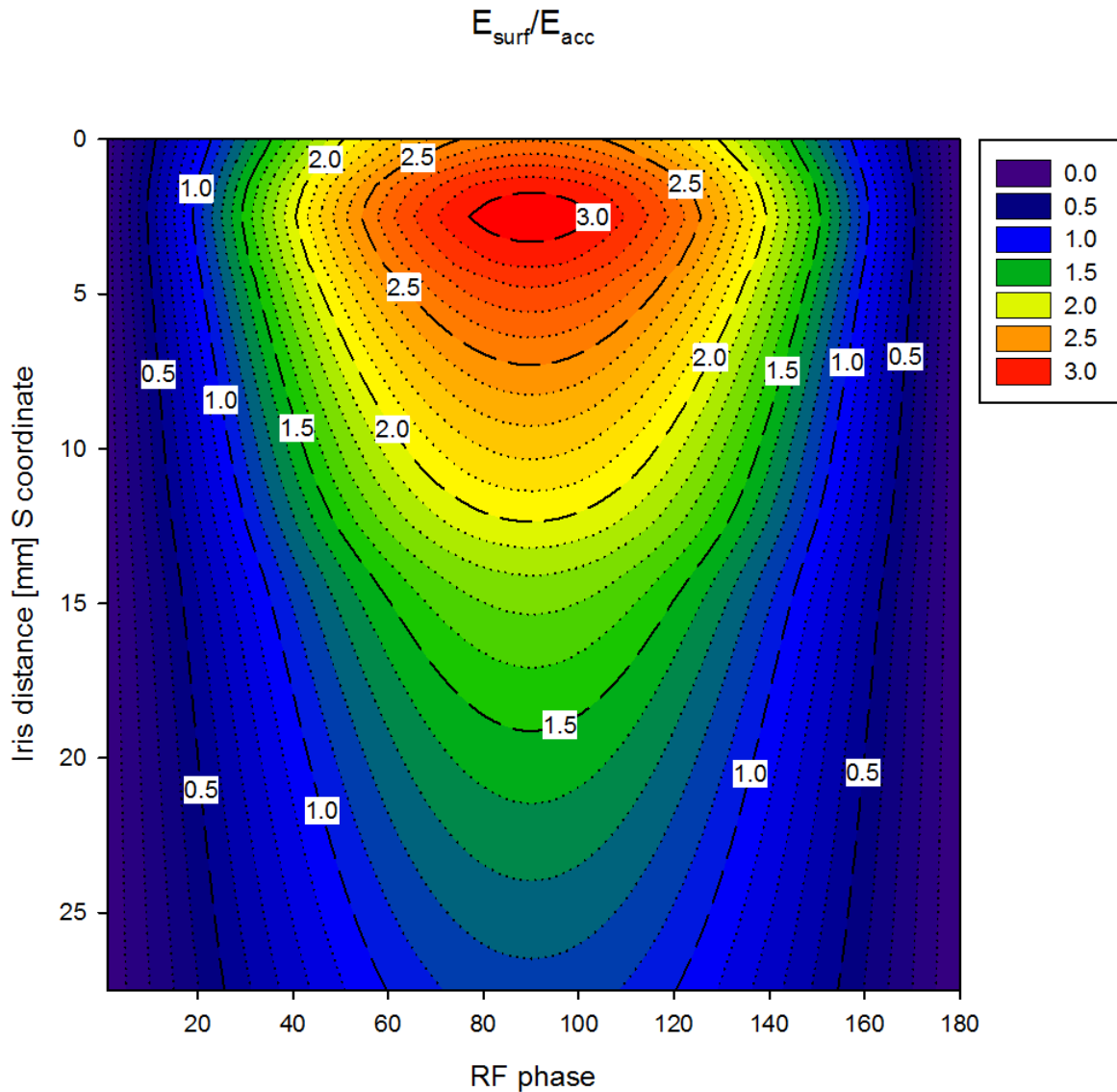


Figure 3.26 Contour plot for $E_{\text{surf}}/E_{\text{acc}}$ with respect to RF phase and S coordinate.

3.5.2 Emitted current

The emitted current is calculated in respect to RF phase and emitter location (the emitter location determines the electric field amplitude on the surface).

In Figure 3.27 the emitted current is shown assuming an accelerating field of 15MV/m, a local enhancing factor (β) equal to 100 and an emitter area of 10^{-13} m^2 [9]. The emission peak is localized where the field amplitude is bigger.

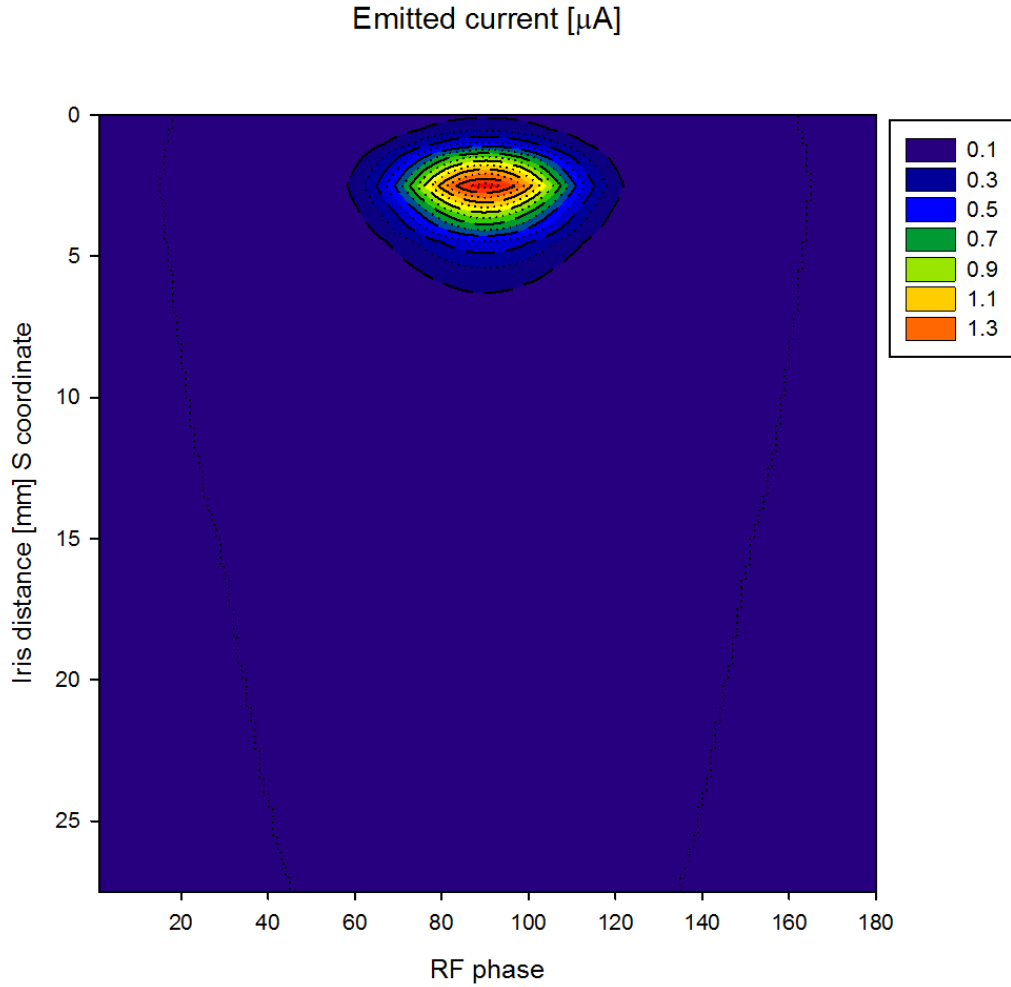


Figure 3.27 Emitted current [μA] with respect to RF phase at $E_{acc}=15\text{MV/m}$, field enhancement factor $\beta=100$ and emitter area 10^{-13} m^2 .

3.5.3 Dissipated power

The emitted current is one part of the information needed to understand the influence of field emission on cavity performance. The dissipated power is calculated by multiplying the emitted current and electron impact energy. Through the particle tracking code it is possible to associate to each RF phase and emitter location a specific impact energy (Figure 3.24 and Figure 3.25). The dissipated power at each RF phase is defined as

$$P_{FE}(\theta) = I_{emitted}(\theta) \cdot Energy_{impact}(\theta). \quad (3.22)$$

At π mode with fixed operating condition and same field enhancing factor, each iris can emit the same amount of current, on the other hand the electrons impact energy change in respect to the iris location (trajectories length is different). Keeping in mind this scenario it is clear that the maximum energy gain can be obtained for electrons emitted from the iris in the end cells (between the 1st and 2nd or 8th and 9th). It can be considered the worst case scenario because the electrons are able to fly along the whole cavity and gain maximum energy possible.

Figure 3.28 shows the result from equation 3.22, each point on the graph define a specific emitter location, RF phase during emission and the corresponding dissipated power. It combines the information from Fowler-Nordheim equation and particle tracking results.

The picture shows a spot where the emitted power is bigger than any other locations, we can define it as a “Danger area” (defined in location-phase space). If an emitter is located inside that area the power loss due to field emission is bigger than in any other case. Due to the field symmetry (in π mode) the same area can be located on each iris (both cell sides), the peak power will depend on iris location in the cavity.

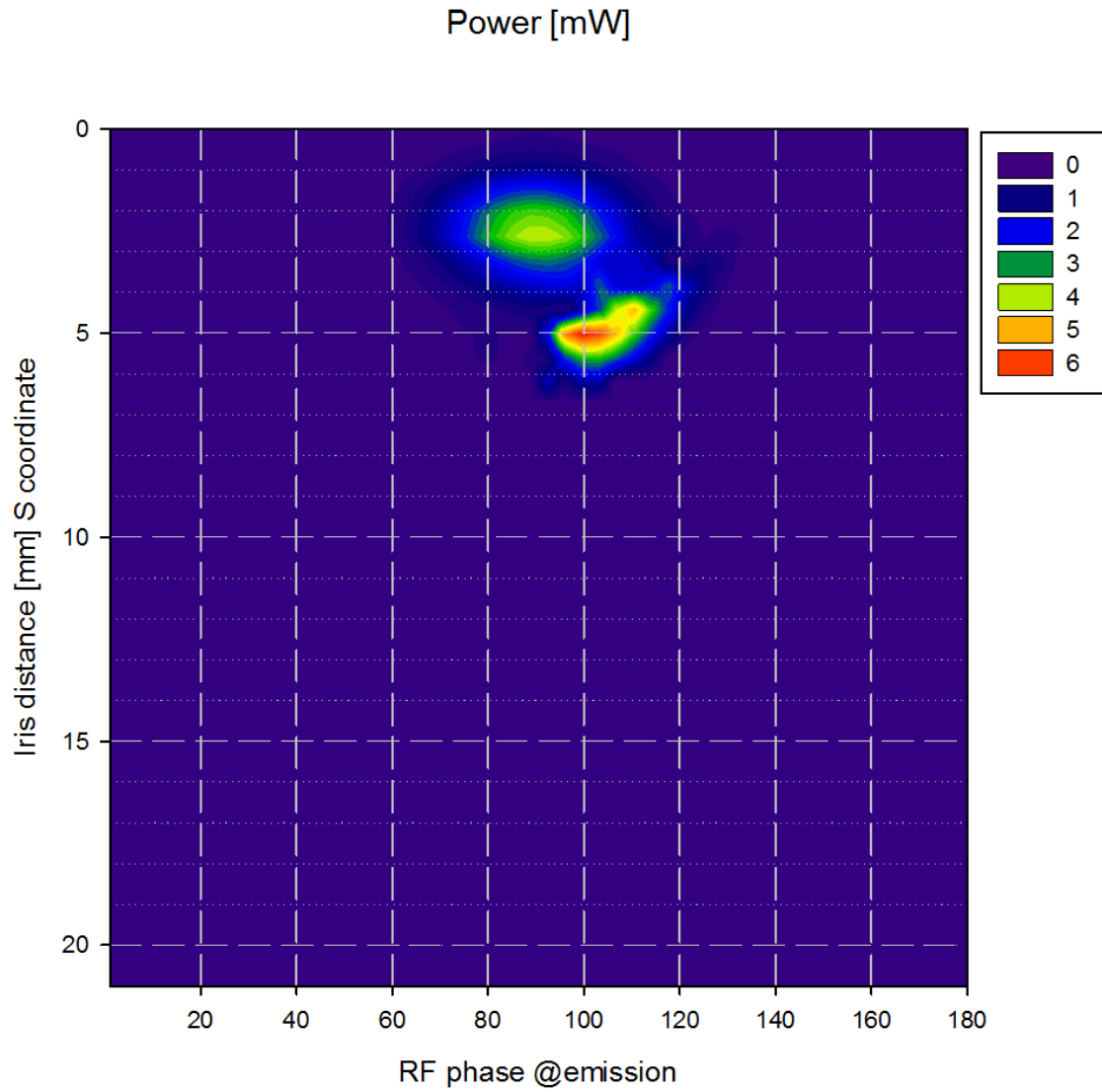


Figure 3.28 Emitted power [mW] with respect to RF phase at $E_{acc}=15\text{MV/m}$, field enhancement factor $\beta=100$ and emitter area 10^{-13} m^2 .

By summing up each phase contribution we can obtain the total dissipated power for each emitters, the result is shown in Figure 3.29, where the total power dissipated from each emitter can be expressed as

$$P_{emitter}^{total} = \sum_{\theta=0}^{180} P_{emitter}(\theta), \quad (3.23)$$

where $P(\theta)$ is the power dissipated at phase θ .

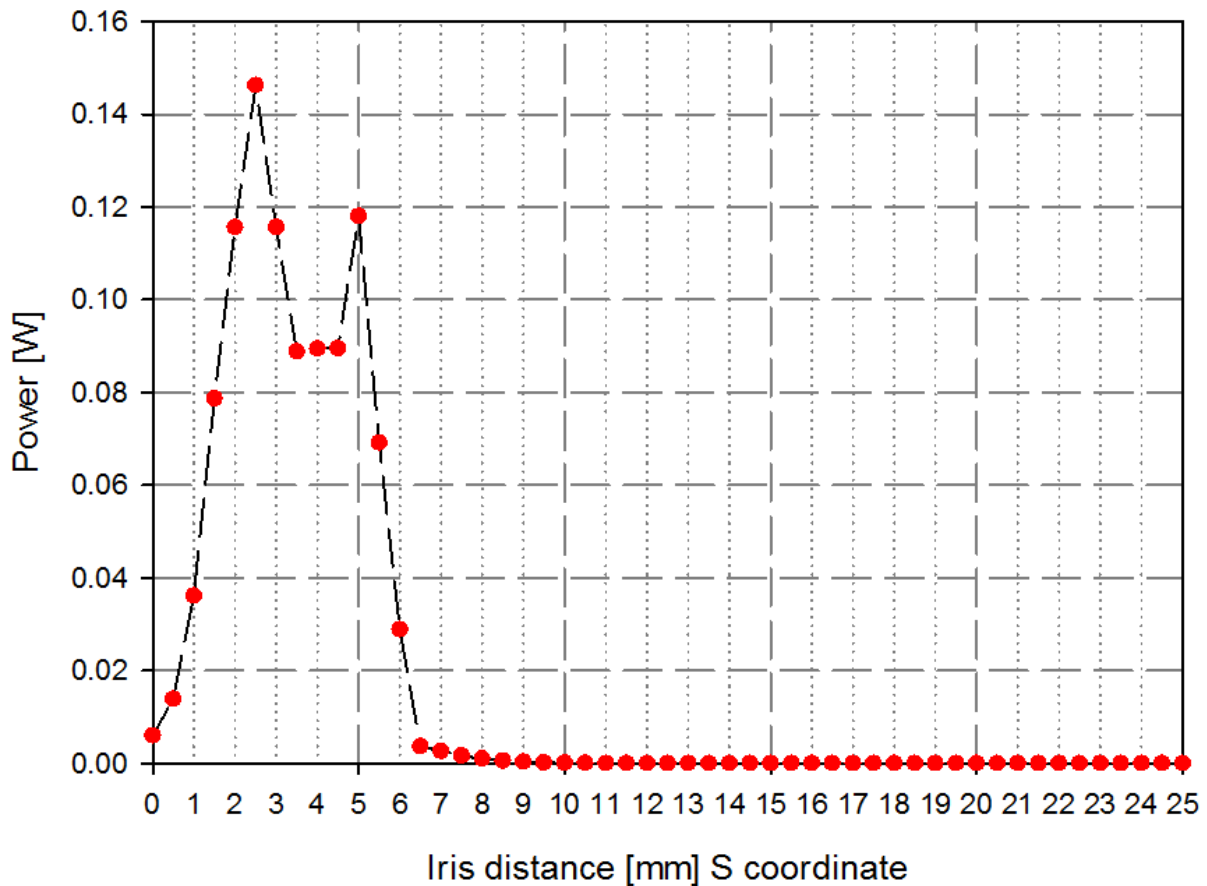


Figure 3.29 Total emitted power [W] or each emitter, with respect to RF phase at $E_{acc}=15\text{MV/m}$, field enhancement factor $\beta=100$ and emitter area 10^{-13} m^2 .

From the figure above it is possible to identify a region where 90% of the power is dissipated (danger area), it is about 6mm long on the cavity surface, with two peaks located between 2-3mm and between 4.5-5.5mm from the iris middle point.

3.6 EGS5 simulation

This last calculation addresses the interaction between the accelerated electrons and the cavity surface (niobium). To solve this kind of problem, the Montecarlo Electron-Gamma Shower (EGS5) codes suite will be used, which has been developed for more than 20 years creating a set of Fortran routines able to account different particle-particle and particle-matter interactions [10].

A detailed discussion on Montecarlo simulation is beyond the purpose of this dissertation so here only a broad view about EGS5 code will be presented.

The EGS5 algorithm can be divided into particle transport and particle interaction. The code takes into account the mean free path to decide if the particle interacts or not, it is defined as

$$\lambda = \frac{M}{N_a \rho \sigma_t}, \quad (3.24)$$

Where M is the molecular weight, N_a is the Avogadro number, ρ is the density and σ_t is the total interaction cross section per molecule.

The interaction probability along the distance dx is defined as

$$Pr\{dx\} = \frac{dx}{\lambda}. \quad (3.25)$$

So the number of free paths traversed by the particle is

$$N_\lambda = \int_{x_0}^x \frac{dx}{\lambda(x)}. \quad (3.26)$$

To decide if an interaction takes place, the code generates a first random number, if it is bigger than N_λ the code considers an interaction event and generates a second random number to decide which type of interaction the particle is undergoing. For charged particles the relevant interactions can be a Coulomb scattering from nuclei, inelastic scattering by atomic electrons, positron annihilation and bremsstrahlung. Each of them has a peculiar cross section and branching ratios defined as

$$F(i) = \frac{\sum_1^i \sigma_j}{\sigma_t}, \quad (3.27)$$

where σ_t is the total interaction cross section and σ_j is the crossing section for the j^{th} type of interaction. If the generated random number r falls within the interval

$$F(i-1) < r < F(i) \quad (3.28)$$

then the i^{th} interaction type is selected and another random number is generated to decide the interaction products by using the final states joint density function.

The following list represents the quantities calculated with EGS5 and used in this dissertation:

- Shower trajectory in terms of positions, angles and energy.
- Deposited energy.
- Reflected energy.
- Transmitted energy.

3.6.1 EGS5 example

Next a simple example will be presented in order to better understand the information that can be gathered from the simulation. For any specific purpose it is necessary to write a customized routine that exploit the EGS5 code, the routine shall define the geometry, the material properties and the energy range where the calculation is confined.

For simple geometry, it is possible to embed the geometry in the main routine but for more complex one it is necessary to use the combinatorial geometry, through it is possible to build quite elaborate element by using elementary solids like parallelepiped, cylinder, sphere, truncated cylinder and torus.

The following example, despite its simplicity, will allow us to compare the results with literature data and estimate the routine goodness. We will calculate the transmission probability for photons through a Niobium slab, a monochromatic pencil-like photon beam will impinge on one side of the slab and the relevant shower quantities will be calculated.

The results will be compared with data published from National Institute of Standard and Technology (NIST) [11, 12] for x-ray mass attenuation.

The model geometry is shown in the next picture

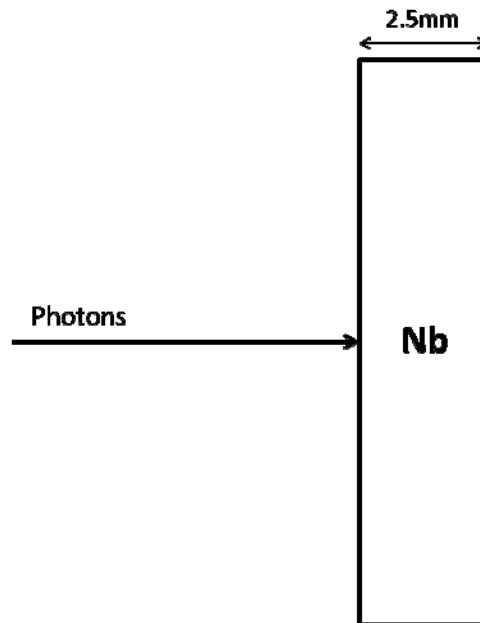


Figure 3.30 EGS5 model geometry.

The photons beam hit the Niobium slab (2.5mm thick) perpendicularly, at each simulation run the photons energy is increased starting from 50KeV up to 20MeV, the results are compared with the data derived from the mass energy-attenuation coefficients.

The attenuation equation state that [11]

$$I(d) = I_0 e^{\frac{-\mu d}{\rho}} \quad (3.29)$$

Where I_0 is the photons beam intensity hitting the slab, d is the slab thickness (2.5mm), ρ is the Niobium density (8.57 g/cm^3), μ is the attenuation coefficient and $I(d)$ is the beam intensity after the slab

Using the geometry shown previously we can identify 3 zone as follow

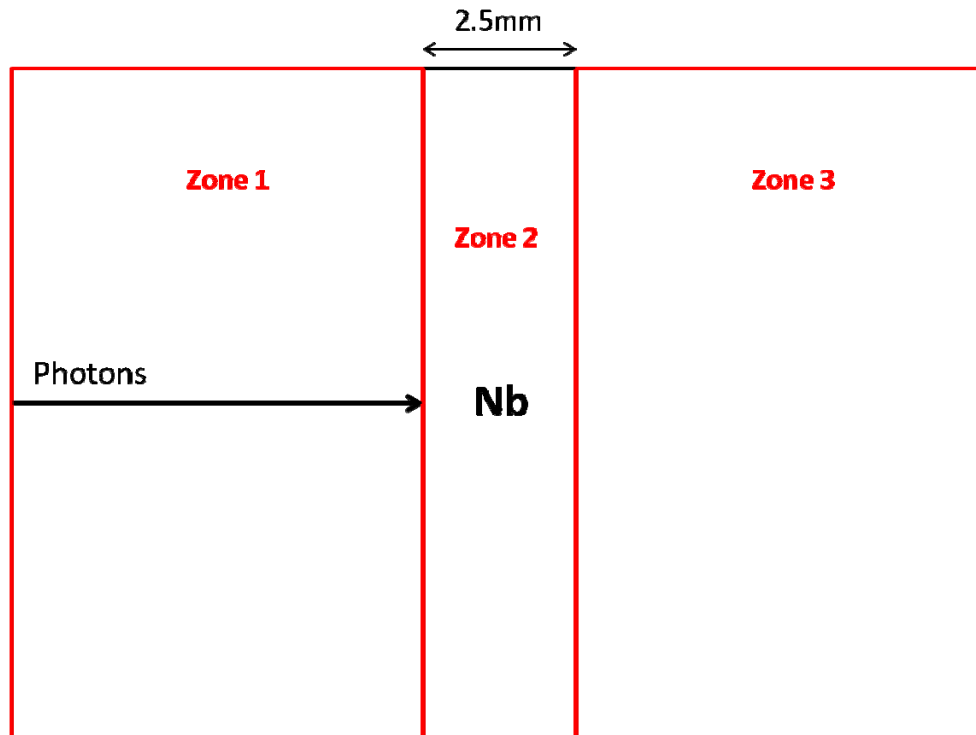


Figure 3. 31 Model zones definition [10].

Zone 1 and 3 are defined as vacuum so the particles can fly freely, Niobium is located in zone 2 where all the interactions take place, if a shower particle arrive in zone 1 will account for reflected energy, if it reaches zone 3 is considered as transmitted, while the particles that leave some energy in zone 2 contribute to the absorbed energy portion.

The attenuation coefficient depends on material properties and photons energy, on NIST website [11] it is possible to find the data obtained from Hubbell and Seltzer [12] for pure elements, compounds and mixture. The data for Niobium are presented in Figure 3.32.

Mass energy-absorption coefficient

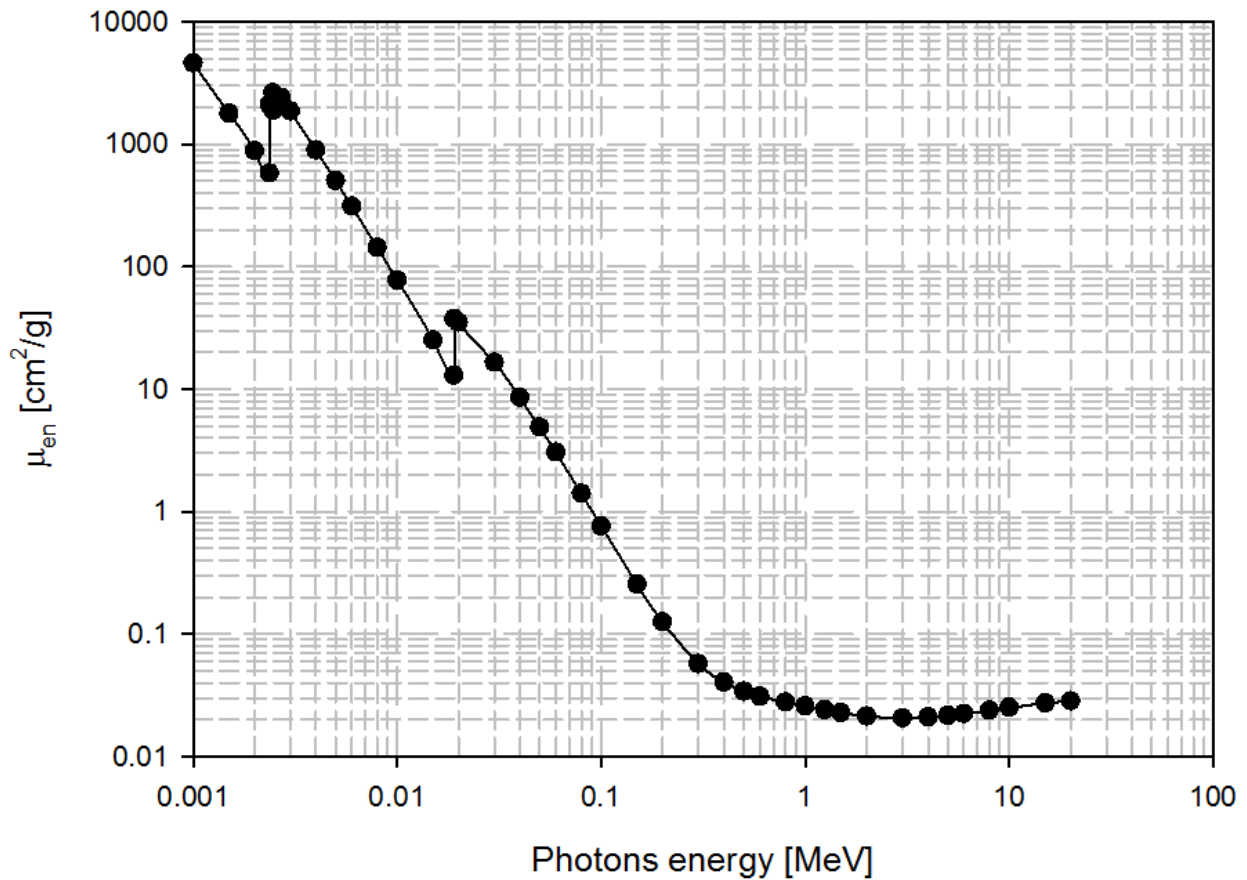


Figure 3.32 Mass energy-absorption coefficient for Niobium as published by Hubbell and Seltzer (NIST)[12].

In the framework of this dissertation we are more interested in the portion of energy that can be transmitted through the Niobium and possibly detected by PIN diode sensors, so despite plotting the energy absorbed percentage is preferable to plot the transmitted one. The two values are strictly related just by reminding that the total amount of energy impinging on the slab can written as:

$$\mathbf{Energy}_{incident} = \mathbf{Energy}_{reflected} + \mathbf{Energy}_{absorbed} + \mathbf{Energy}_{transmitted}. \quad (3.30)$$

The comparison between the simulation (EGS5) and the literature data (NIST) are shown in Figure 3.33, the difference never exceed 7%.

Transmitted energy percentage

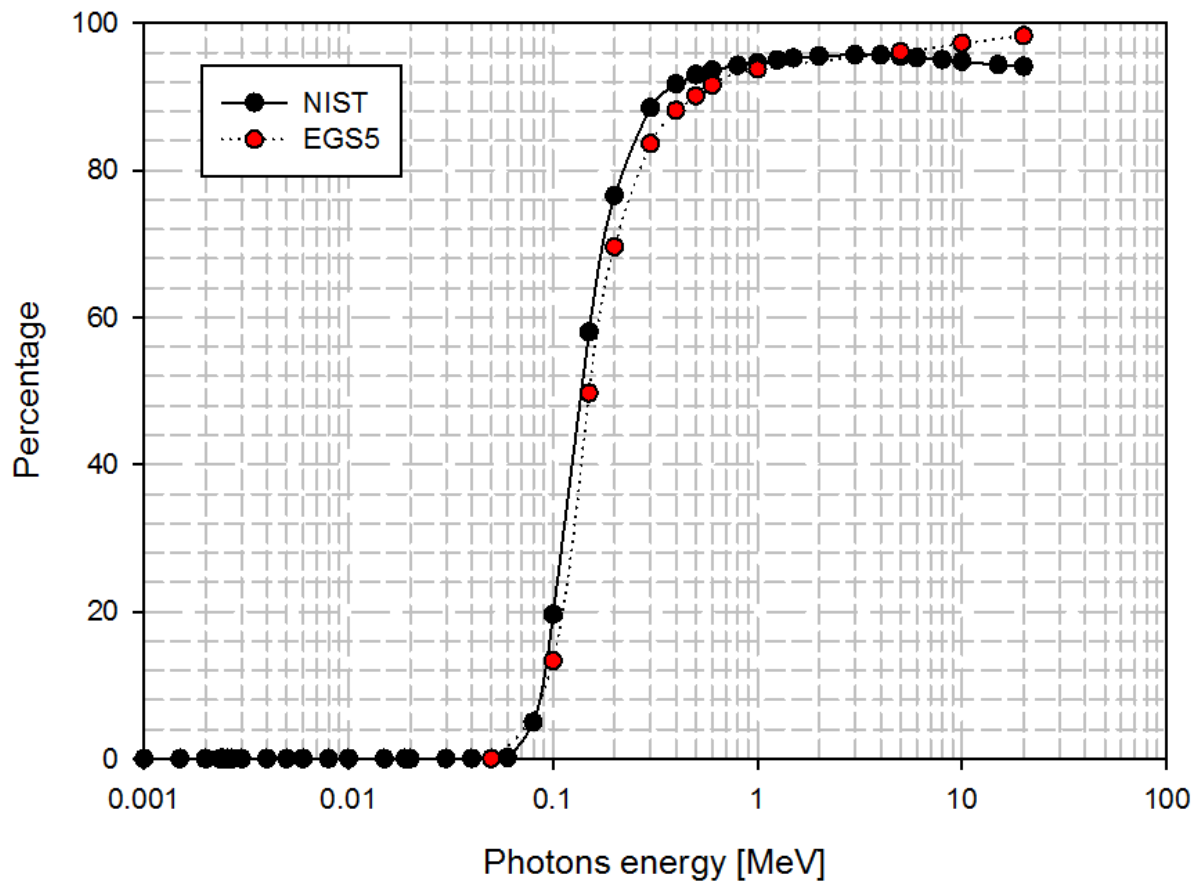


Figure 3.33 Transmitted energy percentage, literature data (black dots) and calculated data with EGS5 (red dots).

The simulation is carried out by launching 100000 photons with the same energy, once they interact with the Niobium a particles shower is produced, its products are tracked until they reach a low energy threshold (1KeV). When all the particles in the shower are discarded a new shower is produced, the amount of energy deposited, transmitted or reflected from the niobium slab is recorded at each simulation step.

More complex simulations will be carried out in chapter 5 in order to calculate the interaction between electrons, niobium and sensors placed around the cavity surface.

Chapter references

1. Halbach, K. and R. Holsinger, *SUPERFISH-a computer program for evaluation of RF cavities with cylindrical symmetry*. part. Accel., 1976. 7(LBL-5040): p. 213-222.
2. Abramowitz, M. and I.A. Stegun, *Handbook of Mathematical Functions: With Formulas, Graphs, and Mathematical Tables*. Vol. 55. 1964: DoverPublications. com.
3. Menzel, M. and H. Stokes, *Users guide for the POISSON/SUPERFISH Group of Codes*, 1987, Los Alamos National Lab., NM (United States).
4. Sun, A., H. Wang, and G. Wu, *Effect of the Tuner on the Field Flatness of SNS Superconducting RF cavities*. LINAC04, Lübeck, Germany, 2004.
5. Geng, R., et al. *Testing the first 1300 MHz reentrant cavity*. in *Proceedings of the Workshop of Pushing the Limits of RF Superconductivity*, Argonne National Laboratory. 2004.
6. Geng, R.-L., *Review of new shapes for higher gradients*. Physica C: Superconductivity, 2006. 441(1): p. 145-150.
7. Umemori, K., et al. *Design of L-band superconducting cavity for the energy recovery linacs*. in APAC. 2007.
8. Wu, G., *FishPact*. <http://code.google.com/p/fishpact/>.
9. Wiener, J. and H. Padamsee, *Thermal and statistical models for quench in superconducting cavities*. TTC-Report, 2008. 8: p. 2008.
10. Hirayama, H., et al., *The EGS5 code system*, 2005, United States. Department of Energy.
11. NIST, <http://www.nist.gov/pml/data/xraycoef/index.cfm>.
12. Hubbell, J.H. and S.M. Seltzer, *Tables of X-ray mass attenuation coefficients and mass energy-absorption coefficients 1 keV to 20 MeV for elements Z= 1 to 92 and 48 additional substances of dosimetric interest*, 1995, National Inst. of Standards and Technology-PL, Gaithersburg, MD (United States). Ionizing Radiation Div.

CHAPTER IV

Experimental setup

Abstract

As the previous chapter describes all the analytical and mathematical tools used for calculation, this chapter will describe all the experimental devices used to measure the superconductive cavity properties and how field emitted electrons affect their performance. Some of these tools are commonly used to qualify the cavity performance, other are specifically designed to detect x-ray produced by the interaction of accelerated electrons striking on the cavity surface. By means of these tools it is possible to gather important information in order to reach a deeper understanding of field emission inside superconductive cavities. Part of the experimental setup description will be done along the next chapter to make even more clear in which conditions the devices were used.

4.1 Vertical test stand

The vertical tests performed on superconducting cavity are performed inside the Superconducting rf Test Facility (STF) building in KEK compound [1].

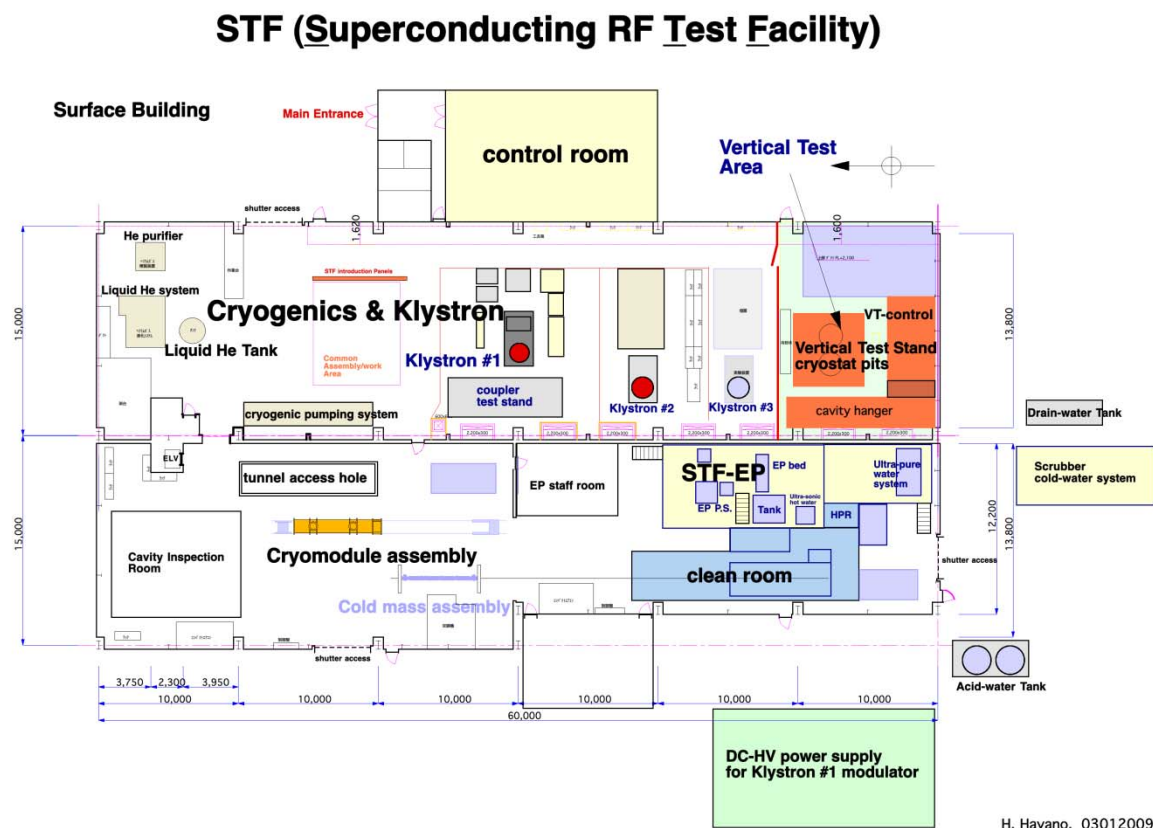


Figure 4.1 STF map [1].

The tests are carried out in the vertical cryostat, located in a pit that can be shielded with a steel movable cover. The cryostat is fed with the liquid Helium coming from two tanks placed outside the pit just before the test, the vertical test control room is at higher level nearby the pit (VT-control on the map), the pumping system is located beneath it near the cavity hanger hut.

Once the system reaches 4K, the roots pump continuously removes the helium gas from the top of the cryostat reducing the Helium temperature down to 2K or even less. All cavity tests are carried

out under these conditions and the cryostat is also equipped with a magnetic shield to protect the cavity from external magnetic field.



Figure 4.2 Cryostat pit for vertical test in STF.

4.2 Low level RF system

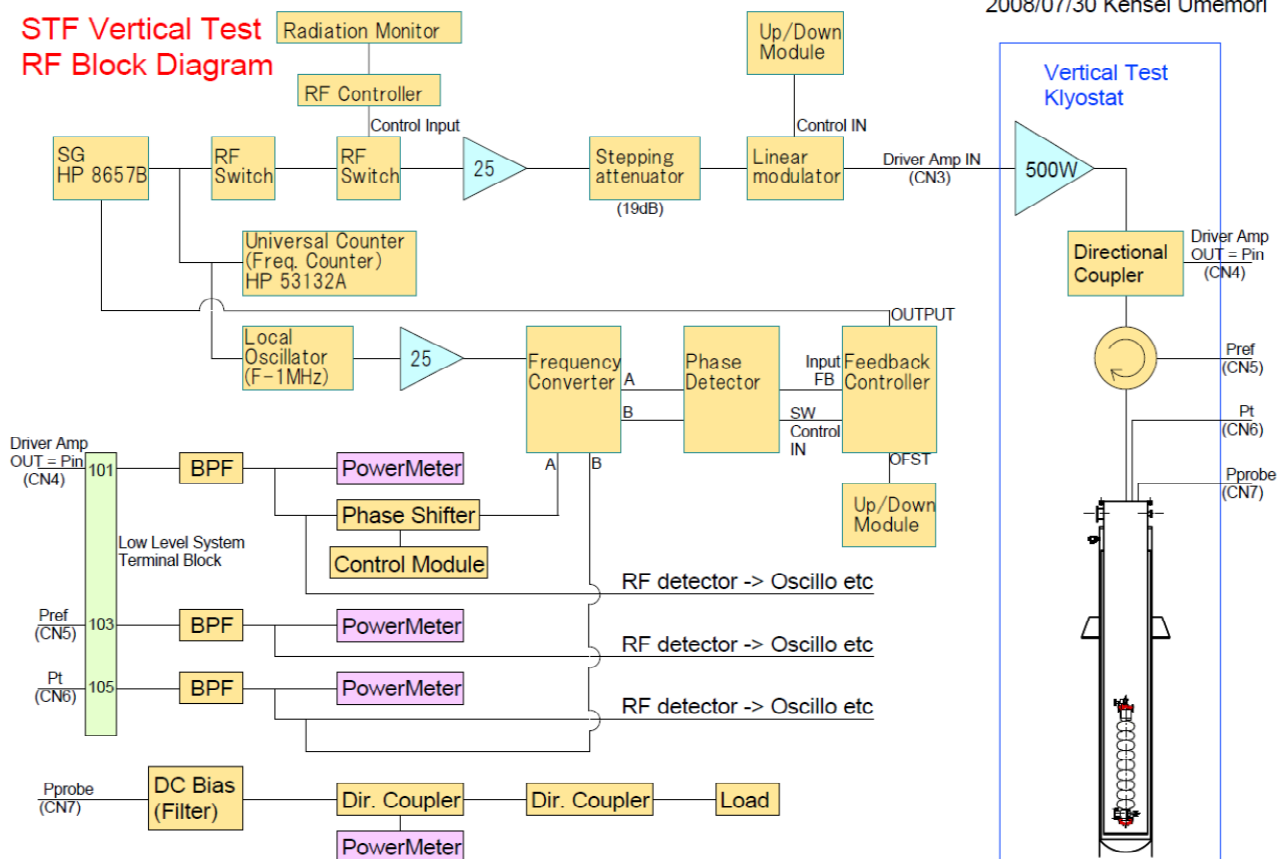


Figure 4.3 LLRF diagram.

The low level RF system is used to excite electromagnetic field in the cavity [2]. The power coupler (bottom side) can be moved inside the cavity to minimize the reflected power. On other ports are installed pick-up probes to measure the transmitted power through the cavity. The measured power is used to calculate the cavity figures of merit as shown in chapter 2.

4.3 Rotating mapping system

A special equipment was designed in order to detect the radiation pattern and the temperature around the cavity surface [3]. It consists of three independent wheels, and each one moved through a stepping motor. Each block rotates around 3 cells, x-ray and temperature sensors are installed on one meridian as shown in the pictures below, the stepping motor allows the system to rotate with an angular resolution of 0.5° .

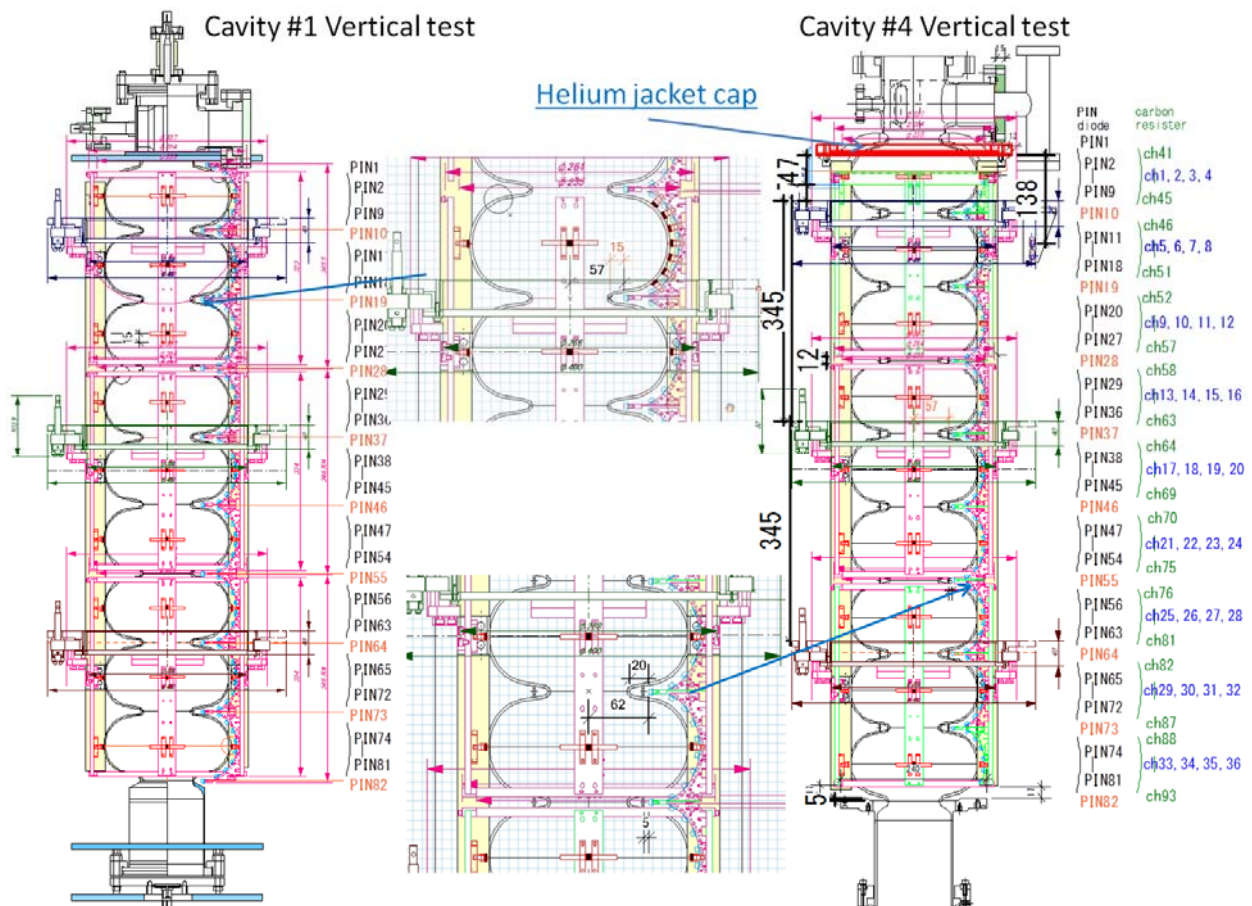


Figure 4.4 Vertical test set up, cavity #1 and #2 (left), cavity #4 and #3 (right).

Due to the difference between the first two cavities [4] and the last two it was necessary to slightly modify the system. Actually the last two cavities planned to be assembled inside the c-ERL cryomodule were equipped with stiffener rings around the iris and the helium jacket cap, where the helium jacket will be welded.

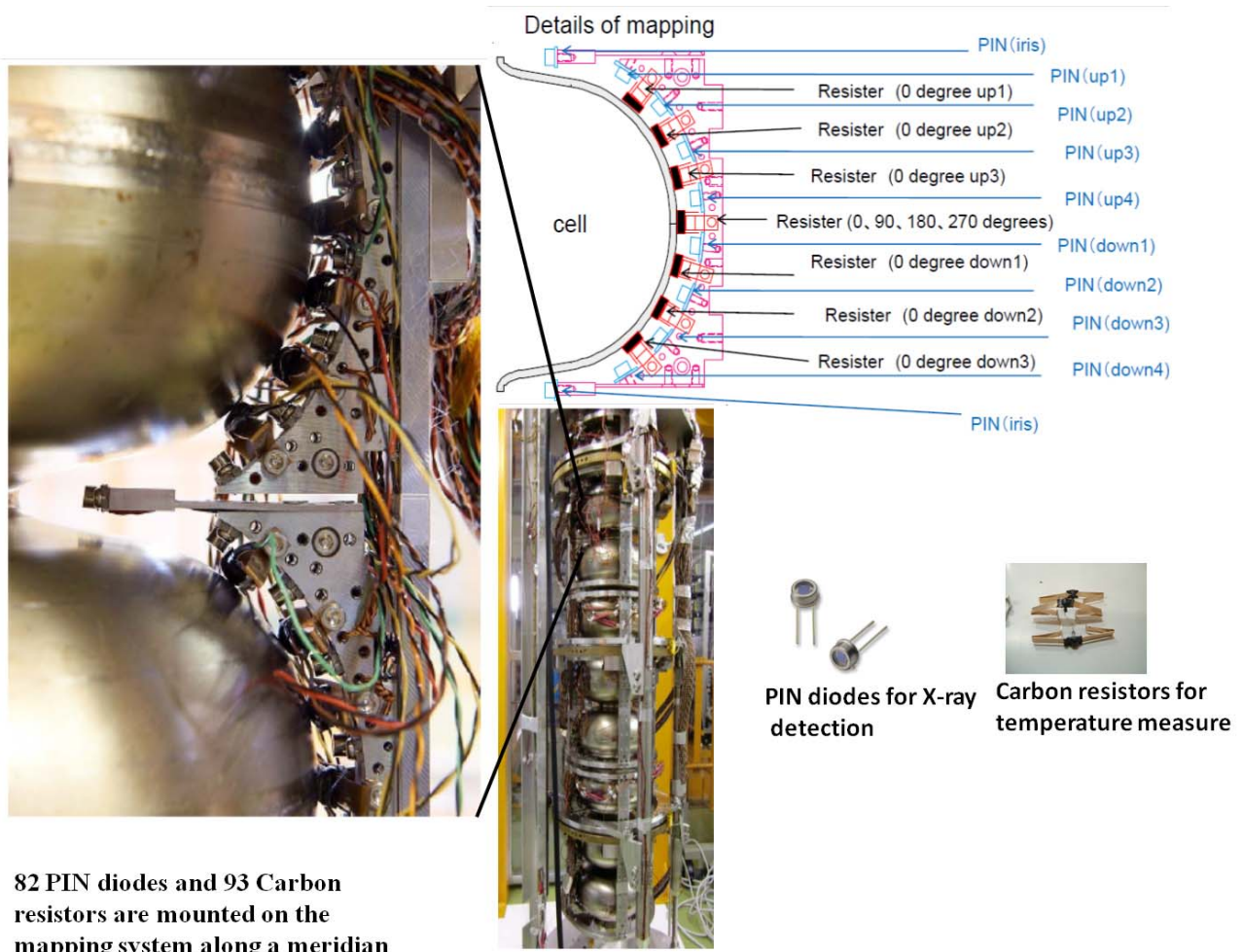


Figure 4.5 Mapping system details.

The mapping system is equipped with PIN diodes in order to detect the radiation coming out from the cavity surface, and carbon resistor to detect temperature changes on the surface. Along this dissertation the radiation pattern produced by electrons emitted by field effect will be extensively discussed, so it worth describing briefly the PIN diode working principle and the electronics used to exploit their capability.

The PIN diodes used on this mapping system are commercialized by Hamamatsu (photonics division) with the label S1223 [5], their design can be seen in the picture below.

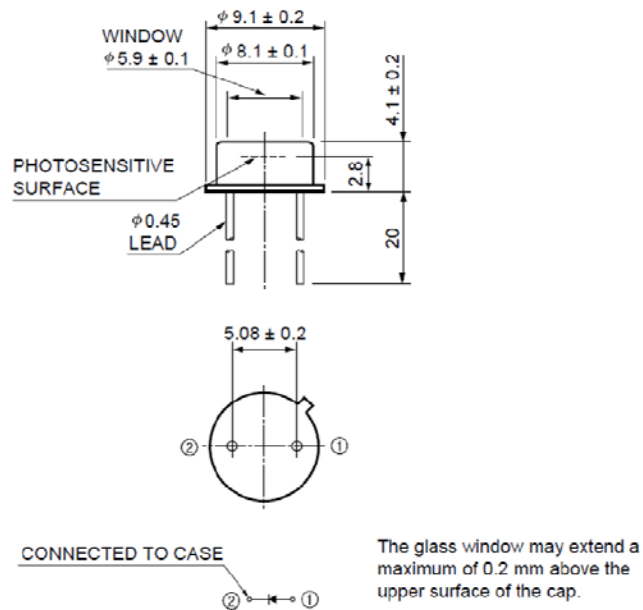


Figure 4.6 PIN diode S1223 details [5].

The active element is a Silicon chip 300 μ m thick with a surface 2.8x2.4mm, that is inserted into a stainless steel case with a borosilicate window, its dimension can be seen in the picture above.

The working principle is quite simple: when an energetic photon hit the PIN junction depletion zone there is some chance that it deposits some energy in the material. Indeed, if its energy is bigger than the energy needed to create an electron-hole pair (ionization energy about 3.6eV for Silicon) it is possible that some current passes through the diode as the electrons are collected on one side of the diode.

The mapping system is equipped with 82 diodes placed along a meridian, 9 of them directly in front of each iris and the rest covering the external cells surface, each diode is connected to an amplification circuit (schematically shown in the next picture) and to a logger system wired to the control room to show the data online during the test.

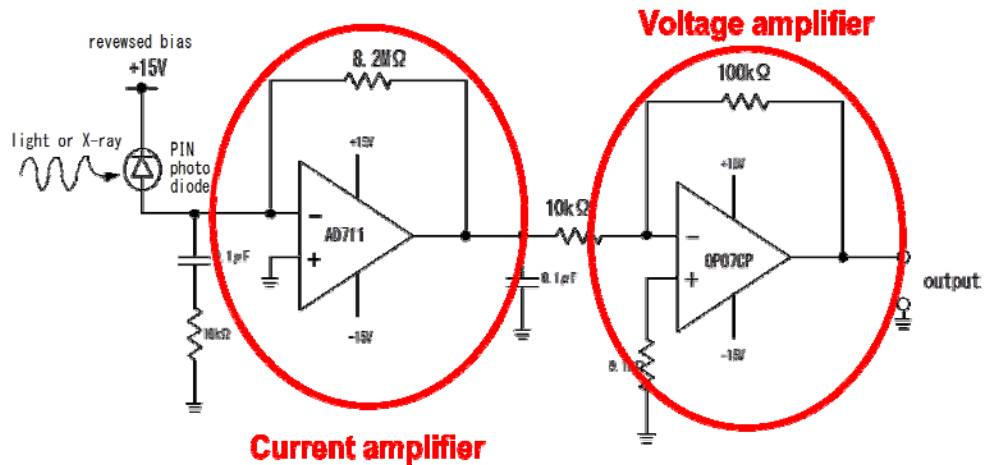


Figure 4.7 PIN diode amplification scheme.

The amplification system consists of two different stages: the first one amplifies the photocurrent usually few nano Ampere with a resistance of $8.2\text{M}\Omega$ [6], the voltage drop across this resistance is then amplified 10 times ($100\text{K}\Omega/10\text{K}\Omega$), the maximum voltage on the output is determined by the voltage feed to the second circuit [7], that is 15V in our case.

The sensor response will be calculated in the next chapter by means of Montecarlo simulation in order to determine the portion of energy deposited into the silicon with respect to incident photons at different energy.

4.4 NaI scintillator

During the cavity high power test, a NaI scintillator [8-10] was used in order to detect the bremsstrahlung radiation produced by field emitted electrons incident on the gate valve placed at the end of the cavities installed in cryomodule.

The crystal is 2 inch diameter attached to a photomultiplier as can be seen in the picture below

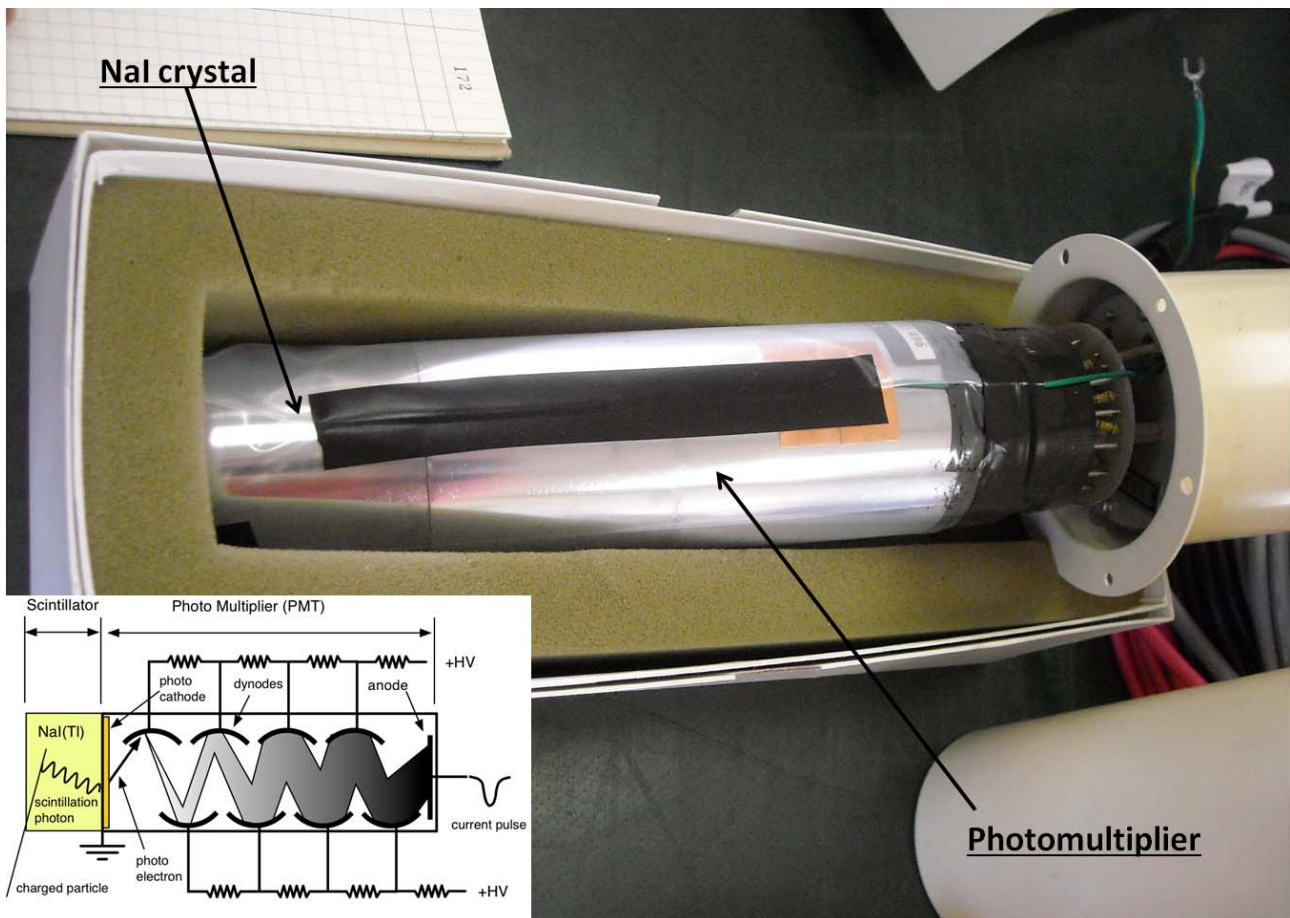


Figure 4.8 NaI scintillator connected to photomultiplier.

The crystal and the photomultiplier are then enclosed into a 1mm thick Aluminum case and placed behind a lead collimator. The photomultiplier is connected to a high voltage generator (HV) that powers the dynodes chain and sends also the signal to an analog-digital converter in order to feed the data to the multichannel analyzer (MCA) as shown in the next pictures.

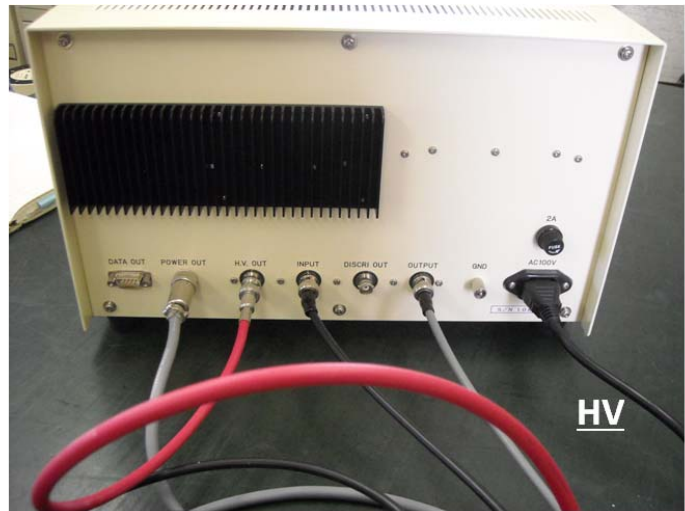
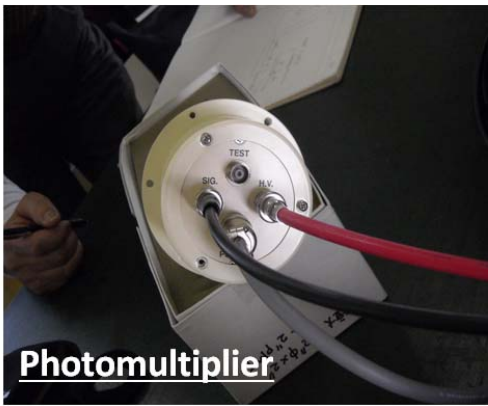


Figure 4.9 NaI scintillator setup, photomultiplier (top left), high voltage generator (top right) and analog-digital converter (bottom right).

Before its installation in the tunnel, the scintillator was calibrated by using known radioactive sources. At this stage the calibration consists in finding a correspondence between each channel on the multi channel analyzer and the energy of the incident photons, the relation between energy and channel along with the used sources can be found in the next table.

Table 4.1 Radioactive source used for calibration, with their energy spectrum [11] and corresponding observed channel on the Multi Channel Analyzer (MCA).

| Source | Energy peak | Detected channel # |
|-------------------|-------------|--------------------|
| Co_{60} | 1173.2KeV | 111 |
| | 1332.5KeV | 125 |
| Cs_{137} | 661.7KeV | 64 |
| Na_{22} | 511KeV | 50 |
| | 1274.5KeV | 120 |

When the relation between channel number and energy is plotted through a linear regression, it is possible to calculate the conversion factor from channel number to energy as can be seen in the figure 4.11, in this configuration (HV adj 5.01) each channel account for 10.9eV, the MCA has 1024 channels so with this configuration it can detect photons up to 11MeV.

The system was also calibrated to detect photons with energy up to 20MeV. This was done by changing the regulation knob inside the high voltage generator from 5.01 to 4.53.



Figure 4.10 Voltage adjustment knob.

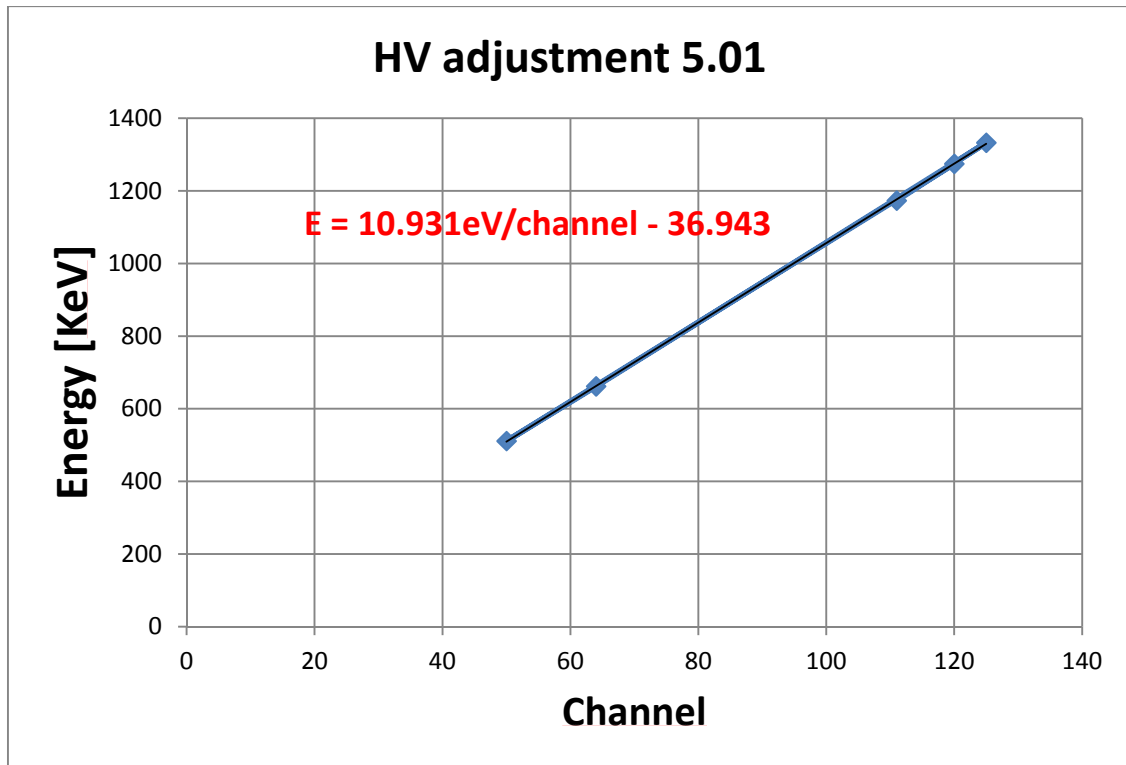


Figure 4.11 NaI scintillator calibration curve, each channel accounts for 10.9eV.

Chapter references

1. STF, <http://ilc.kek.jp/STF/>.
2. Padamsee, H., et al., *RF Superconductivity for Accelerators*. Physics Today, 1999. **52**: p. 54.
3. Sakai, H., et al., *Cavity diagnostics using rotating mapping system for 1.3 GHz ERL 9-cell superconducting cavity*. IPAC. **10**: p. 2950.
4. Umemori, K., et al., *Status of main linac cryomodule development for Compact ERL Project*. IPAC, 2012. **12**: p. 67.
5. HamatsuPhotonics, S1223.
<http://www.hamamatsu.com/us/en/product/category/3100/4001/4103/S1223/index.html>.
6. AnalogDevices, AD711. http://www.analog.com/static/imported-files/data_sheets/AD711.pdf.
7. TexasInstruments, *OP07CP*. <http://www.ti.com/lit/ds/symlink/op07c.pdf>.
8. SaintGobain, *NaI Scintillator.* <http://www.detectors.saint-gobain.com/uploadedFiles/SGdetectors/Documents/Product-Configurations/Integral-Detectors.pdf>.
9. Leo, W.R., *Techniques for nuclear and particle physics experiments: a how-to approach*1994: Springer.
10. Knoll, G.F., *Radiation detection and measurement*2010: Wiley. com.
11. LBNL, *The Berkeley Laboratory Isotopes Project's*. <http://ie.lbl.gov/education/isotopes.htm>.

CHAPTER V

Experimental data and Discussion

Abstract

In this chapter, the experimental data gathered during vertical test and high power test (cavities installed in the c-ERL horizontal cryostat) will be presented. The data will be analyzed by means of calculations and simulations, as explained in chapter 2, to obtain precious information concerning field emission events. Discussion concerning the results will be carried out along with data analysis. Finally, some remarks on field emission respect to different cavities design will be presented.

5.1 Vertical test data analysis

Before starting the data analysis, some consideration shall be made concerning how the electrons interact with the cavity surface once they are accelerated by electric field, in order to compare data and the post-processed simulations results.

Electrons incident on the Niobium can generate different effects depending on energy and impact angle, a EGS5 simulation is designed to investigate these process.

Through the tracking code, it is possible to calculate electron energy and impact angle with respect to RF phase and accelerating field, each trajectory is tracked until the electron hit the surface recording the impact location along other relevant quantities.

In the picture below are shown electron trajectories departing from an emitter located between 1st and 2nd cell: each line is a trajectory with a different RF phase at the moment of electron emission.

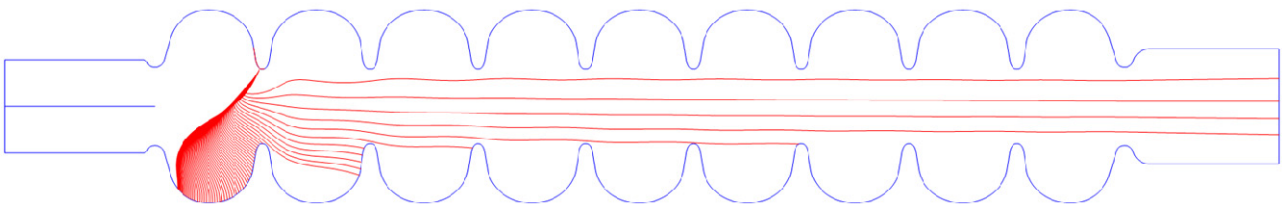


Figure 5. 1 Electron trajectories starting at different RF phases form an emitter located between 1st and 2nd cell, $E_{acc}=15\text{MV/m}$.

We can plot the impact energy with respect to impact location, as shown in the next picture, each triangle is the impact energy for electrons departing at different RF phases. It is important to notice that electrons that land in the cell where the emitter belongs have energy in the interval between 400KeV-1MeV, while for electrons flying along the axis the energy progressively increases until reaching the maximum for particles landing in the LBP.

Impact energy

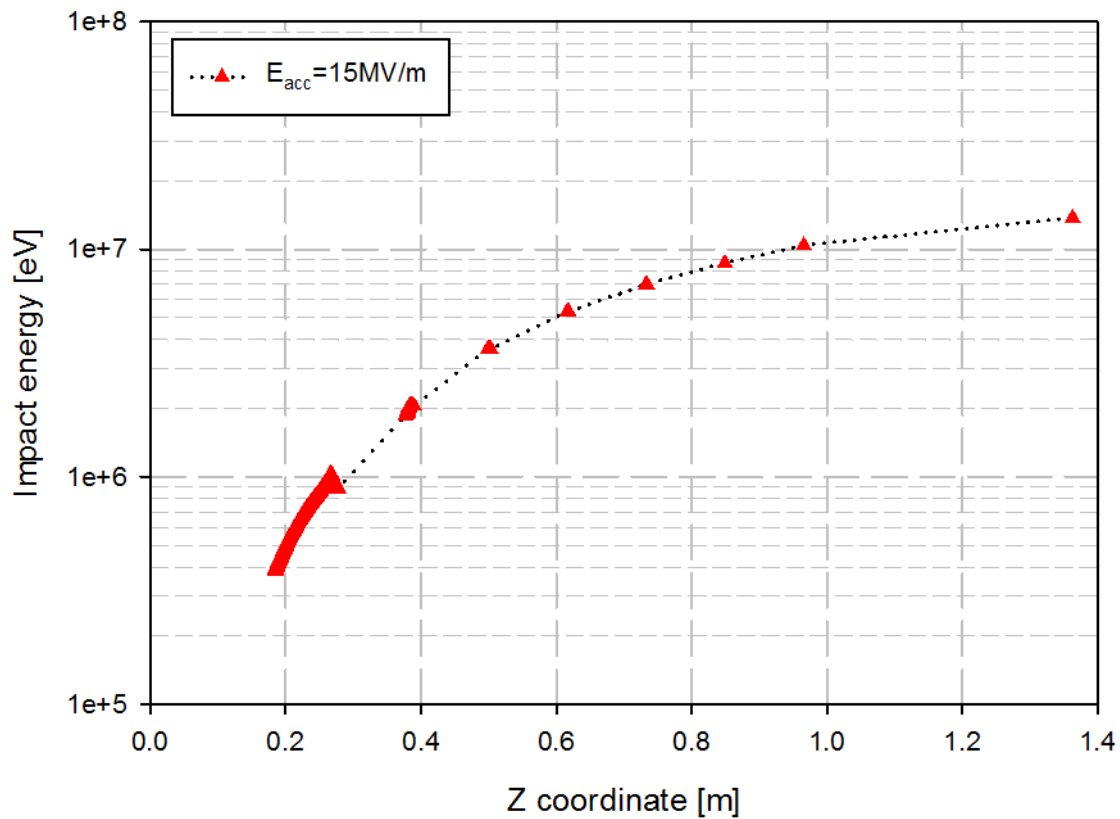


Figure 5. 2 Impact Energy for electron trajectories starting at different RF phases from an emitter located between 1st and 2nd cell, $E_{acc}=15\text{MV/m}$.

5.1.1 Secondary electron yield

Considering the impact energy range we can neglect, as first approximation, secondary electrons production. As shown in the next picture, the Niobium secondary electron yield (SEY) is bigger than 1 between 100eV-1000eV while it drops for lower and higher energies (at $E_{acc}=15\text{MV/m}$ the impact energy span from 400KeV to 11MeV) .

| Element | δ_{\max} | $E_{p\max}$ (eV) | E_I (eV) | E_{II} (eV) |
|---------|-----------------|---------------------|---------------|------------------|
| Li | 0.5 | 85 | None | None |
| Mg | 0.95 | 300 | None | None |
| Mo | 1.25 | 375 | 150 | 1200 |
| Na | 0.82 | 300 | None | None |
| Nb | 1.2 | 375 | 150 | 1050 |
| Ni | 1.3 | 550 | 150 | >1500 |
| Pb | 1.1 | 500 | 250 | 1000 |
| Pd | >1.3 | >250 | 120 | None |
| Pt | 1.8 | 700 | 350 | 3000 |
| Rb | 0.9 | 350 | None | None |
| Sb | 1.3 | 600 | 250 | 2000 |
| Si | 1.1 | 250 | 125 | 500 |
| Sn | 1.35 | 500 | None | None |
| Ta | 1.3 | 600 | 250 | >2000 |
| Th | 1.1 | 800 | None | None |
| Ti | 0.9 | 280 | None | None |
| Tl | 1.7 | 650 | 70 | >1500 |
| W | 1.4 | 650 | 250 | >1500 |
| Zr | 1.1 | 350 | None | None |

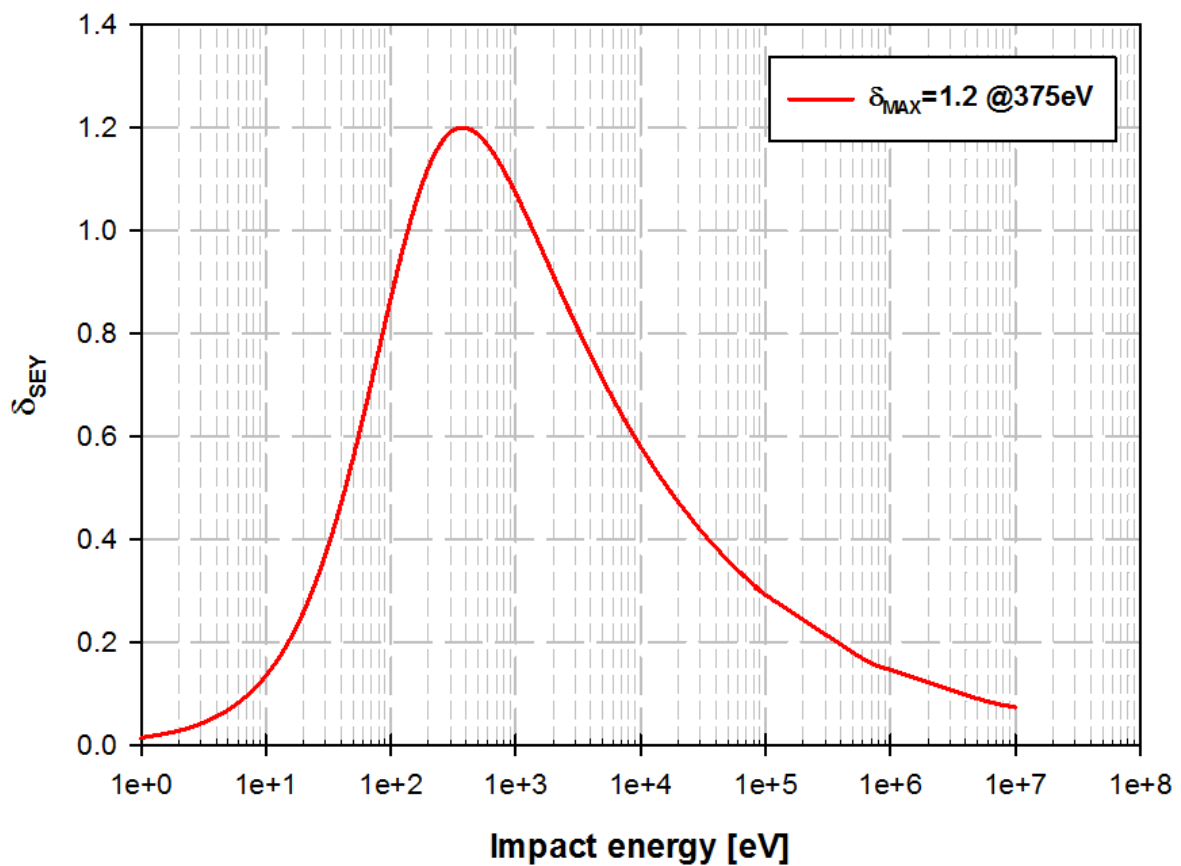


Figure 5. 3 SEY graph for Niobium (below) [1] and metals properties respect to secondary electrons emission (above).

In order to understand how electrons interact with the Niobium surface we can carry out some EGS5 simulation [2]. First, we can calculate the amount of energy transmitted through the a Niobium plate with the same cavity thickness (about 2.5mm), in the simulation an electron beam hit the plate perpendicularly, the portion of energy transmitted, absorbed or reflected is recorded, subsequently the energy is increased and the calculation repeated. The geometry is the same as the one used in chapter 3 but in this case electron beam instead of photons will be used.

Figure 5.4 represents the percentage of energy transmitted, absorbed or reflected by the Niobium plate when hit by electron beams with different energies.

Electron beam (Nb plate 2.5mm)

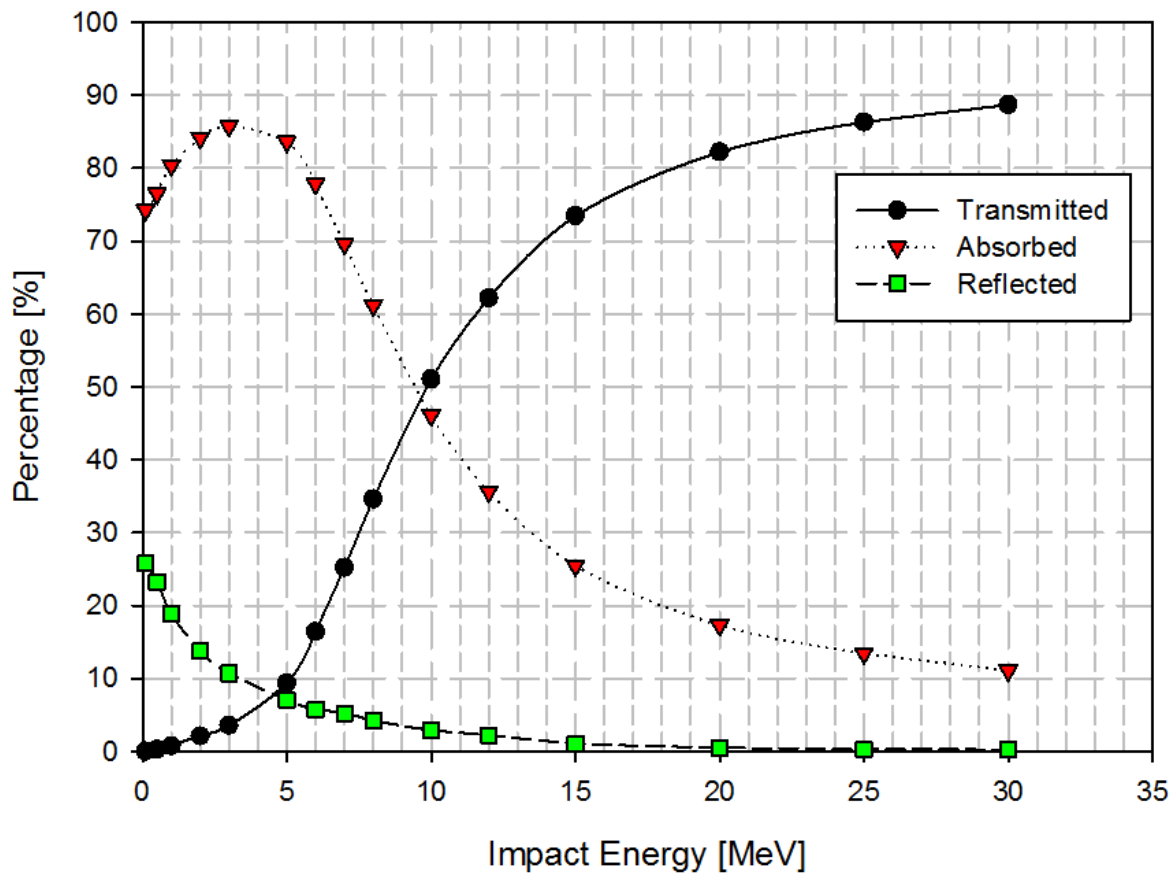


Figure 5.4 Percentage of energy transmitted, absorbed or reflected by a 2.5mm Niobium plate upon electron impact perpendicular to the surface.

In this condition the absorbed energy is dominant up to 10MeV. After that, the transmitted portion becomes more relevant, the reflected part decrease, systematically and is lower than the transmitted after 5MeV. the reflected energy mainly accounts for electron elastic scattering.

Figure 5.5 presents the total amount of energy transmitted, absorbed or reflected respect to different electrons impact energy the different regimes are clearly visible.

Electron beam (Nb plate 2.5mm)

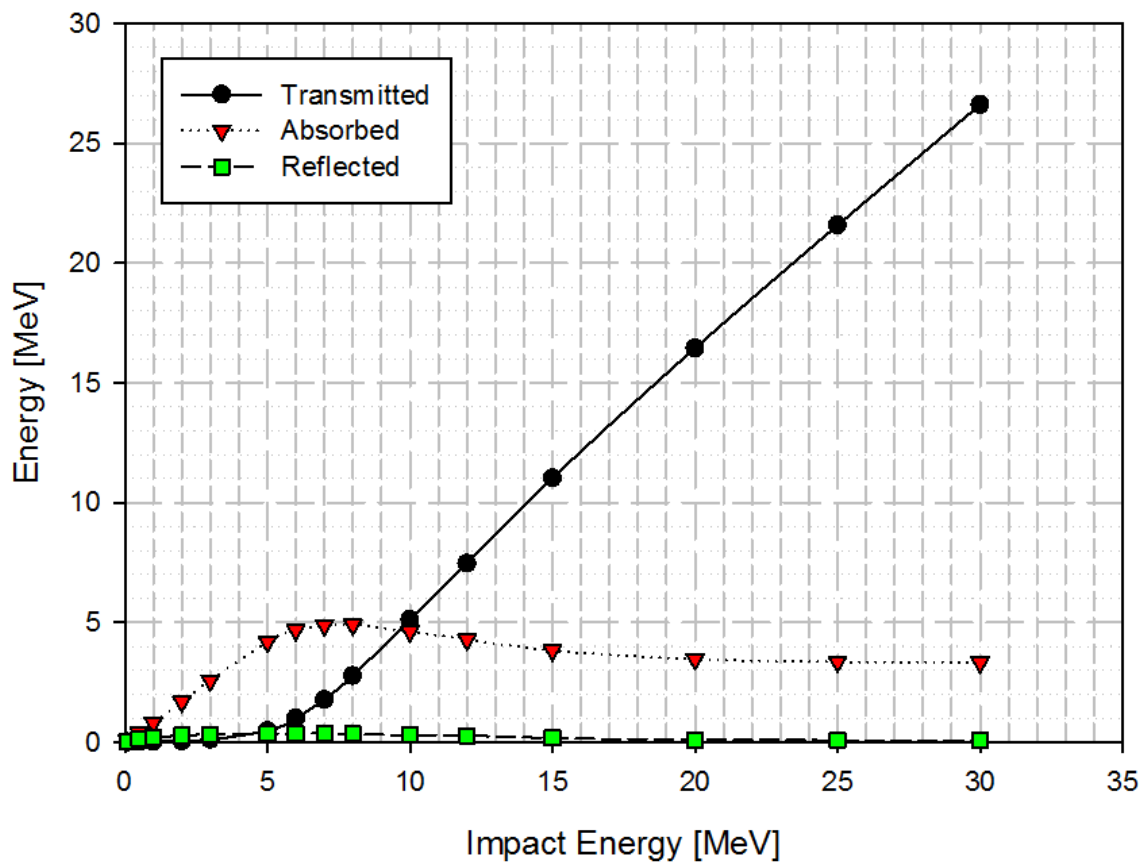


Figure 5.5 Total amount of energy transmitted, absorbed or reflected by a 2.5mm Niobium plate upon electron impact perpendicular to the surface.

From the plot above it is clear that up to 10MeV the absorbed energy is bigger than any other contribution. After that, the transmitted portion increases linearly with the impact energy. The total amount of absorbed energy fluctuates between 3MeV and 5MeV in the impact energy range between 5MeV and 30MeV, in this range the absorbed energy can be considered almost independent from the impact energy value.

In the example above, an electron beam hitting perpendicularly the cavity surface has been considered, but as we can see from the picture below the actual impact angles in the cavity span

from few degrees to 90° , so it is important to evaluate how the above quantities change with respect to the impact angle.

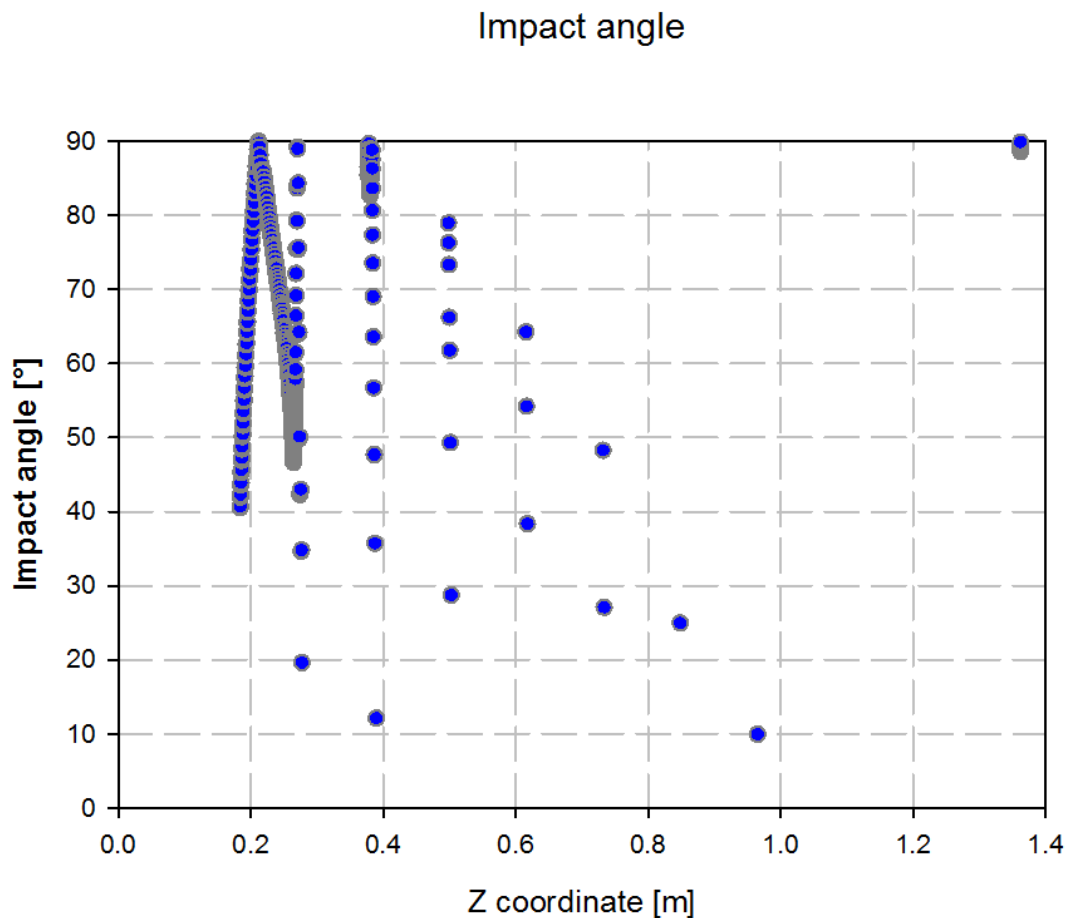


Figure 5.6 Impact angle for electron trajectories starting at different RF phases from an emitter located between 1st and 2nd cell (as shown in figure 5.1), $E_{acc}=15\text{MV/m}$.

By comparing the angle values with the iris locations, it can be noticed that near the iris the impact angle becomes grazing while it increases up to 90° when the impact is inside the cell or at cavity ends (LBP or SBP).

Another EGS5 simulation is used to calculate the transmitted, absorbed and reflected energy portion once the impact angle is changed, in this calculation the impact energy is fixed to 10MeV (where transmitted and absorbed energy are almost equal) while the impact angle is changed between 5° and 90° .

Electron beam (Nb plate 2.5mm)

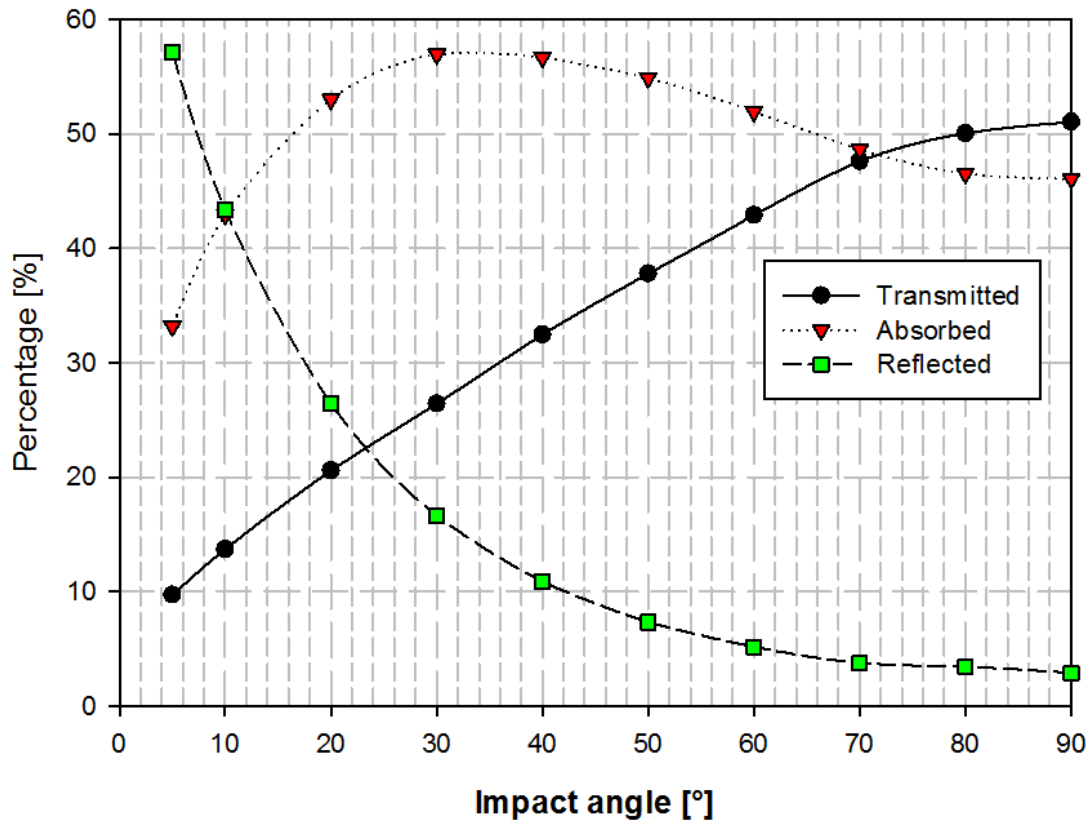


Figure 5.7 Percentage of energy transmitted, absorbed or reflected by a 2.5mm Niobium plate upon electron impact with 10MeV at different incident angles.

It is clear that the reflected portion is dominant up to 10° impact angle. Considering the previous results on the impact angles in the cavity, it means that the reflected energy from cavity iris shall be taken into account, while for other impact location mainly the energy is divided between transmission and absorption.

The last information we could need is how much energy will be deposited in the PIN diode sensors once electrons hit the cavity surface. Also in this case a specific designed EGS5 code was used to calculate the PIN diode response with respect electrons energy.

The model geometry is derived from the Hamamatsu S1223 datasheet [3] as shown below.

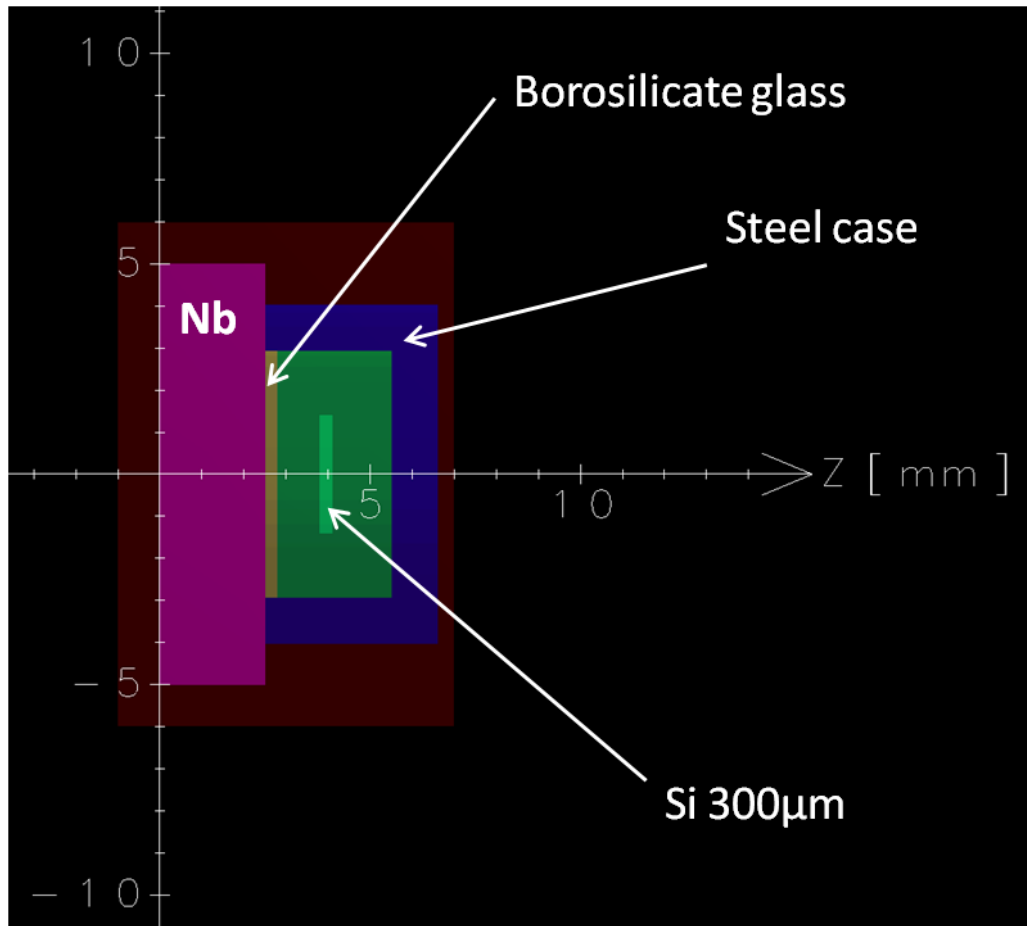


Figure 5.8 PIN diode geometry model for EGS5.

When electrons hit the Niobium plate, a particle shower is generated and a part of it deposit energy in the Silicon. If the deposited energy is high enough to ionize the crystal (creates an electron-hole couple), a current can be collected on the diode. At least about 3.6eV [4, 5] is needed to ionize the Silicon so we can define the diode current as

$$I = \frac{E_{dep}}{3.6} e \quad (5.1)$$

Where E_{dep} is the deposited energy in the Silicon crystal each second [eV/s] and e is the electron charge. The next picture shows the shower produced by 10MeV electrons, red lines represent electron trajectories and yellow ones represent photons. It should be noticed how populated is the shower compared with the same image taken for 2MeV electrons.

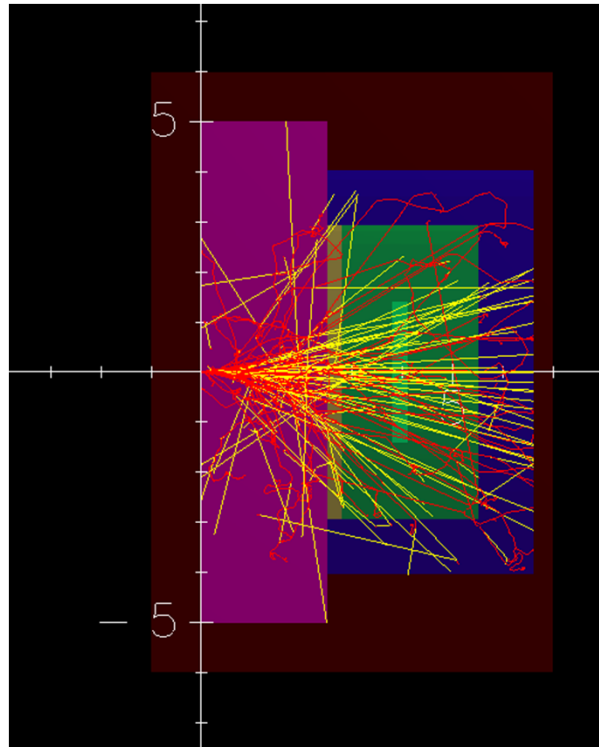


Figure 5.9 Particle shower produced by 10 MeV electrons hitting Niobium (left side), electron trajectories (red lines) and photon trajectories (yellow lines).

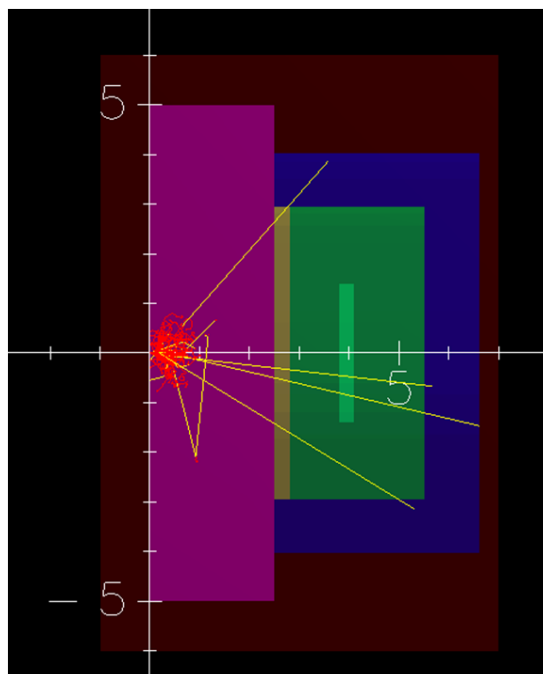


Figure 5.10 Particle shower produced by 2 MeV electrons hitting Niobium (left side), electron trajectories (red lines) and photon trajectories (yellow lines).

As expected from previous calculations, most part of the shower remains confined into Niobium (absorption is dominant) and few photons can pass through the material and deposit some energy in the Silicon crystal.

The PIN diode response is calculated, in terms of current, by launching one million electrons with energy between 500KeV and 30MeV in order to consider different cavity operating conditions, the current is calculated from the average amount of deposited energy as explained before (eq. 5.1)

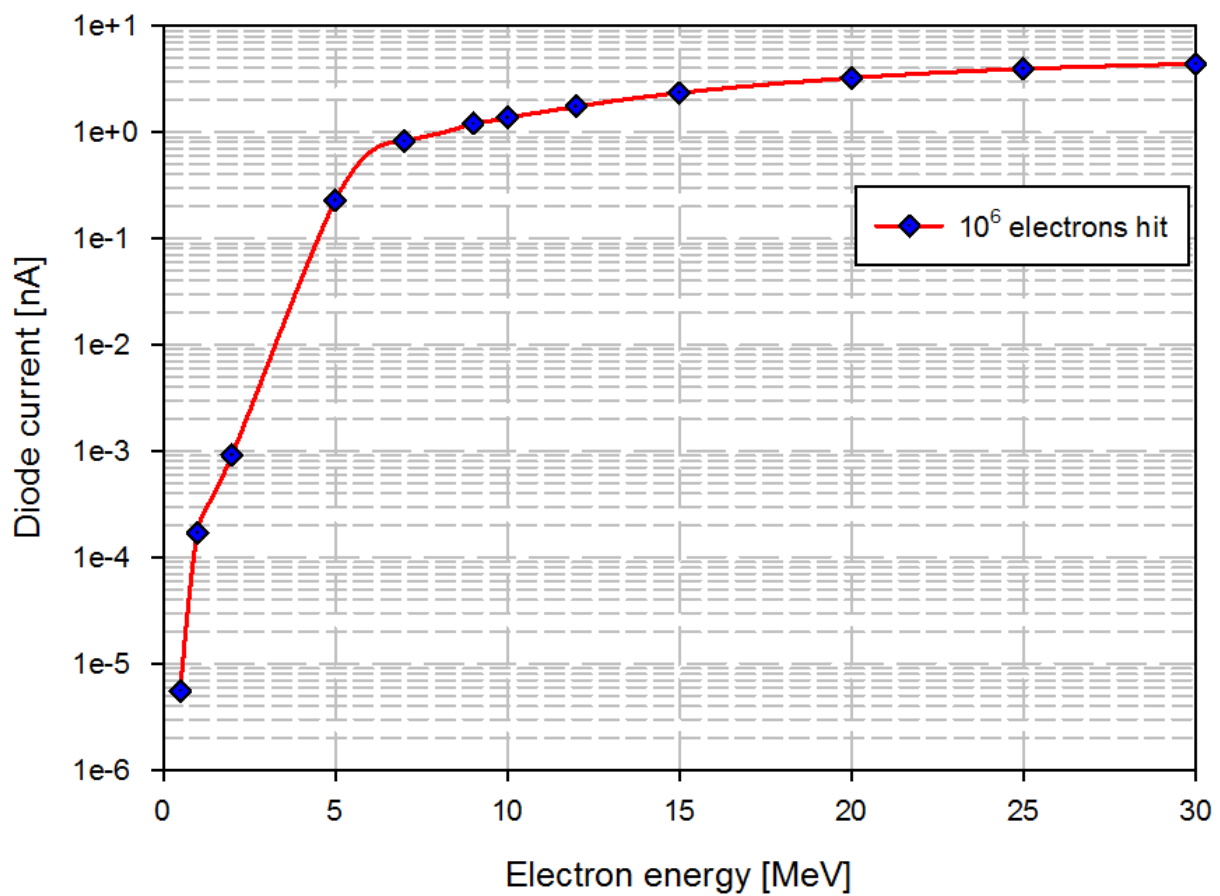


Figure 5.11 Diode current with respect to electron impact energy.

In the next picture is shown the average deposited energy with respect to electron impact energy, below 1MeV (about 0.8MeV). In that case, the electron energy is not high enough to generate an electron-hole pair in the silicon crystal. This can be considered as the detectable threshold with respect to this particular configuration, where the detector is just behind the Niobium plate and electrons hit a point in front of the sensor. Depending on the configuration, the threshold can change. However in this dissertation we will consider as a first approximation that electrons with impact energy less than 1MeV are not detectable, other possibility will be explored later.

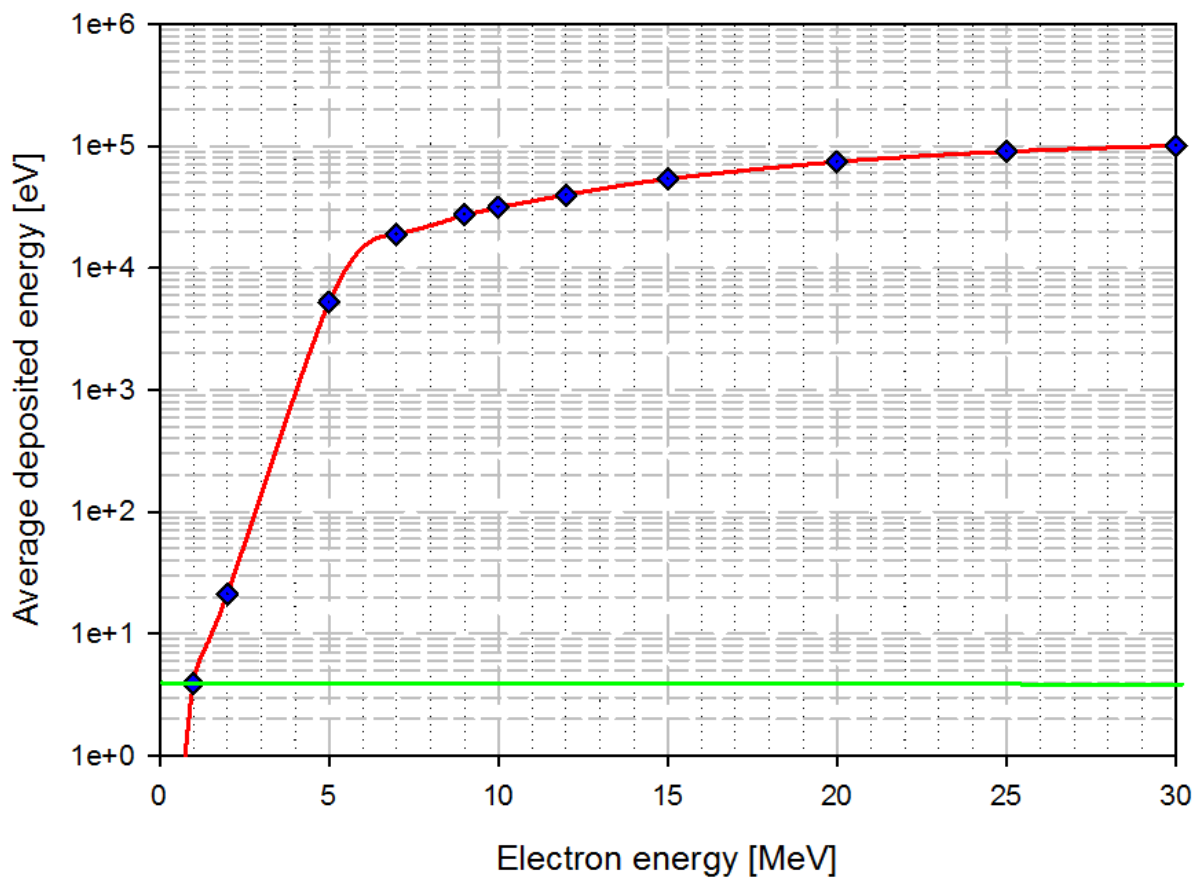


Figure 5.12 Average deposited energy in the Silicon crystal with respect to electrons impact energy, the green line represents the energy needed to produce at least one electron-hole pair.

During cavity test, the PIN diode signal is amplified through the circuit shown in the next picture. After a first current amplification the voltage drop is measured on a $8.2\text{M}\Omega$ resistance, and , the output is a voltage signal between 0-15V [6, 7].

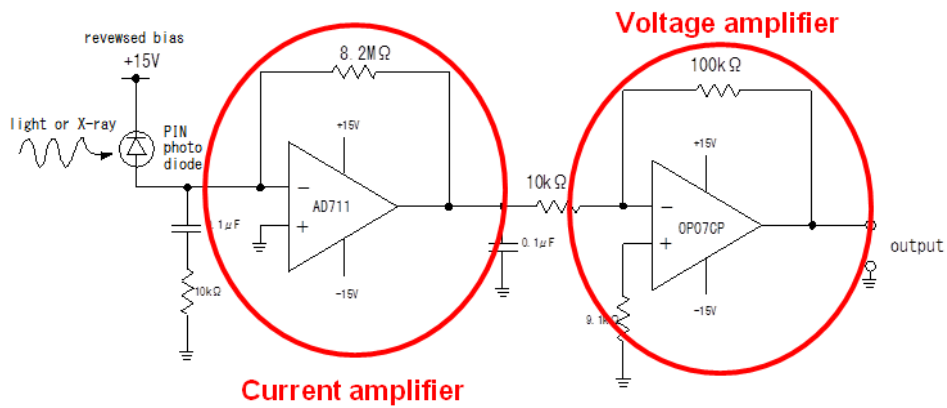


Figure 5.13 PIN diode amplification circuit schematic.

Finally, we can plot the PIN diode circuit voltage when the same amount of electrons hit the cavity surface with different impact energy.

Amplification factor: 10x
Resistance: 8.2 M Ω

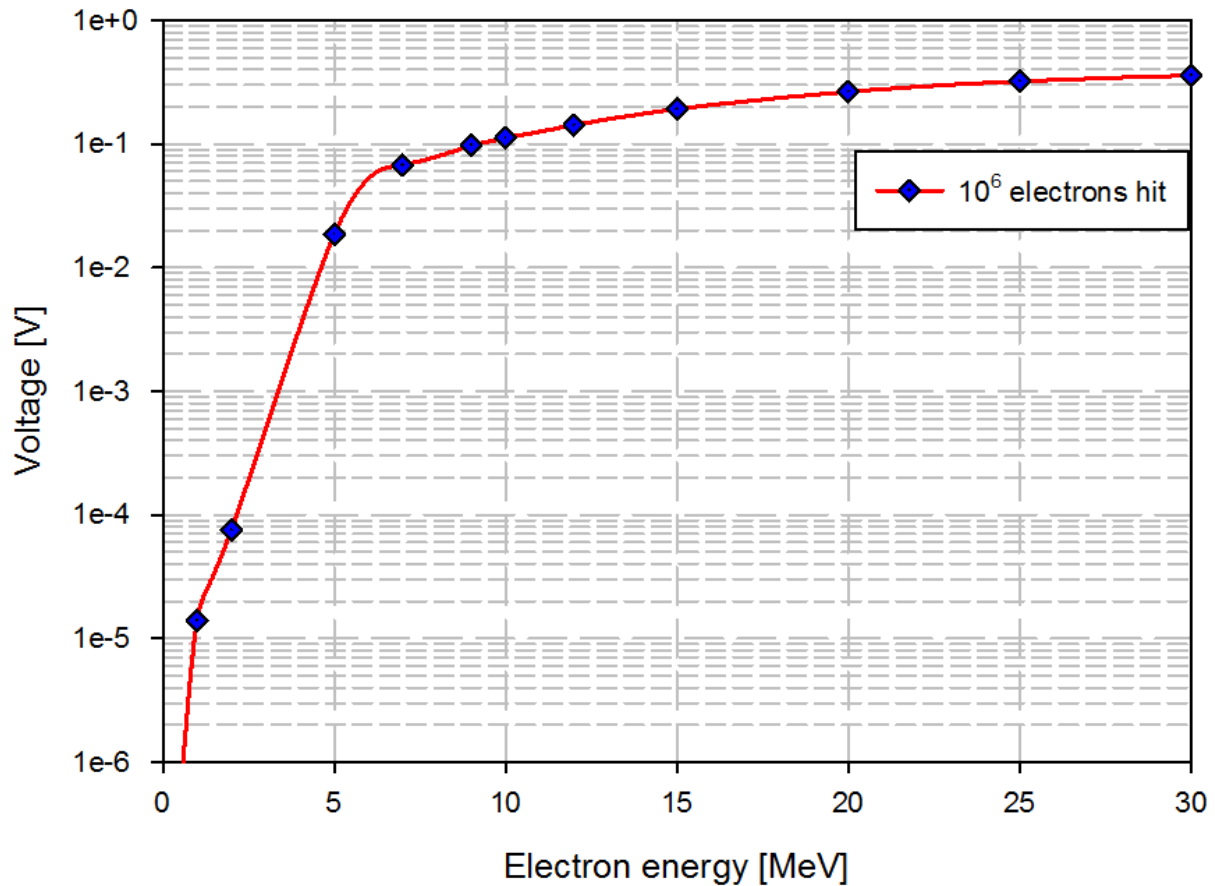


Figure 5. 14 Voltage response from PIN diodes circuit as calculated through EGS5 (average deposited energy) respect to electrons impact energy.

During post-processing all the above information are included in the analysis code, allowing to calculate all the relevant information, from electrons emission until they interact with the cavity surface and sensors around it. More simulation will be discussed during the data analysis, but for a first approximation the ones exposed above are enough.

5.2 Cavity #1 4th and 5th Vertical Test

The data gathered during this vertical test are important because it was one of the few time when the emitter location can be see with the inspection camera (Kyoto-camera) and the data collected have shown different features than from the next tests.

Before showing the data, it is relevant to describe the cavity preparation and condition before the test, consisting in chemistry processes applied on its surface, vacuum treatment and cleaning.

Table 5.1 Cavity #1 preparation and test history.

| <i>Test #</i> | <i>Surface treatment</i> | <i>Maximum gradient (end test)</i> |
|--------------------------------------|---|--|
| <i>Before vertical tests</i> | EP (130 μ m), Annealing, EP2 (20 μ m), HPR, Baking | --- |
| <i>1st test</i> | --- | 15MV/m |
| <i>2nd test</i> | Baking | 15MV/m |
| <i>3rd test</i> | HPR, Baking | 15MV/m |
| <i>4th test</i> | EP2 (50 μ m), HPR, Baking | 17MV/m |
| <i>5th test</i> | Warm up | 16MV/m |

The cavity surface was electro polished (EP) using a mixture of hydrofluoric and sulfuric acid (as described in chapter 2) in order to remove 130 μ m of Niobium, then annealed in a vacuum furnace. A second step of electro polishing took place (EP2) to remove 20 μ m of material, then the surface was cleaned by means of High Pressure Rinsing (HPR) with ultrapure water at 100bar and finally baked for 48 hours at 150°. As the table above shows, some of the step was repeated from one vertical test to the next in order to obtain a better cavity surface and achieve higher accelerating fields.

In fact before the 4th vertical test was applied an electro polishing to remove 50 μ m of Niobium from the surface, then the cavity was rinsed with high pressure water and baked.

5.2.1 Vertical test schedule

Table 5.2 Cavity #1 vertical tests schedule [8].

| <i>4th Vertical test modes</i> | <i>Max E_{acc} [MV/m]</i> | <i>5th Vertical test modes</i> | <i>Max E_{acc} [MV/m]</i> |
|---|--|---|--|
| π | 10 | π | 16 |
| $8/9 \pi$ | 13 | $8/9 \pi$ | 12.5 |
| $7/9 \pi$ | 16 | $7/9 \pi$ | 14 |
| $6/9 \pi$ | 18 | $6/9 \pi$ | 20 |
| $\pi(2)$ | 17.2 | $5/9 \pi$ | 20 |
| $3/9 \pi$ | 14 | $4/9 \pi$ | 13 |
| $1/9 \pi$ | 17 | $3/9 \pi$ | 8 |
| | | $2/9 \pi$ | 8 |
| | | $1/9 \pi$ | 3 |
| | | $\pi(2)$ | 16 |

5.2.2 Surface resistance

During the cavity cool down it was possible to measure the surface resistance and by fitting to obtain the value of the Niobium residual resistance

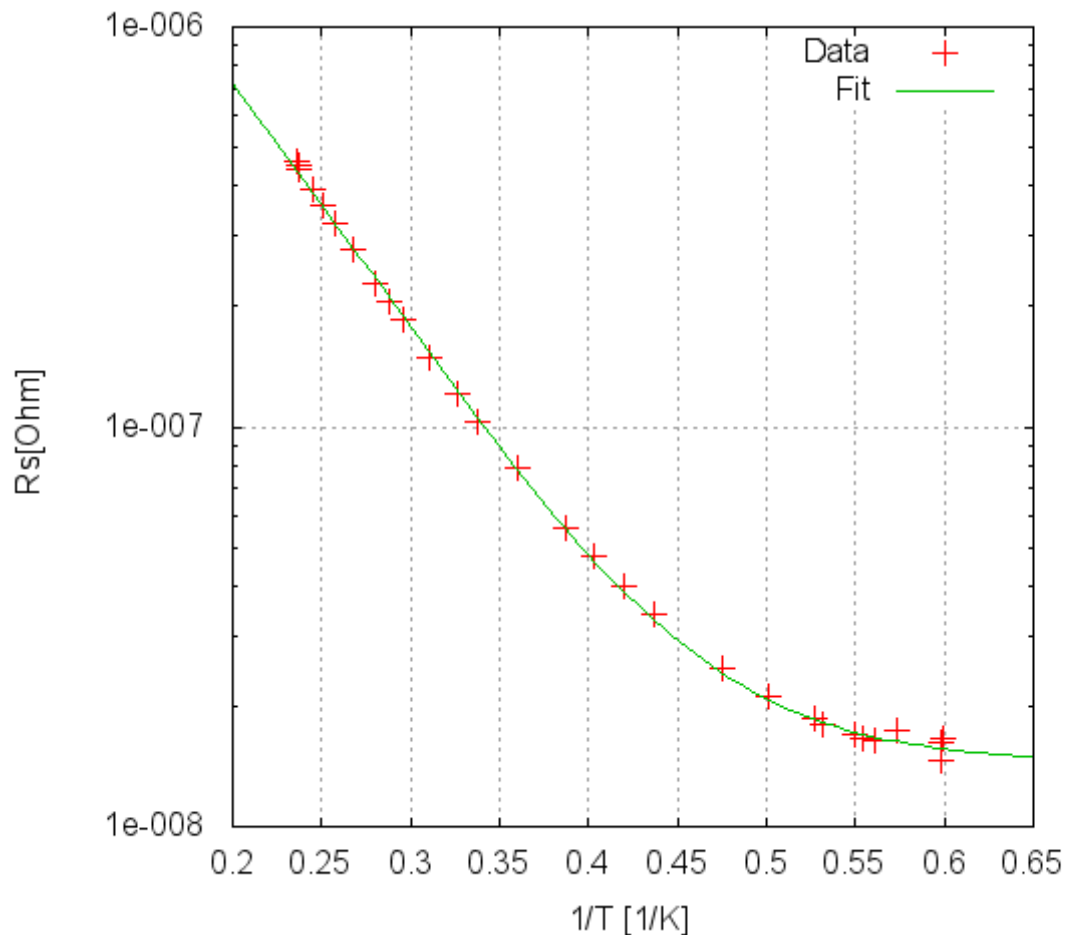
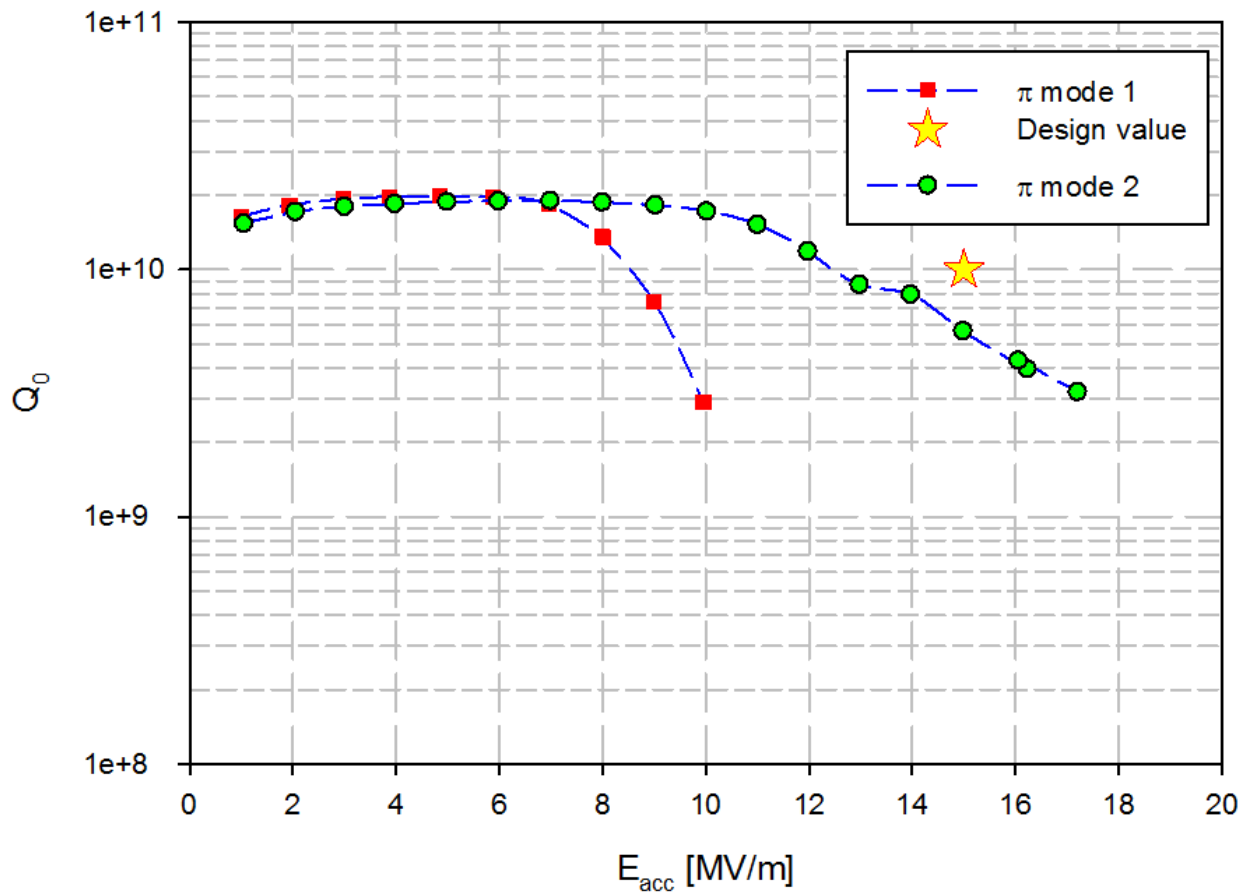


Figure 5.15 Cavity #1 surface resistance, the residual resistance was 14nΩ.

the residual resistance determined through fitting is about 14nΩ. With this information, it is possible to separate the power loss induced by RF electro-magnetic field and other loss sources such as field emission. As we know, from chapter 2, the loss due to RF field depends on the square of the surface electric field. In the next picture, the Q-E plot and the power loss during π mode operations is shown..

4th Vertical testFigure 5.16 Cavity #1 π modes Q-E plot.

As explained in chapter 2, Q_0 depends on cavity loss so we can also express the total power loss with respect to accelerating field (next picture). Basically it is the same information but through it we can see more clearly the amount of power dissipated by means of residual resistance and through field emission.

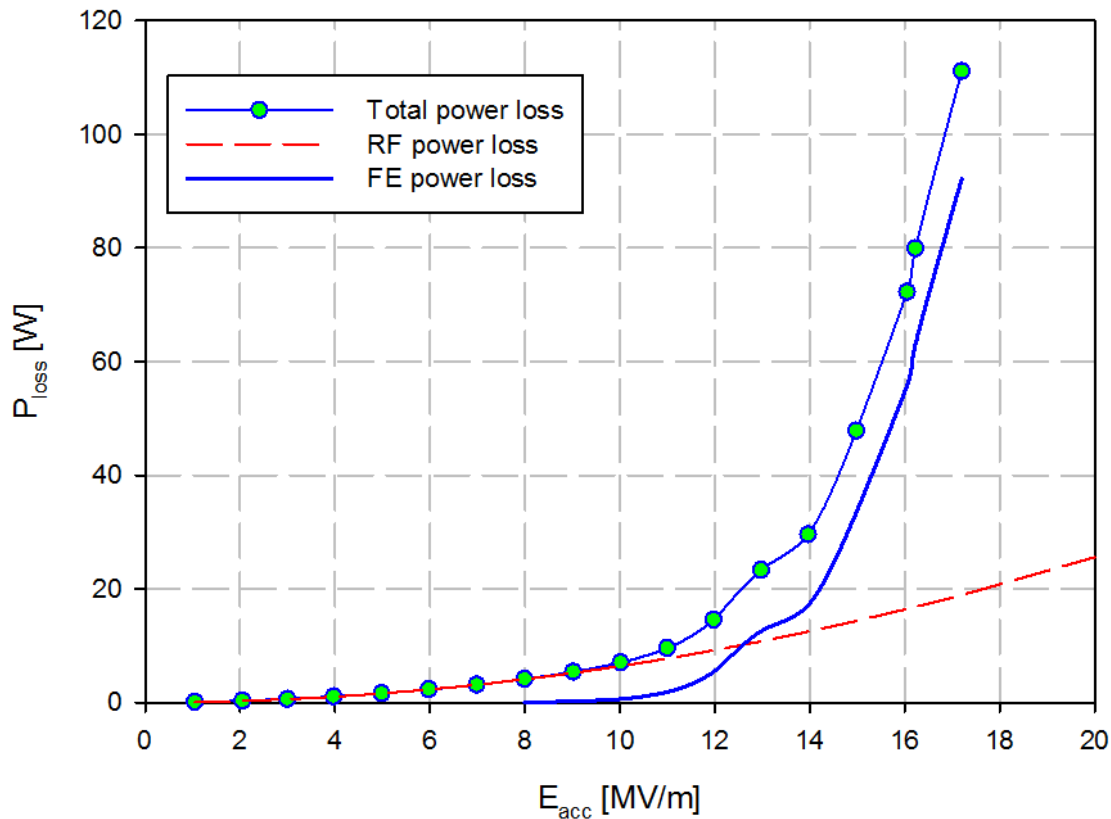
4th Vertical test π mode 2

Figure 5.17 Cavity #1 π mode 2 power dissipation with respect to accelerating field, total power loss (dotted line), RF field loss (red line) and field emission loss (blue line).

By removing the power dissipated through the surface resistance (red line) from the total loss we can obtain the power dissipated mainly through field emission (blue line), the bumps in curve can be originated from some processing occurred during the test. The power loss due to field emission is about 0.5W at 10MV/m and rise to 92W at 17.2MV/m, the data are consistent with the information gathered from the radiation monitor placed at cavity ends (LBP-side and SBP side).

The next picture shows the radiation dose in arbitrary unit with respect to the accelerating field. The radiation dose on LBP side is below the detection limit while the signal on the SBP side starts to rise up clearly around 10MV/m (as seen also for the dissipated power). This first information tells us that there is an asymmetry on the radiation detected at the cavity ends and that the radiation onset

is about 10MV/m. The asymmetry give us important information about electron trajectories: wherever the location it shall emit electrons that can move only towards the SBP.

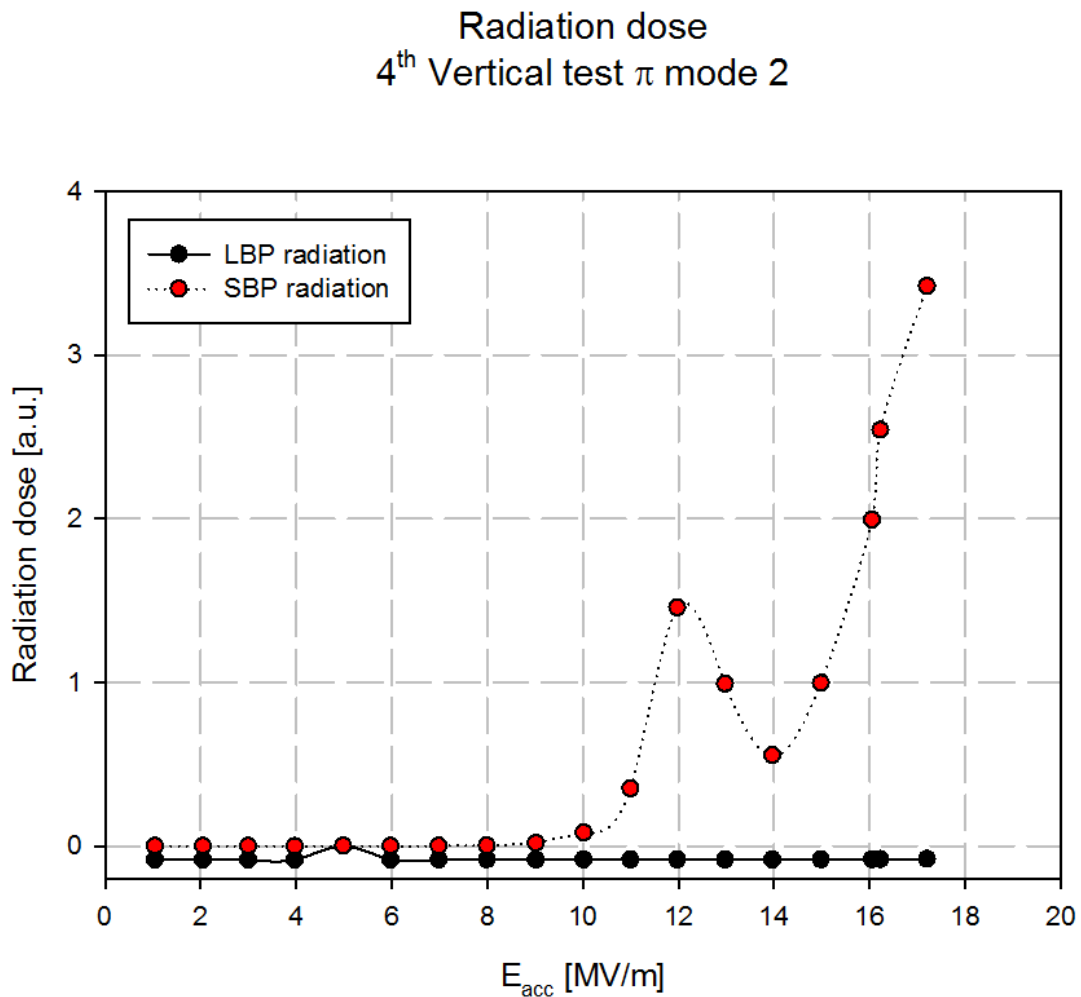


Figure 5. 18 Cavity #1 π mode 2 radiation dose at cavity ends.

The bump visible around 12MV/m can be produced by a processing event during cavity operation. It corresponds to the same location for the bump in the power loss graph.

During the 2nd π mode operation, a measure using the rotating mapping system was done. The accelerating field was kept at 13.9MV/m, the resulting x-ray pattern detected by the PIN diodes is shown in the next picture

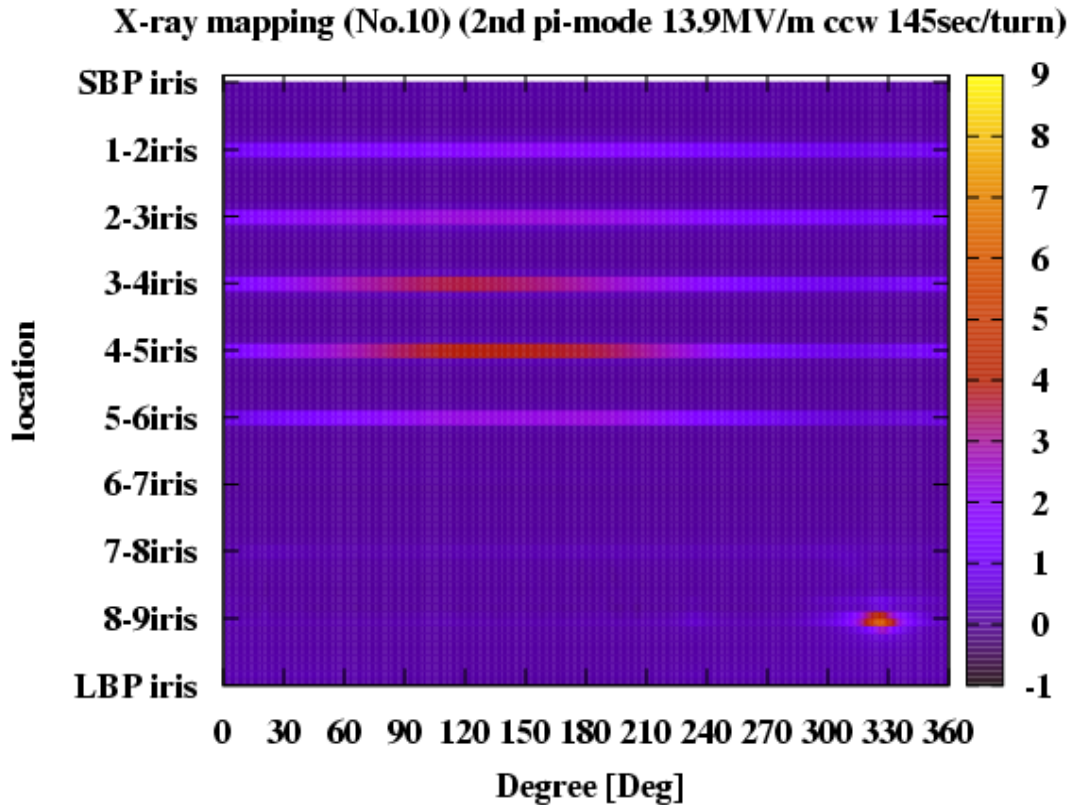


Figure 5. 19 Cavity #1 4th vertical test π mode (2), $E_{acc}=13.9\text{MV/m}$ $Q_0=7.93\times 10^9$, $P_{loss}=29.56\text{W}$, x-ray pattern detected by PIN diodes (rotating mapping system).

The map shows a small x-ray hotspot on the iris between cell 9 and 8 on the 330° meridian, and a broad x-ray spot located around the 150° meridian. The cavity was excited with π -mode at 13.9MV/m. The figure shows some peculiar features that will be found also in the following vertical tests. Typically when field emission occurs a sharp spot is detected near a iris region. At 180° from the sharp spot can be found a broad x-ray signal with a wide angular aperture.

These are also clue, as the radiation dose asymmetry, on the electron trajectories pattern, as it is an important information to understand the complex relation between the field emitted electrons, cavity performance and operating condition.

This vertical test has represented until now, a unique chance because after in other vertical tests the cavity was inspected by means of high resolution camera driven inside the cavity (Kyoto camera) [9-11].

The image taken during that inspection is shown below, the defect was found on the iris between the 9th and 8th cell on the 150° meridian, it was a Niobium tip near the welding seam.

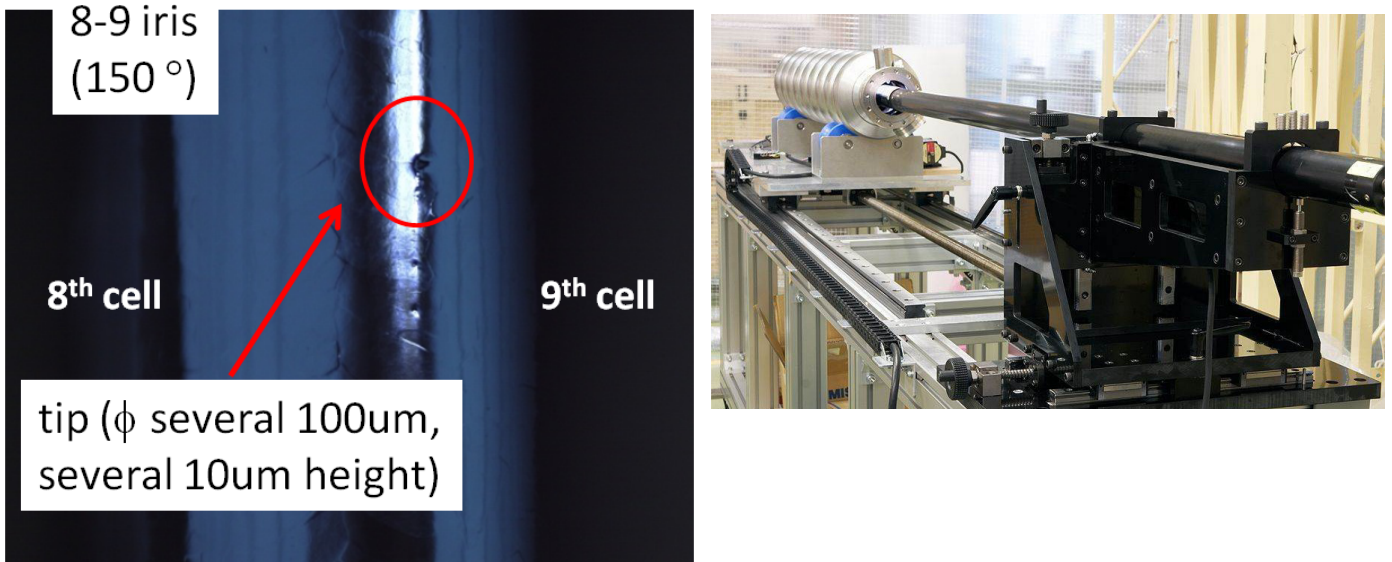


Figure 5. 20 Cavity #1 optical inspection result (left) after 5th vertical test, Kyoto camera set up (right).

The tip was located on the opposite side with respect to the sharp x-ray spot detected with the mapping system, the sharp spot was located at 330° while the tip was at 150° on the same iris [12].

At this point we have enough information to start the comparison between measured data and calculation. First of the emitter location along with accelerating field are input in the particle tracking code in order to calculate electron trajectories, impact location and kinetic energy, the picture below shows electron trajectories generated by an emitter in a position similar to the one observed with the Kyoto camera.

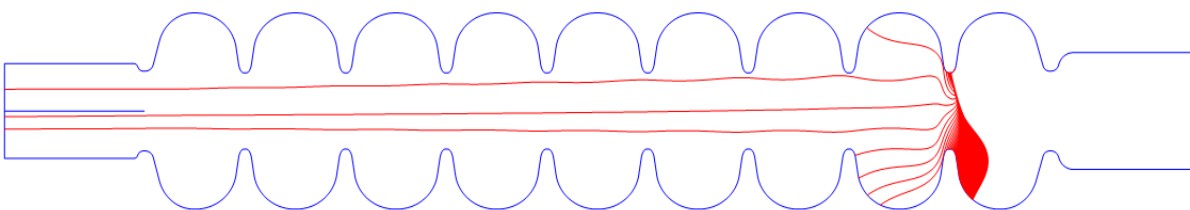


Figure 5. 21 Electron trajectories at different RF phase, π mode $E_{acc}=13.9\text{MV/m}$.

The picture above shows the electrons trajectories at different RF starting phases, the emitter is located in the upper part of the iris between the 8th and 9th cell. We can obtain the following information:

- Many trajectories land on the opposite side with respect to the emitter location.
- Some trajectory flies along the cavity axis near the iris edges.
- Some trajectories that fly along the cavity axis land on the SBP flange (left side)

In a next step, we can plot the impact energy with respect to cavity location and emission RF phase, the picture below shows the electron kinetic energy when it hit the cavity surface

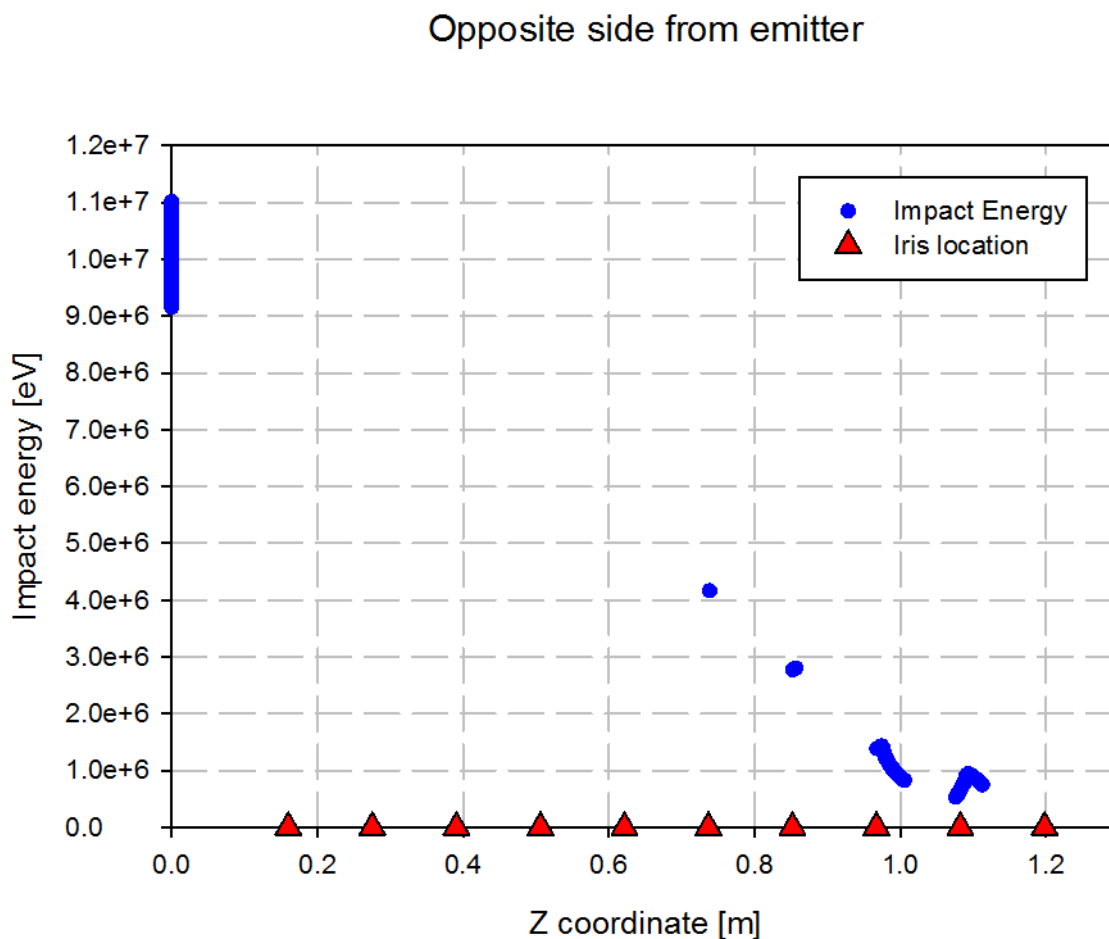


Figure 5. 22 Impact locations and energy at different RF phase, π mode $E_{acc}=13.9\text{MV/m}$.

In order to calculate the dissipated power through field emission we need to know the amount of current emitted, by recalling the Fowler-Nordheim equation [13]

$$I = S \frac{A (\beta E_s \sin(\theta))^2}{\Phi} e^{-B \frac{\Phi^{1.5}}{\beta E_s \sin(\theta)}} \quad (5.2)$$

We can notice that the current depends on the electric field on the surface (E_s) with respect to the RF phase θ , on the material working function and the emitter geometry through the two factor S (emission area) and β (field enhancing factor). The electron impact energy is proportional to the accelerating field so that

$$\text{Energy}_{kinetic} \sim E_{acc} \quad (5.3)$$

Also the surface field is related to the E_{acc} through a constant that depends on the emitter location and it is determined by the cavity geometry.

$$E_s = \alpha E_{acc} \quad (5.4)$$

For the ERL cavity this value reaches a maximum of 3 (E_{pk}/E_{acc}), and it changes according to the picture shown below

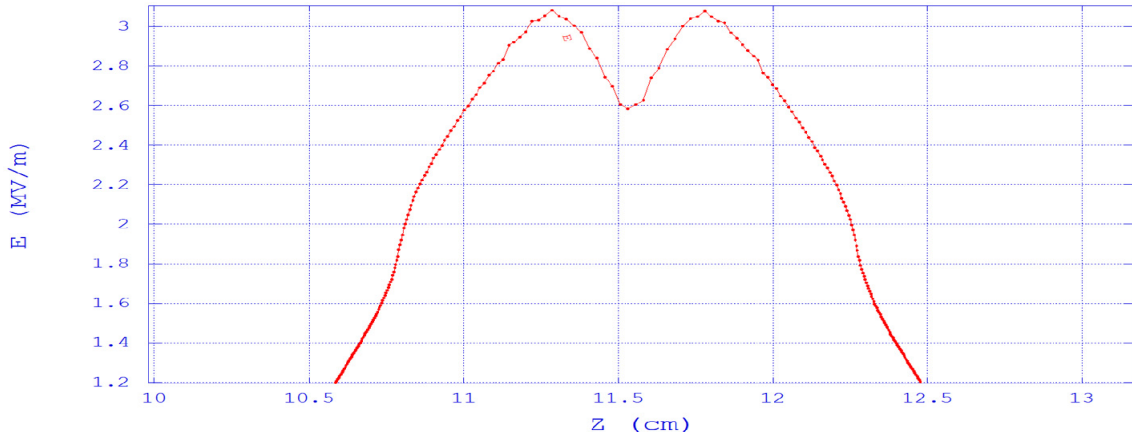


Figure 5. 23 Electric field on the surface for TM010 π mode and $E_{acc}=1\text{MV/m}$, with respect to Z coordinate near the iris between first and second cell

So we can write the field emission dissipated power as

$$P_{FE-loss} = \int I(\theta) \cdot Energy_{kinetic} d\theta \quad (5.5)$$

Despite the rough approximation we can use the above integral to extrapolate the emitters geometric parameters from the power loss data, then by means of particle tracking calculation we can obtain more accurate results.

In this framework the power loss can be written as [14, 15]

$$P_{FE-loss} \approx K E_{acc}^{3.5} \beta^{-\frac{C}{E_{acc}}} \quad (5.6)$$

Where K and C are two constant that gather all the previous values just to make the equation easier to read, in the first one is hidden the emitter area while the β is explicit. At this point we can extract the logarithm from both sides in order to obtain a linear equation

$$\text{Ln} \left(\frac{P_{FE-loss}}{E_{acc}^{3.5}} \right) = -\frac{C}{\beta} \frac{1}{E_{acc}} + \text{Ln}(K) \quad (5.7)$$

By defining

$$Y = \text{Ln} \left(\frac{P_{FE-1000}}{E_{acc}^{\beta} E} \right) \quad (5.8)$$

$$X = \frac{1}{E_{acc}} \quad (5.9)$$

$$m = \frac{C}{\beta} \text{ and } q = \text{Ln}(K) \quad (5.10)$$

The previous equation becomes simply

$$Y = -mX + q \quad (5.11)$$

Before approaching the real data, it is possible to numerically integrate the above integral and apply this rough method to estimate how coarse is the approximation.

The picture below shows the dissipated power calculated with a numerical integration using Mathematica. The enhancing factor determines the rate of rise of the power with respect to the accelerating field while the emitter area is basically a scale factor.

Numerical integration
 $\beta=100$ $S=10^{-13}$ $\alpha=3$

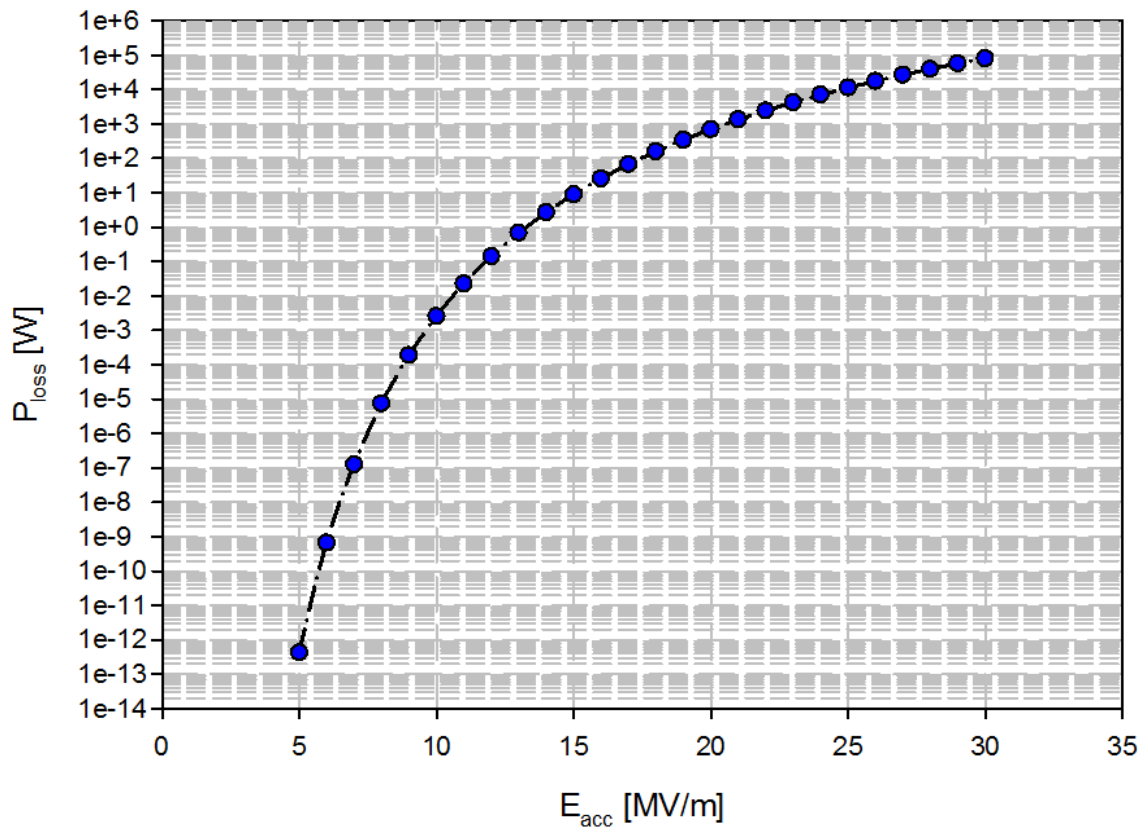


Figure 5. 24 Numerical integration to calculate the dissipated power with respect to the accelerating field.

In the next picture is shown the fitting using the simplification described above, where

$$Y = \text{Ln} \left(\frac{P_{FE} - (I_{FE})^2}{E_{acc}^2} \right) \text{ and } X = \frac{1}{E_{acc}}$$

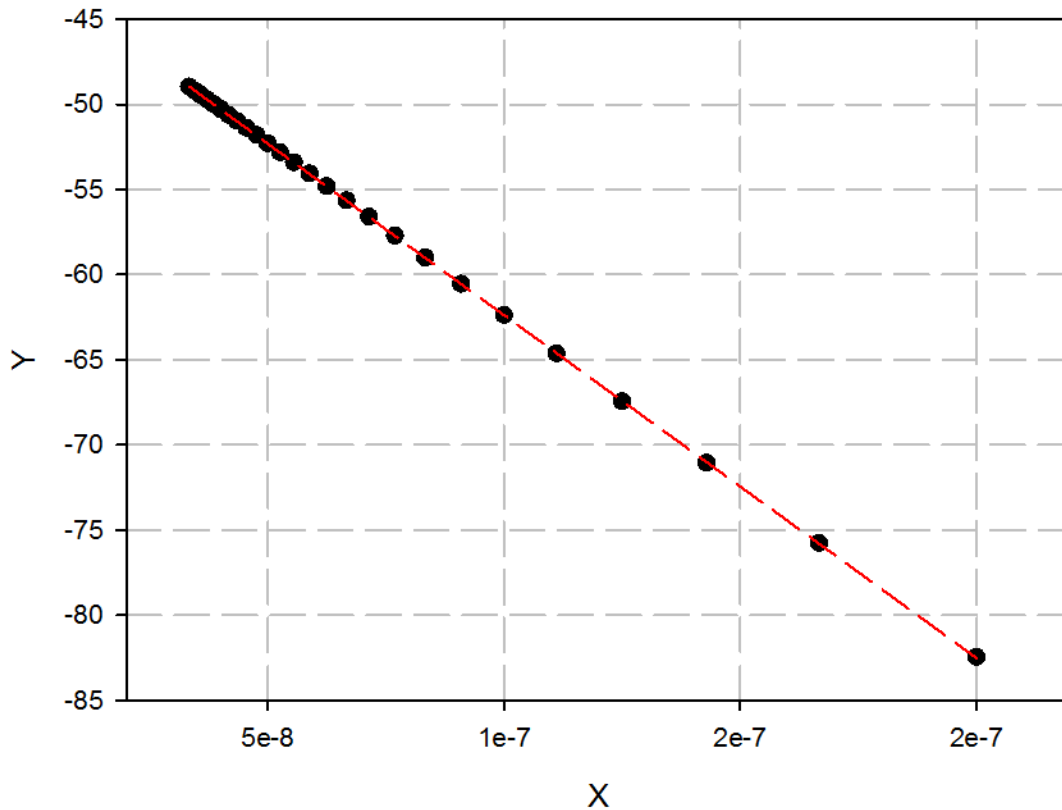


Figure 5. 25 Linear fitting for field emission power loss respect to accelerating field.

From the fitting the calculated β is 101 and the emitter area is $3 \times 10^{-18} \text{m}^2$. Generally we can expect at least 10% uncertainty concerning the enhancing factor and some order of magnitude difference in the emitter area. The error is related to the lack of knowledge on the exact material working function, that can change respect to emitter composition, surface chemical contamination and gas deposition [16]. Following the advice of Forbes [17] it is better to use this kind of approach to estimate the β more than the area. The error related to the area is also related to the unknown constant between the accelerating field E_{acc} and the impact energy.

5.2.3 Dissipated power

Now we can use the calculation tool to derive the emitter geometric values from the vertical test data, mainly it will be used to derive the enhancing factor. This value will be used as a starting point for the complete calculation involving the particle tracking code.

In the next picture, the power loss measured during the 4th vertical test and 5th will be shown. The second one took place after a cavity warm up without any surface treatment, the data result to be more smooth due to the absence of processing event during the measure.

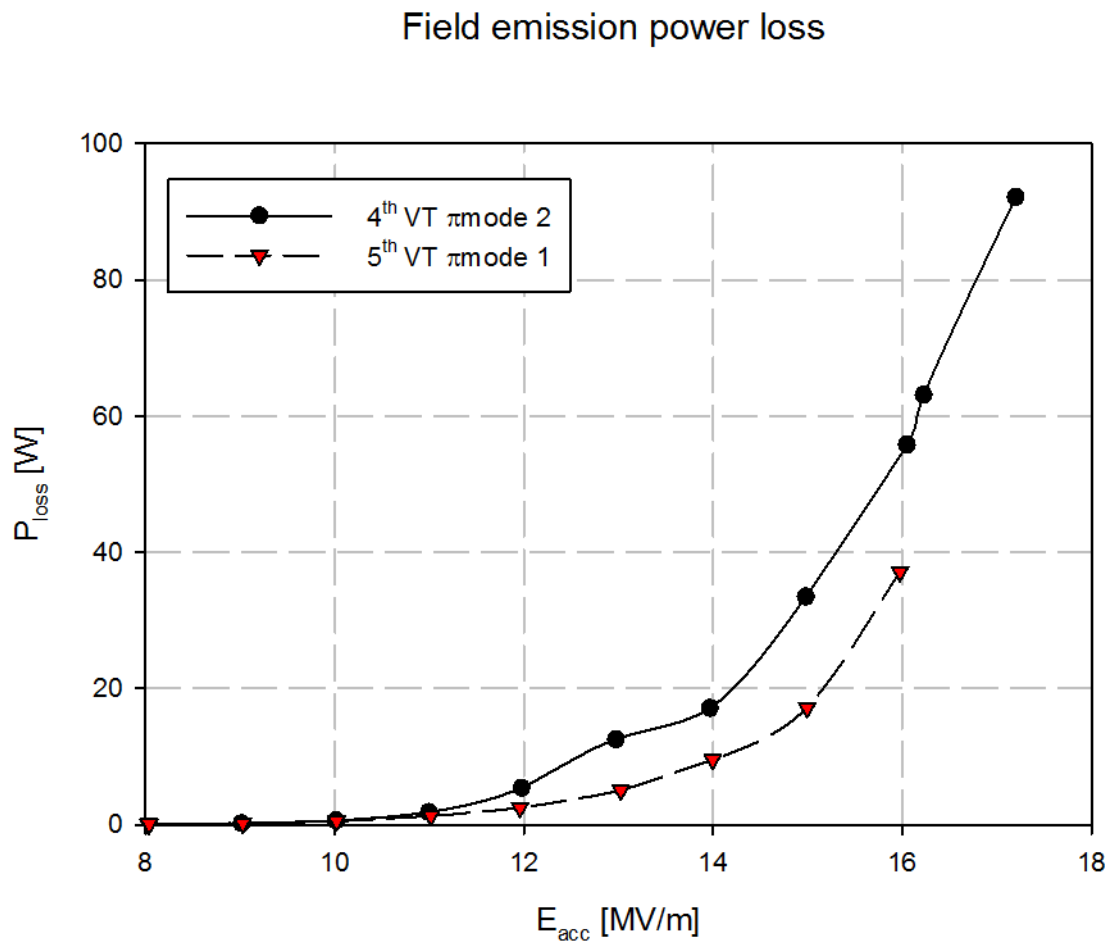


Figure 5. 26 Power loss due to field emission during 4th and 5th vertical test.

We can now extract the β factor from both data sets, the expected results shall be similar because the cavity was just warmed up without any additional surface treatment, so the emitter location and geometry should not be changed.

In both tests the power loss due to field emission is about 0.5W at 10MV/m. This seems to be the field emission onset for this emitter, the value is consistent with the measured radiation dose from LBP and SBP as shown before.

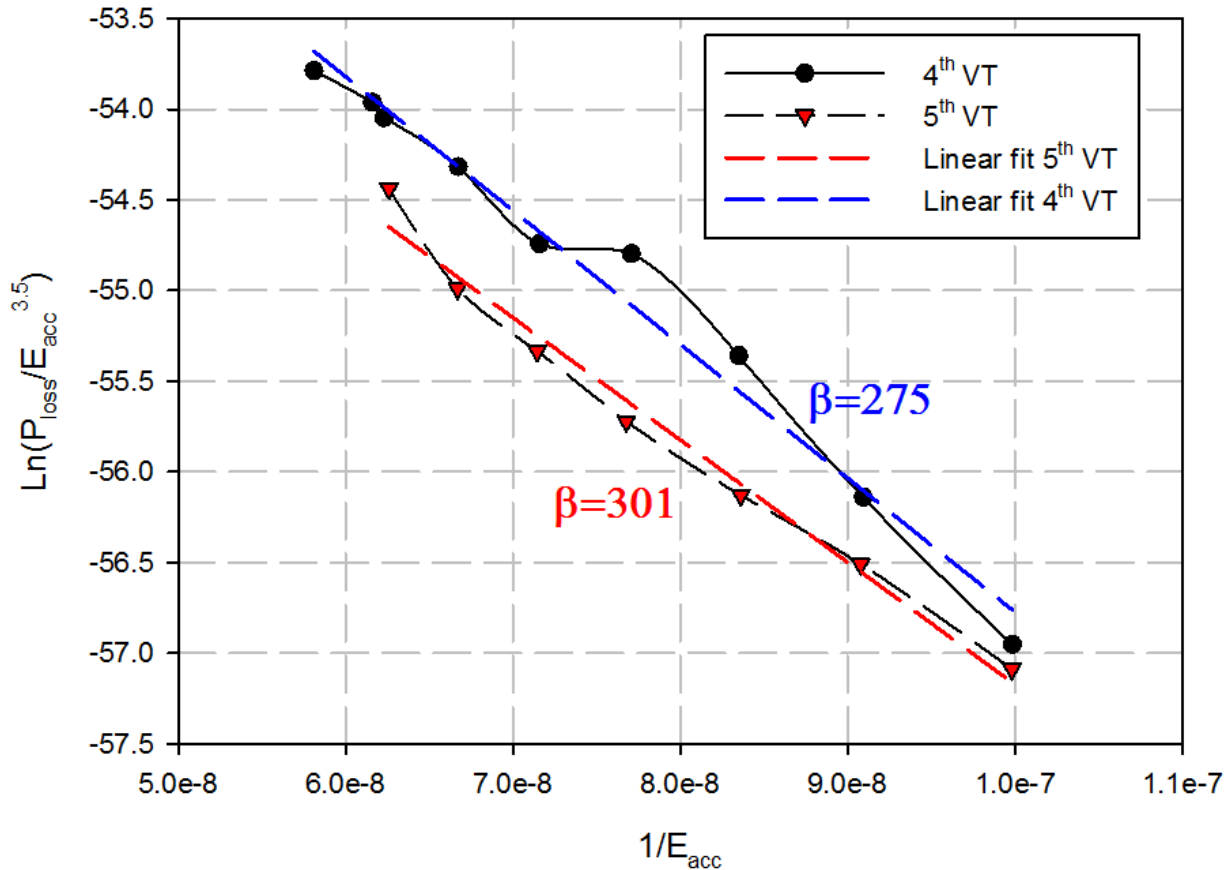


Figure 5. 27 Linear fitting to calculate the emitter geometric parameters.

The calculated β results to be 275 for the 4th vertical test and 301 for the 5th, the difference is within 10% as expected, the emission area differs about one order of magnitude (2×10^{-21} for VT4 and 9×10^{-22} for VT5), during the analysis with the particle tracking code it will be used as a free parameter for the fitting.

Now that we have obtained an estimation for the enhancing factor, we can use this information as input in the simulation code along with the emitter location detected with the optical inspection.

With this information we can calculate the quantities related to the emitted current such as the dissipated power and the detected portion of it, this is done by post-processing the data generated by

the particle tracking code that relates each trajectory to emission phase, impact location, impact angle and kinetic energy.

First it is possible to compare the dissipated power at different accelerating field, we can start by fixing the emitter location and the enhancing factor but keeping the emitter area as fitting parameter, the resulting plot is shown in the picture below, where the simulation data are compared to the measure done during 5th vertical test π -mode(1). The cavity surface condition is the same of 4th vertical test (no surface treatment done) but the data are more smooth and easier to compare avoiding the complication involving processing events.

Field emission power losses

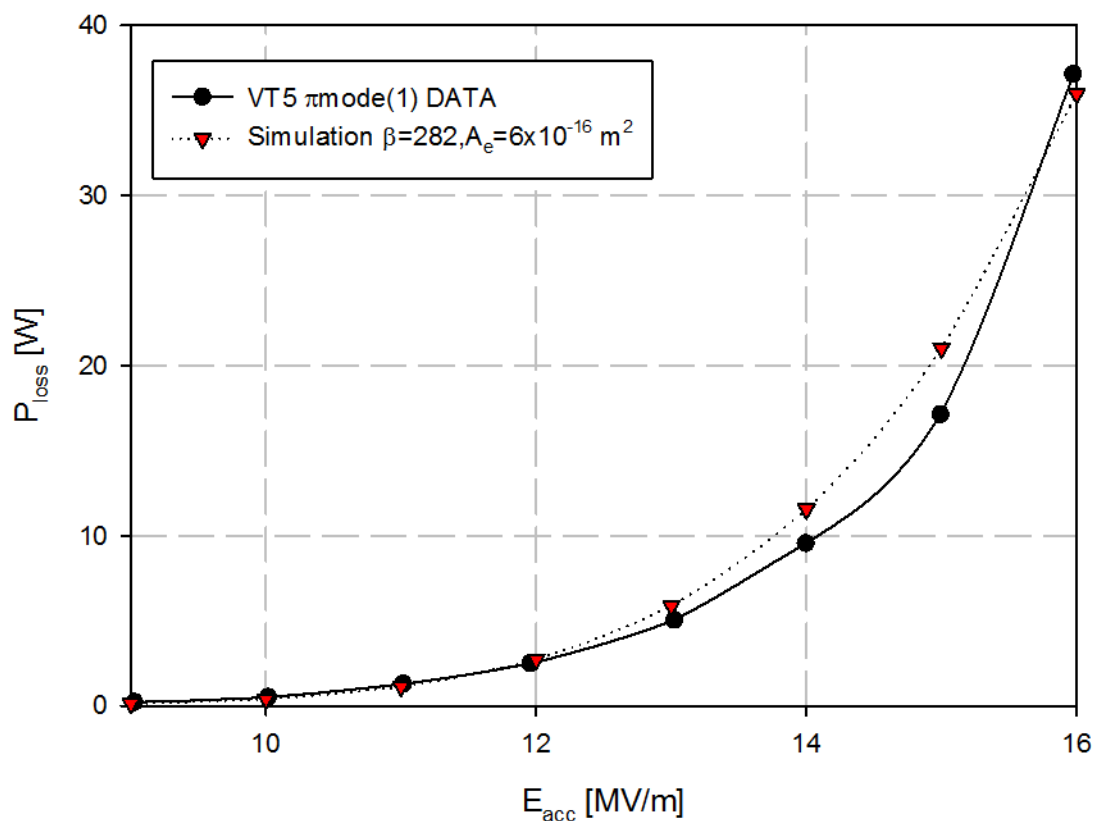


Figure 5. 28 Power dissipation as measured during the 5th vertical test π -mode(1) and calculated with simulation code.

Once we have obtained the dissipated power, it is possible to compare also the Q-E plot. The measured data are shown in the picture below for 1st and 2nd π -mode, the first were measured at the beginning of the test while the second at the end after pass-band modes measures.

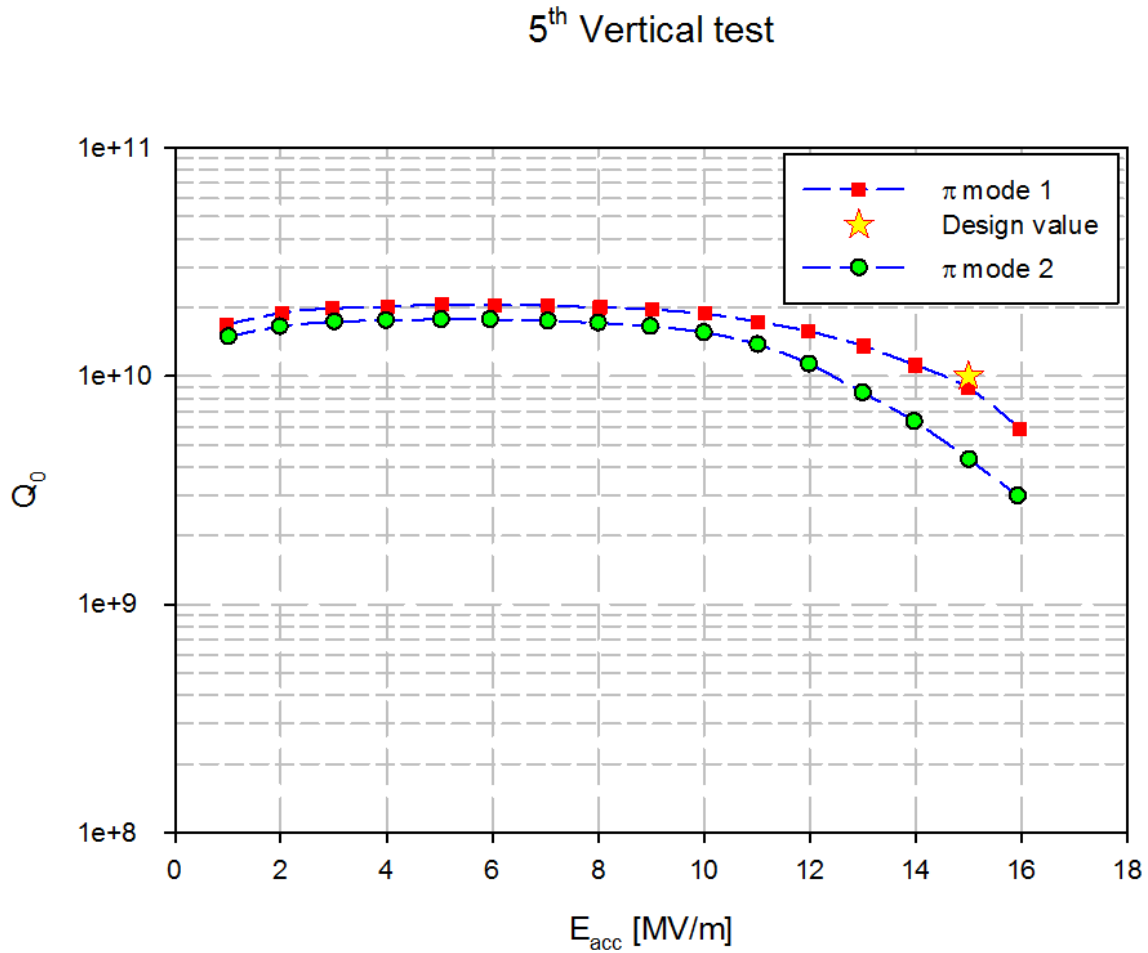


Figure 5. 29 Q-E plot from 5th vertical test π -mode(1) and π -mode(2).

The next picture displays the comparison between the Q-E curve for π -mode(1) obtained during the vertical test and the simulation data by using $\beta=282$ and an emission area of $6 \times 10^{-16} \text{ m}^2$, the two curve are in good agreement.

Q-E plot

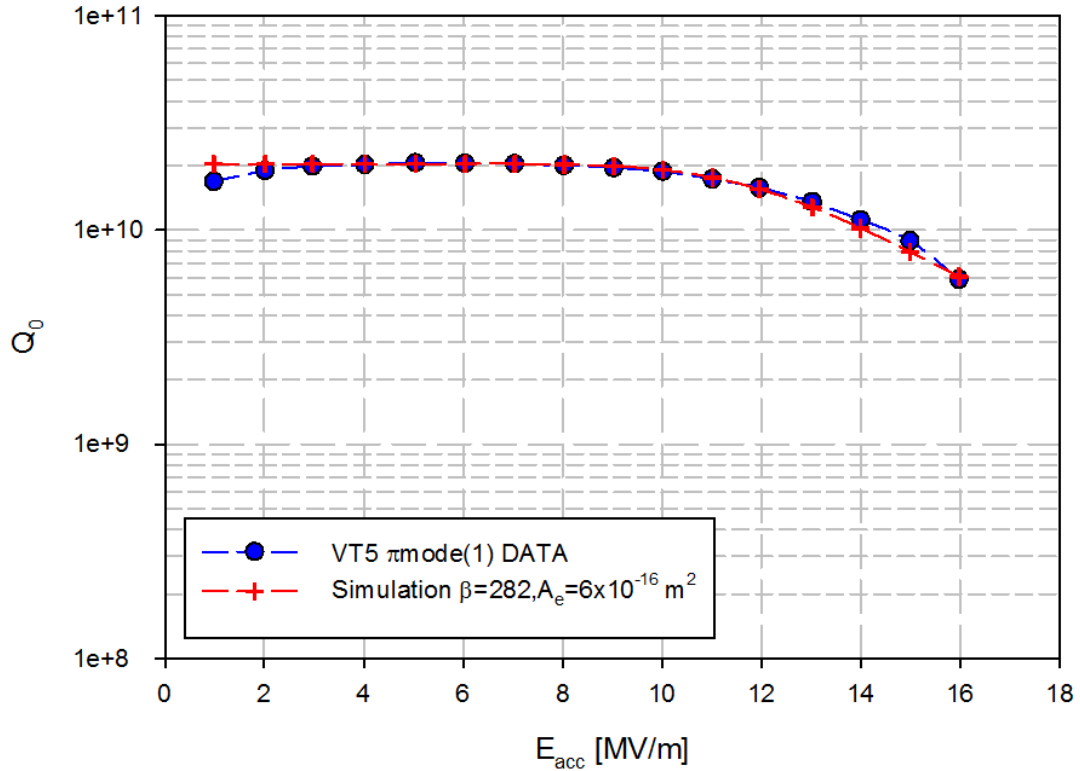


Figure 5. 30 Q-E plot comparing vertical test data and simulation result.

The data obtained during the test are consistent with the results obtained with the simulation. An even better agreement can be reached by using also the enhancing factor as a free parameter or by moving the emitter position a bit (0.5mm).

It is possible to calculate the difference between the power loss measured and the one obtained through the simulation by changing the enhancing factor and the emission area, but keeping the same emitter location as seen during the optical inspection. It is convenient to define a quantity to understand the goodness of the parameters choice, the sum of the squared difference seems to be useful for this kind of calculation, it is defined as follow

$$\Delta^2(\beta, S) = \sum (P_{data} - P_{SIM}(\beta, S))^2 \quad (5.12)$$

When the parameters choice is good, this quantity should approach to zero, while it increases rapidly when the choice is away from the best fit.

In the picture below is shown a result from this calculation, the enhancing parameter was chosen between 250 and 310, while the area between 10^{-17} and $5 \times 10^{-15} \text{ m}^2$,

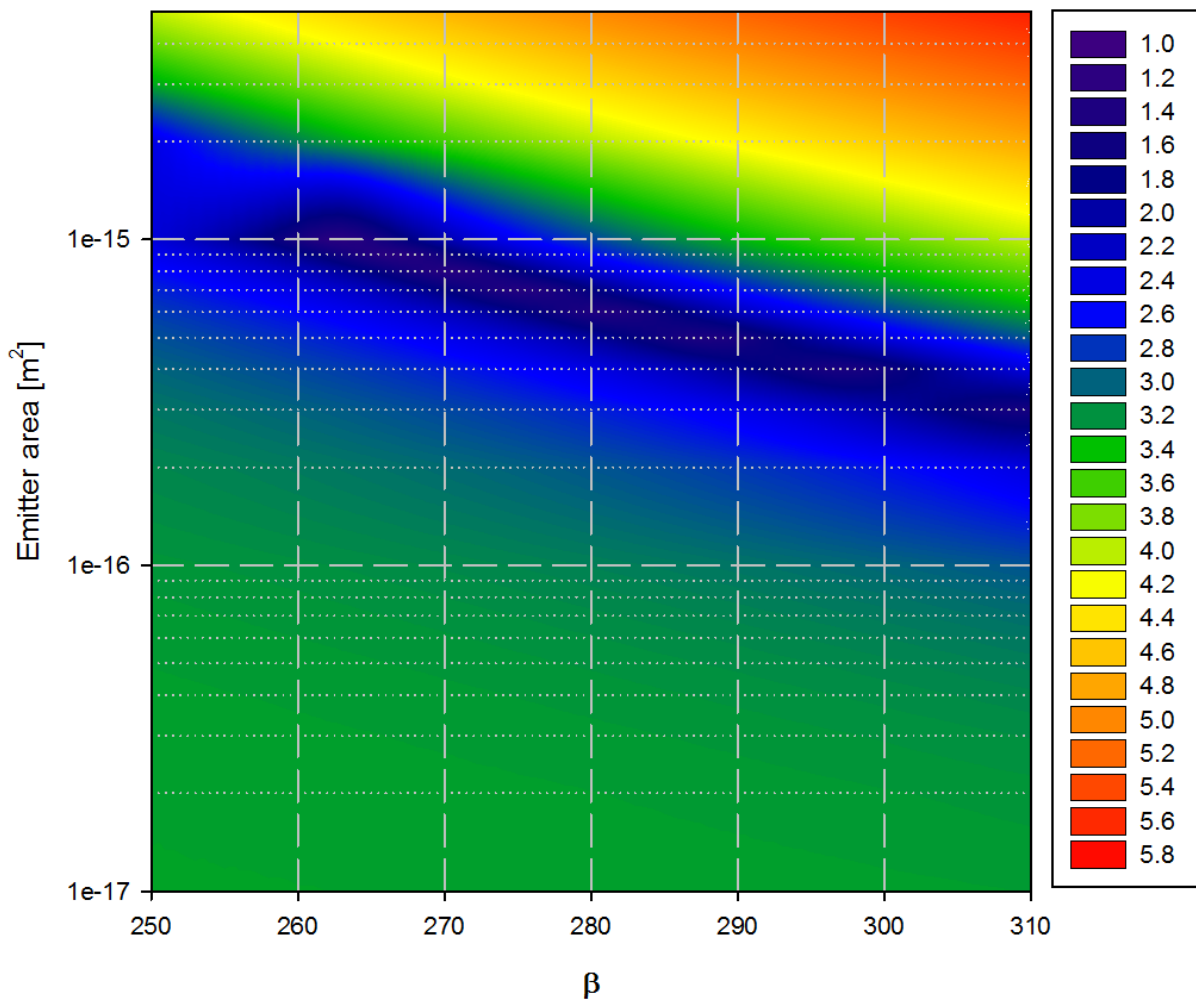


Figure 5. 31 Δ^2 contour plot, comparing 5th vertical test π mode(1) with simulation results.

The height of the contour is expressed by a logarithmic scale due to the rapid power increase with respect to parameters change. It is possible to notice that in the interval between 250 and 310 is located a minimum region (dark blue) consistent with the β value extrapolated from the data ($282 \pm 10\%$). In this region, the total dissipated power difference between the measure and the simulation is about 3W.

We can create the same map showed above with the power dissipated from an emitter near the previous one, this second emitter is located 0.5mm away from the previous, towards the inner part of the cell.

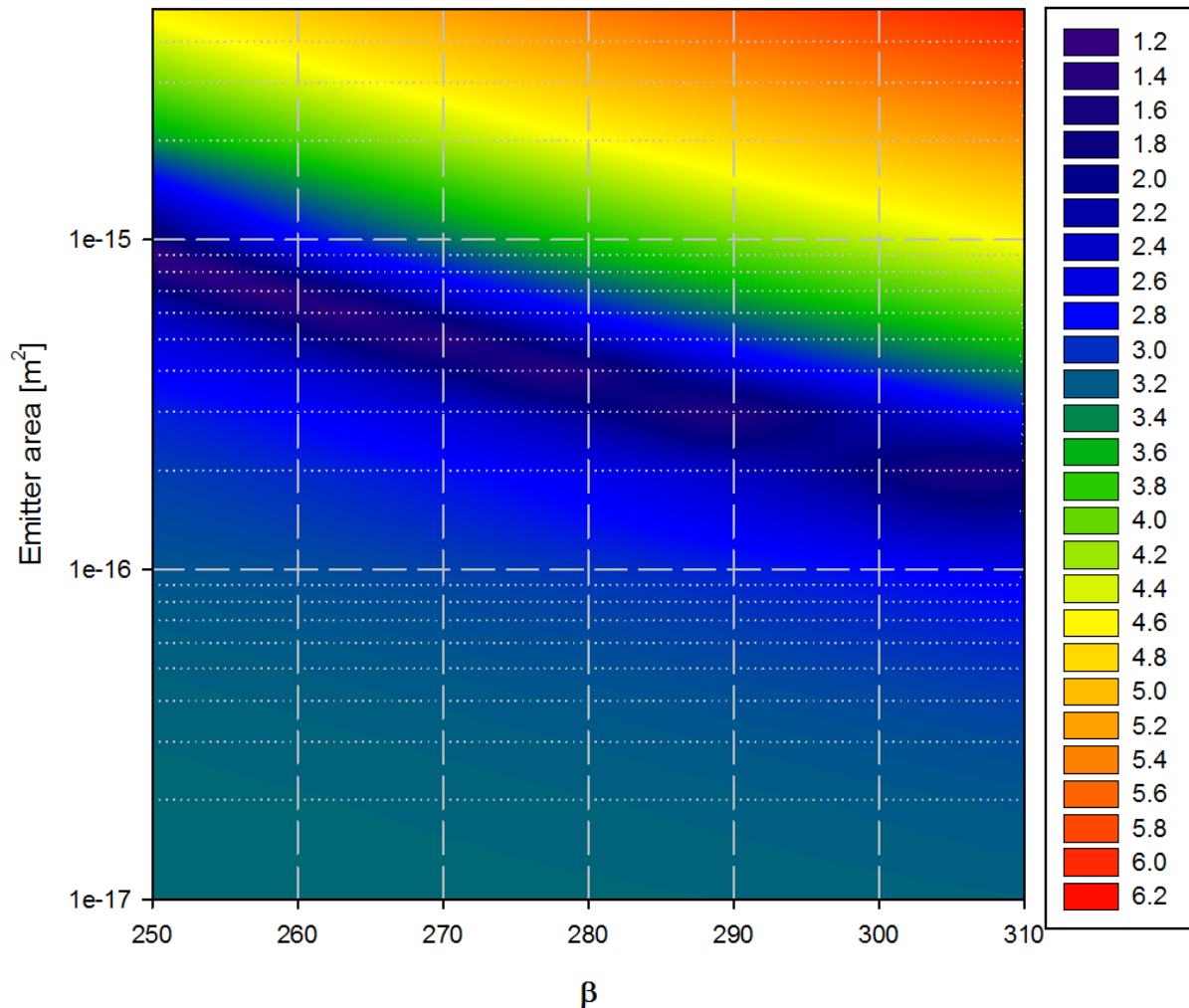


Figure 5.32 Δ^2 contour plot, comparing 5th vertical test π mode(1) with simulation results, emitter location is 0.5mm away from the observed position.

Even though the emitter was moved away from the observed position, it is still possible to obtain a reasonable agreement between the measure power loss and the one obtained through the simulation. In fact, the minimum region is consistent with an enhancing factor about $282 \pm 10\%$, also the emitter area is similar to the previous calculation, up to this point the agreement between observed emitter

position and simulated position is not better than 0.5-1mm. This uncertainty will be considered also in next paragraph in order to understand the x-ray mapping obtained with the PIN diodes measure.

5.2.4 X-ray mapping

At this point of the study, we can also try to understand the x-ray pattern observed with the PIN diodes installed on the rotating mapping system. The field emitted electrons accelerated in the cavity hit the surface in different location with different kinetic energy and different angles, each impact can produce a particle shower that can deposit some energy in the sensors. Through the information gathered up to this point, it is possible to compare the x-ray map obtained during the vertical test and the one produced by the simulation code, the main features we want to check are:

- The sharp spot location
- The broad spot location
- The radiation asymmetry between LBP and SBP side

First we can recall the mapping data seen above, it was taken during 4th vertical test when the accelerating field was about 13.9MV/m

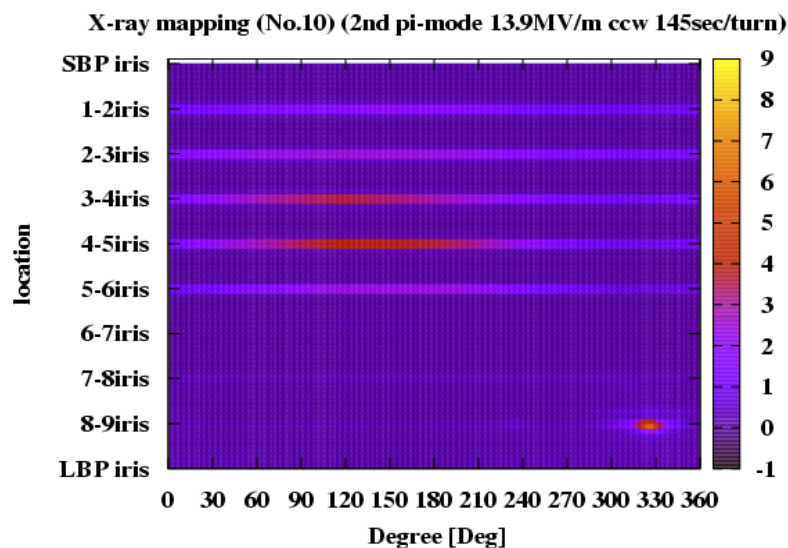


Figure 5. 33 Cavity #1 4th vertical test π mode (2), $E_{acc}=13.9\text{MV/m}$ $Q_0=7.93 \times 10^9$, $P_{loss}=29.56\text{W}$, x-ray pattern detected by PIN diodes (rotating mapping system), dashed line is at 310°meridian.

When the PIN diodes move around the cavity surface, they intercept part of the particle shower produced by emitted electrons, the x axis in the mapping figure above represent the meridian location while the y axis represent the Z coordinate along the cavity axis. The step motor can rotate the PIN diodes with 0.5° step, each diode is about 6mm wide and is about 10mm away from the next one.

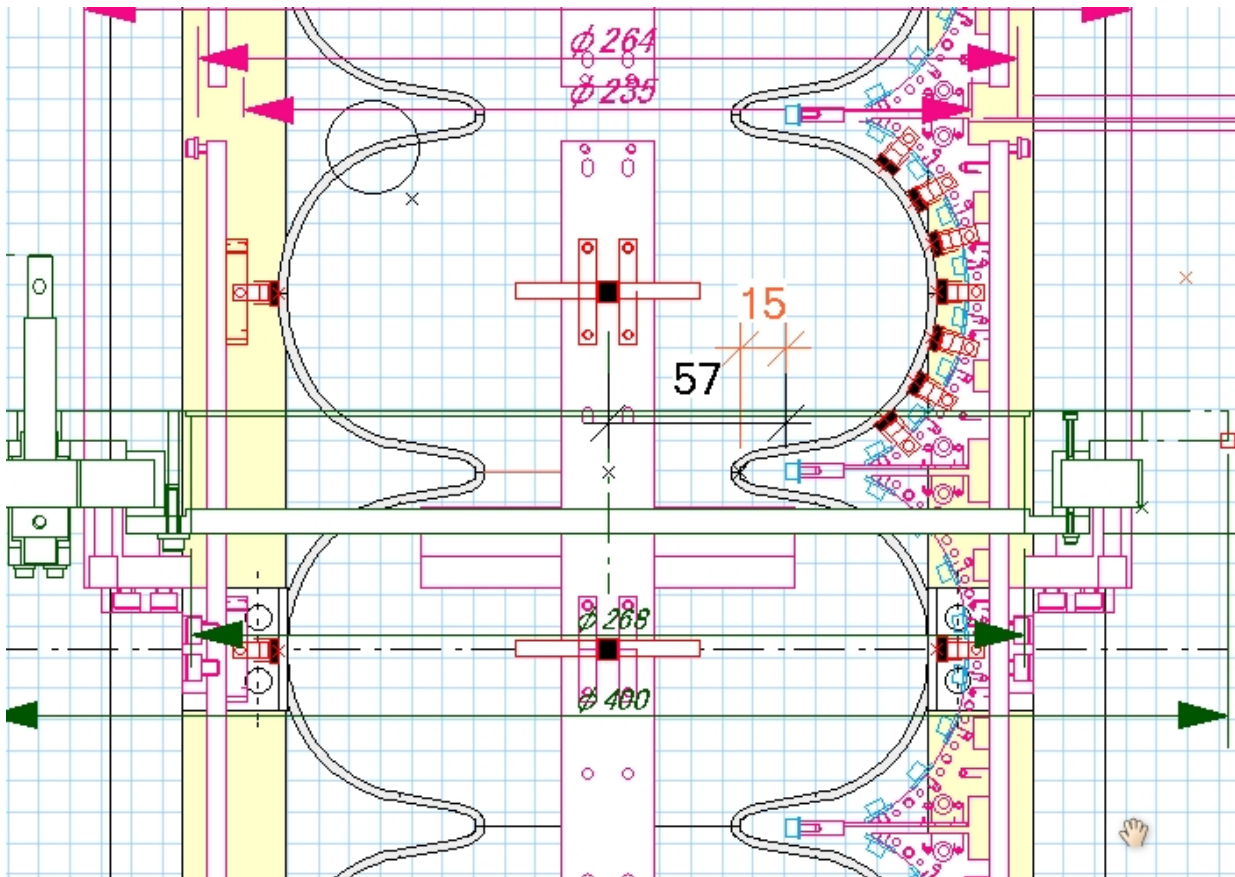


Figure 5. 34 Cavity #1 4th vertical test mapping system set up, PIN diodes (blue), carbon resistor (black).

5.2.5 The sharp spot

In the x-ray map image a sharp spot located on 310° meridian and near the iris between the 8th and 9th cell is clearly seen. It becomes even more clear when the signal from the diodes located on the iris its position is removed, as shown in the picture below.

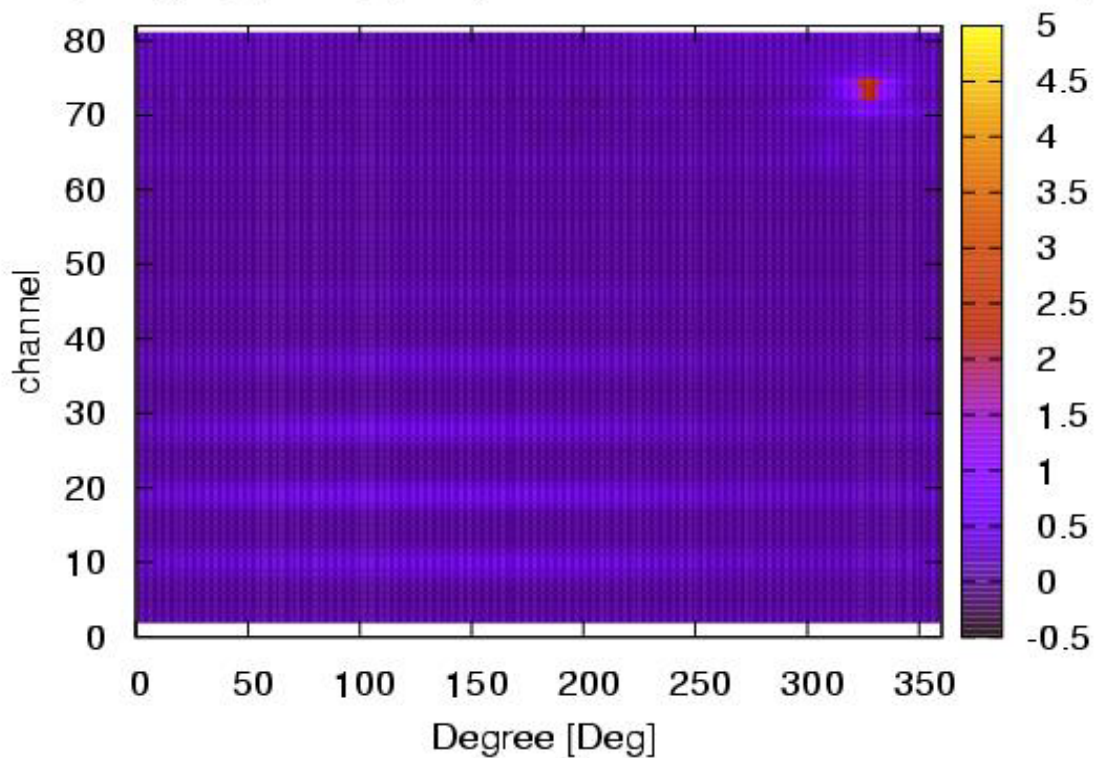


Figure 5. 35 Cavity #1 4th vertical test π mode (2), $E_{acc}=13.9\text{MV/m}$ $Q_0=7.93\times 10^9$, $P_{loss}=29.56\text{W}$, x-ray pattern detected by PIN diodes (rotating mapping system) without iris signal (The image is reversed respect to the previous one).

We can still see the bright spot on 8th-9th iris and a faint signal coming from the broad spot located at 180° from the sharp one, all this signal is coming from detector inside the cavity cells.

By using the particle tracking code, we can learn something about electron trajectories. For example, despite their lower energy (typically 1MeV) many electrons have a trajectory that land in the same cell and specifically the one that are emitted near the iris have a high probability to land on the opposite meridian, this concept is better explained with the following two pictures.

The first picture below represents the electron trajectories departing from the emitter seen through the optical inspection.

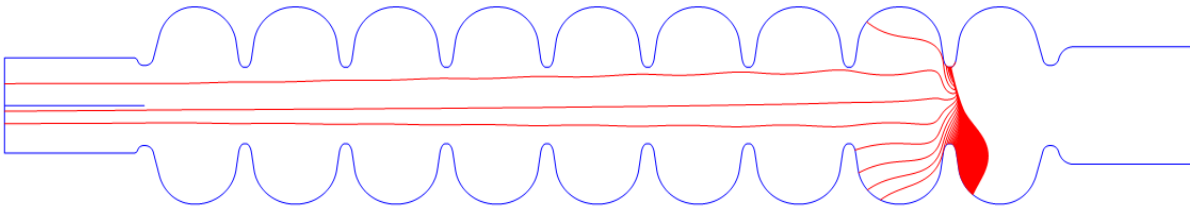


Figure 5.36 Electron trajectories at different RF phase, π mode $E_{acc}=13.9\text{MV/m}$.

It is clear that many trajectories land in the same cell on the opposite meridian with respect to the emitter (that is located in the upper part), each trajectory correspond to a specific RF phase during emission, in particular the picture above represent all the emission phases from 0° to 180° with 1° of step. The second picture is a reminder from chapter 3, it tell us with respect to emitter location and emission phase where the electron trajectory will fly, a blue dot means that the electron will remain in the same cell.

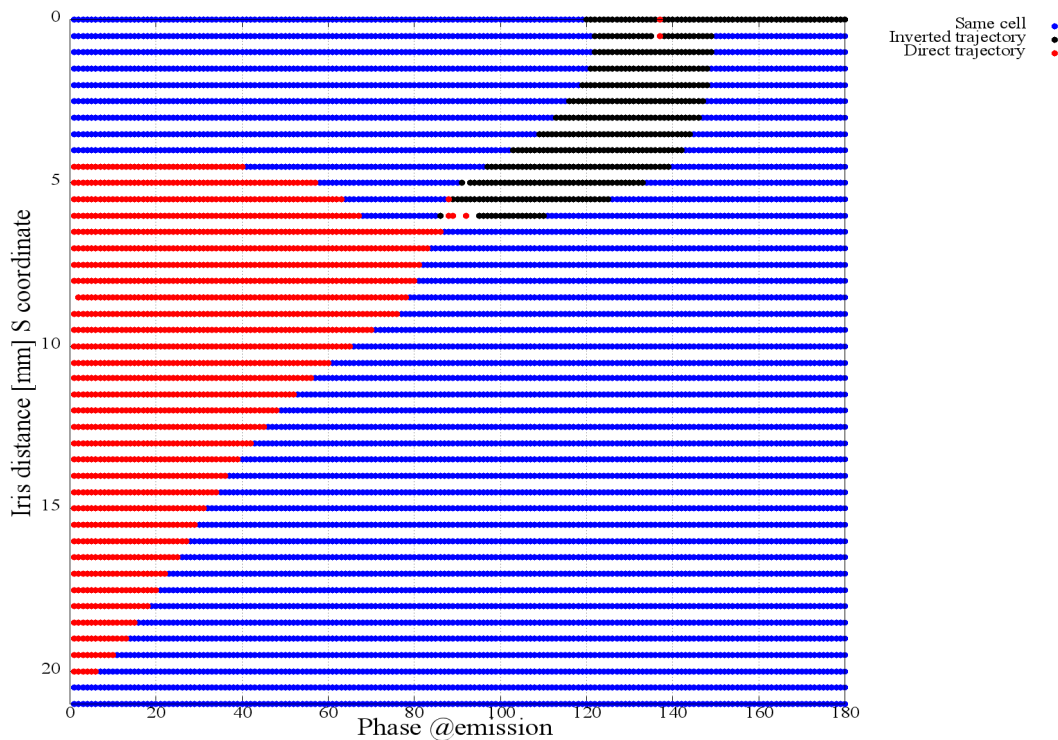


Figure 5. 37 Flying direction with respect to emitter location (S-coordinate) and emission RF phase at 15MV/m π mode, the plot is generalized for any iris.

The emitter found in the cavity after the 4th and 5th vertical test is located in the upper part of the previous figure, few millimeter away from the iris, the expectation from this emitter is to produce electrons that will land in the same cell or will fly towards the SBP with an “inverted trajectory”, as described in chapter 3.

It is possible to estimate the amount of power landing on the cavity surface by using the enhancing factor and the emitter area previously calculated along with the emitter location detected during optical inspection. The power landing on the cavity surface on the meridian opposite to the emitter (310°) is plotted in the figure below with respect to the Z-coordinate, along with the observed emitter location (identified with the letter A) is also plotted the power delivered from an emitter 0.5mm away from it (identified with the letter B).

Power landing on the cavity surface

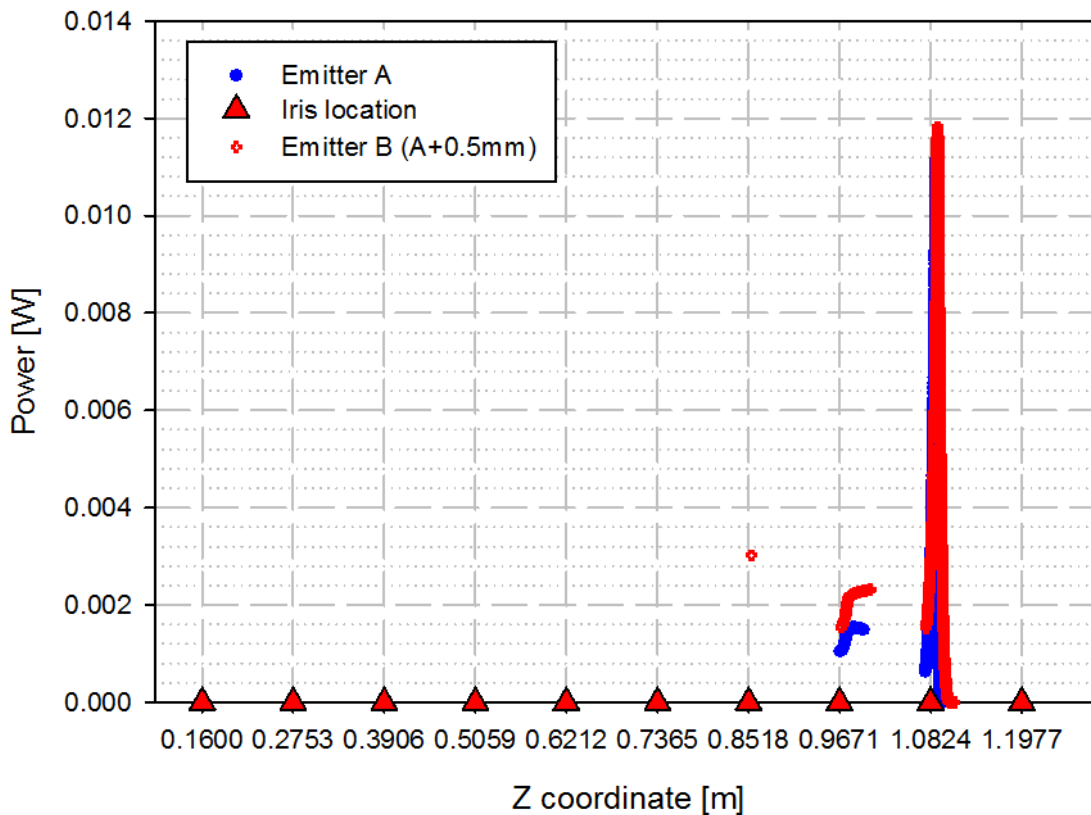


Figure 5. 38 Power landing on the cavity surface at 13.9MV/m π mode, the two emitters are located on iris between 8th and 9th cell, emitter A is the location detected during optical inspection and emitter B is 0.5mm distance from A (inside the 9th cell).

In the next picture will be shown a zoom of the iris location near the two power peaks, they are mainly overlapped, while trajectories from emitter A land on iris 8-9 and 7-8 the trajectories from B can land also on iris between 6th and 7th cell, in both cases the remaining trajectories land in the 9th cell or on the SBP flange.

Power landing on the cavity surface

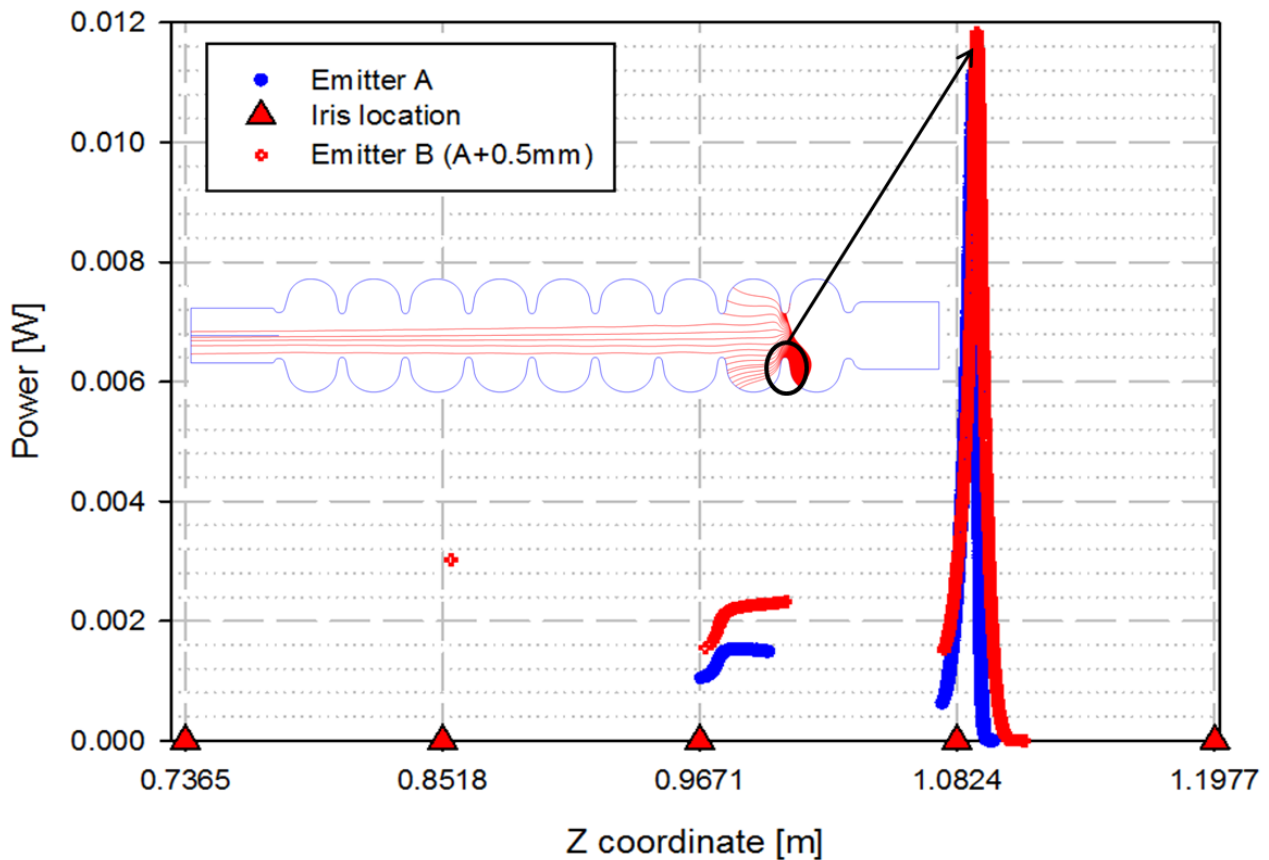


Figure 5. 39 Power landing on the cavity surface at 13.9MV/m π mode, the two emitters are located on iris between 8th and 9th cell, emitter A is the location detected during optical inspection and emitter B is 0.5mm distance from A (inside the 9th cell) Zoom from previous image.

In both cases the spot location is consistent with the position observed during the vertical tests, the second peak is faint but can be seen in the data collected during the test. Moreover , the simulation shows a clear asymmetry in the radiation pattern between SBP and LBP, the simulation produces trajectories that can land on SBP but none that can hit the LBP side.

We can also plot the transmitted power through the Niobium, by accounting impact angles and impact kinetic energy. It is proportional to the deposited power on the surface, the main peak is reduced due to the lower energy impact, its ratio with the secondary peak drops from 6 times to 2.5 times.

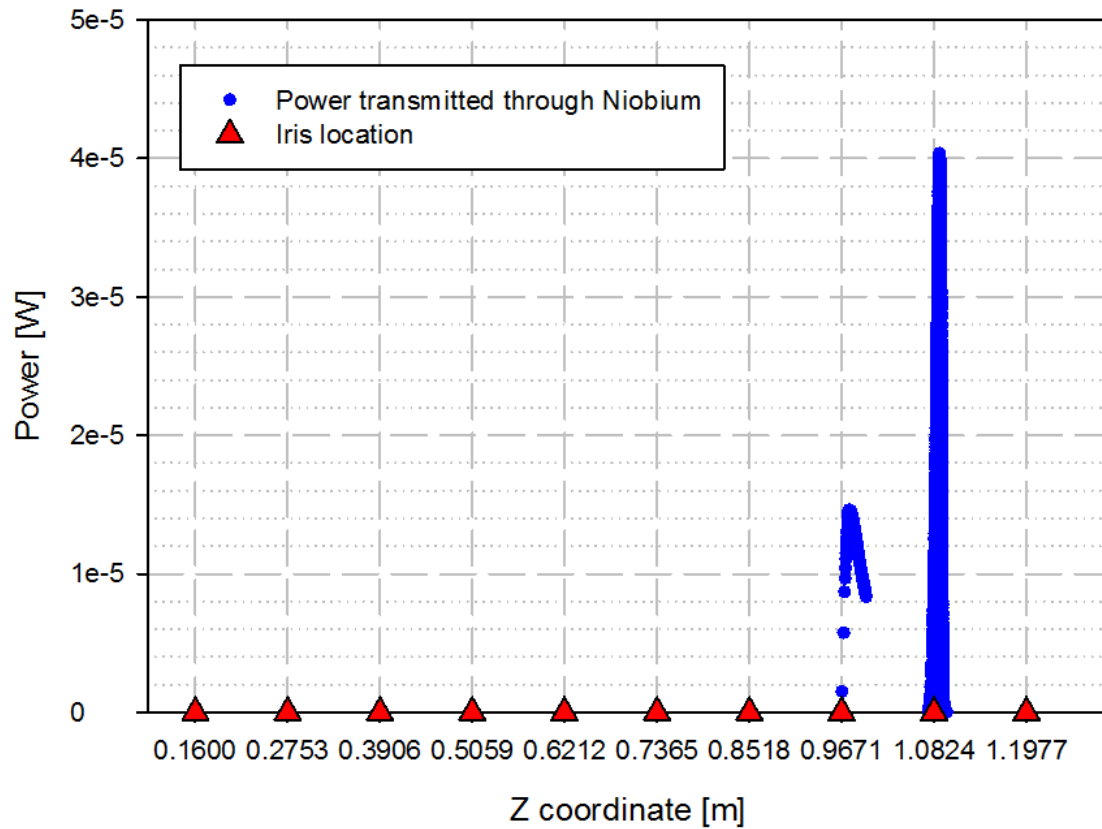


Figure 5. 40 Power transmitted through Niobium at 13.9MV/m π mode, the emitter is located on iris between 8th and 9th cell.

By plotting the signal detected from each PIN diode during the measure, the two peaks are clearly visible.

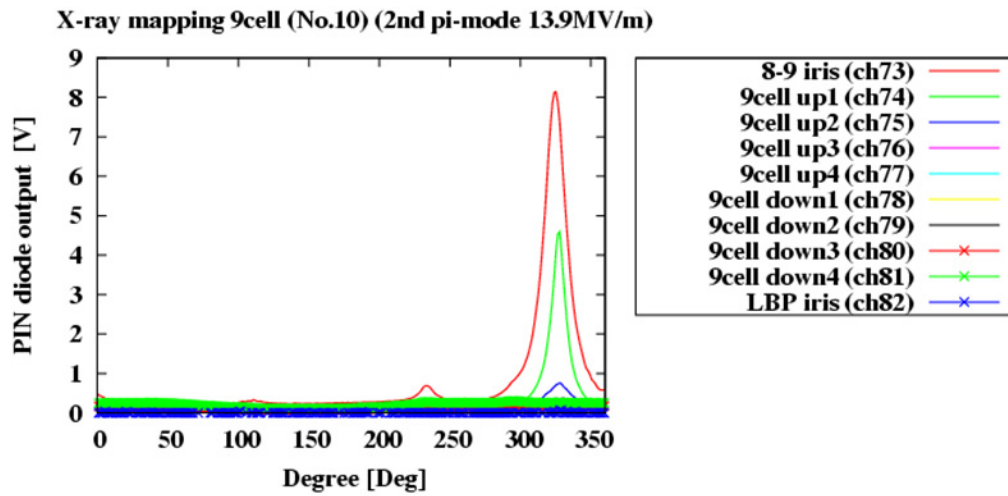
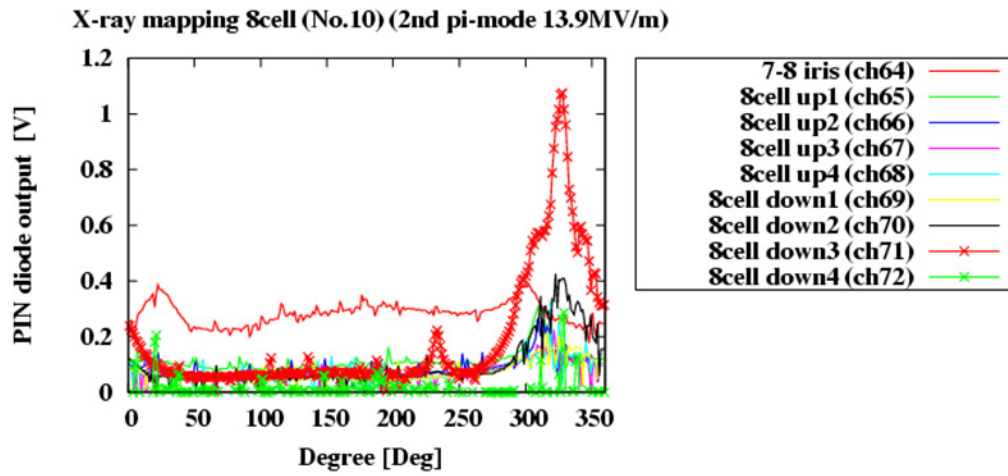


Figure 5. 41 PIN diodes voltage at 13.9MV/m π mode, the signal is measured inside the 8th and 9th cell, the signal coming from 8-9Iris is about 8 times bigger than the one detected from 7-8Iris.

The last information we need to describe is the mechanism that produces a broad x-ray spot on the same side of the emitter location. Due to it, we shall consider the electron impact angle once they hit the iris during their fly toward the SBP. By refining the step size in the simulation we can obtain detailed information on hit location and impact angles on iris between the emitter and the SBP.

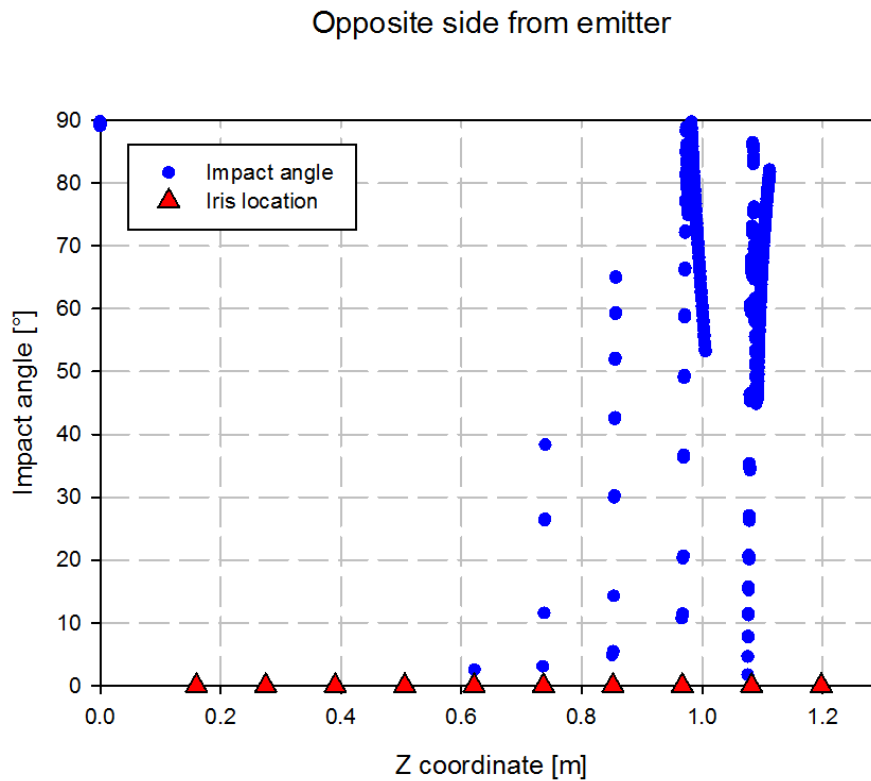


Figure 5. 42 Impact angles from emitter B at 13.9MV/m π mode, starting from iris between 6th and 7th cell the impact angle start to be lower than 10°.

Considering the above emitter we can notice that starting from the iris between 6th and 7th cell the impact angle is below 10°, we know from previous calculation that for angle less than 10° the portion of energy reflected from the Niobium surface is relevant. To account this effect, a specific EGS5 simulation was designed, electron with the same kinetic energy and same impact angle, observed from the particle tracking results, is used as input in the EGS5 calculation.

5.2.6 The broad spot

In the next picture is shown the electron kinetic energy at the impact location. Before we have focused our attention on the peak near the 8th and 9th iris cell to account for the sharp spot location, next we shall focus on the iris between 6th and 7th cell, 5th and 6th, 4th and 5th. On these irises, the kinetic energy reaches respectively about 2.8MeV, 4.2MeV and 5.6MeV while the impact angle are about 5°, 3° and 2°. With these information it is possible to calculate the amount of electrons reflected from the cavity surface and their distribution inside the cells.

Opposite side from emitter

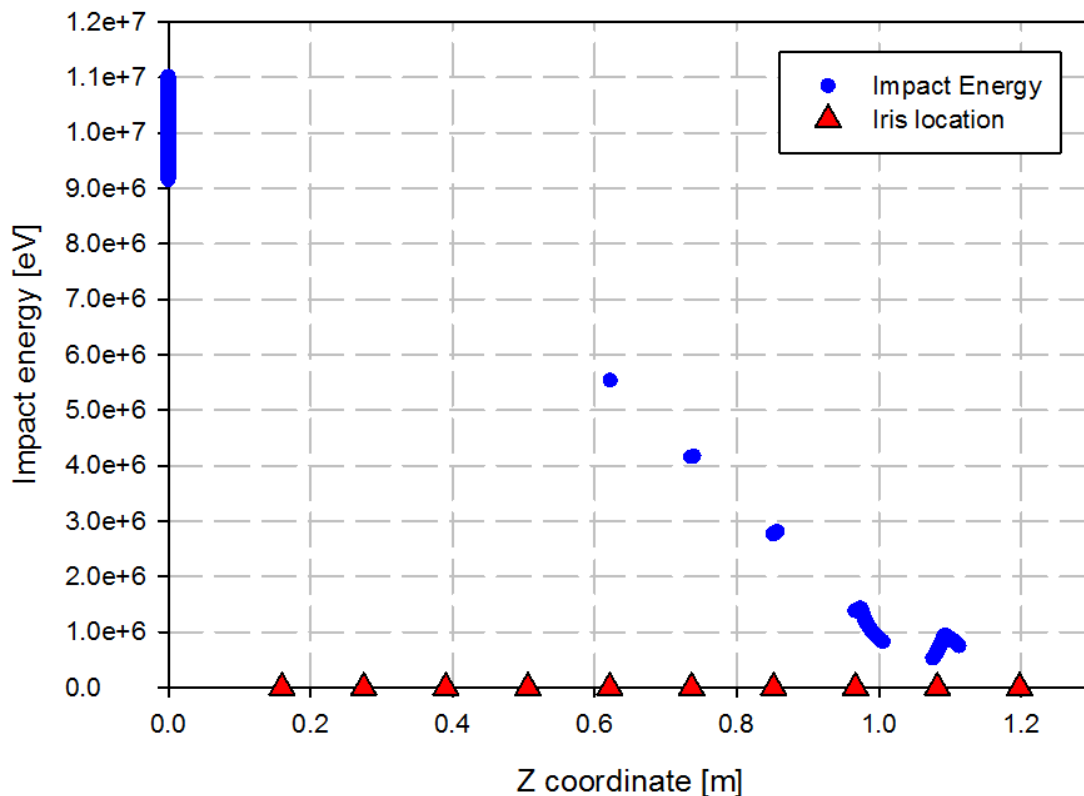


Figure 5. 43 Impact kinetic energy from emitter B at 13.9MV/m π mode.

It is worth mentioning that the blue dots located at $Z=0$ are trajectories that land on the SBP. It can be noticed that there is no trajectory that fly towards the LBP, this preliminary result is consistent with the observed asymmetry between the radiation detected on the SBP and the on the LBP.

In the EGS5 geometry is a simplified model of actual cavity, the electric field is neglected (as a first approximation its contribution to high energy reflected electron can be avoided) and the cavity shape is approximated by using the elementary geometry available in the code like cylinder and torus.

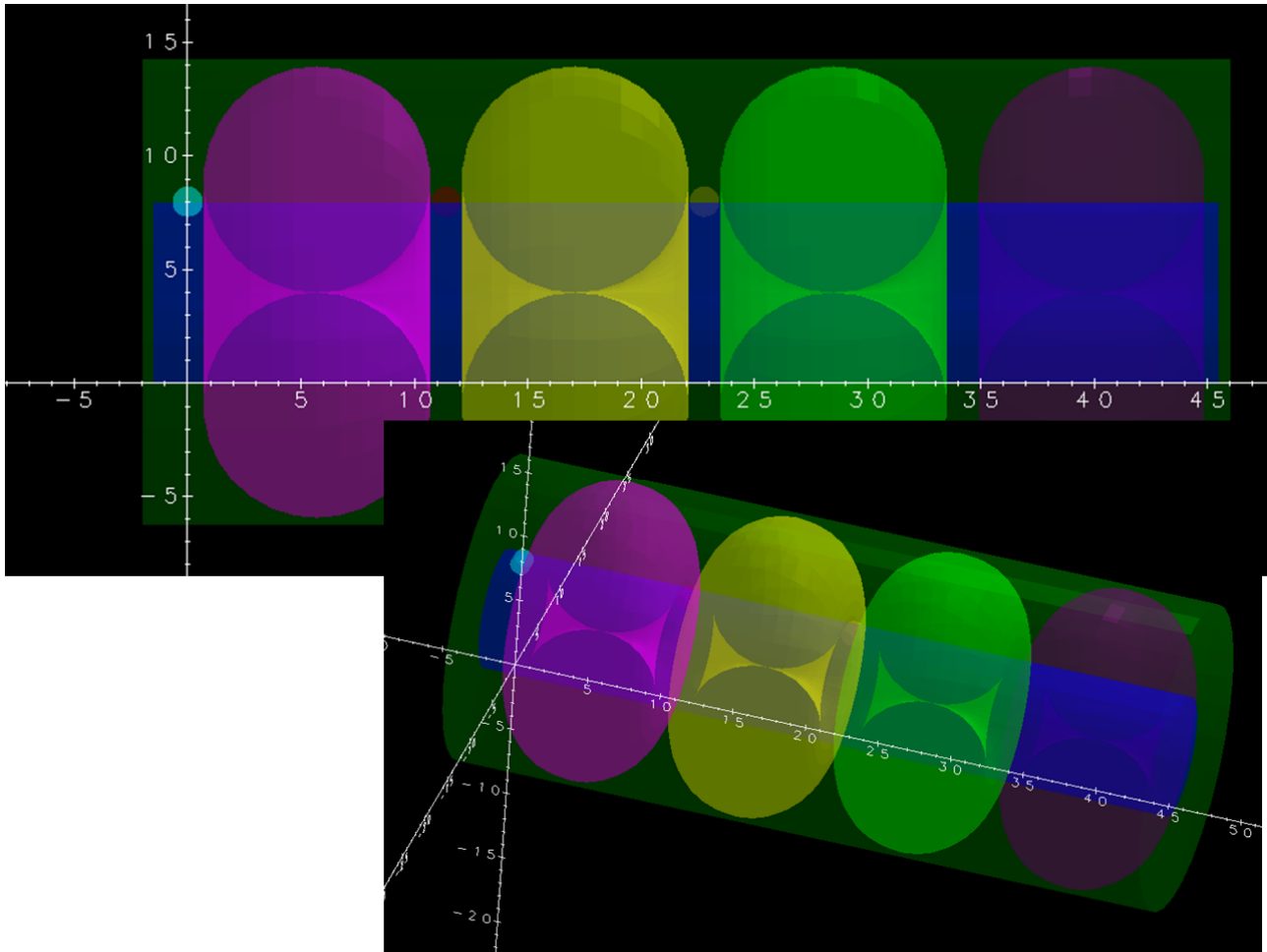


Figure 5. 44 EGS5 cavity model, cells are designed with torus, and iris with cylinder with the same curvature radius.

Despite the approximation, it is still possible to catch the electron behavior after they hit the cavity iris, the model takes into account only few cells where the impact at low angle occurs. A Niobium cylinder is used to simulate the iris curvature radius, each iris intercepts an electron fan that moves parallel to the cavity axis, similar to what happen in the particle tracking simulation, the resulting particle shower are shown in the pictures below.

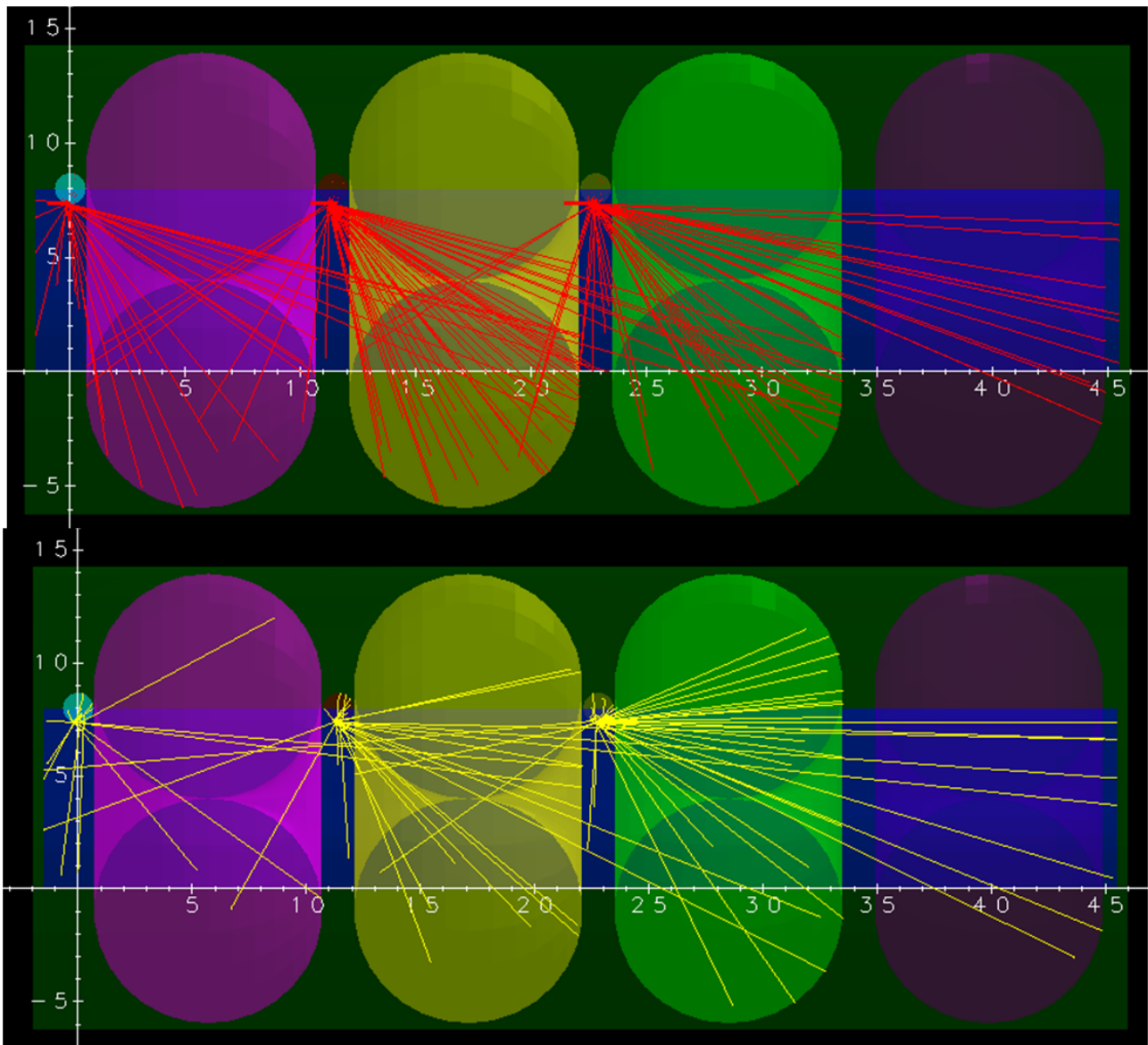


Figure 5. 45 EGS5 cavity model, shower produced by electron impact on iris, electrons (red lines) and photons (yellow lines).

The picture above shows the shower produced by electrons with a low angle of impact on iris. It can be seen how the electrons are reflected mainly on the opposite side while photons have the tendency to produce a shower on the same side of the impact location, the emitter is supposed to be in the lower part on the left side.

To appreciate the particle distribution, we can represent the impact location and the shower products kinetic energy.

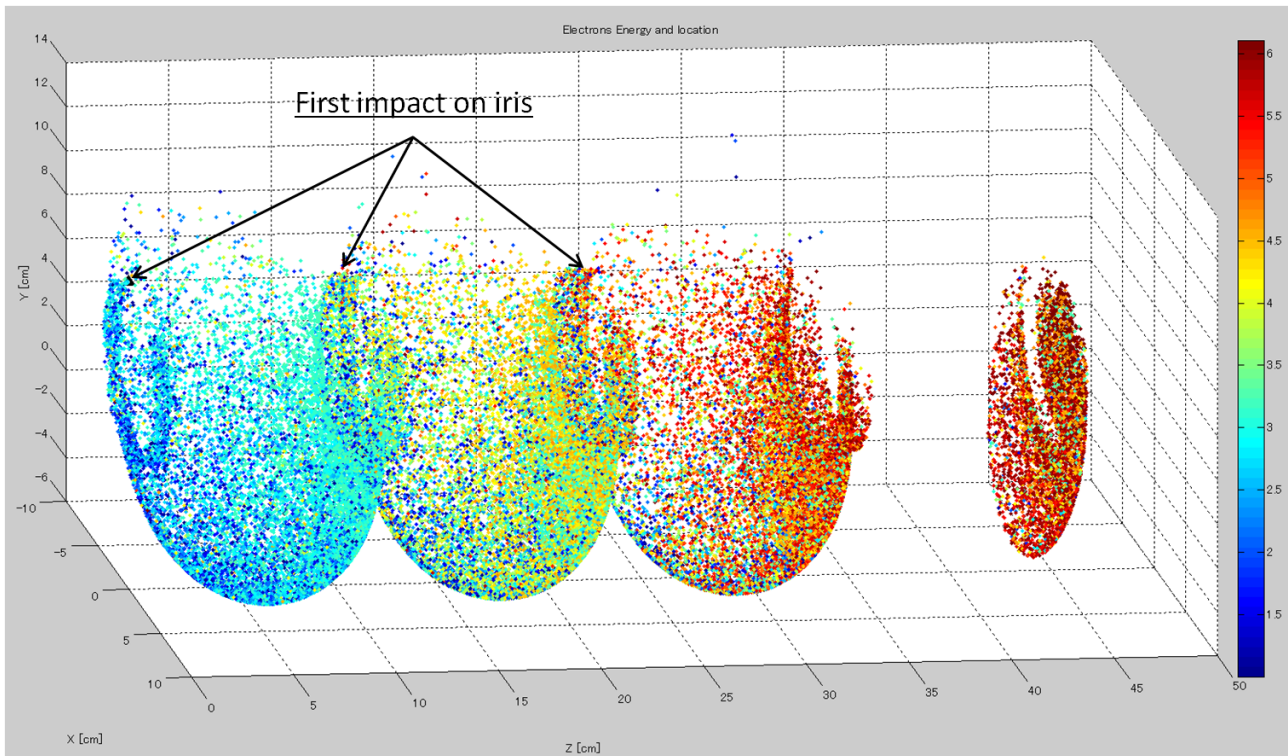


Figure 5. 46 EGS5 cavity model, shower electrons energy and location.

We can notice how the electron shower hit the opposite side of the cavity with respect of the iris that generates the shower. On the other hand, photons produce a shower that remains on the same side. In the next picture will be shown a front view of the cavity with electrons and photons impact location and energy, to be more specific and related to the vertical test, the emitter is located on the 150° meridian (the bottom part in the picture above), the sharp spot is produced by electron impact near the iris on 330° meridian, at the same meridian the electrons that hit the iris along their flight to the SBP are reflected producing a broad spot on the 150° meridian.

In the picture below it is possible to see the contour map for electrons impact locations, the y axis represents the meridian angle while the x axis is the distance along the cavity axis. The brighter region are hit by a higher number of electrons with respect to the darker one. The iris hit by electrons are located at 0° (360°) degree meridian.

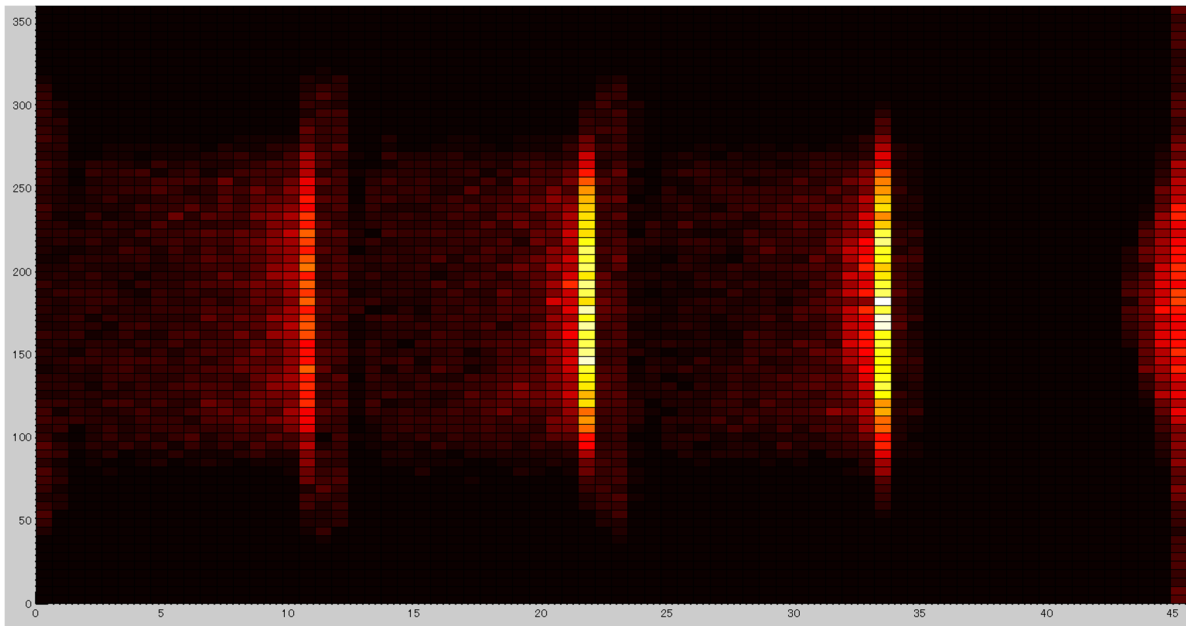


Figure 5. 47 Electrons impact, meridian and z coordinate location.

The pattern obtained with the EGS5 simulation is consistent with the one observed during the vertical test: the electrons hit a broad area, more intensely near the iris and less inside each cell.

Though the relative intensity is not yet normalized by using the transmission coefficient, the pattern represents a reasonable approximation of the vertical test observation.

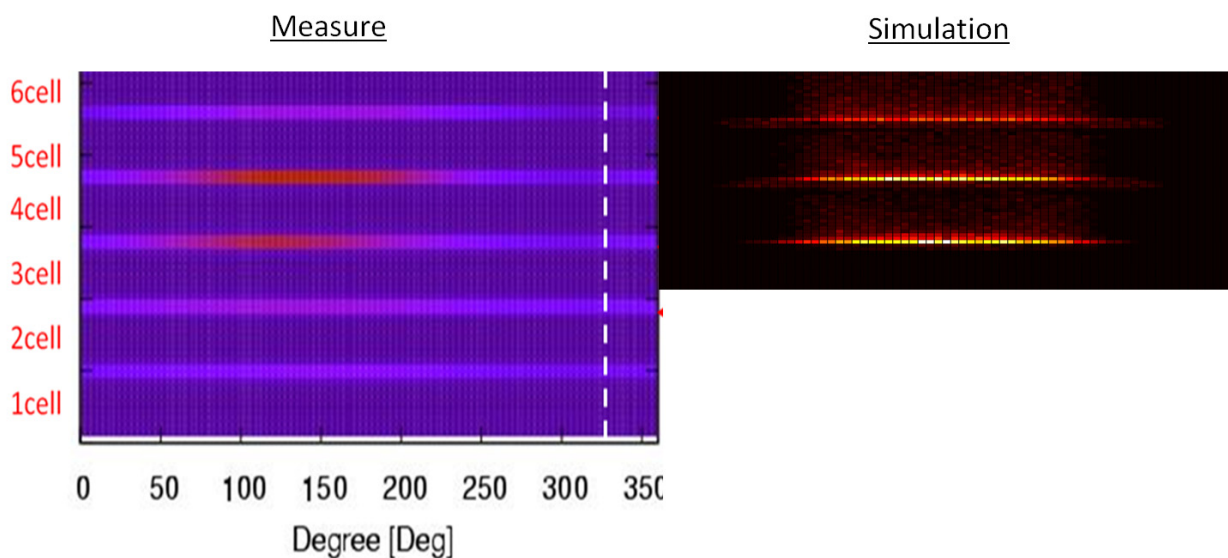


Figure 5. 48 Comparison between the observed broad peak during vertical test (left) and the simulation result (right)

5.2.7 4th and 5th vertical test π modes summary

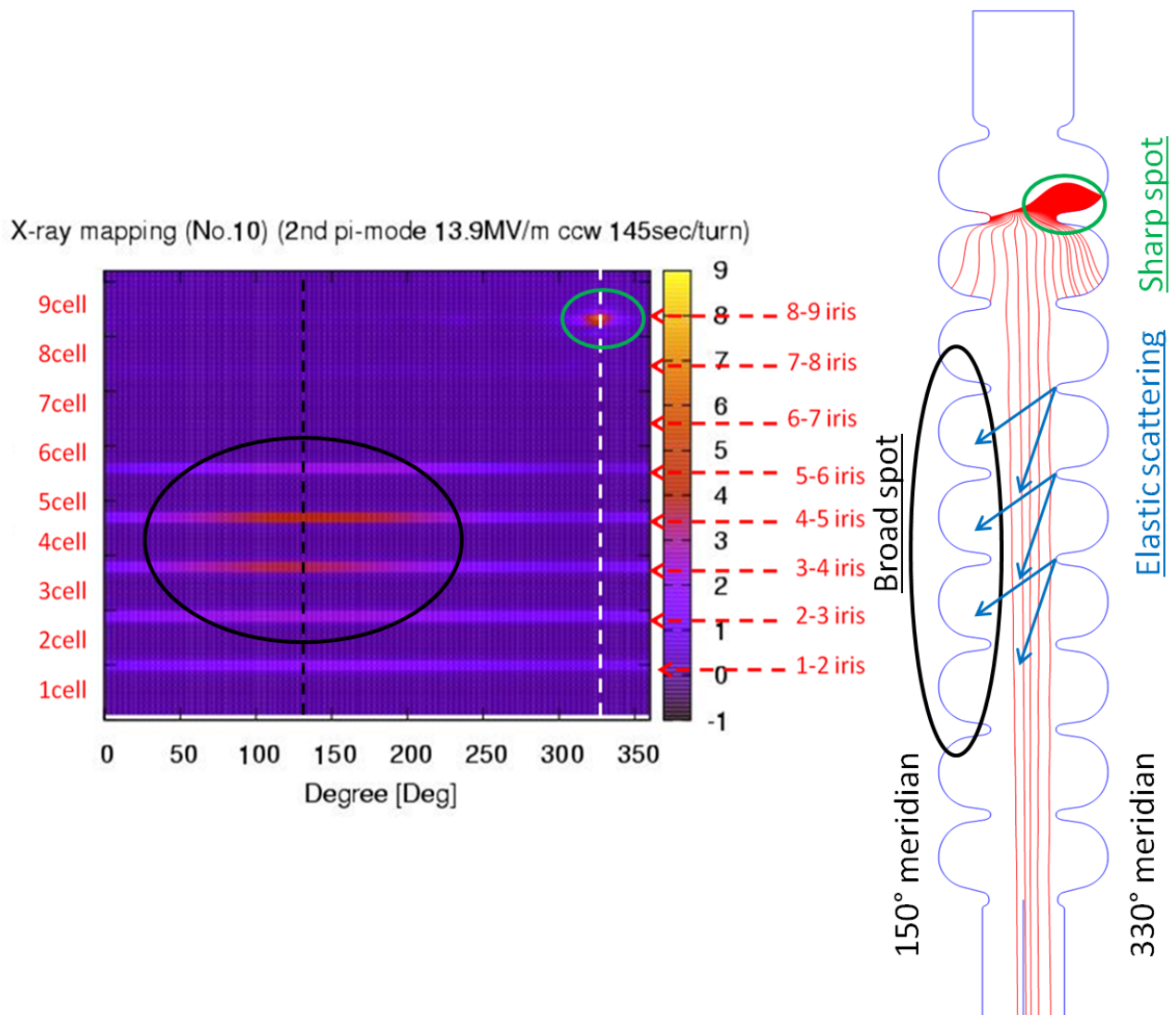


Figure 5. 49 Summary of the spot location in the measured data and simulation set up, emitter is located at 150° meridian.

At some extent the simulations and calculation are consistent with the observation done during the vertical test. Using the emitter location spotted during the optical inspection, it is possible to reproduce the radiation pattern and the power dissipation due to the field emission process, in the table 5.2 it is possible to compare the results.

Table 5. 3 Comparison between data derived from measure and simulation

| <i>Quantity</i> | <i>Calculated</i> | <i>From VT data</i> |
|----------------------------|-----------------------------------|-----------------------------------|
| β | 282±10% | 301 |
| S | $6 \times 10^{-16} \text{ m}^2$ | $9 \times 10^{-22} \text{ m}^2$ |
| Emitter location | 8-9 Iris±1mm | 8-9 Iris |
| Sharp spot | 8-9 Iris | 8-9 Iris |
| Broad spot | Below 6-7Iris | Below 6-7Iris |
| Radiation asymmetry | Higher radiation dose on SBP side | Higher radiation dose on SBP side |

Simulation combined with x-ray information can be a valuable asset to determine the emitter property and location due to the fact that usually it is not possible to “see” the emitter without using an electron microscope

In the next section, we will follow the same line of thinking to analyze another vertical test result, the test was performed on cavity #4, one of the cavities installed in the compact ERL cryomodule

5.3 Cavity #4 1st vertical test

The cavity surface treatment was carried out as the previous case through electropolishing, high pressure rinsing and baking, the main difference with the previous test set up were:

- Stiffener ring located on the iris
- Helium jacket cap welded on SBP and LBP
- PIN diodes located also on the Helium jacket cap

In the images below, it is possible to appreciate the differences between the two test set up

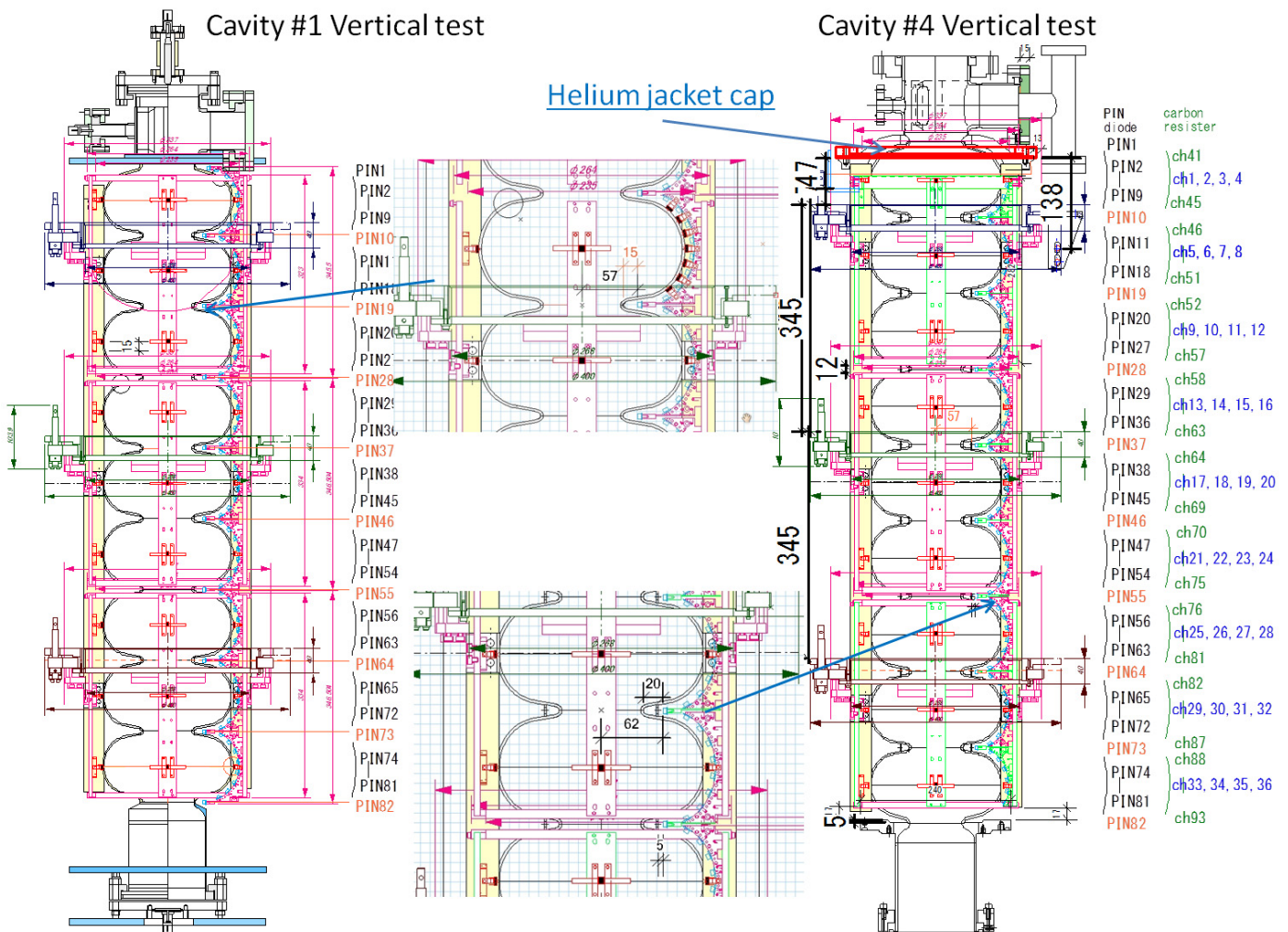


Figure 5. 50 Vertical test set up, cavity #1 (left),cavity #4 (right).

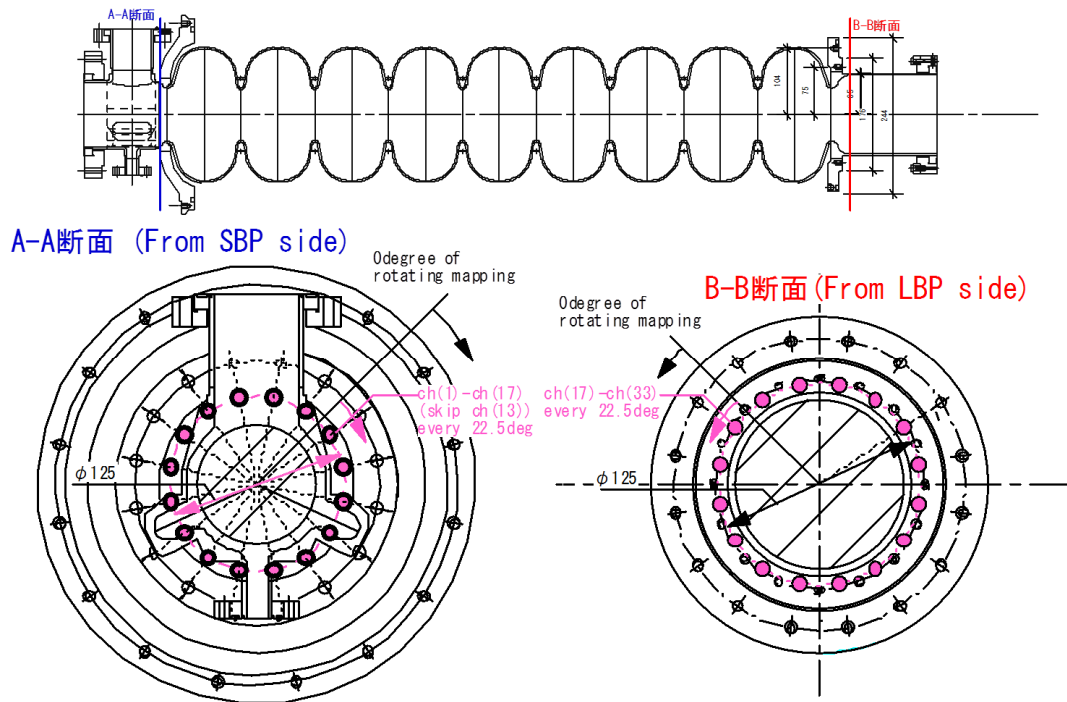


Figure 5. 51 PIN diodes installed on helium jacket cap, on SBP and LBP side.

5.3.1 Surface resistance

During the cavity cooling was performed the surface resistance measurement: at around 2K, the residual resistance was about 17nΩ

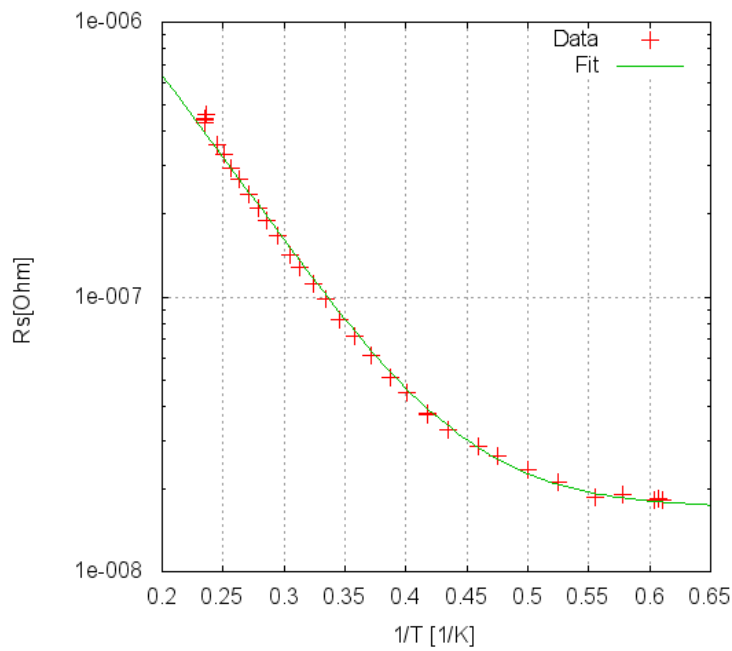


Figure 5. 52 Cavity #4 surface resistance, the residual resistance was 17nΩ.

5.3.2 Accelerating modes measures

The Q-E plot for the accelerating modes are shown below, the first was measured at the beginning of the test while the second one at the end, after $8/9\pi$ mode measure.

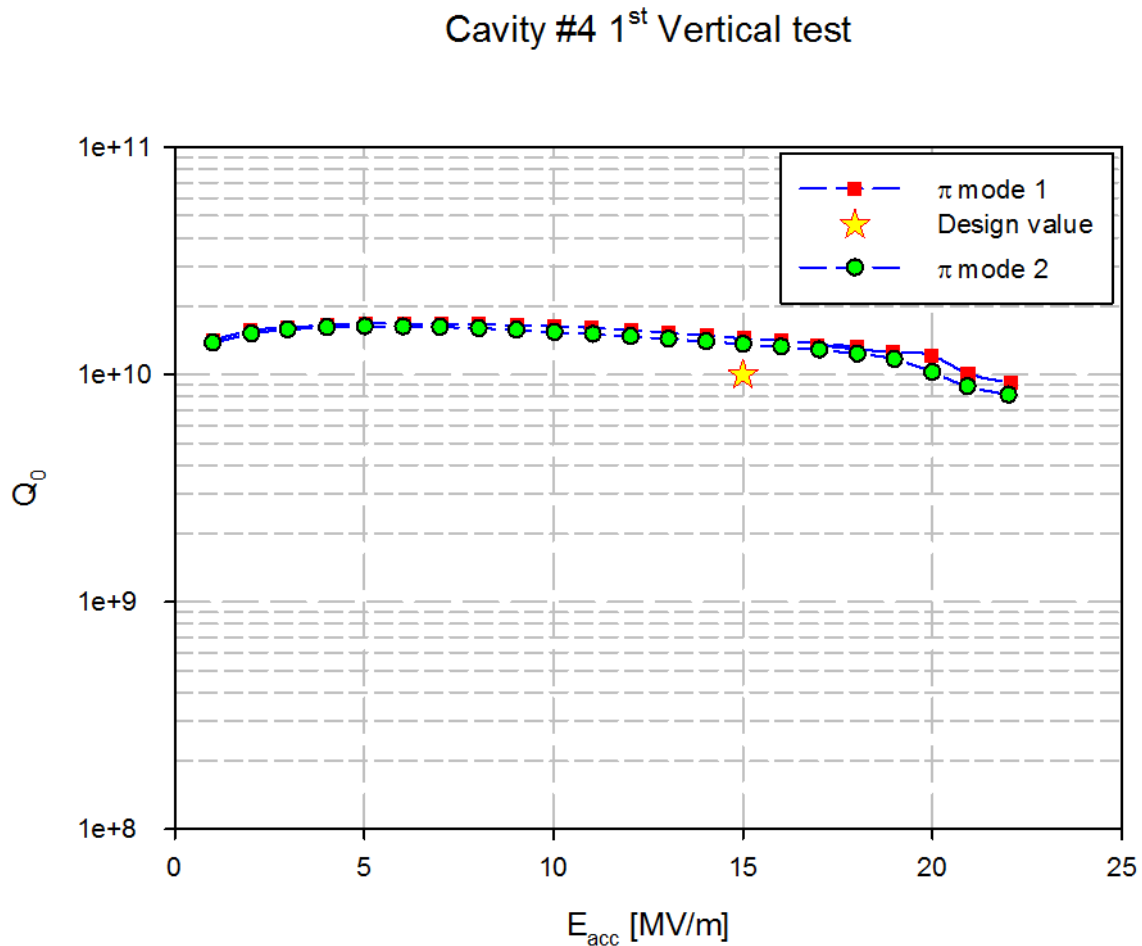


Figure 5. 53 Cavity #4 π modes Q-E plot.

The cavity performance exceeded the design requirement in both case searching 22MV/m, while the cavity was kept at 15MV the Q_0 value was respectively 1.44×10^{10} and 1.36×10^{10} about 40% higher than the design value. At 14MV/m radiation start to be detected on the LBP side as can be seen in the next paragraph, a clear field emission signal can be detected around 16MV/m in the x-ray mapping.

5.3.3 Power loss and field emission onset

We can extrapolate the power loss due to field emission, as we did before, by removing the power loss due to surface resistance from the total power dissipated at each accelerating field, the field emission onset is consistent with the other measure performed during the test (radiation monitor and x-ray mapping).

The next figure shows the power loss that can be accounted to field emission during accelerating mode.

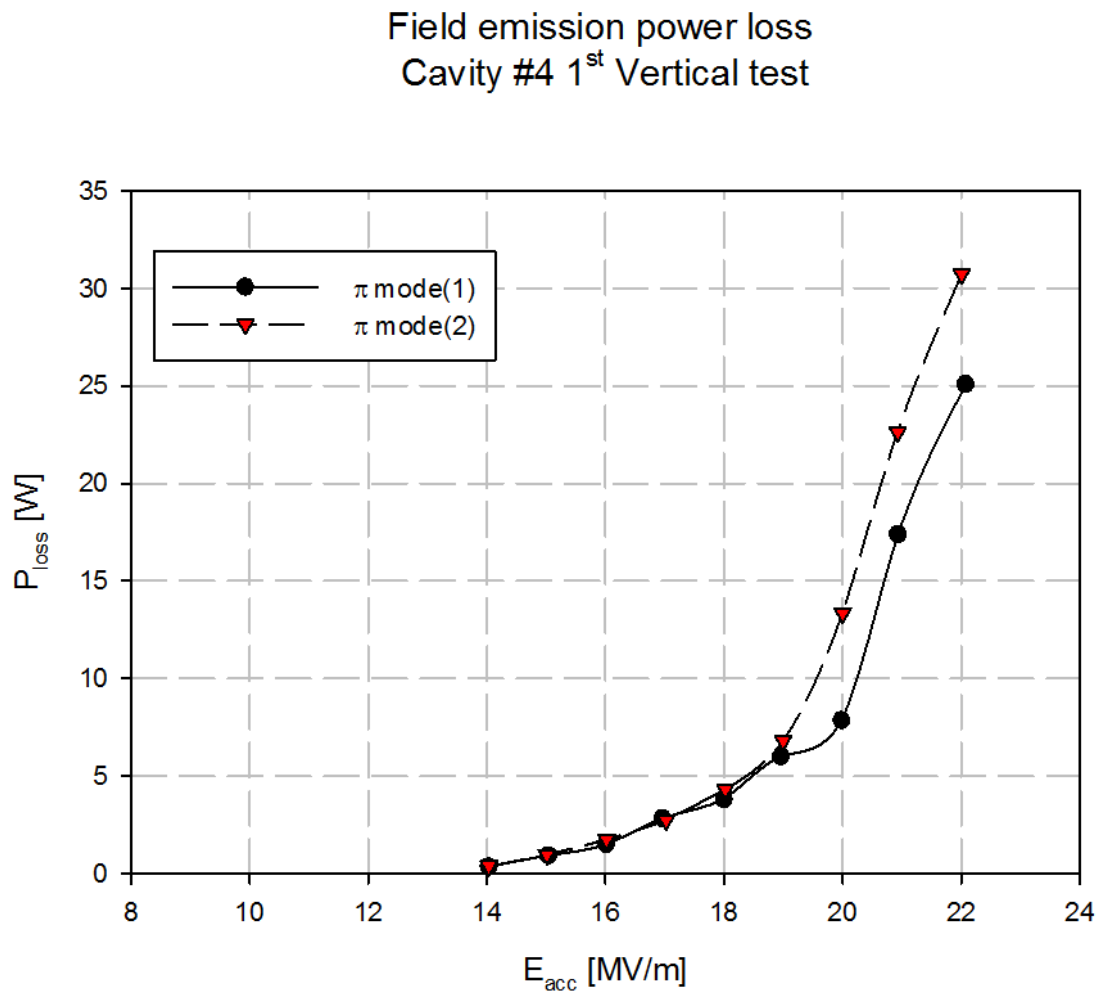


Figure 5. 54 Cavity #4 π modes field emission power loss.

The power loss is about 0.3W at 14MV//m and increase to about 1W at 15MV/m in both cases.

Radiation dose 1st Vertical test π mode 2

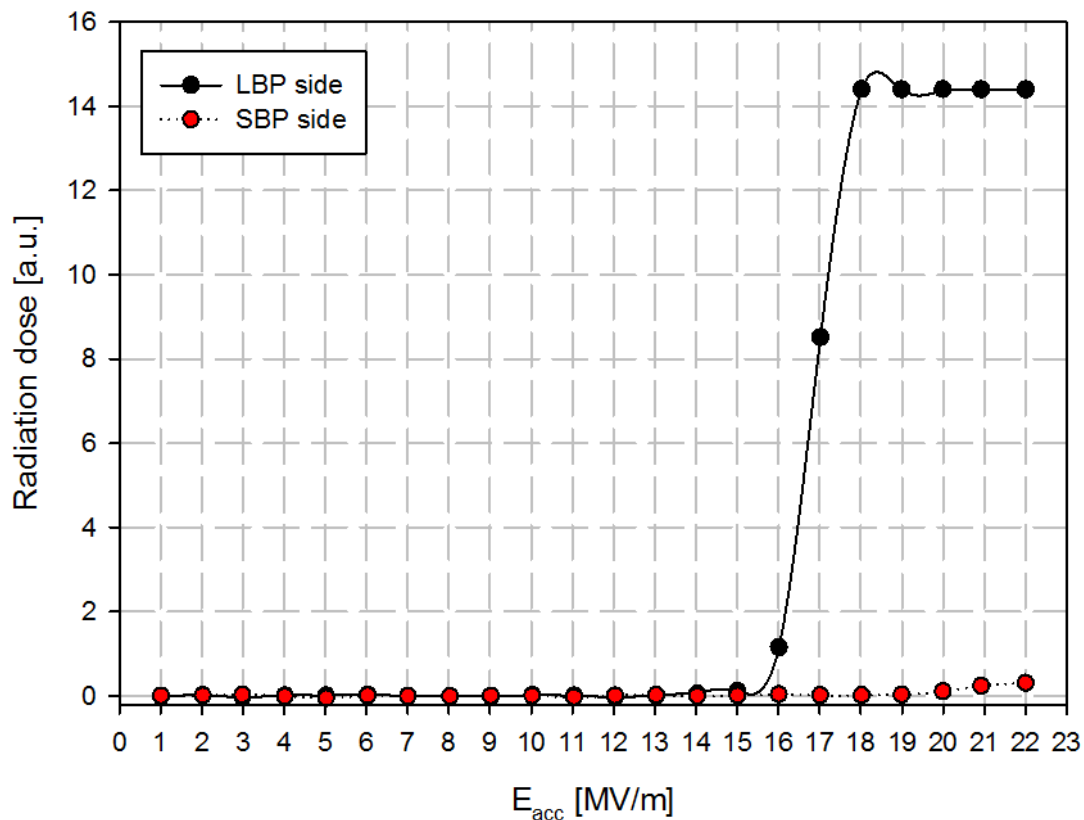


Figure 5.55 Cavity #4 π modes field emission power loss.

A radiation asymmetry is clearly visible between the LBP side and SBP side: this information tells us that the emitter is located on the iris side where its trajectories can reach only one part of the cavity, that is its distance (in S coordinate) shall be less than 5mm.

During the test, different x-ray maps were taken showing a good agreement with the field emission onset revealed by power loss and radiation dose, in the picture below are shown different x-ray mapping taken from 15MV/m (no signal is detected) up to 22MV/m. The x-ray pattern remains stable since 16MV/m showing the same spot at all accelerating fields, only the signal amplitude changes due to the field emission current increase.

Field emission on-set x-ray mapping

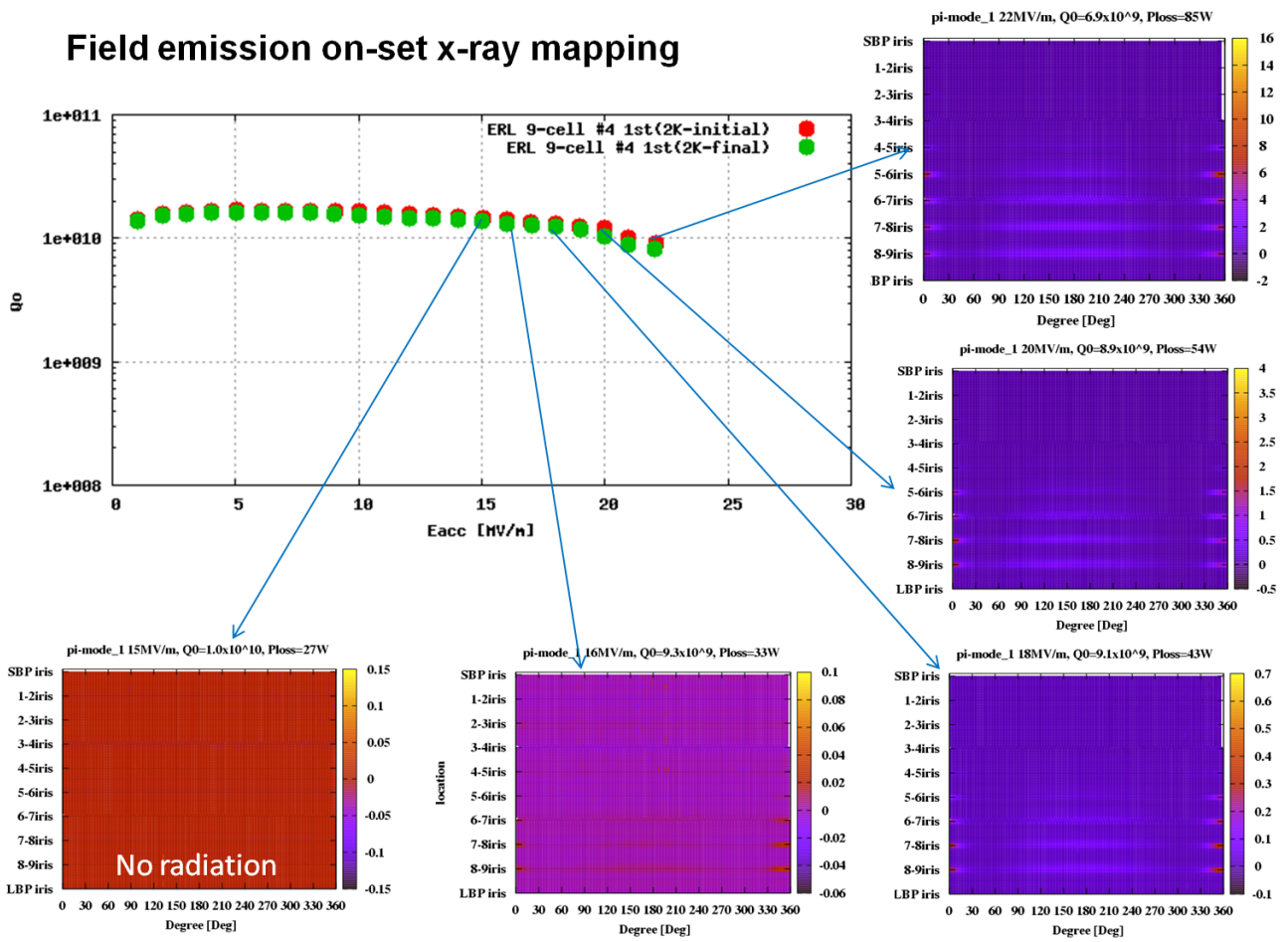


Figure 5. 56 Cavity #4 π mode x-ray mapping from 15MV/m to 22MV/m, the field emission signal is visible from 16MV/m, the spots location remain the same.

5.3.4 Enhancing factor from data

As we did in the previous data set, we can extrapolate the emitters parameters from the power loss data, the obtained enhancing factor is displayed in the next figure.

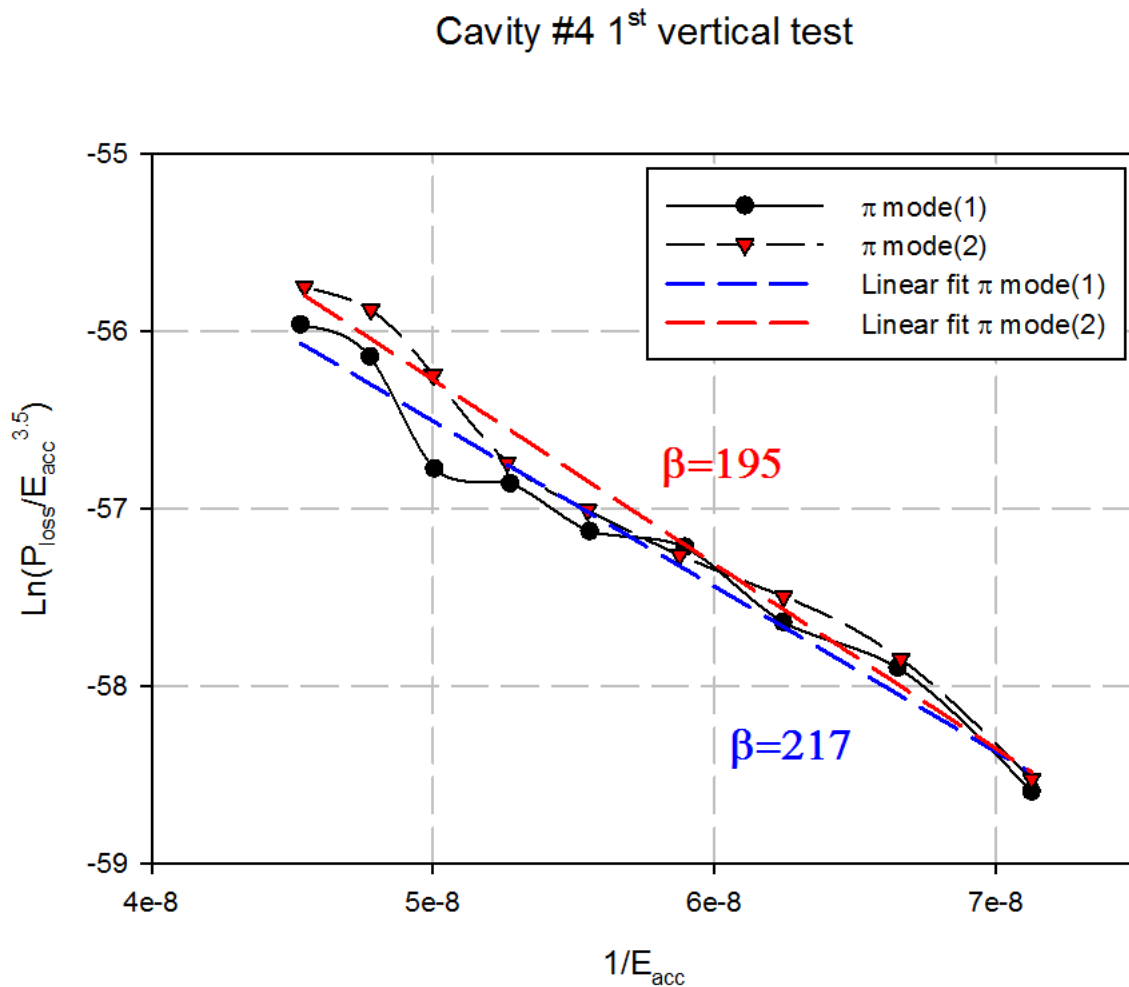


Figure 5. 57 Cavity #4 π modes extrapolated β .

For the first π mode the $\beta=217$ and the emitter area is $5 \times 10^{-23} \text{ m}^2$ while for the second π mode $\beta=195$ and the emitter area is $1 \times 10^{-22} \text{ m}^2$, the enhancing factor fluctuation is within 10% while the area varies about one order of magnitude. We will use the β values as a starting point to find the best fitting parameters in terms of area and location in order to minimize the difference between the dissipated power calculated through the simulation and the one derived from vertical test data.

The first assumption derived from the vertical test data, is that the emitter can be located between the 1st and 2nd cell, from the previous experience we know that an emitter produces a small signal near the iris opposite to its location. From the on-line data this kind of signal can be detected inside the 1st cell in the proximity of the iris connecting the 2nd cell.

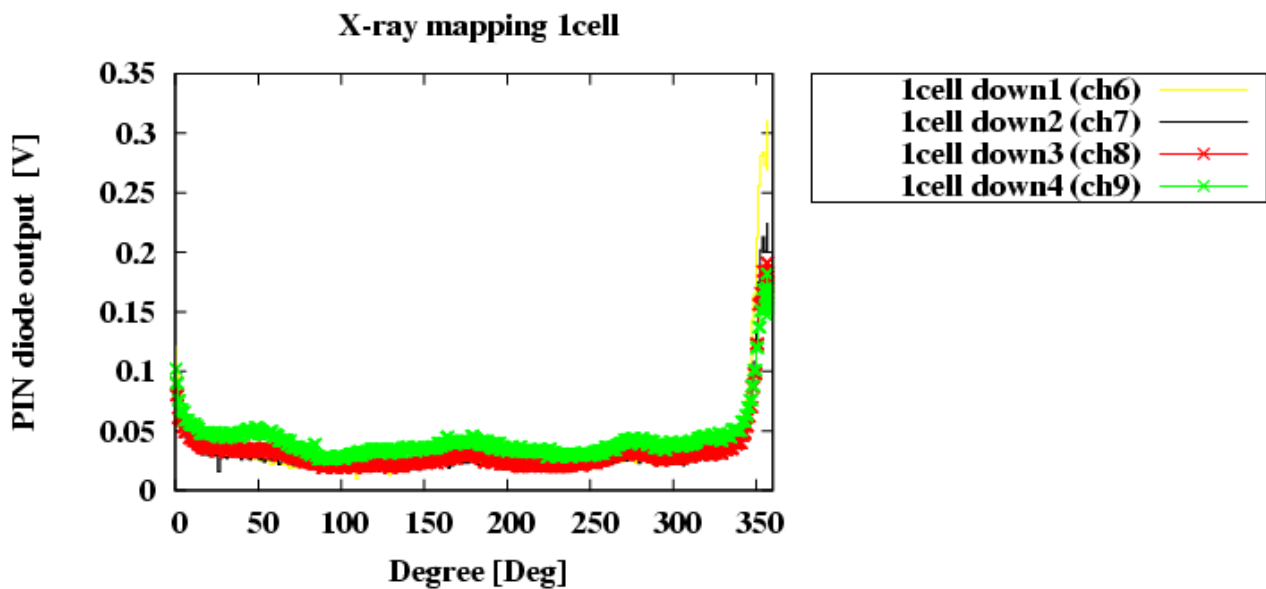


Figure 5. 58 Cavity #4 π modes at 22MV/m, signal from PIN diodes in the 1st cell, the graph represent the PIN voltage against the meridian angle.

The sharp spot is located at 360° meridian while the broad one is, as expected, at 180°, the first trial position is in a region where the electron trajectories can reach only the LBP side and not the SBP, like shown in the picture below.

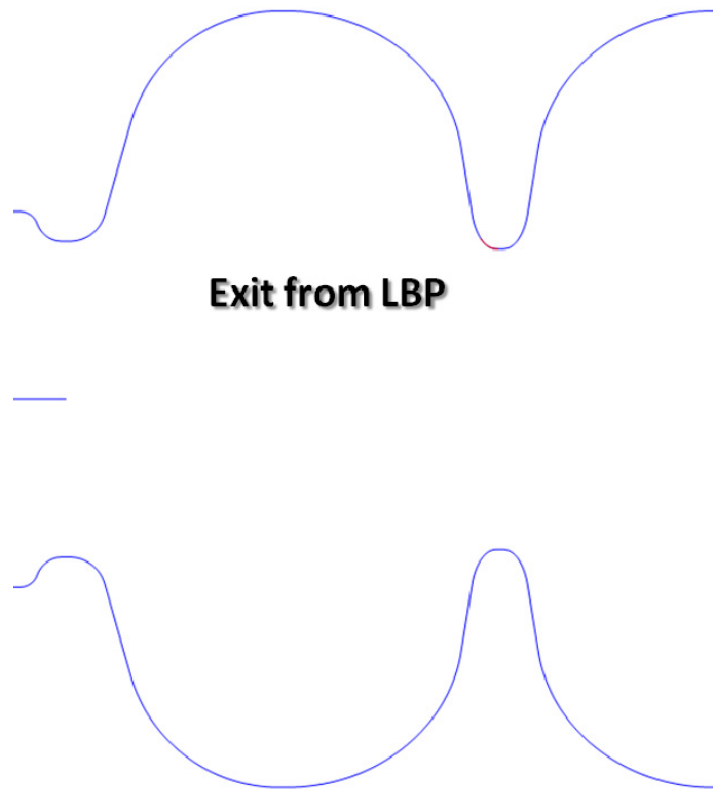


Figure 5. 59 Region to test the emitter location, from this area the electron trajectories are towards the LBP side (right side of the picture)

The total length of this region is about 5mm, but only few emitters can match both the x-ray map and the dissipated power as observed during the vertical test. In the next steps we will try to analyze this region in order to determine which emitter (or emitters) are more likely responsible for the signal detected during the test.

Another precious information to discriminate among different emitters is the signal amplitude detected on different iris, as can be seen in the next picture, it reaches a peak on the iris between 5th and 6th cell, this could be helpful in order to define the boundary conditions within looking for the emitter.

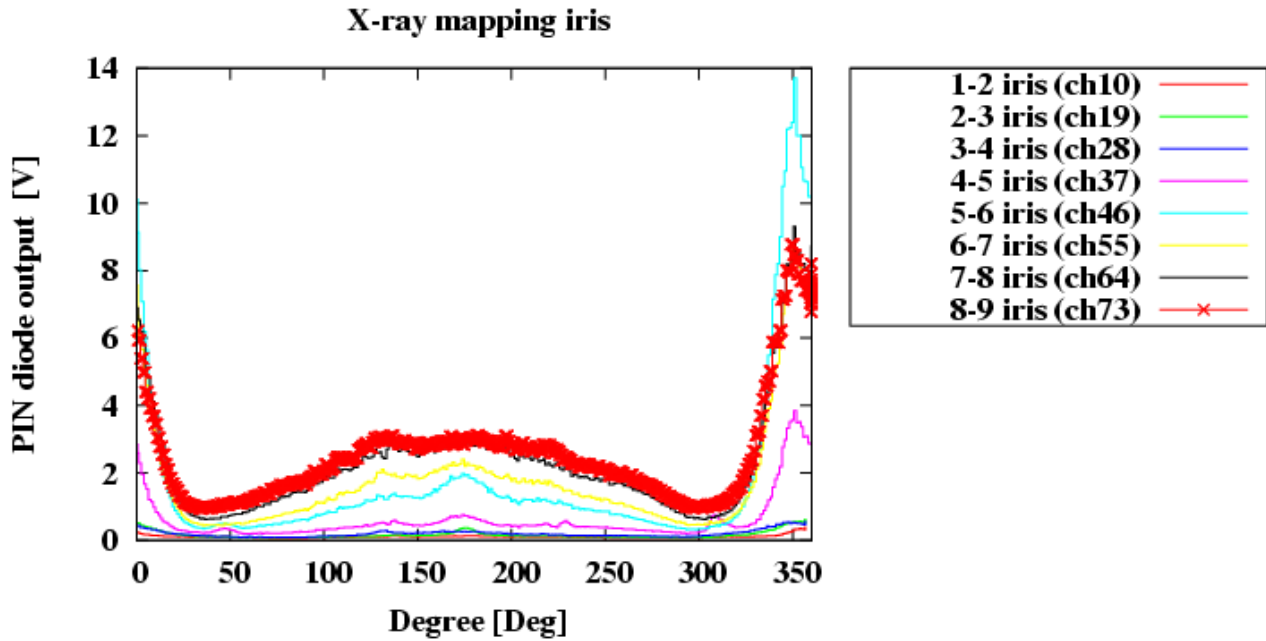


Figure 5. 60 PIN diode voltage against meridian angle, the PIN diodes are located in front of iris

Few emitters can produce trajectories consistent with the picture above, assuming that the signal detected by PIN diodes is proportional to the transmitted power through the Niobium surface is possible to list them through their distance along the cavity surface.

Table 5. 4 *Emitters location used in the simulation*

| Emitter # | S coordinate |
|-----------|----------------------------|
| | Distance from iris [mm] |
| 47 | 4.5 |
| 48 | 4 |
| 49 | 3.5 |
| 50 | 3 |
| 51 | 2.5 |
| 52 | 2 |

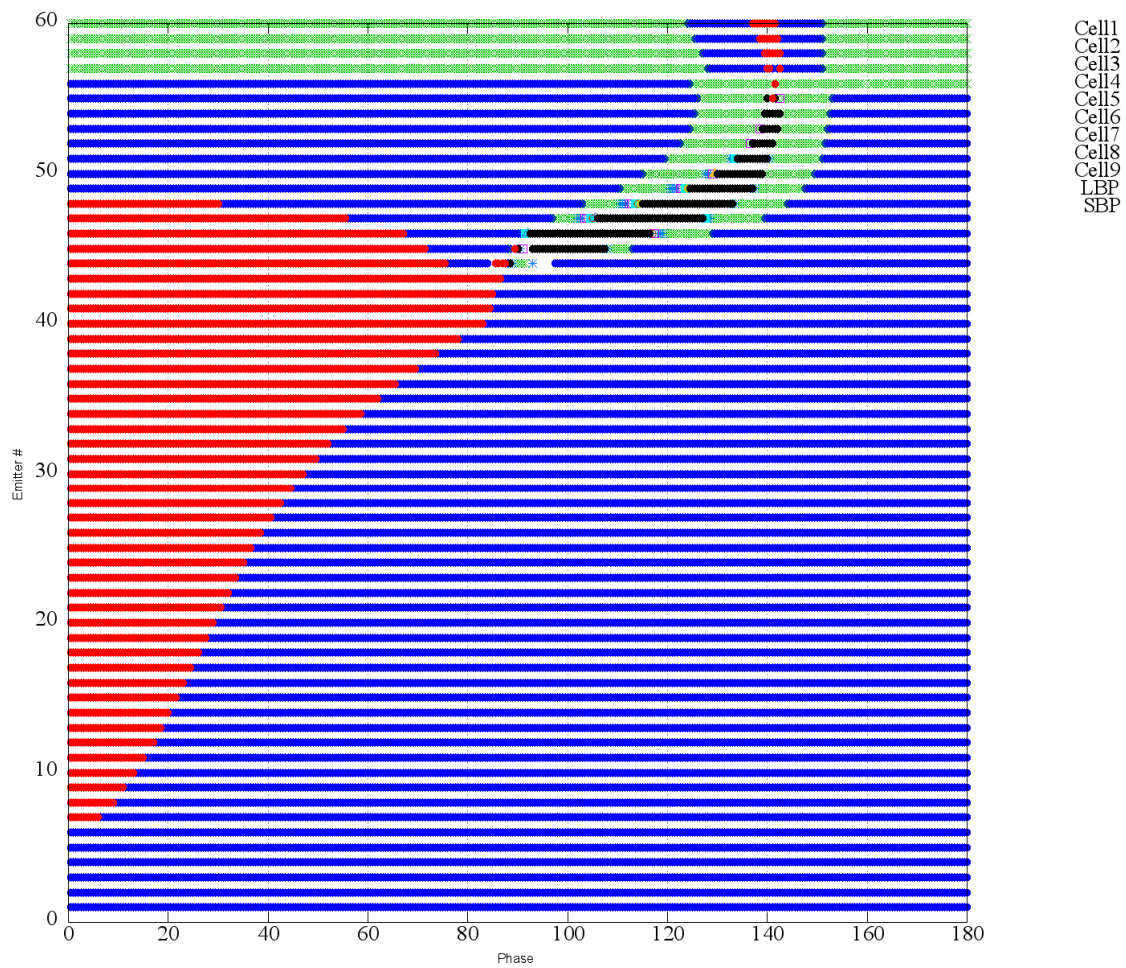


Figure 5. 61 Landing location from emitters located on 1st-2nd cell iris, on the Y axis is represented the emitter number, the X axis represent the RF emission phase, the cavity is at 22MV/m π mode.

Few of them are compatible with a strong emission towards the LBP (black dots) and small or no radiation towards SBP (red dots), the list of them are presented in the table 5.3.

With the emitter list, we can scan the β and emitter area parameter in order to find the best couple to fit the dissipated power curve obtained during the vertical test.

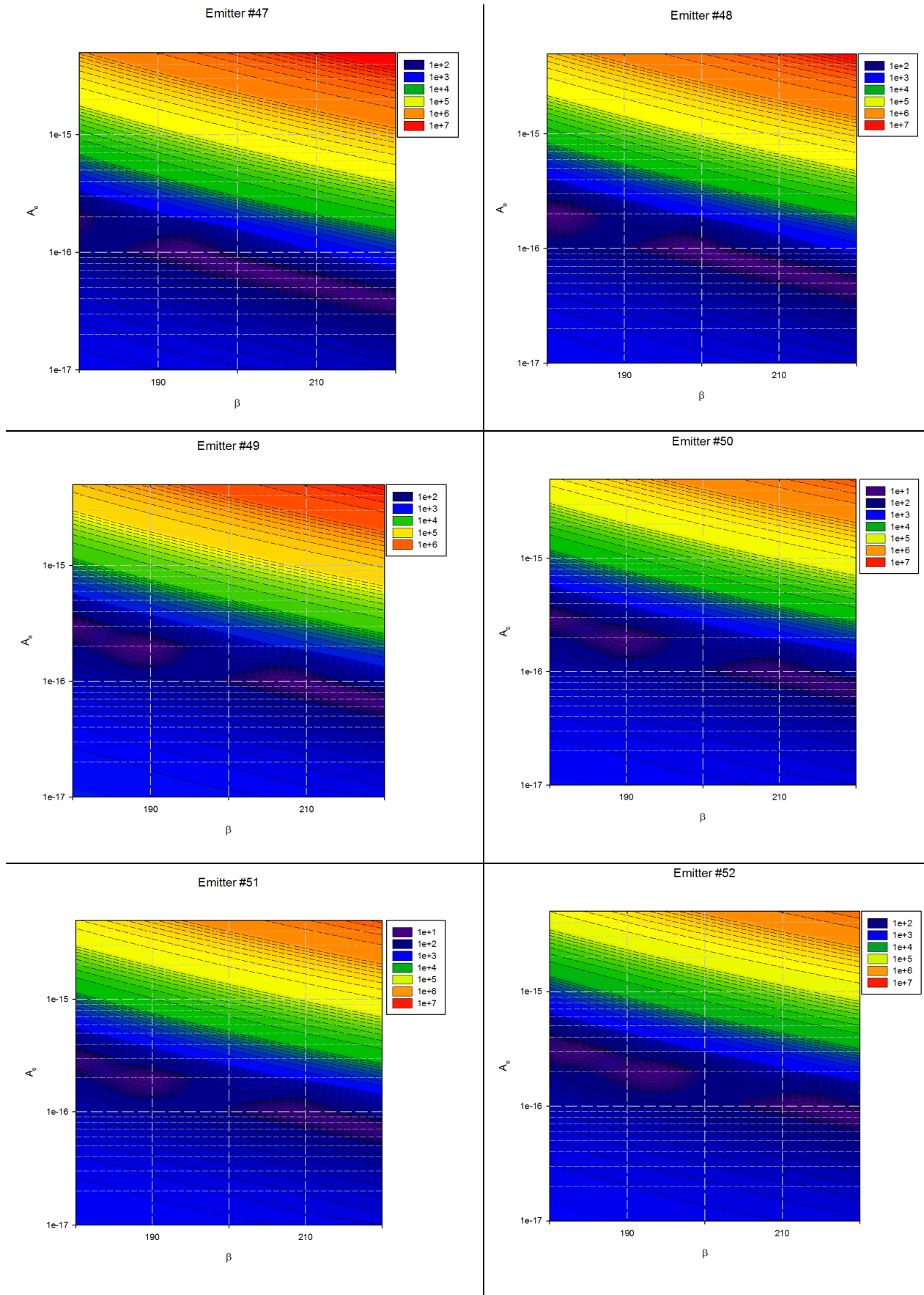


Figure 5. $62 \Delta^2$ calculated for different emitter locations, different emitter area and different β .

The pictures above show the calculated squared difference between the dissipated power calculated and measured during the vertical test, the interval within the enhancing factor is scanned is $200\pm 10\%$ as extrapolated from the slope of the power loss data. All the listed emitter present a local minimum in the squared power difference contour plot (Δ^2), for this case we are not able to narrow the emitter candidates number through this analysis, up to now the emitter region is 2.5mm long, all the emitters inside this region are compatible with the extrapolated β and the dissipated power.

We need to do a step forward to refine the search. First we can compare the x-ray pattern along the cavity for π mode and $8/9\pi$ mode in order to understand which emitter more probably can produce the same map. Then, it is possible to use also the information gathered from the PIN diodes installed around the LBP and SBP.

Next three groups of pictures will be presented, figure 5.63 shows the x-ray map at 22MV/m (π mode), figure 5.64 shows the map at 23.5MV/m ($8/9\pi$ mode) and figure 5.65 shows the radiation pattern detected by diodes installed on the LBP and SBP during π mode and $8/9\pi$ mode operation.

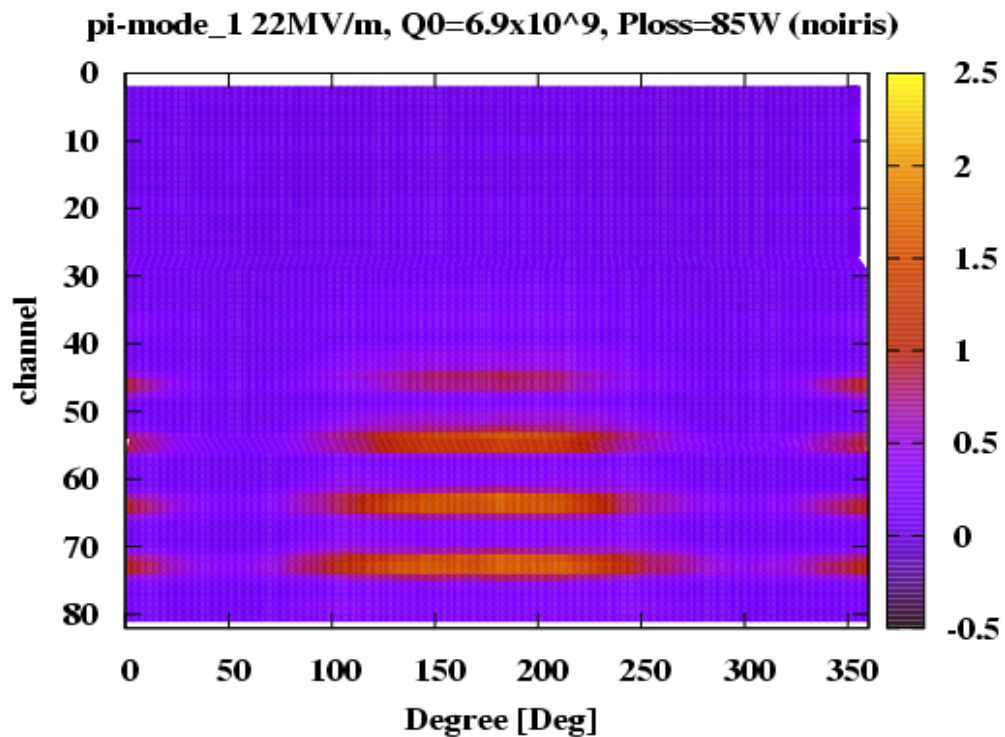
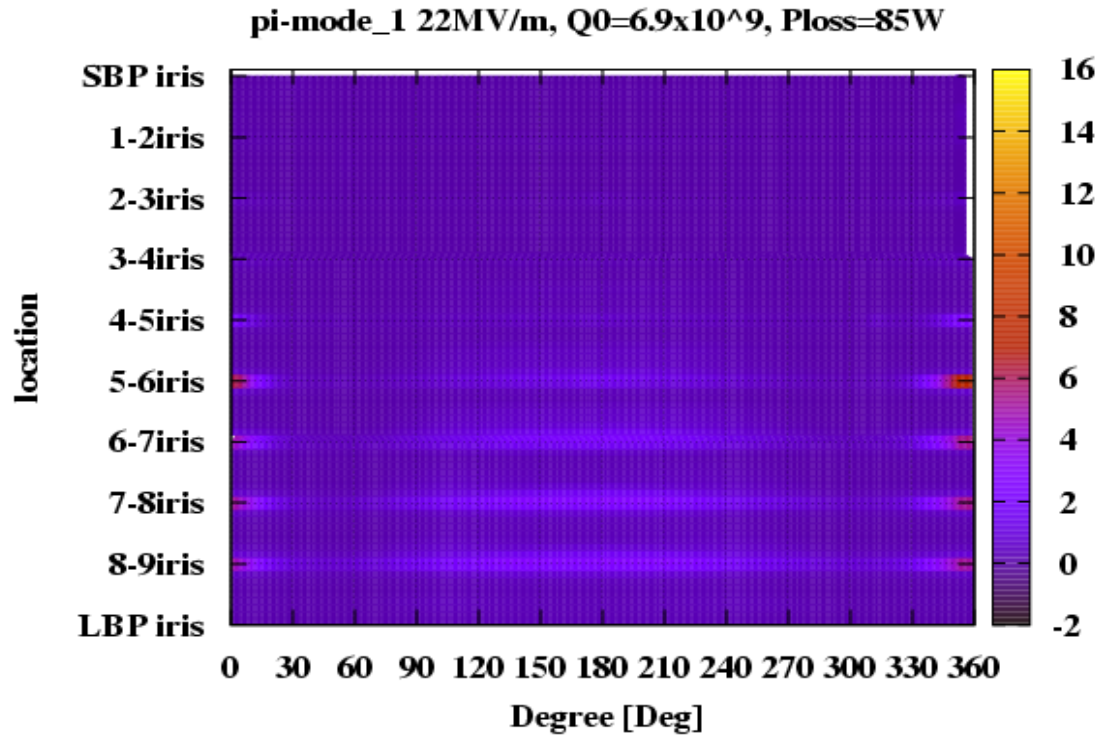


Figure 5. 63 Radiation map for π mode at 22MV/m, with iris signal (top) and without iris signal (bottom).

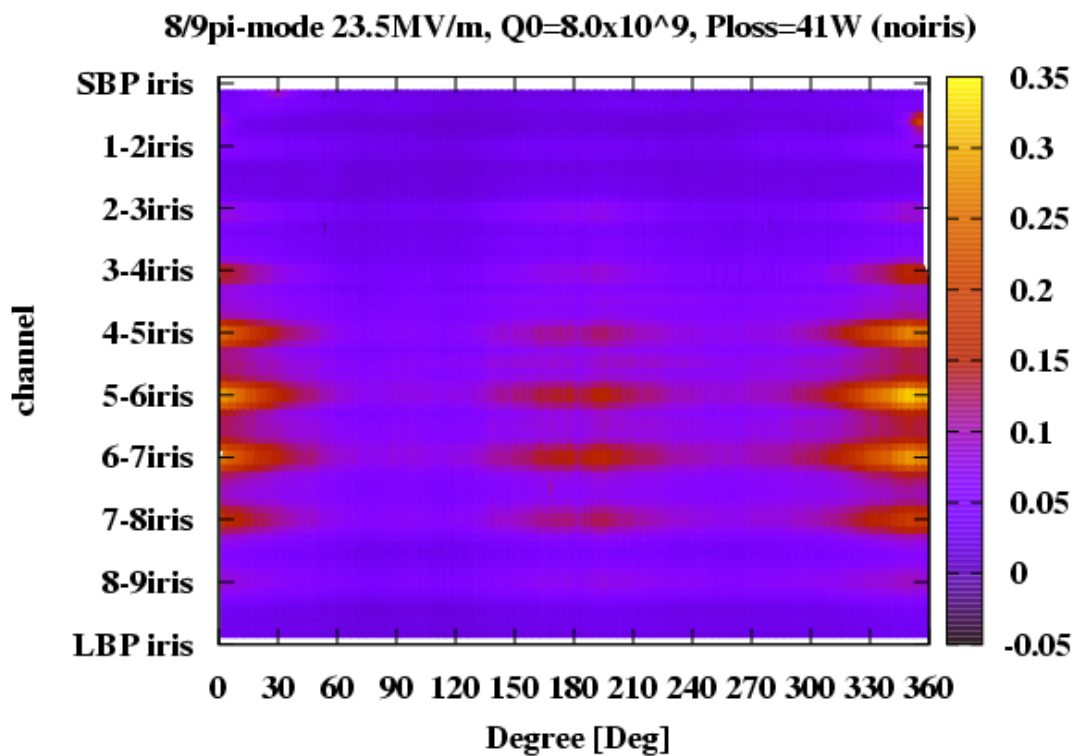
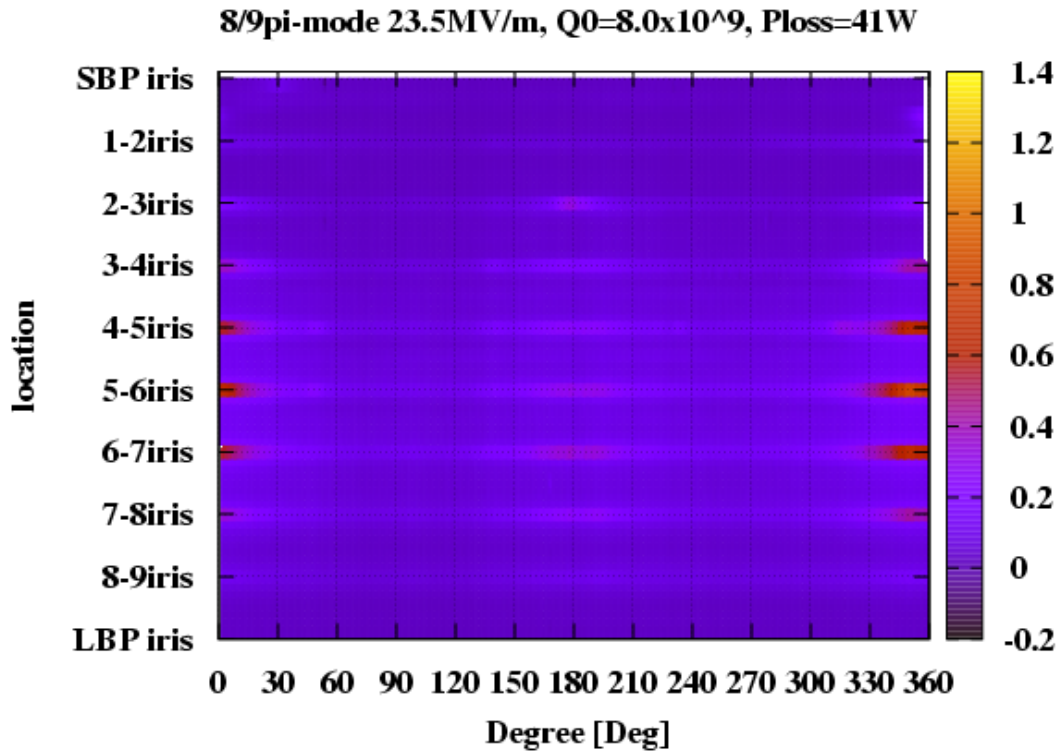


Figure 5. 64 Radiation map for $8/9\pi$ mode at 23.5MV/m, with iris signal (top) and without iris signal (bottom).

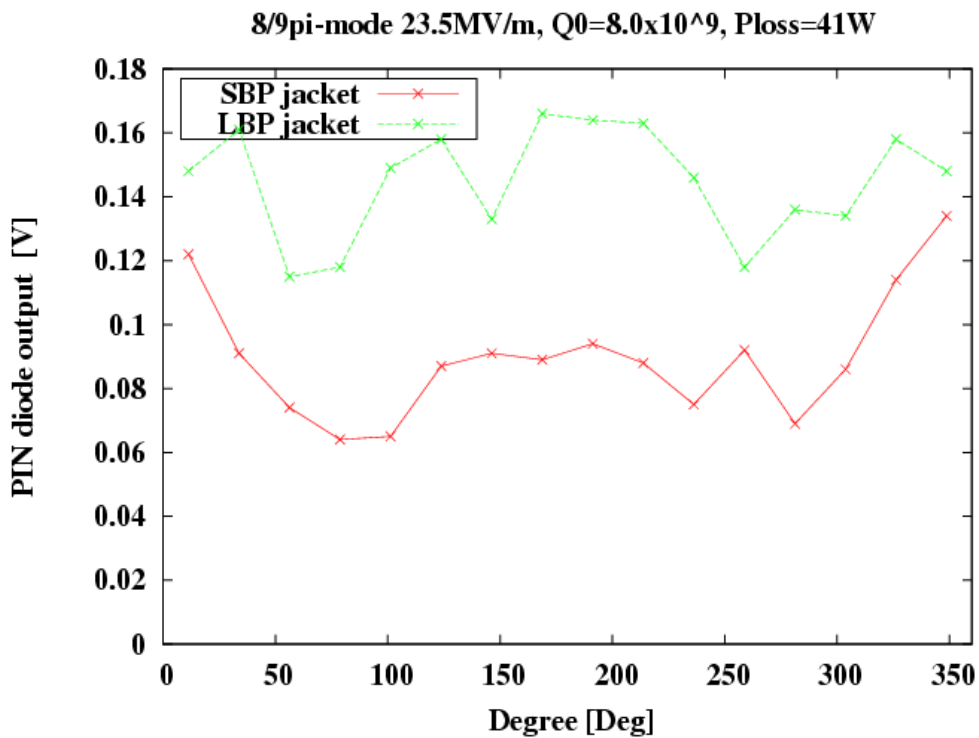
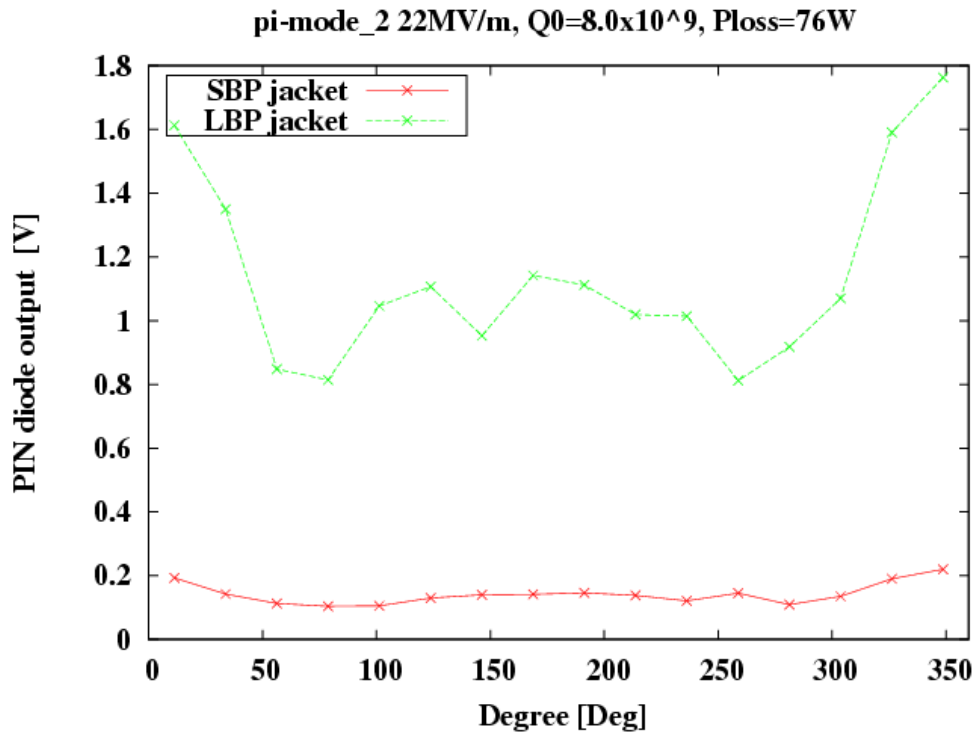


Figure 5. 65 PIN diode signal from LBP and SBP ring for π mode at 22MV/m (top) and $8/9\pi$ mode at 23.5MV/m (bottom).

The radiation patterns shows some peculiar aspect that can be summarized as follow:

π mode at 22MV/m

- a. Low amplitude spot inside 1st cell at 360° meridian
- b. Broad spots along 180° meridian starting from iris between 5th and 6th cell
- c. Narrow spots along 360° meridian from iris between 5th and 6th cell
- d. Strong radiation on LBP side compared to SBP side
- e. Broad spot on 180° meridian (LBP diodes)
- f. Narrow spot on 360° meridian (LBP diodes)

$8/9\pi$ mode at 23.5MV/m

- g. Sharp spot inside 1st cell at 360° meridian
- h. Broad spots along 180° meridian with increasing intensity from iris between 3rd and 4th cell
a maximum around 5th -6th iris and then decreasing
- i. Narrow spots along 360° meridian with increasing intensity from iris between 3rd and 4th cell
a maximum around 5th -6th iris and then decreasing
- j. Broad spot on 180° meridian (LBP and SBP diodes)
- k. Narrow spot on 360° meridian (LBP diodes and SBP diodes)

Considering what we learned from the previous case, it is possible to assume that the broad peak is produced by reflected electrons while the narrow ones are generated by photon shower. To make this possible, it is necessary that the incident electrons hit the cavity surface with an angle at least less than 10°.

It is now possible to calculate for each emitter the transmitted power through the cavity surface, this should reproduce the radiation pattern observed on 360° meridian. To account for the 180° meridian, it is necessary to calculate the electrons incident angle.

In order to find the most probable emitter, it is necessary to find which emitter is consistent with most of the properties listed above, higher the number of matched properties higher the probability that the emitter is the correct one.

In the next sets of pictures the transmitted power calculation on 360° meridian, assuming emitters located between 1st and 2nd cell with $\beta=200$, Area= 2×10^{-16} m² will be shown

5.3.5 π mode at 22MV/m transmitted power

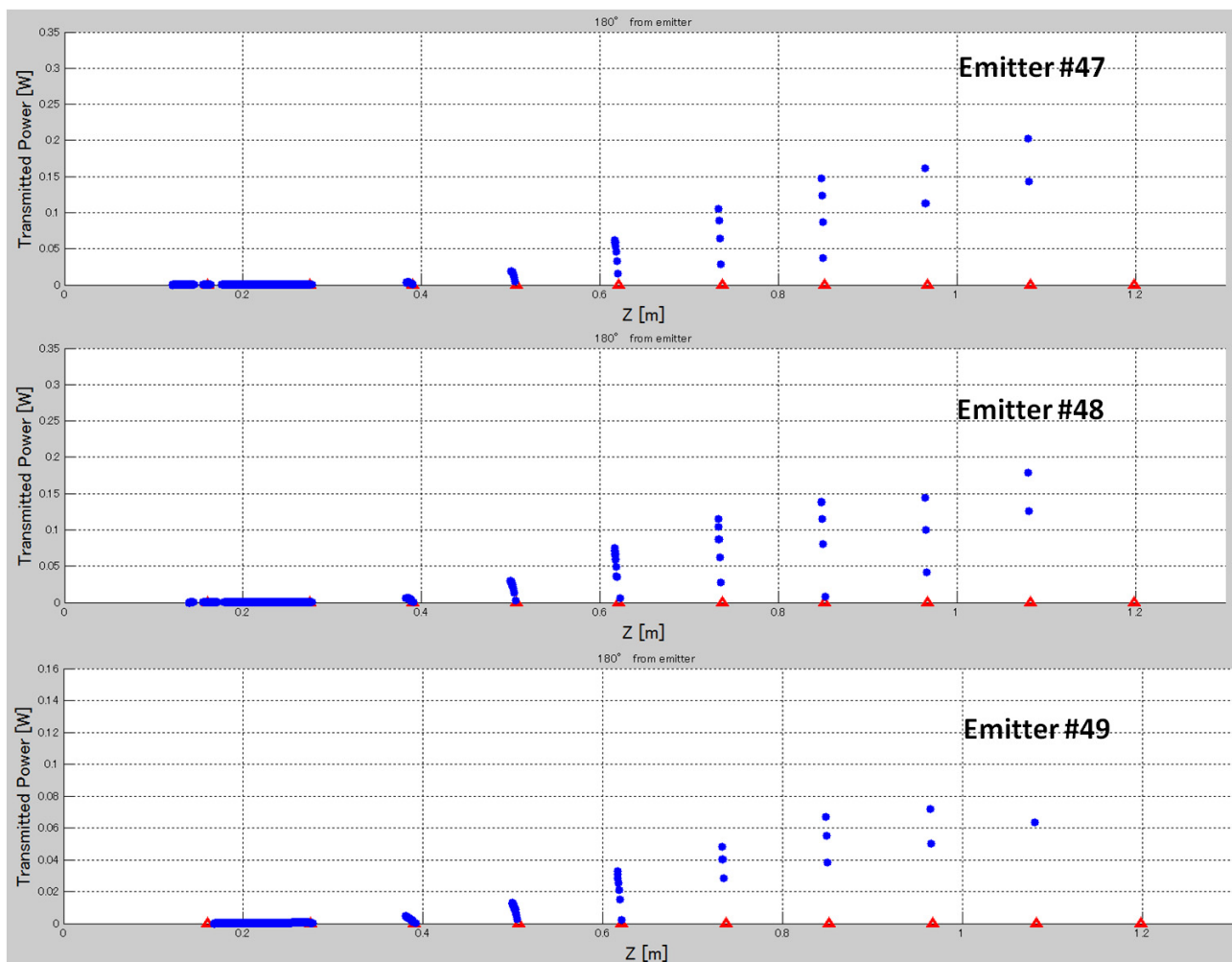


Figure 5. 66 Transmitted power along 360° meridian for π mode at 22MV/m for emitters 47, 48 and 49.

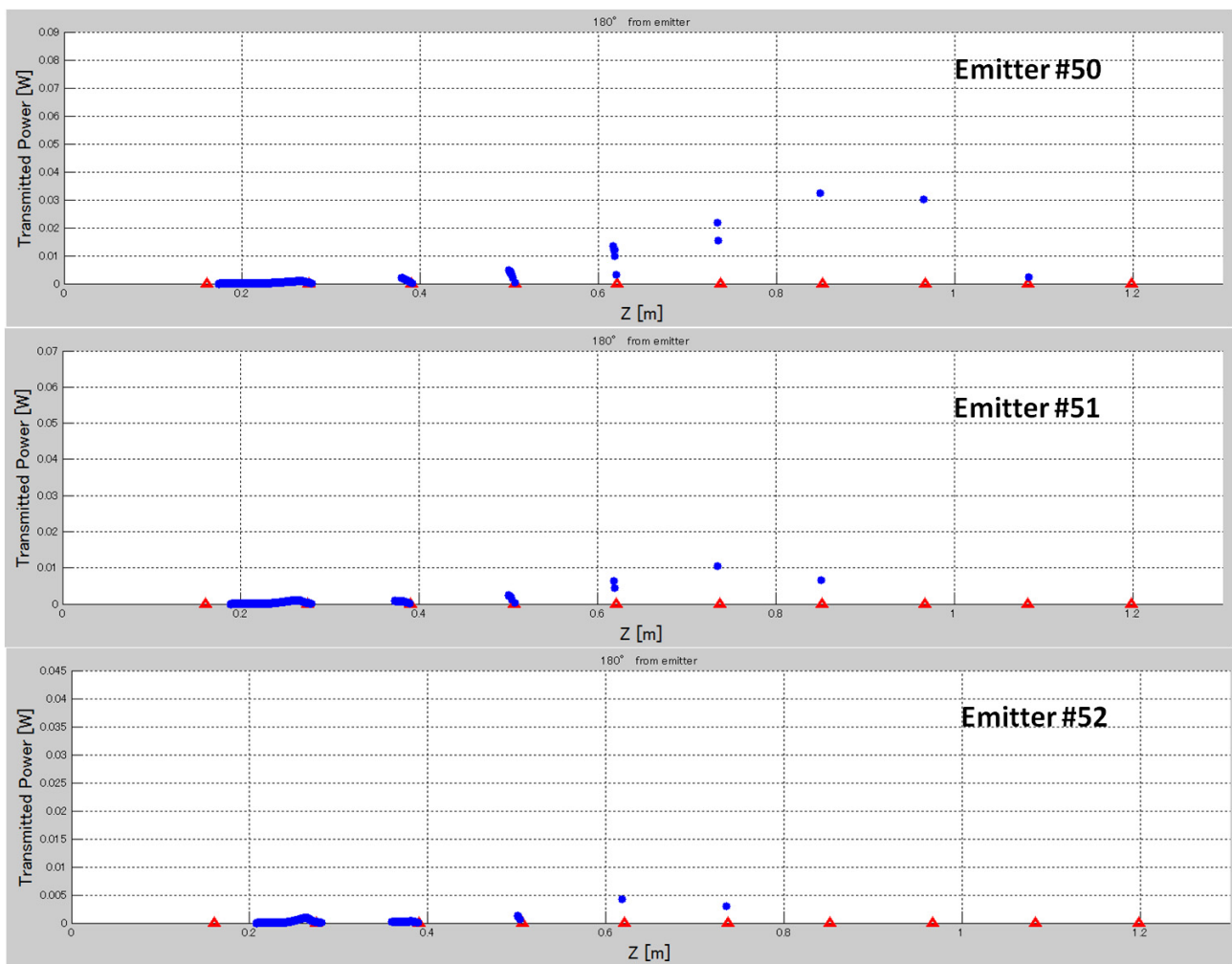


Figure 5. 67 Transmitted power along 360° meridian for π mode at 22MV/m for emitters 50, 51 and 52.

5.3.6 $8/9\pi$ mode at 23.5MV/m transmitted power

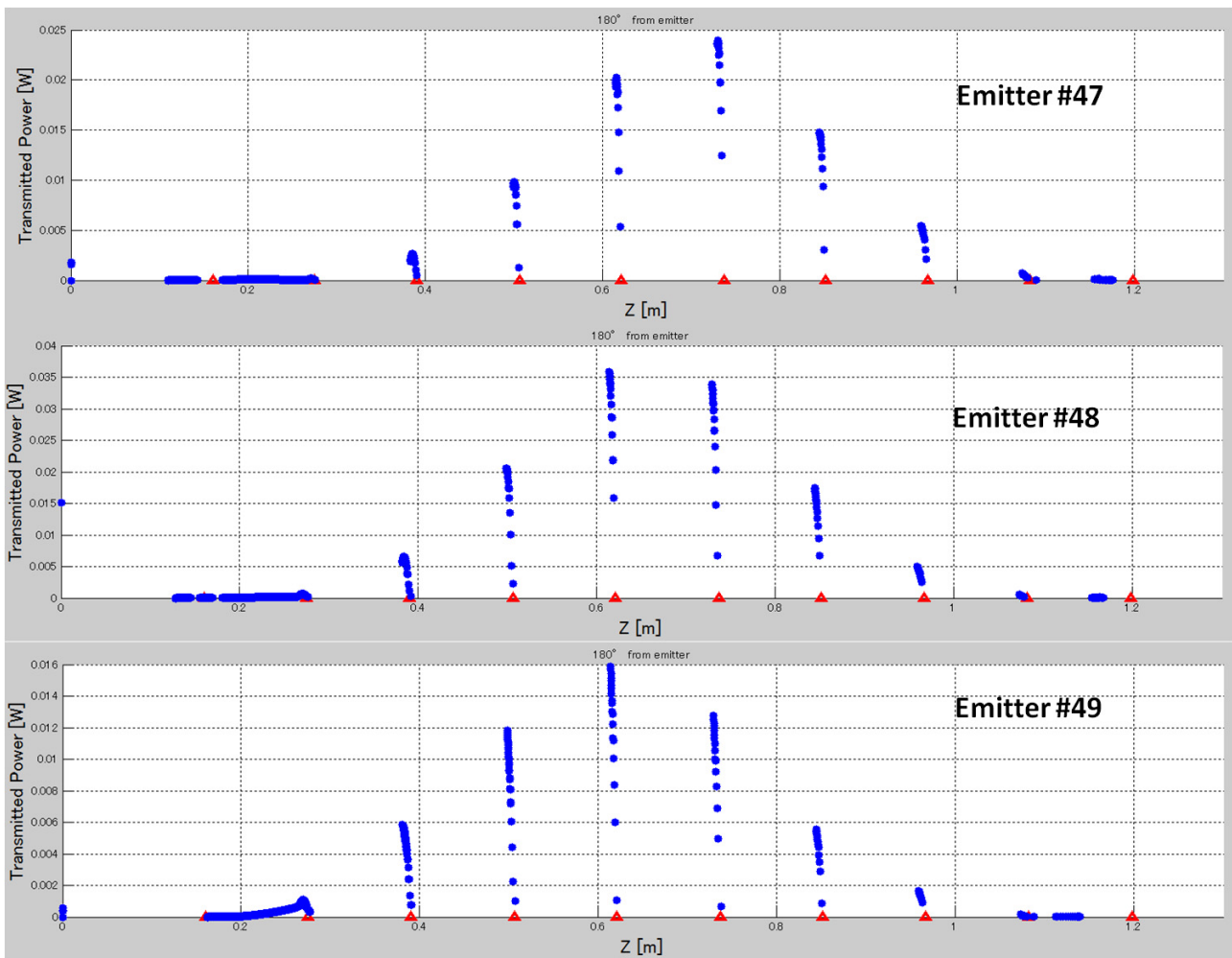


Figure 5. 68 Transmitted power along 360° meridian for $8/9\pi$ mode at 23.5MV/m for emitters 47, 48 and 49.

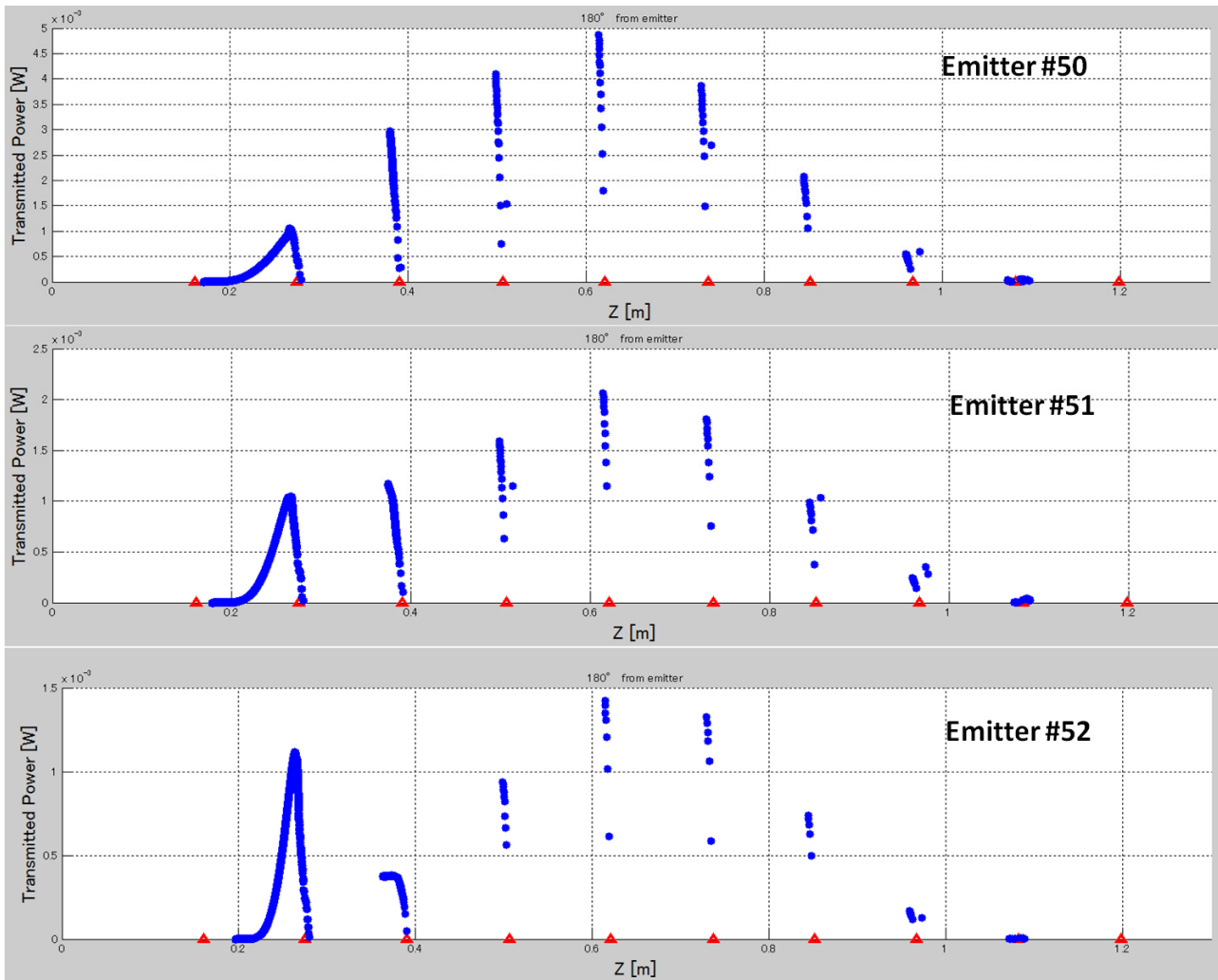


Figure 5. 69 Transmitted power along 360° meridian for $8/9\pi$ mode at 23.5MV/m for emitters 50, 51 and 52.

To account for the electron reflection from 360° meridian towards 180° meridian it is necessary to check if there is some impact location where the incident angle is about 10° or less. In pictures below are presented the calculated impact angles for different emitters in π mode and $8/9\pi$ mode.

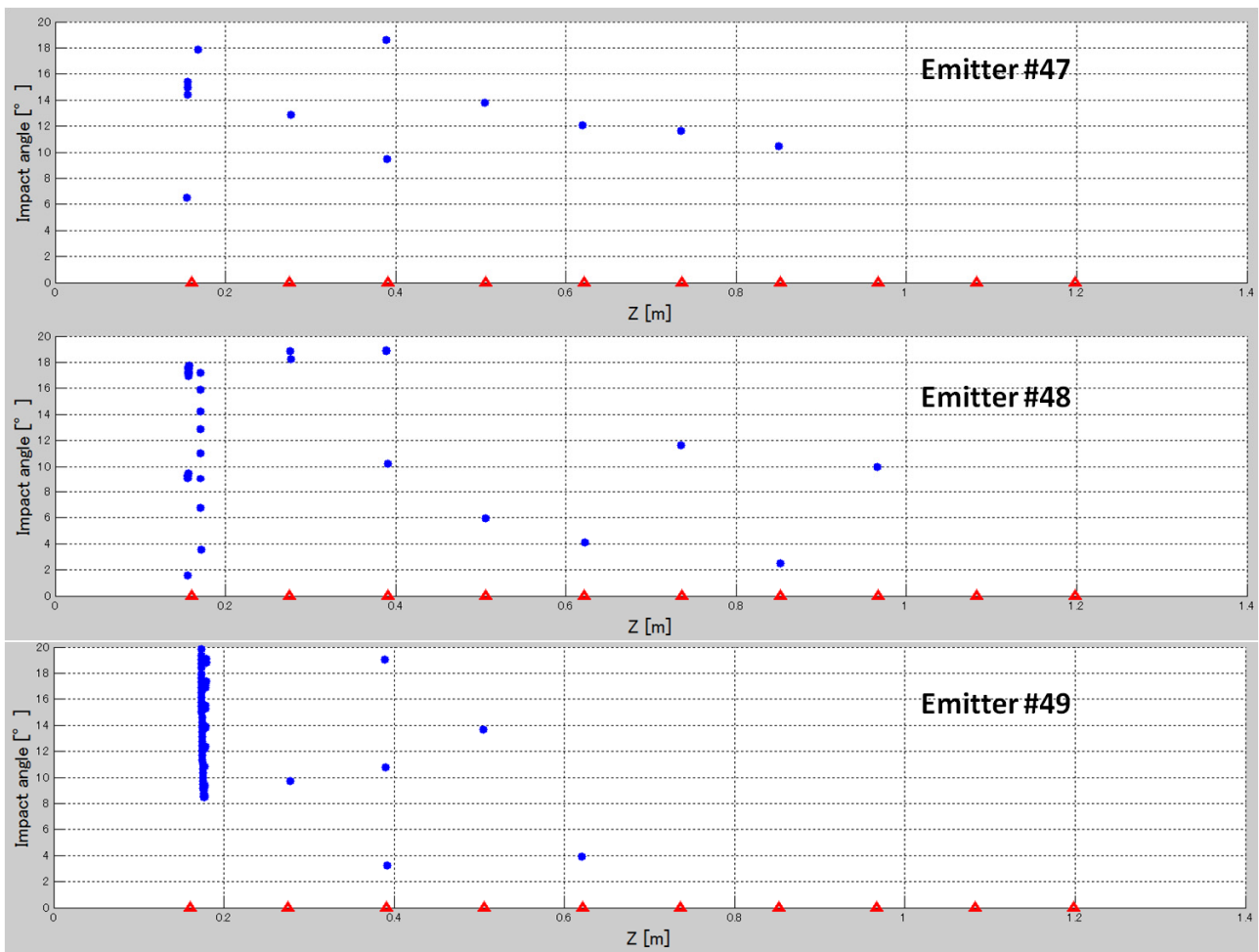
5.3.7 π mode at 22MV/m incident angle

Figure 5. 70 Incident angle along 360° meridian for π mode at 22MV/m for emitters 47, 48 and 49.

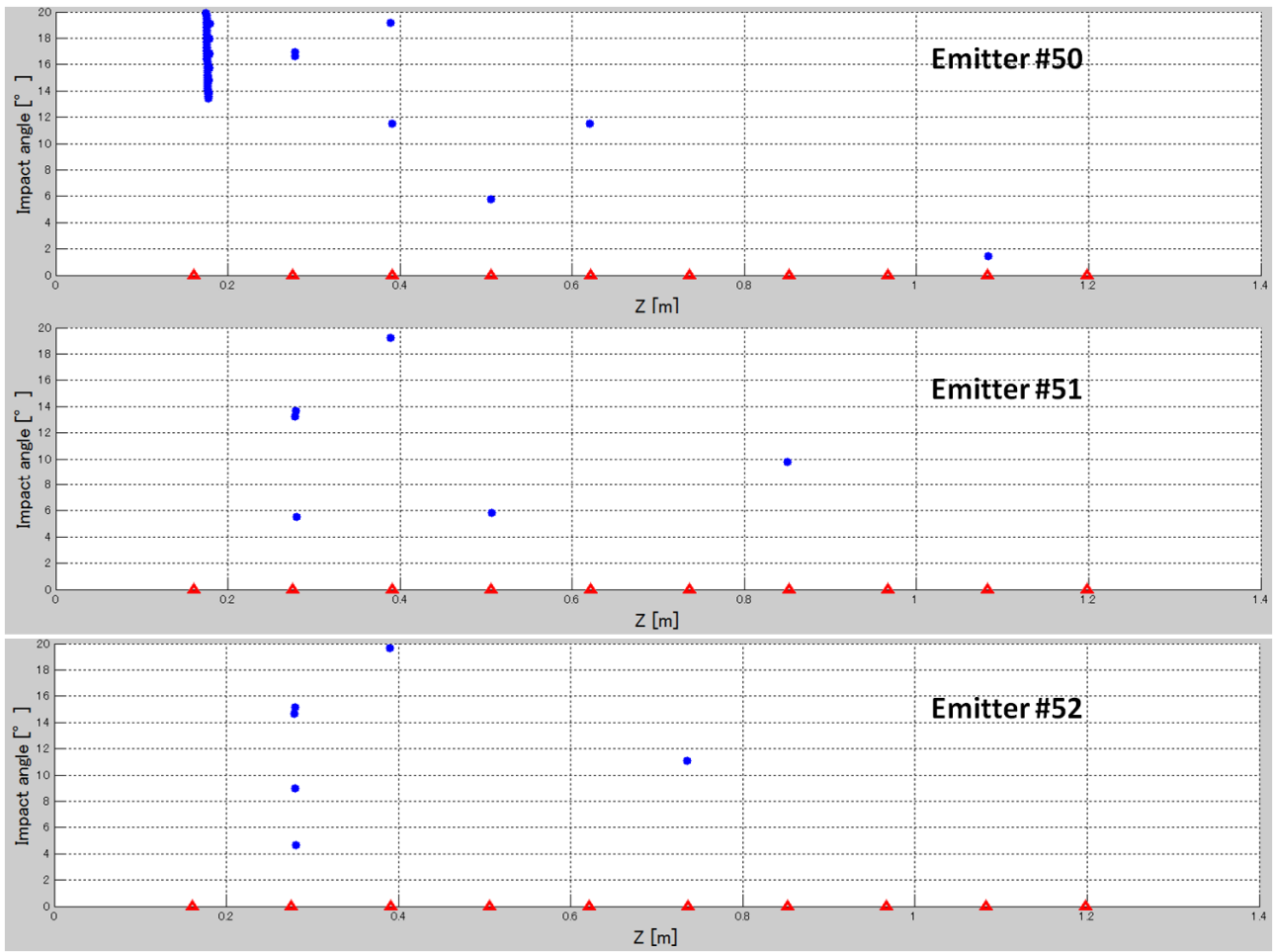


Figure 5.71 Incident angle along 360° meridian for π mode at 22MV/m for emitters 50, 51 and 52.

5.3.8 $8/9\pi$ mode at 23.5MV/m incident angle

Figure 5. 72 Incident angle along 360° meridian for $8/9 \pi$ mode at 23.5MV/m for emitters 47, 48 and 49.

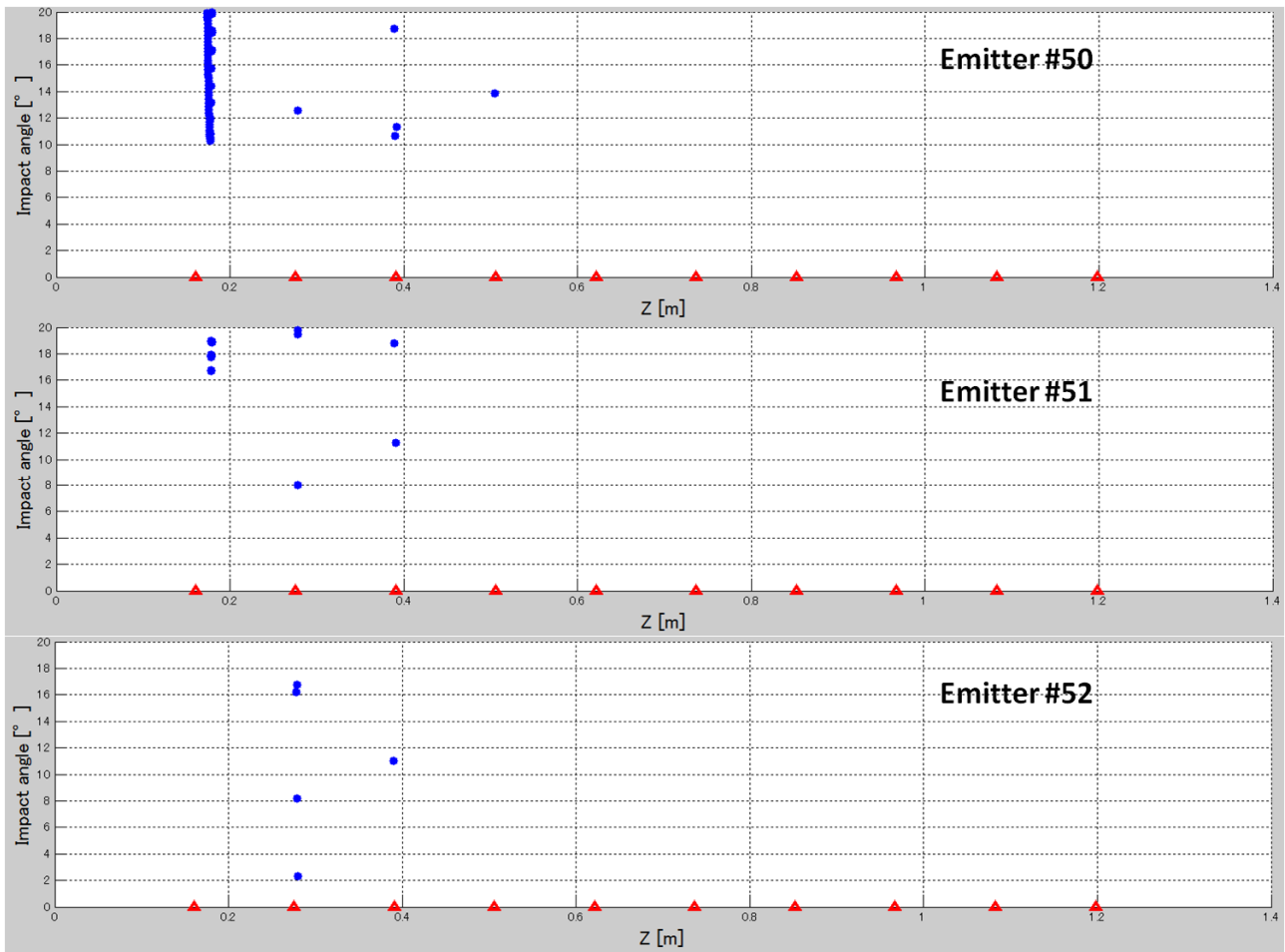


Figure 5. 73 Incident angle along 360° meridian for $8/9 \pi$ mode at 23.5MV/m for emitters 50, 51 and 52.

Analyzing the simulation results against the feature listed above for each mode, it is possible to compile a table in order to understand which emitter fulfill more requirements. Those results are presented in the next table :

Table 5. 5 Comparison between requirements derived from mapping data and simulation results.

| Emitter # | Properties list | | | | | | | | | | |
|--------------|-----------------|---|---|---|---|---|----------------|---|---|---|---|
| | π -mode | | | | | | $8/9\pi$ -mode | | | | |
| | a | b | c | d | e | f | g | h | i | j | k |
| 47 | ○ | ○ | ○ | ○ | ○ | ○ | | ○ | ○ | ○ | ○ |
| 48 | ○ | ○ | ○ | ○ | ○ | ○ | ○ | ○ | ○ | ○ | ○ |
| 49 | ○ | | ○ | ○ | | ○ | ○ | | ○ | | |
| 50 | ○ | | ○ | ○ | | ○ | ○ | | ○ | | |
| 51 | ○ | | ○ | ○ | | ○ | ○ | | ○ | | |
| 52 | ○ | | ○ | ○ | | ○ | ○ | | ○ | | |

The most probable emitter location is the number 48, located 4mm away respect to the iris between the 1st and 2nd cell. With this information we can compare the Q-E plot obtained during the vertical test and from simulation.

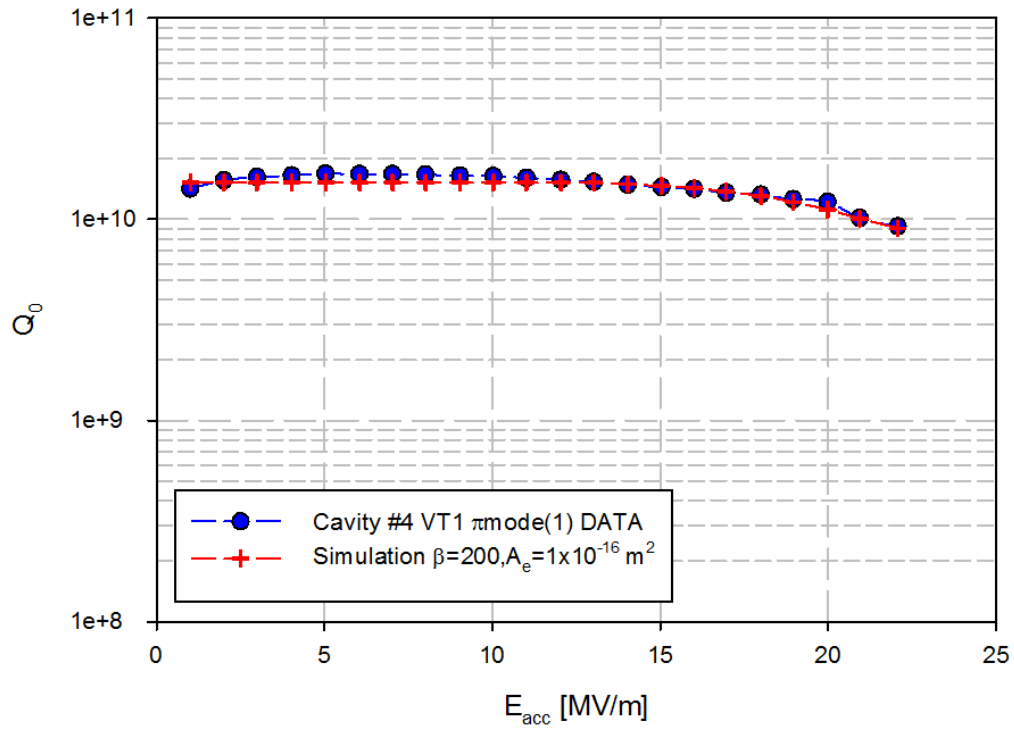


Figure 5.74 Q-E plot comparison between measured and simulation, cavity #4 π mode(1).

5.4 High power test

After the vertical tests, the cavity #3 and cavity #4 were sent to the manufacturer in order to weld the helium jacket. After that, they were installed inside the compact ERL cryomodule. Due to the lack of space around the cavity it was not possible to install the PIN diodes near the cavity surface so another detection system was needed in order to evaluate the field emission process during the high power test and possibly after commissioning.

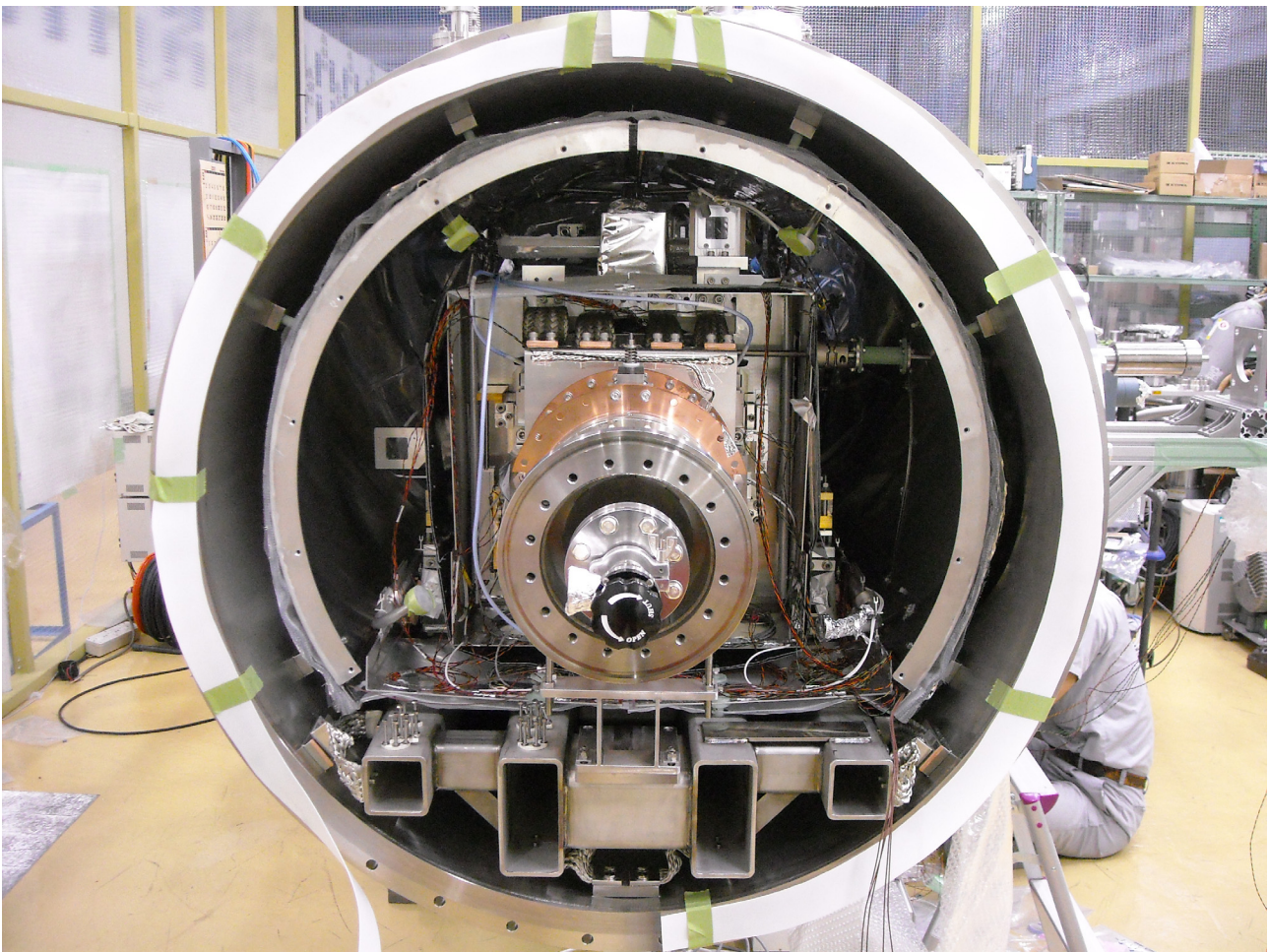


Figure 5. 75 Cavities inside the cryomodule (front view).

From our experience from vertical test we knew that the radiation pattern detected around the helium jacket cap can give some hint on the meridian where the emitter is located. For this test, we decided to exploit this information and implement a specific detection system for the cryomodule.

In order to understand the choice, it is important to recall what it is necessary to know in order to locate an emitter, the rotating mapping system proved the importance of the x-ray map showing the field emitted electron behaviour in terms of radiation pattern.

To locate the emitter position two coordinates are necessary, one is the meridian and the second is the location along the *Z* axis, with these two information it is possible to pin point the location. During the vertical test this two coordinates were given by the rotating mapping system able to show the typical sharp spot in front of the emitter and the broad spot on its own meridian, but during the high power test this two information shall be collected with two different devices.

5.4.1 PIN diodes setup

To determine the meridian, we decided to install two sets of PIN diodes for each cavity (64 diodes total), one set (16 diodes) is positioned on a circumference around the SBP helium jacket while the second set on the damper tube after the LBP.

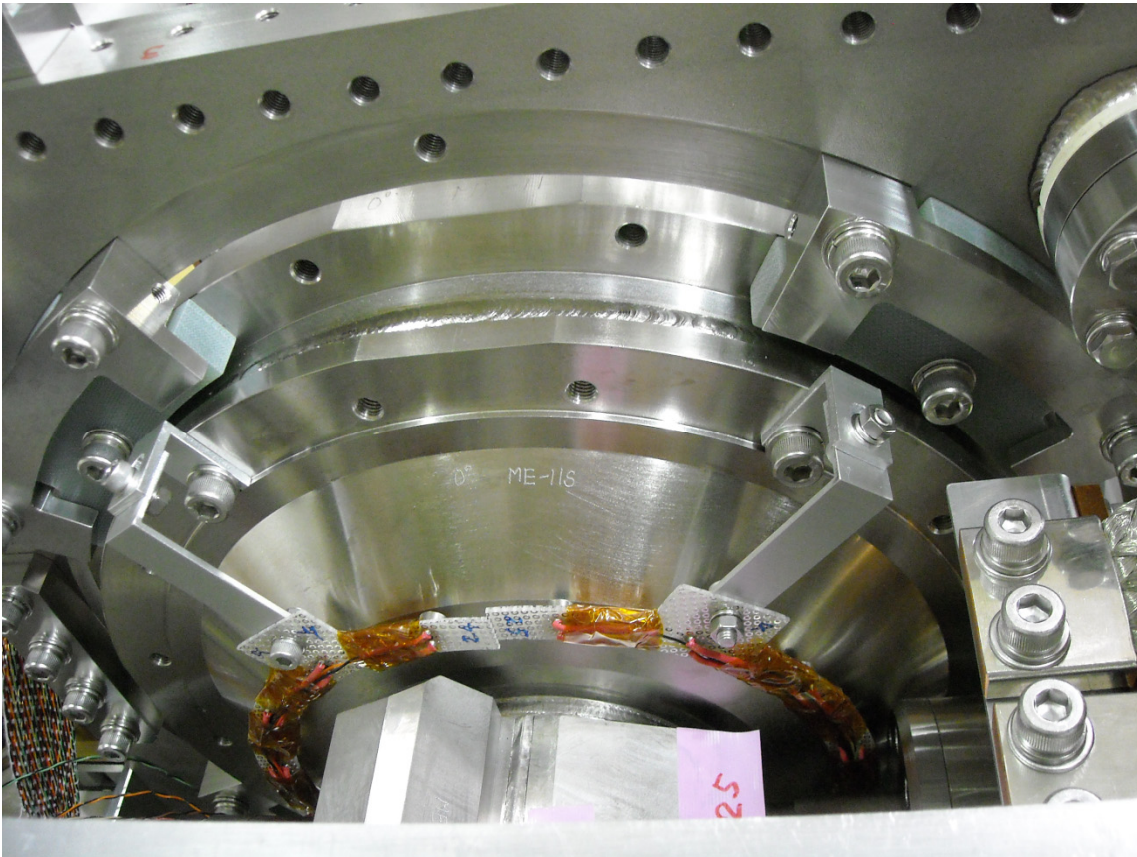


Figure 5.76 PIN diodes installed on the SBP side, around the Helium jacket cap.

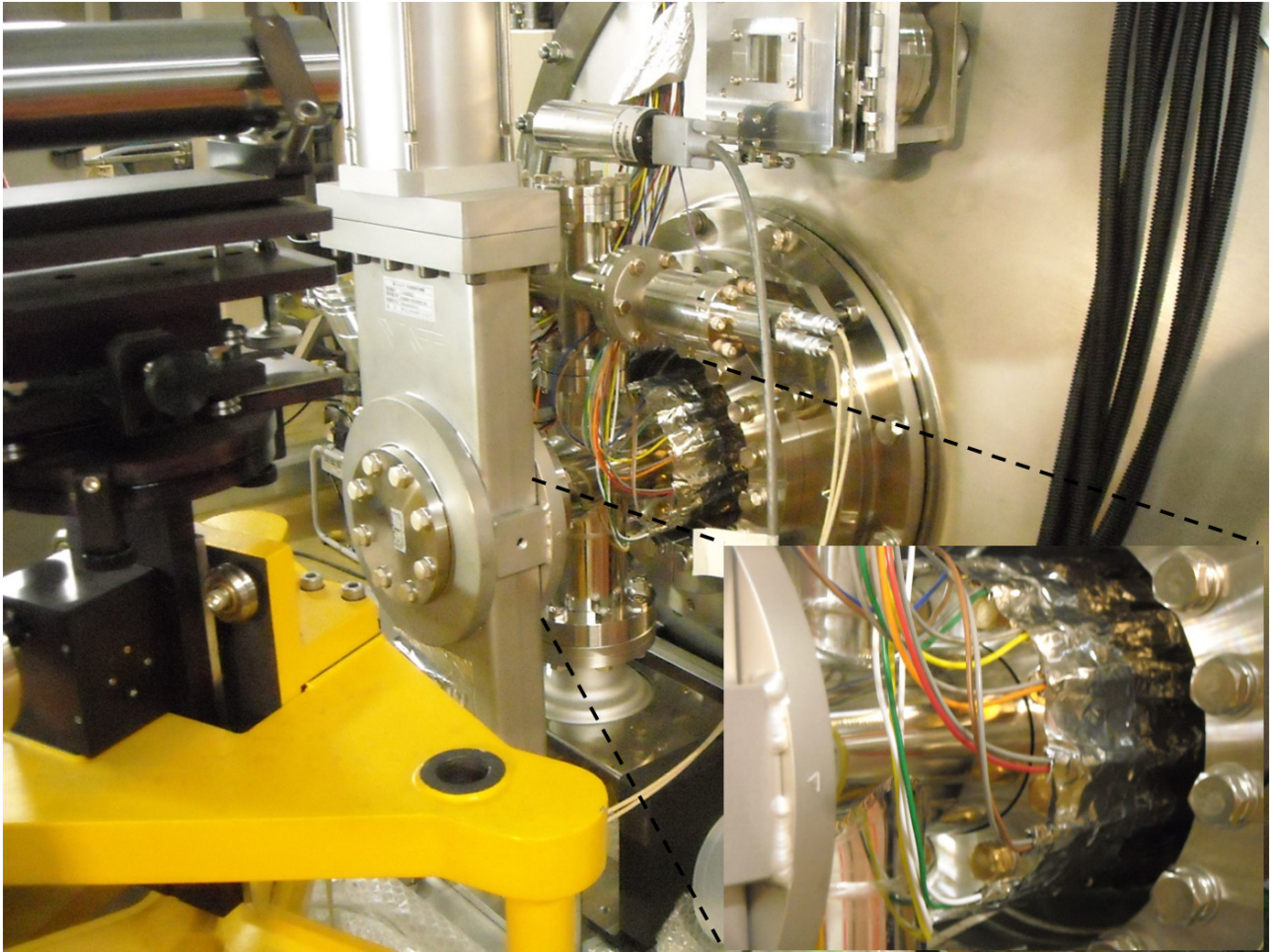


Figure 5.77 PIN diodes installed on the LBP side, around the damper tube on a diameter about 60mm.

The diodes on the LBP side are positioned on the damper tube around a circumference with a diameter about 60mm. Considering that the cavity iris has a 80mm diameter, this means that the sensors have a line of view inside the cavity, and we can expect that some electron trajectory can directly hit this area, producing a shower near the sensor without any other material that intercept it.

To determine the emitter location along the cavity axis, we decided to measure the electron kinetic energy once they impact on the gate valve, by knowing the accelerating field it is possible to determine how far the electrons flew in the cavity. To measure the electrons kinetic energy we used a NaI scintillator to observe the bremsstrahlung radiation and its end point energy after the impact with the gate valve. At last other 25 PIN diodes were installed into an array shape in front of the

gate valve in order to detect radiation pattern, their configuration and installation can be seen in the next pictures.

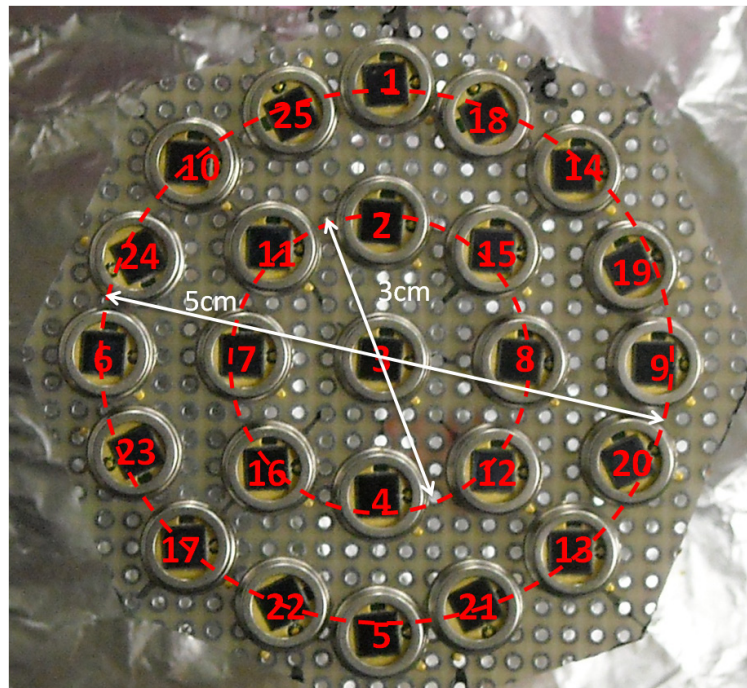


Figure 5.78 PIN diodes configuration for the profile monitor installed in front of the gate valve (LBP side).

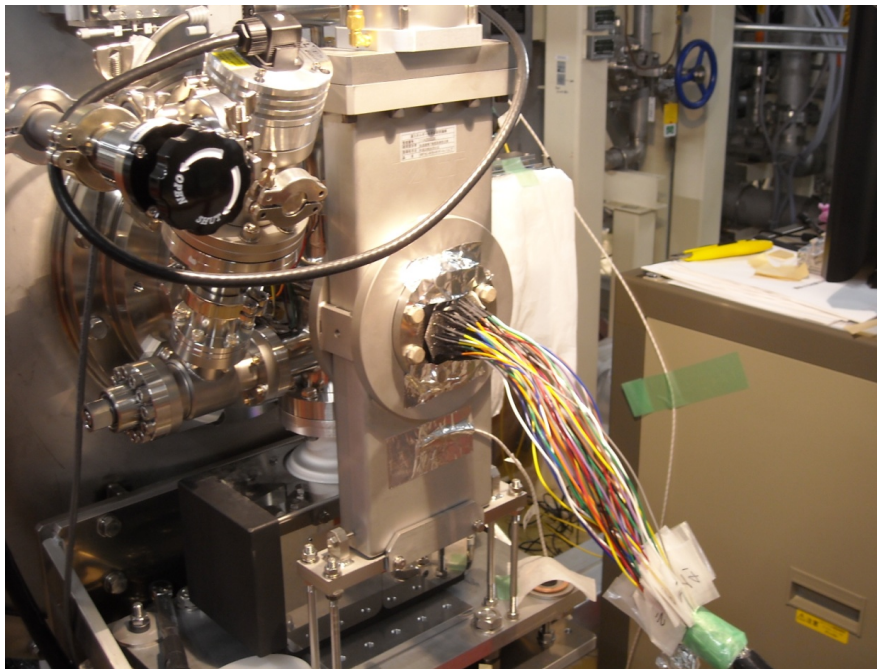


Figure 5.79 Profile monitor installed during the high power test.

A specific code was written to read the EPICS data online during the test. For the scintillator data a Matlab code that bin the data and analyze them was necessary, in the picture below can be seen a screen capture during the test.

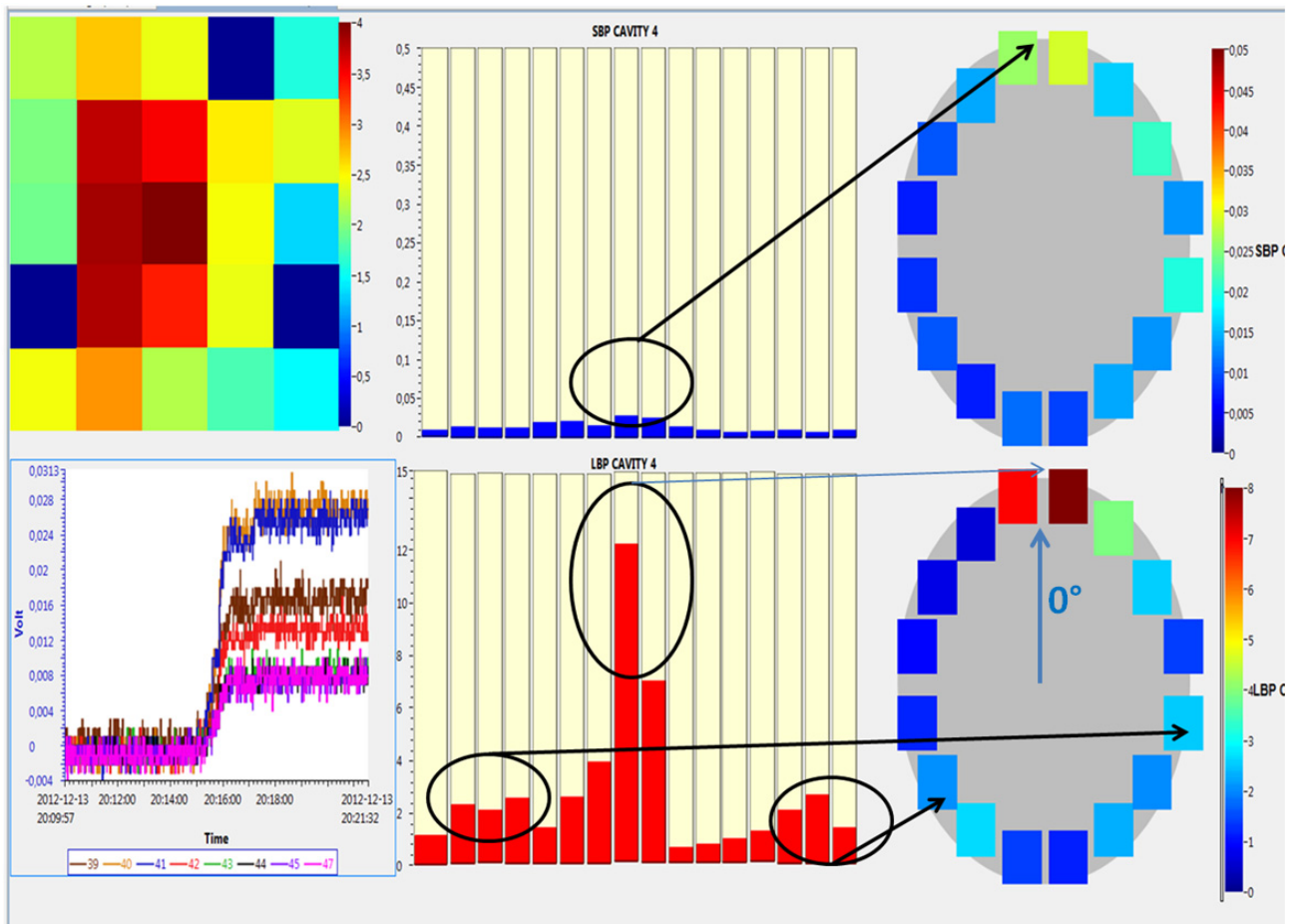


Figure 5.80 Online screen capture for the EPICS code, profile monitor (top left), SBP ring diodes (top center and right), LBP ring diodes (bottom center and right), all the quantities are volts measured in the PIN diode circuit, the meridian angles are calculated starting at 0° (top PIN diode) increasing clockwise up to 360° .

5.4.2 Cavities condition during last vertical test

Before discussing the detail of the high power test, it is worth recalling the cavity condition after their last vertical test, specifically in terms of radiation onset and radiation pattern.

In the table below can be found the relevant information concerning field emission as we expected to observe also during the high power test, assuming that no perturbation occur to the cavity surface such as scratches and dust.

Table 5. 6 *Cavities condition during their last vertical test in π mode operation*

| | <i>Radiation onset π-mode [MV/m]</i> | <i>Meridian on LBP side (cryomodule configuration)</i> |
|------------------|---|--|
| Cavity #3 | 13 | 112.5°-292.5° |
| Cavity #4 | ≥ 22 | 112.5°-292.5° |

With respect to their vertical test performance, it was decided to put the best cavity near the injector in order to avoid strong radiation towards it, despite the #3 cavity showed a lower onset was difficult to detect any radiation pattern, with the PIN diodes, up to 18MV/m, both cavity fulfilled the design values in terms of unloaded Q and accelerating field, by chance their only emitter is located on the same meridian.

5.4.3 High power test schedule

The two cavities installed in the main linac cryomodule were tested separately, at that time only one RF line was installed and shall be moved from one cavity to the other during the test days. In order to perform the overall performance, different stages were carried out. After the cool down, the cavity voltage was slowly raised up to 14MV and kept stable in order to perform all the radiation safety inspection, finally a static and dynamic loss was measured.

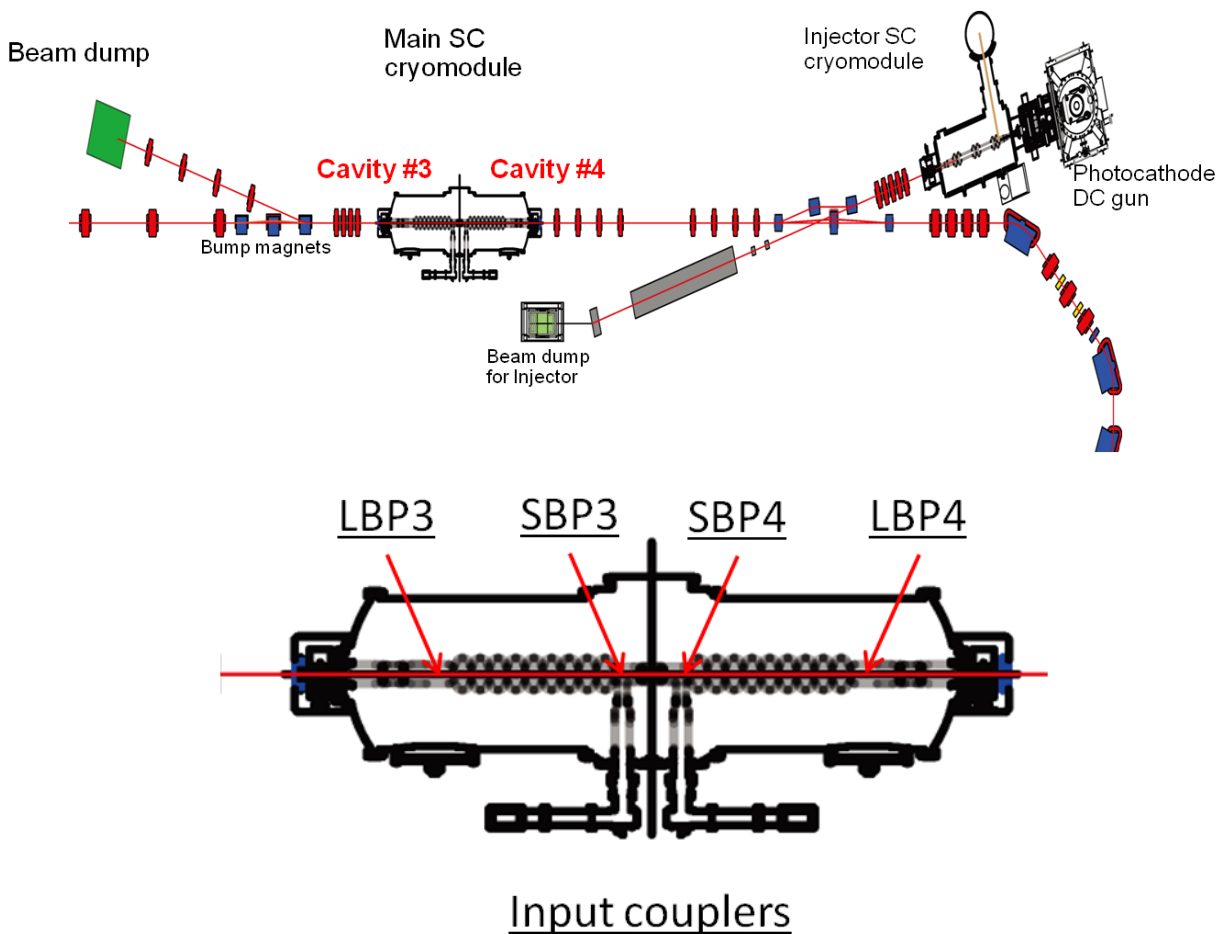


Figure 5.81 Cavity location inside the c-ERL and sensors location.

The first cavity tested was the cavity #4 (upstream with respect to the injector), for this cavity it is possible to distinguish two different conditions, with respect to field emission, one before the 14MV stable operation and one after it.

5.4.4 Upstream cavity radiation pattern

Before keeping the cavity voltage at 14MV the field emission pattern was like the one shown in the next picture. A strong radiation signal is clearly visible in the upper part of the LBP damper tube (0° meridian), other small peak can be seen at about 90° and 225° but their intensity is smaller.

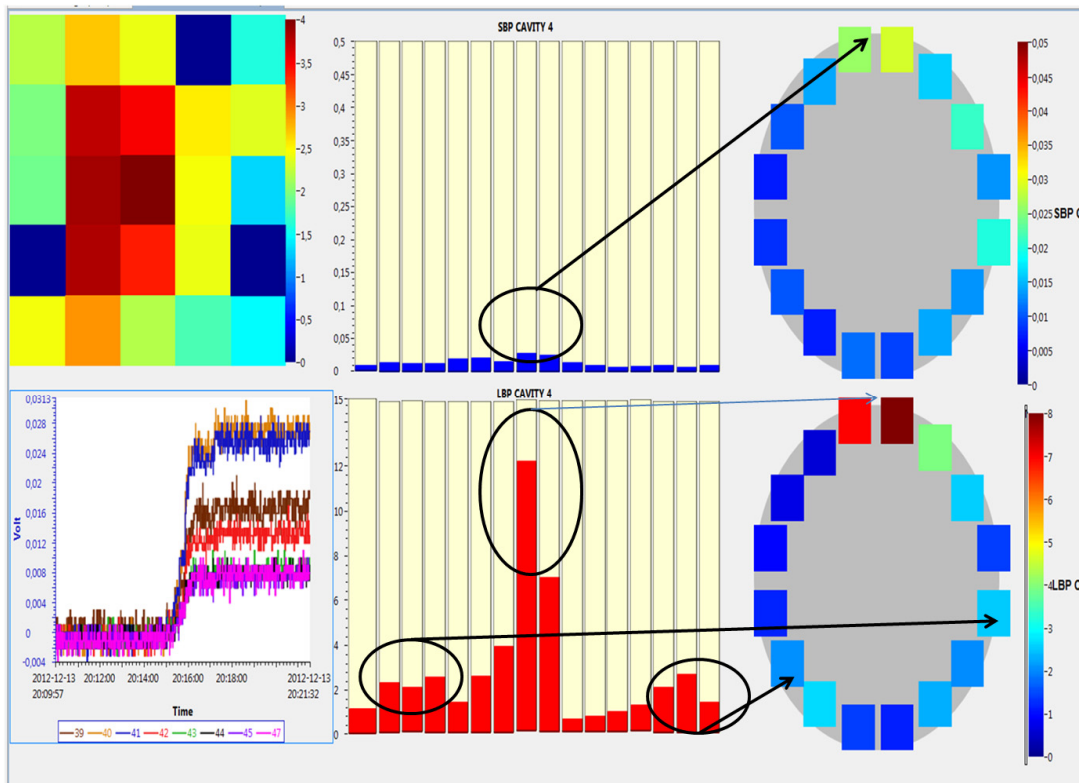


Figure 5.82 Cavity #4 at 14MV.

During the stable field operation a strong radiation was suddenly detected and a new strong emitter appeared producing a radiation pattern different from before. In the next picture is presented the event, the graph represents the PIN diodes voltage with respect to time, it is possible to notice the step increase at 17:00 (sensor #49 and #53).

The conditions before and after the burst are drastically different with respect to the cavity last vertical test, both radiation onset and x-ray pattern have changed leading to the conclusion that the cavity surface condition underwent some change, probably some dust entered the cavity during the

period of time between the Argon purging and the final assembly, the information gathered during this test can give us some clue on its location (meridian and along the cavity axis).

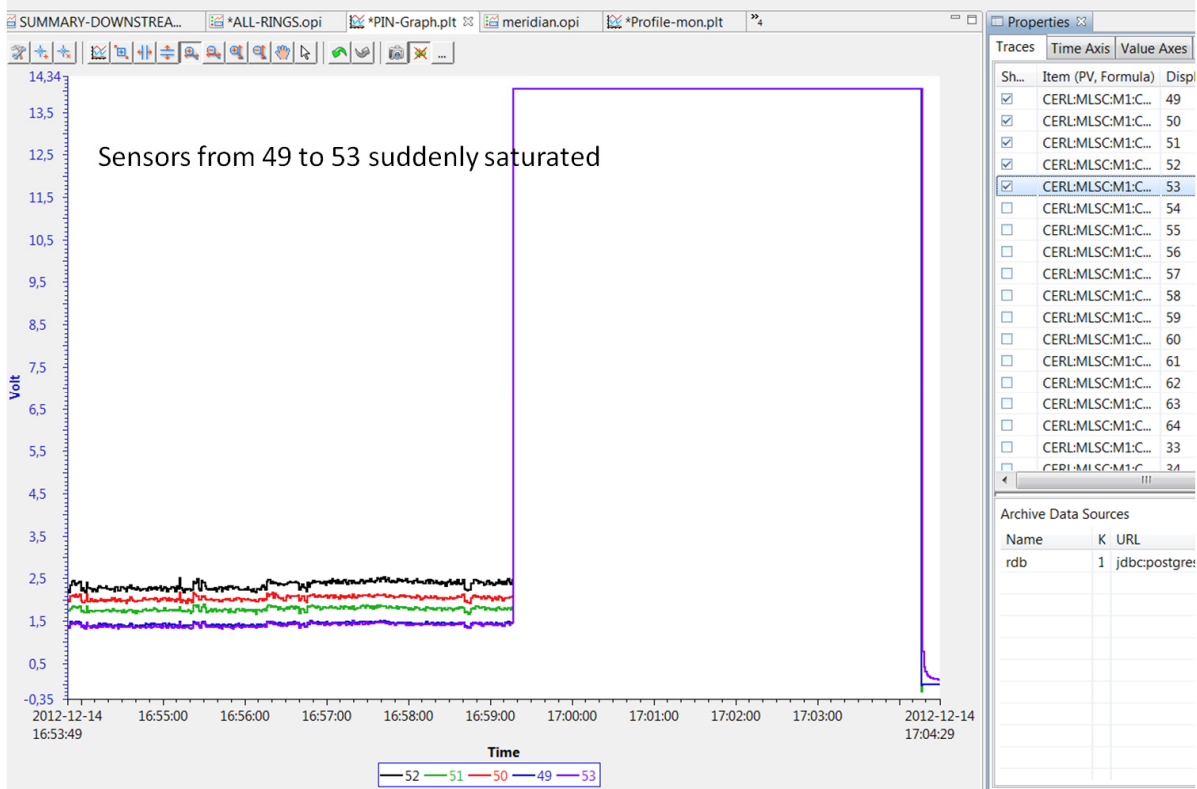
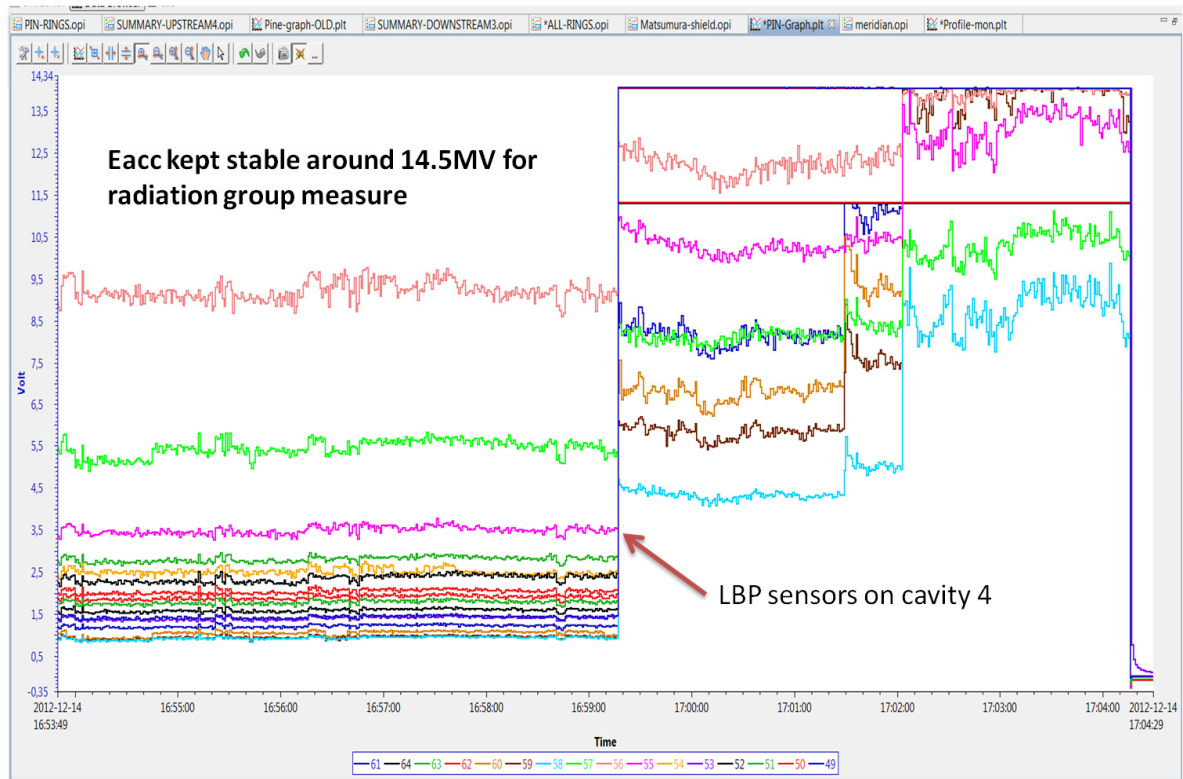


Figure 5. 83 Cavity #4 PIN diodes voltage from sensors installed on the LBP damper tube.

After this event the radiation pattern was like the one shown in the next figure, the cavity voltage was about 12MV and the sensor located on 90° meridian was already saturated, showing a drastic change from the previous measure.

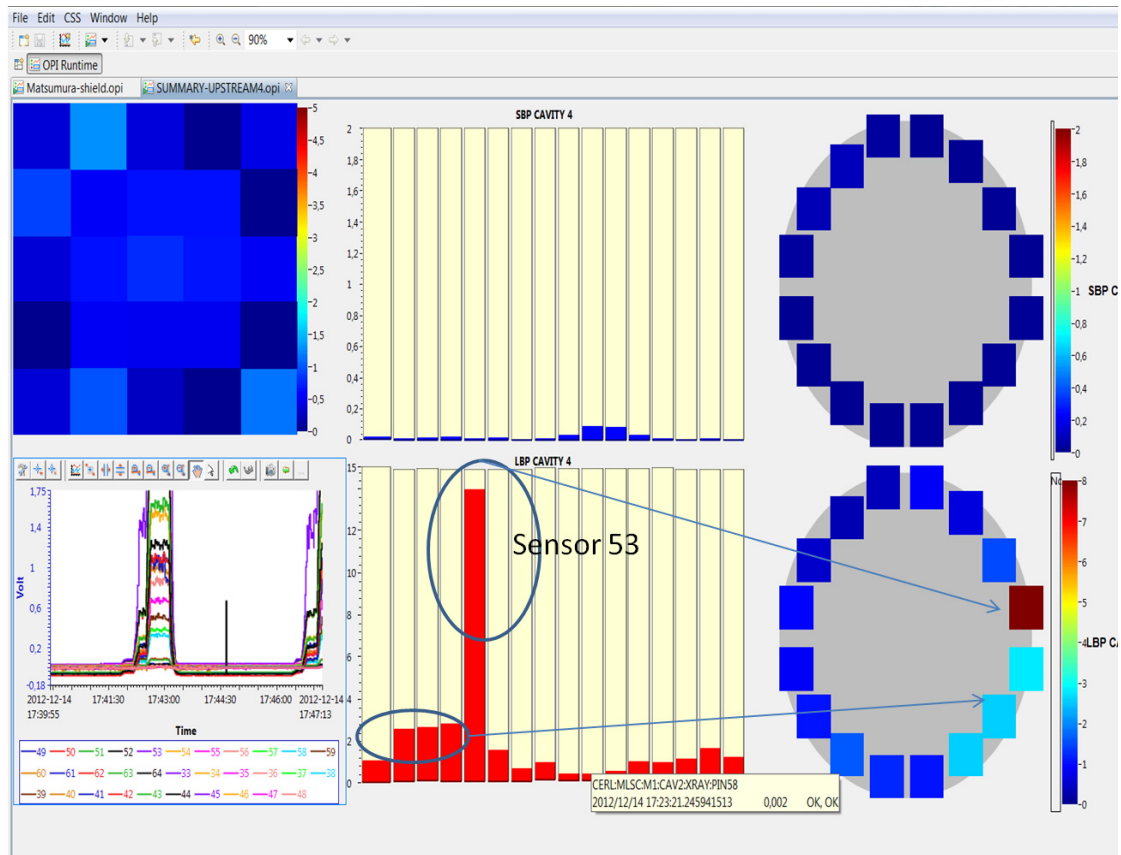


Figure 5. 84 Cavity #4 radiation pattern after x-ray burst, the cavity voltage is about 12MV.

From the online data we can already draw some conclusion concerning the strongest emitter, it is located on the horizontal meridian (about $90^{\circ} \pm 22.5^{\circ}$ lower part) and due to the fact that usually the strongest radiation is on the opposite side with respect to the emitter we can assume that it is located on the Input coupler side (left side looking at the cavity from the LBP as in the online data). The radiation detected on the SBP is negligibly smaller, so we can assume that mainly the electrons fly from the iris to the LBP, this information tells us that emitter shall be on the iris region facing the SBP side.

In the next section we will try to understand in which cell the emitters is more likely located.

5.4.5 Upstream NaI scintillator measure

As shown in chapter 4, during this test we have place a NaI scintillator in front of the cavity on the LBP side as shown in the picture below.

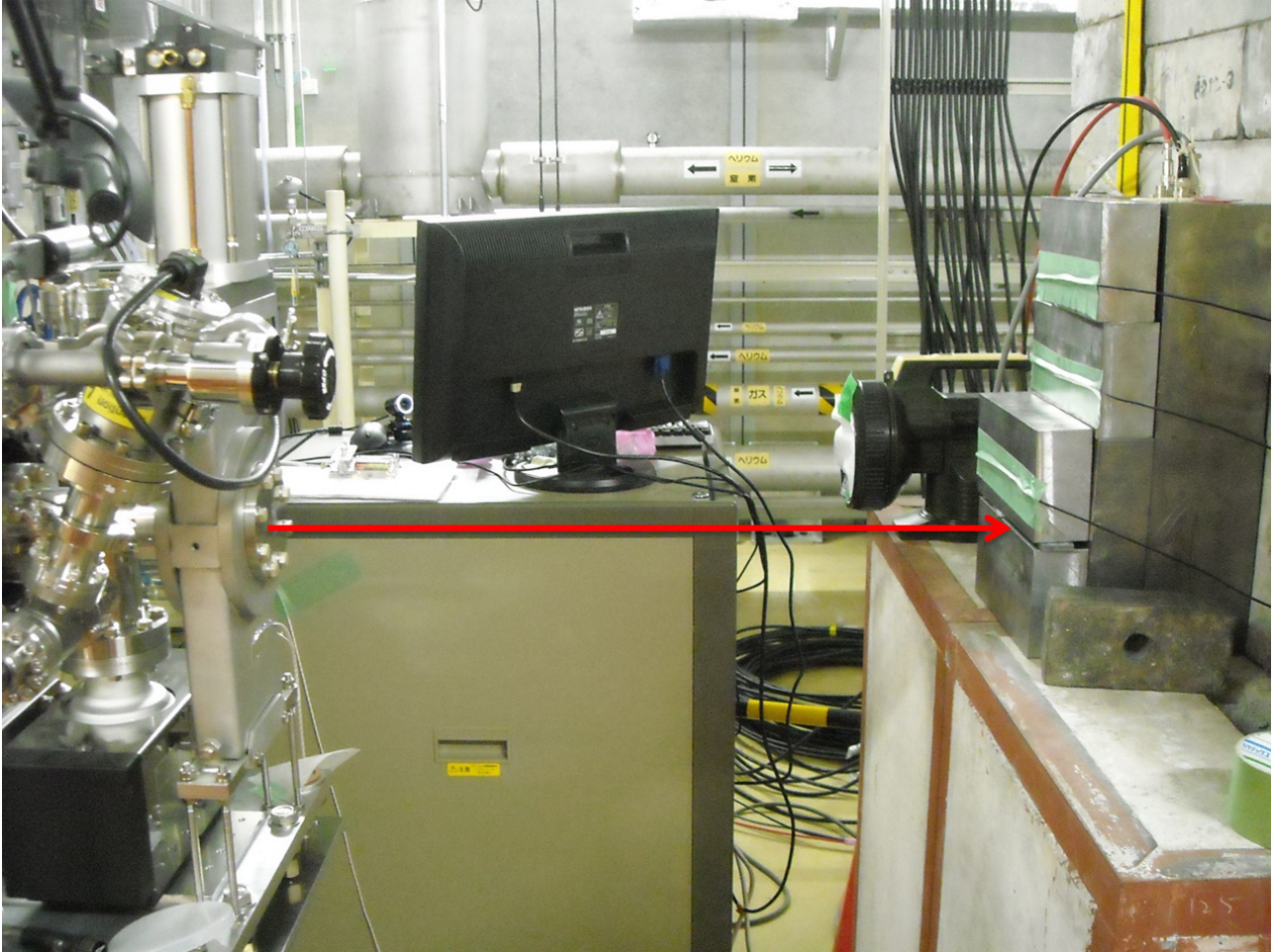


Figure 5. 85 NaI scintillator positioned in front of cavity #4 LBP side.

The scintillator was shielded by 10cm lead block with a collimation aperture (2mmx2mm) located on the beam axis (120cm from ground level) and 70cm away from the gate valve. Due to high radiation dose, it was possible to operate the scintillator only around the field emission onset, few MV above it, so it was possible to investigate mainly the strongest emitter radiation.

Before and during the test, the scintillator was calibrated by using known active sample like Na_{22} , CS_{137} and Co_{60} , the background signal was measured (and subtracted from low field measures), a typical background signal can be seen in the next plot.

NaI scintillator background signal

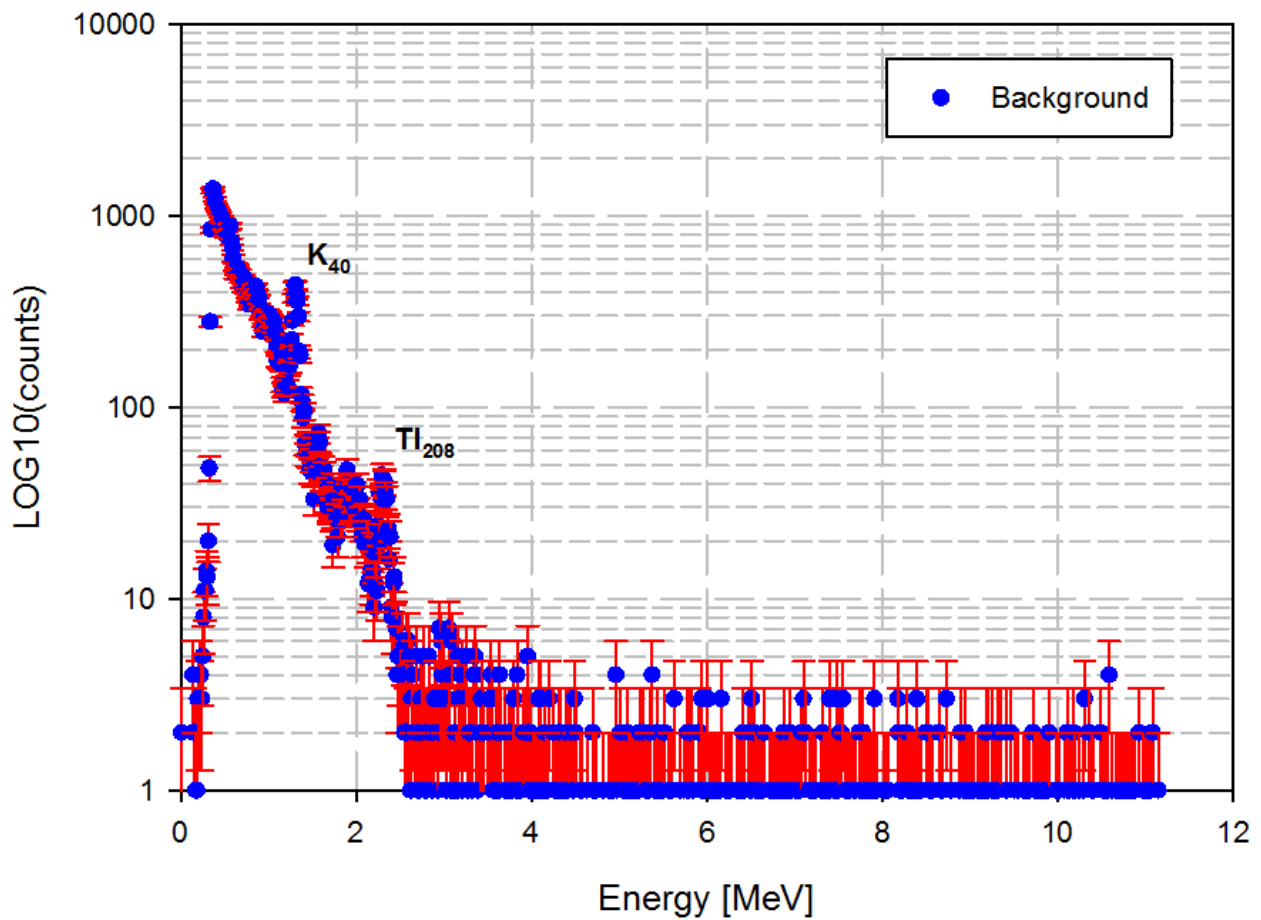


Figure 5.86 NaI scintillator background signal taken for 120 minutes.

In the scintillator background signal, it is possible to see two peaks corresponding to K_{40} (about 1.3 MeV) present in the concrete behind the scintillator and Tl_{208} (about 2.4 MeV) present in the soil.

Upstream cavity

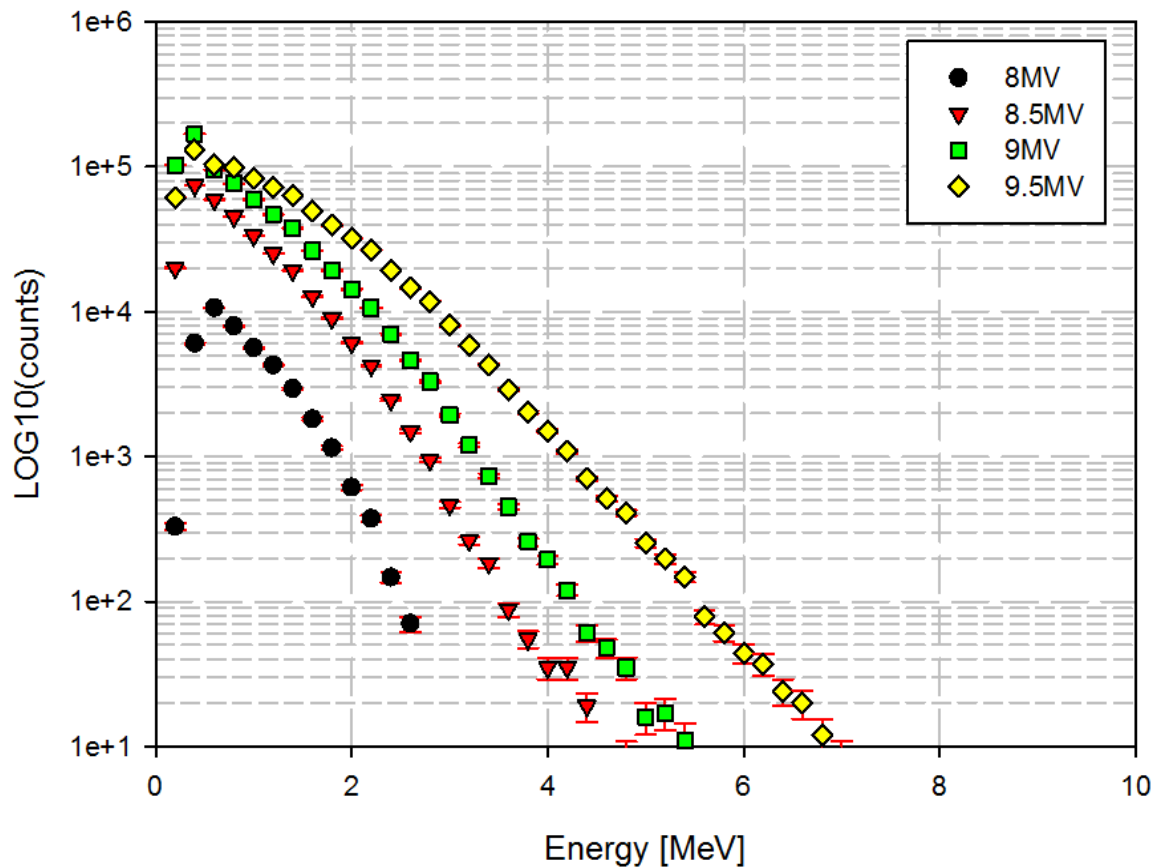


Figure 5.87 NaI scintillator measure near field emission onset, each measure is taken at different cavity voltage for 2 minutes.

From the above data it is possible to extrapolate the endpoint energy corresponding approximately to the maximum electron kinetic energy that hit the gate valve. To avoid pile up problem or low counting fluctuation a linear fitting was performed for signal bigger than 100 counting and with energy bigger than 1MeV, this reduces the area of interest to the graph central region.

A typical bremsstrahlung spectrum decreases like an hyperbole at lower energies, then becomes almost linear to drop more rapidly near the endpoint energy, the corresponding energies can be found in the next table and figure.

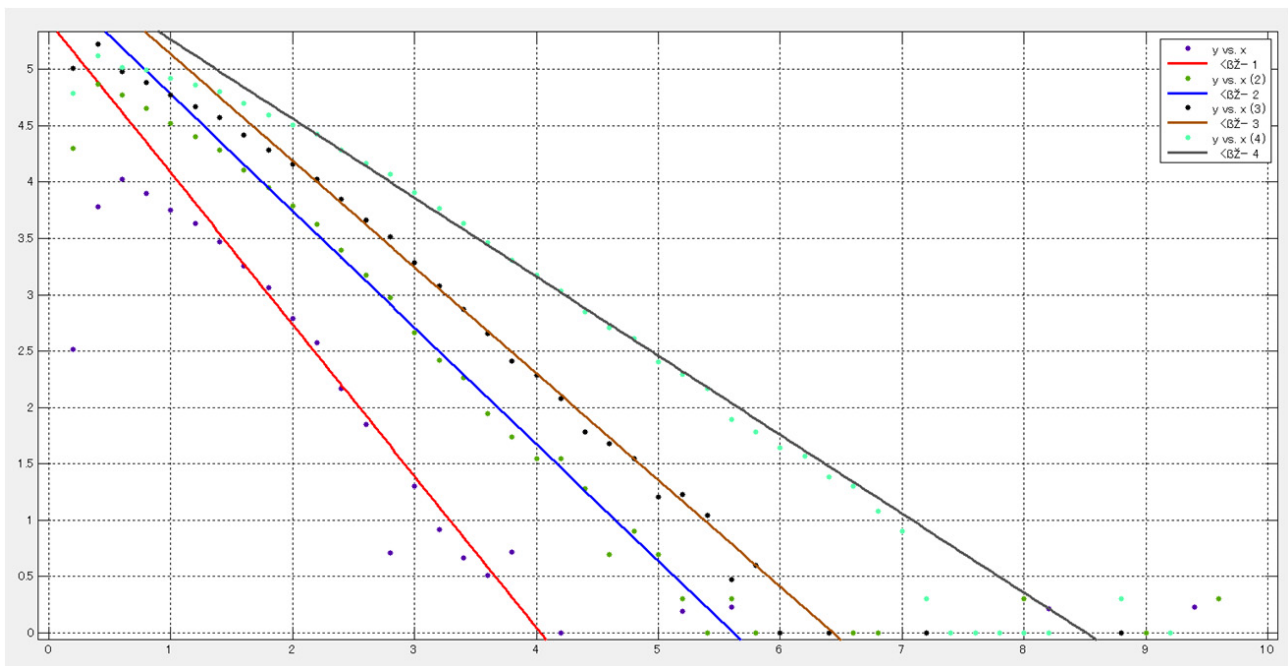


Figure 5.88 Scintillator data fitting from left to right 8MV, 8.5MV, 9MV and 9.5MV spectra and linear fitting.

Table 5. 7 End point energy extrapolated from scintillator measure

| Cavity Voltage [MV] | End point energy [MeV] |
|---------------------|------------------------|
| 8 | 4 |
| 8.5 | 5.5 |
| 9 | 6.4 |
| 9.5 | 8.5 |

Due to the approximation done, we can easily expect more than 1MeV error for this kind of fitting leading to some uncertainty on the emitter location, particularly for the last measure where the scintillator dead time start to be bigger than 10%.

In order to evaluate the probable emitter location, a systematic simulation was performed. Emitters were placed on each iris at 0.5mm distance each other, the cavity was excited with π mode at

accelerating field between 4MV/m and 20MV/m. For each emitter was recorded the maximum electron kinetic energy for trajectories reaching a spot 1cm radius located at the LBP end, in order to simulate the electron reaching the gate valve and producing particle shower able to enter the scintillator collimator. Each iris produces a spectrum of possible impact energy as can be seen in the graph below.

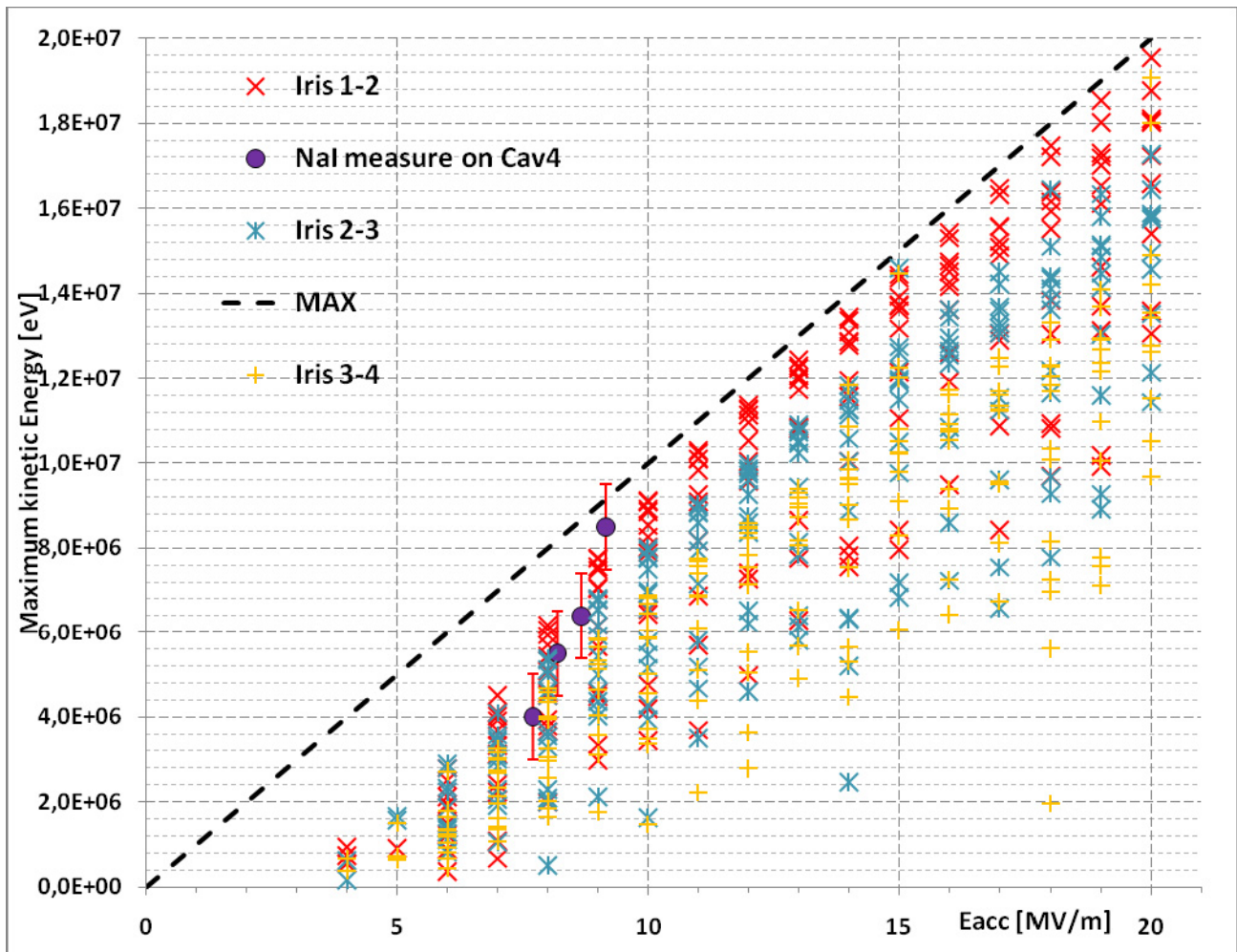


Figure 5. 89 Comparison between energy spectrum produced by emitters on different iris and measured data for cavity #4 (upstream).

The electrons energy starting from iris between 1st and 2nd cell are depicted in red, from 2nd-3rd Iris in blue and 3rd -4th in orange, each iris produces a band of possible maximum energy that partially overlap with the next one, the purple dots represent the value extrapolated from the scintillator data.

At low accelerating field, the electrons are not able to reach the maximum energy due to the fact that their speed is low compared to $\beta=1$ design value, so the total energy gain is a fraction of the maximum, at higher accelerating fields the emitted electrons can reach almost $\beta=1$ within one cell.

The band structure is due to different electron trajectories and RF phase during emission leading to a fluctuation in the final kinetic energy.

Looking at the position and trend of the data gathered from the scintillator we can reasonably assume that the emitter can be placed between cell 2 and 3 or cell 1 and 2, if we consider the first 3 data (excluding the 9.5MV measure that is more imprecise) the most probable location is on the iris between 2nd and 3rd cell.

By drawing the possible impact location for each emitter on this iris we can refine the area where the emitter can be located, in the picture below can be seen a graph with the impact location with respect to the emission RF phase and emitter location (respect to iris), the cavity voltage is 8.5MV π mode.

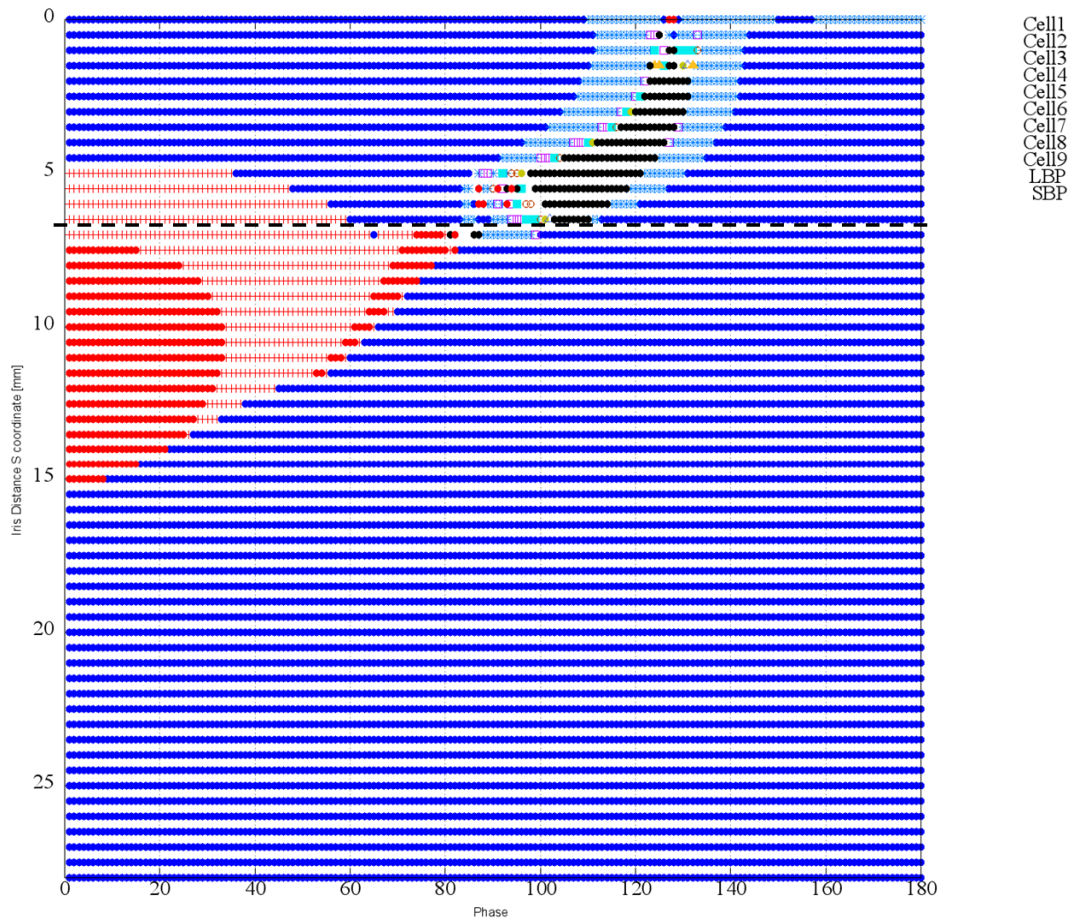


Figure 5. 90 Landing location with respect to emission phase and emitter location from iris between 2nd and 3rd cell at 8.5MV. Trajectories that can reach the LBP are represented as black dots.

From the picture above we can deduce that for emitted electrons it is possible to reach the LBP only if the emitter is located within 7mm from the iris, this refine the possible location further.

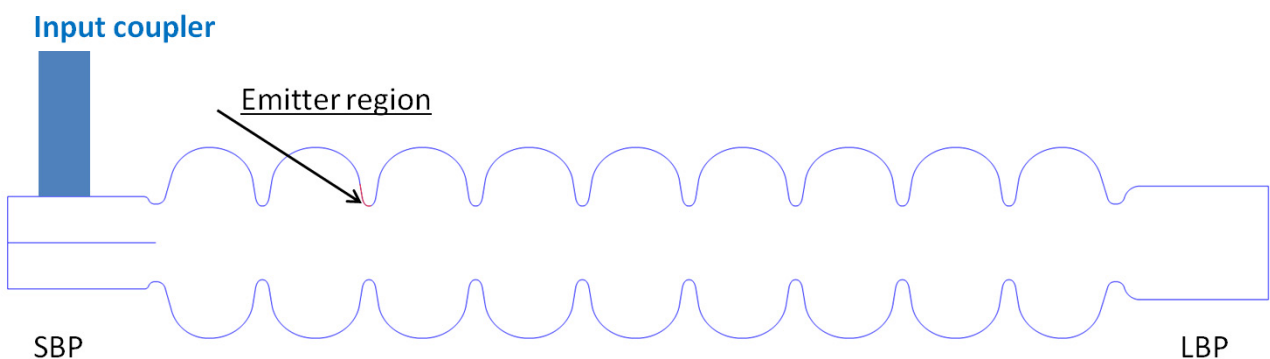


Figure 5.91 Possible emitters region, in the figure is represented a red line covering 30mm surface length, the estimated region is 7mm too small to be appreciated in the figure.

5.4.6 Downstream cavity radiation pattern

Cavity #3 was tested following the same procedure explained before, also in this case the radiation pattern and the onset were different from the last vertical test, leading to the same conclusion as before, during the Argon purging or the final assembly some dust particle could be landed on the cavity iris.

The experimental set up is the same as for cavity #4, 16 diodes on the SBP and 16 diodes near the LBP in a ring shape arrangement, the profile monitor is attached to the gate valve flange.

Also in this case a strong emitter can be located as can be seen from the figures below

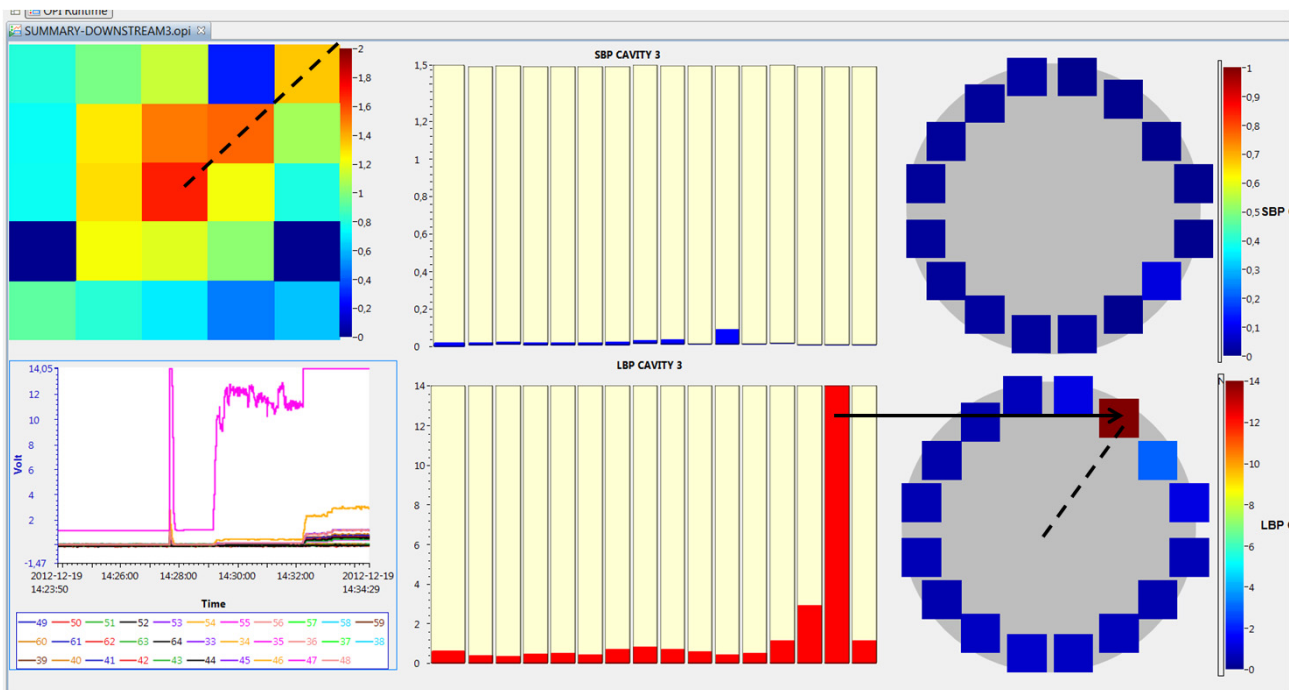


Figure 5.92 Cavity #3 radiation pattern at 11MV cavity voltage.

The strong emitter is located around 45° meridian, at 11MV is saturated the same pattern can be seen on the profile monitor, the up-right diagonal is oriented as the 45° meridian and appear to detected a stronger signal with respect to the neighbor diodes. Also in this case, the emitter has a strong radiation towards the LBP and a negligible toward the SBP so it shall be located on the iris region facing the SBP.

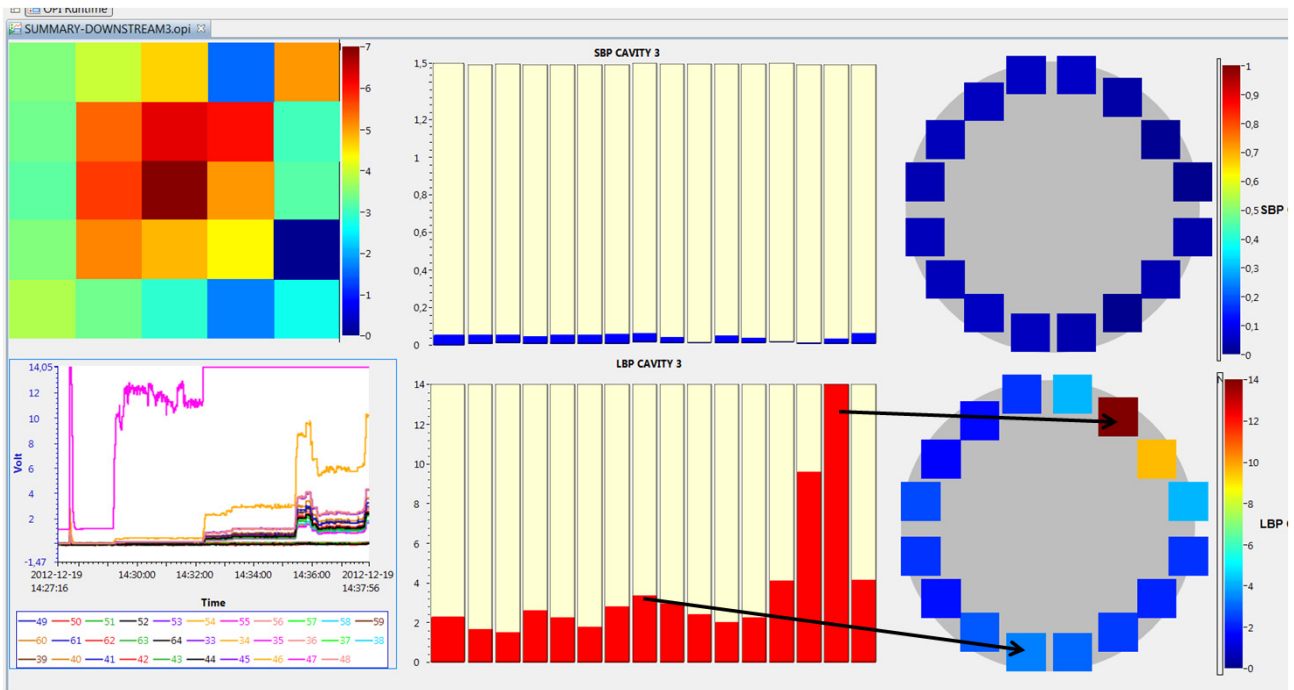


Figure 5.93 Cavity #3 radiation pattern at 12MV cavity voltage.

By increasing the cavity voltage to 12MV other radiation pattern start to appear, mainly in the bottom part of the LBP. Still no radiation can be detected on the SBP side, the emitters shall be located on the iris region facing the SBP the electrons follow an “inverted” trajectory to reach the LBP. It is also possible to distinguish two radiation pattern leading to the conclusion that in the cavity exist at least two emitters none of them detected during the last vertical test.

5.4.7 Upstream NaI scintillator measure

The scintillator was positioned in a similar configuration as it was for the previous test, also in this case the measures were taken near the field emission onset due to the high radiation dose.

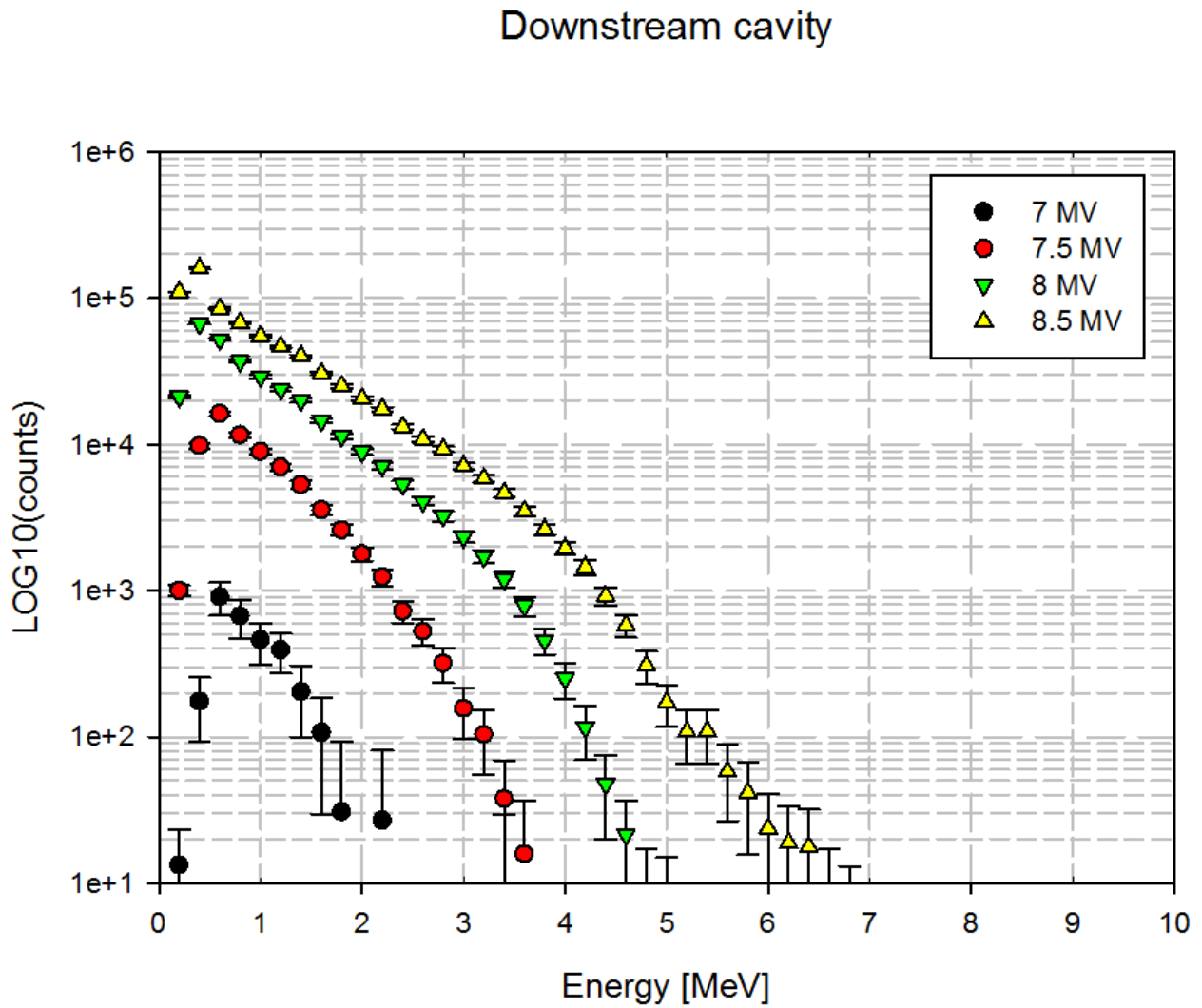


Figure 5.94 NaI scintillator measure near field emission onset, each measure is taken at different cavity voltage for 2 minutes.

The endpoint energy obtained after the linear fitting can be seen in the next table

Table 5. 8 End point energy extrapolated from scintillator measure.

| Cavity Voltage [MV] | End point energy [MeV] |
|---------------------|------------------------|
| 7 | 3 |
| 7.5 | 4.5 |
| 8 | 5.6 |
| 8.5 | 7.2 |

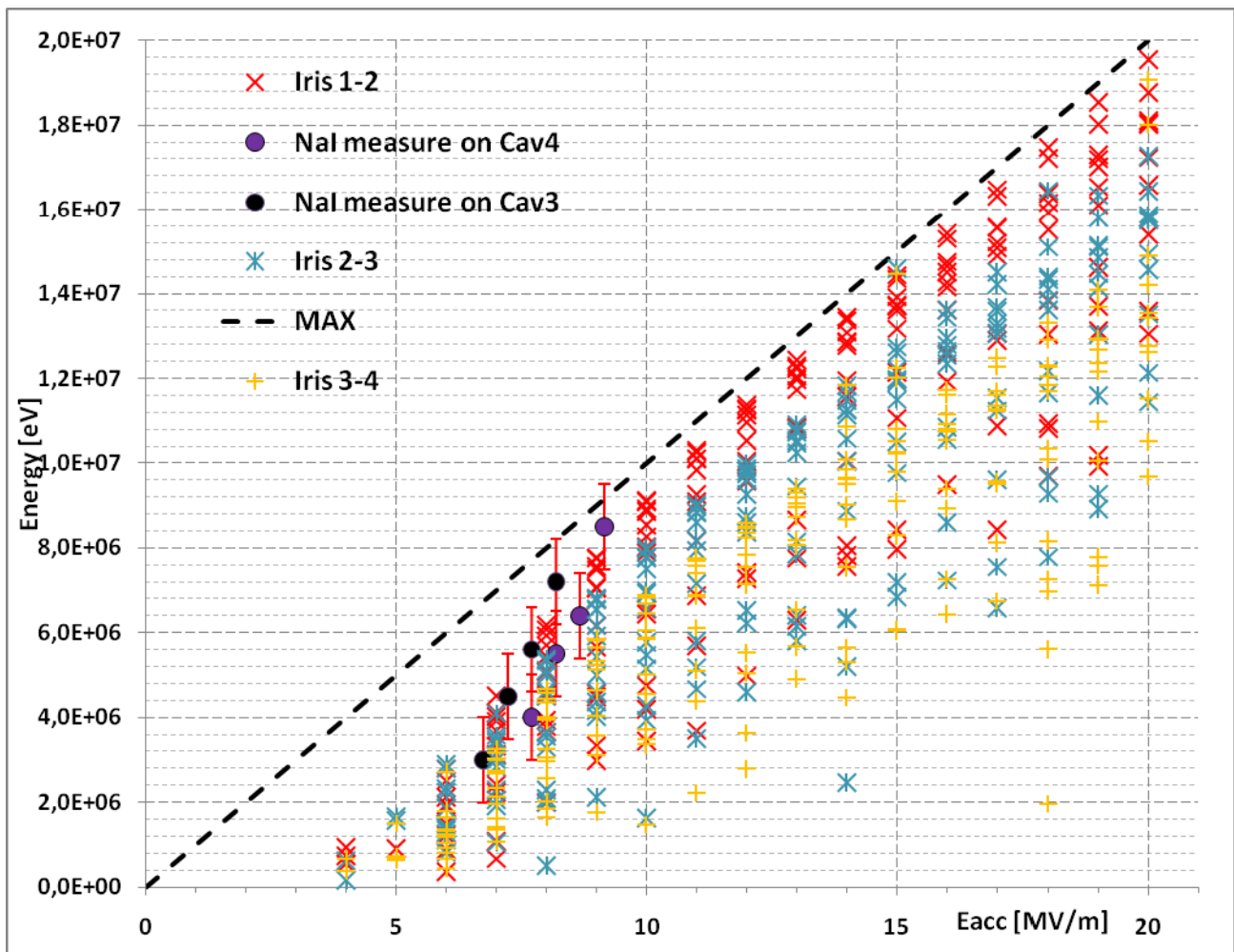


Figure 5. 95 Comparison between energy spectrum produced by emitters on different iris and measured data for cavity #3 (black dots) and cavity #4 (purple dots).

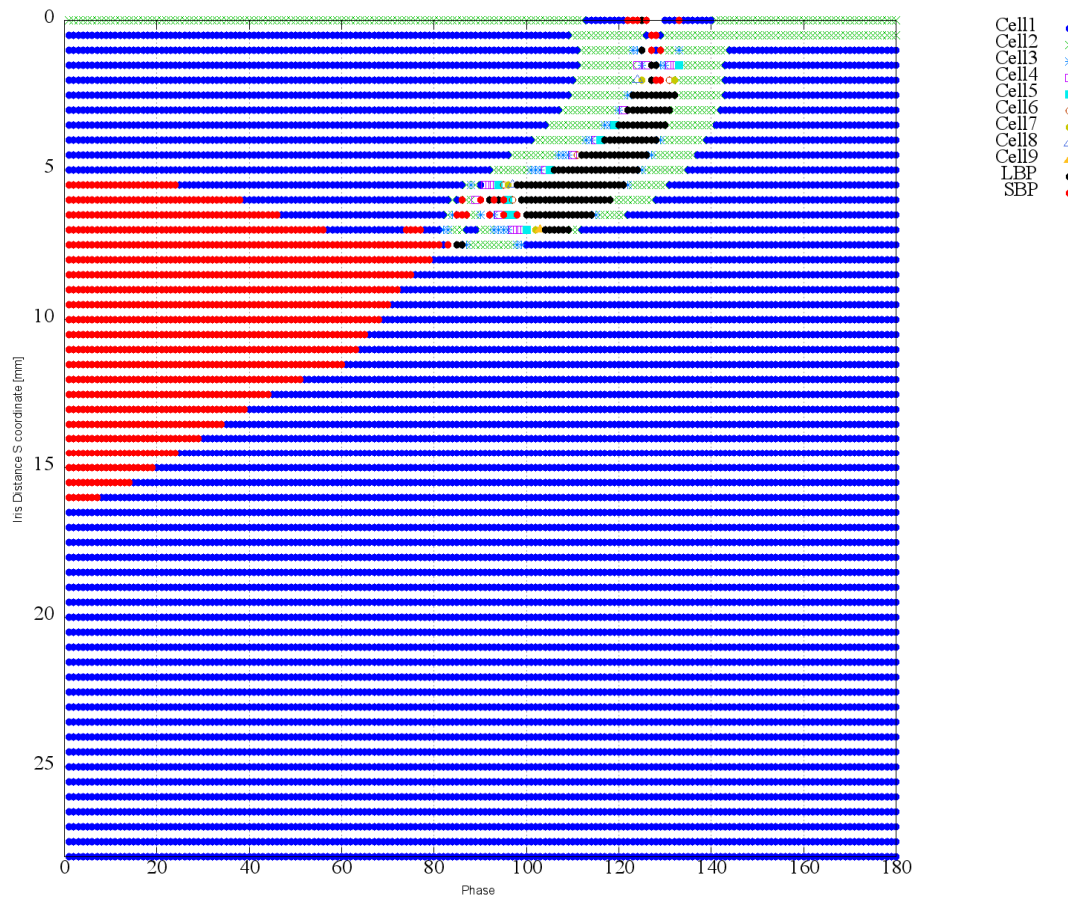


Figure 5. 96 Landing location with respect to emission phase and emitter location from iris between 1st and 2nd cell. Trajectories that can reach the LBP are represented as black dots.

Considering all the information gathered ,the emitter could be located on the iris between the 1st and 2nd cell in the bottom part of the cavity (about meridian 225°) in a region about 5mm long (black area in the above picture)

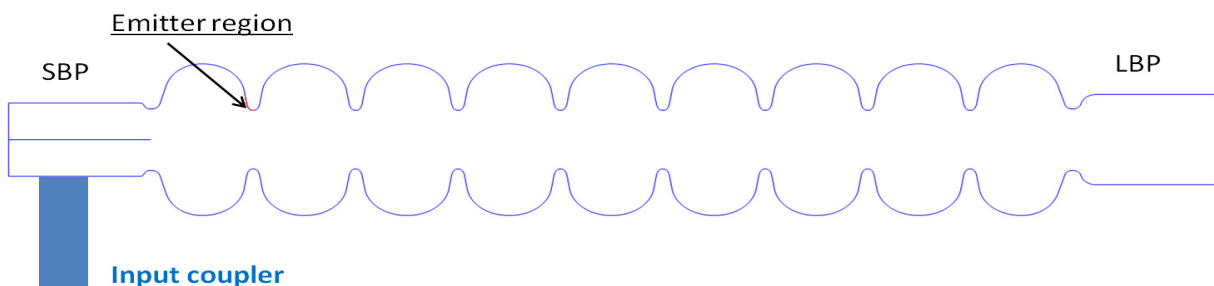


Figure 5. 97 Possible emitters region, in the figure is represented a red line covering 30mm surface length, the estimated region is 7mm too small to be appreciated in the figure.

5.4.8 High power test summary

During the test a drastic change in the radiation pattern and field emission onset respect to the last vertical test undertaken by both cavity was observed. The appearance of new emitter could be related to the cavity handling during Argon purge or final assembly, probably some dust particle landed on the cavity iris a more drastic surface change, like a scratch, is less probable. The simulation results strongly suggest that the emitters location, in both case, are near the cavity entrance (cell 1 and cell 2) facing the SBP (the nearest opening). The emitters location still cannot be pinpointed but their position can be narrowed to about 2cm^2 . It was also possible to determine the emitters number by detecting different x-ray pattern with the PIN diodes ring.

Up to now we have few data to analyze statistically the occurrence of specific locations and radiation onset value, but in the future it could be possible to gather more information and analyze them statistically in order to obtain some insight in the emitters appearance.

With the installed PIN diodes it will be possible to monitor the cavity performance during operation and detect any change in the radiation pattern.

5.5 Cavities model comparison

To end this discussion chapter, comparisons between different cavity models using the same analysis tools developed for the KEK-ERL cavities [18] will be shown. The comparison will be made to have a broad view on field emission effect considering also other superconducting multi-cell cavities like ILC cavity [19, 20] and JLAB Low Loss cavity [21]. The quantities used to create a simulation model are obtained from literature data, they are listed in the next table.

It will be considered a set of emitters located on the first iris in each cavity model, the electron kinetic energy and deposited power on the surface will be calculated and compared considering different operating condition.

The first set of figures represent the electron impact energy and the deposited energy on the cavity surface with respect to the emitter location and RF phase during the emission, will used emitters with $\beta=100$ and an emitting surface of $1 \times 10^{-13} \text{ m}^2$ [22]. The relevant quantities will be calculated for π mode operation at 15MV/m for ERL mod2, 35MV/m for ILC and 12MV/m for JLAB, nominally their working conditions.

Table 5. 9 Cavities model figures of merit.

| Property | KEK-ERL mod2 | ILC | JLAB-LL |
|-------------------------------------|---|---|---|
| Operating field | $15 \frac{\text{MV}}{\text{m}}$ | $35 \frac{\text{MV}}{\text{m}}$ | $12 \frac{\text{MV}}{\text{m}}$ |
| Operation mode | CW | Pulsed (1%) | CW |
| Cavity Length (L) | 103.77 cm ($9 \frac{\lambda}{2}$) | 103.77 cm ($9 \frac{\lambda}{2}$) | 70.18 cm ($7 \frac{\lambda}{2}$) |
| Cavity diameter | 20.66cm | 20.66cm | 17.4cm |
| ω_0 TM010 | 1300 MHz | 1300 MHz | 1495 MHz |
| Temperature | 2K | 2K | 2K |
| Surface resistance (R_s) | 26 n Ω | 26 n Ω | 22 n Ω |
| Accelerating Field (E_{acc}) | $1 \frac{\text{MV}}{\text{m}}$ | $1 \frac{\text{MV}}{\text{m}}$ | $1 \frac{\text{MV}}{\text{m}}$ |
| Power dissipation (P_{loss}) | 111 mW | 102 mW | 49 mW |
| Stored Energy (U) | 0.15 J | 0.13 J | 0.06 J |
| Transit time factor | 0.72 | 0.72 | 0.67 |
| Quality factor (Q_0) | 10^{10} | 10^{10} | $1.2 \cdot 10^{10}$ |
| R/Q | 896 Ω | 1018 Ω | 785 Ω |
| Geometry Factor (G) | 289 Ω | 277 Ω | 281 Ω |
| Iris radius | 4 cm | 3.5 cm | 2.65 cm |
| E_{pk}/E_{acc} | 3.0 | 2.0 | 2.3 |
| H_{pk}/E_{acc} | $42 \frac{\text{Oe}}{\text{MV m}^{-1}}$ | $42 \frac{\text{Oe}}{\text{MV m}^{-1}}$ | $40 \frac{\text{Oe}}{\text{MV m}^{-1}}$ |
| K_{cc} (cell to cell coupling) | 3.8% | 1.87% | 1.49% |

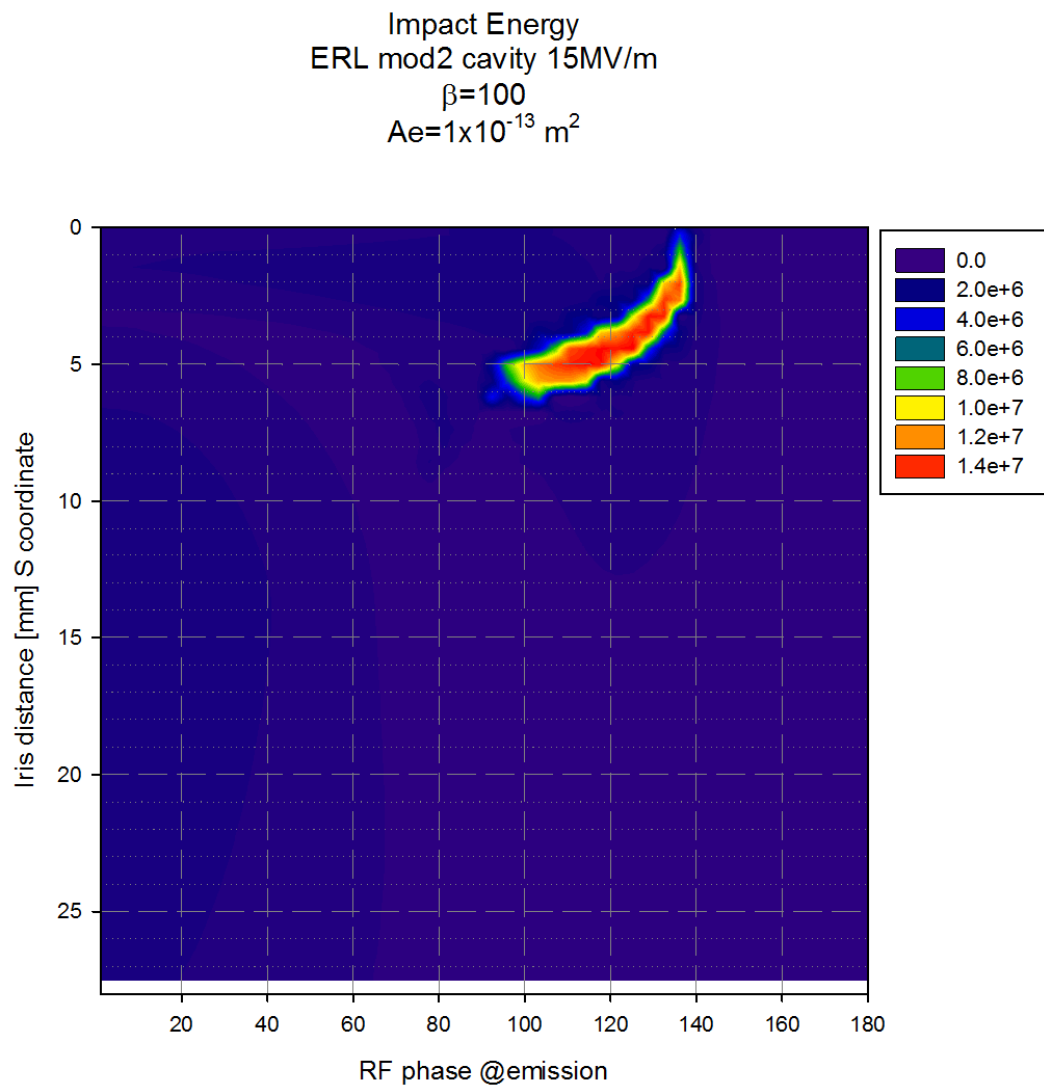


Figure 5. 98 Electron impact energy, ERL mod2 cavity π mode 15MV/m.

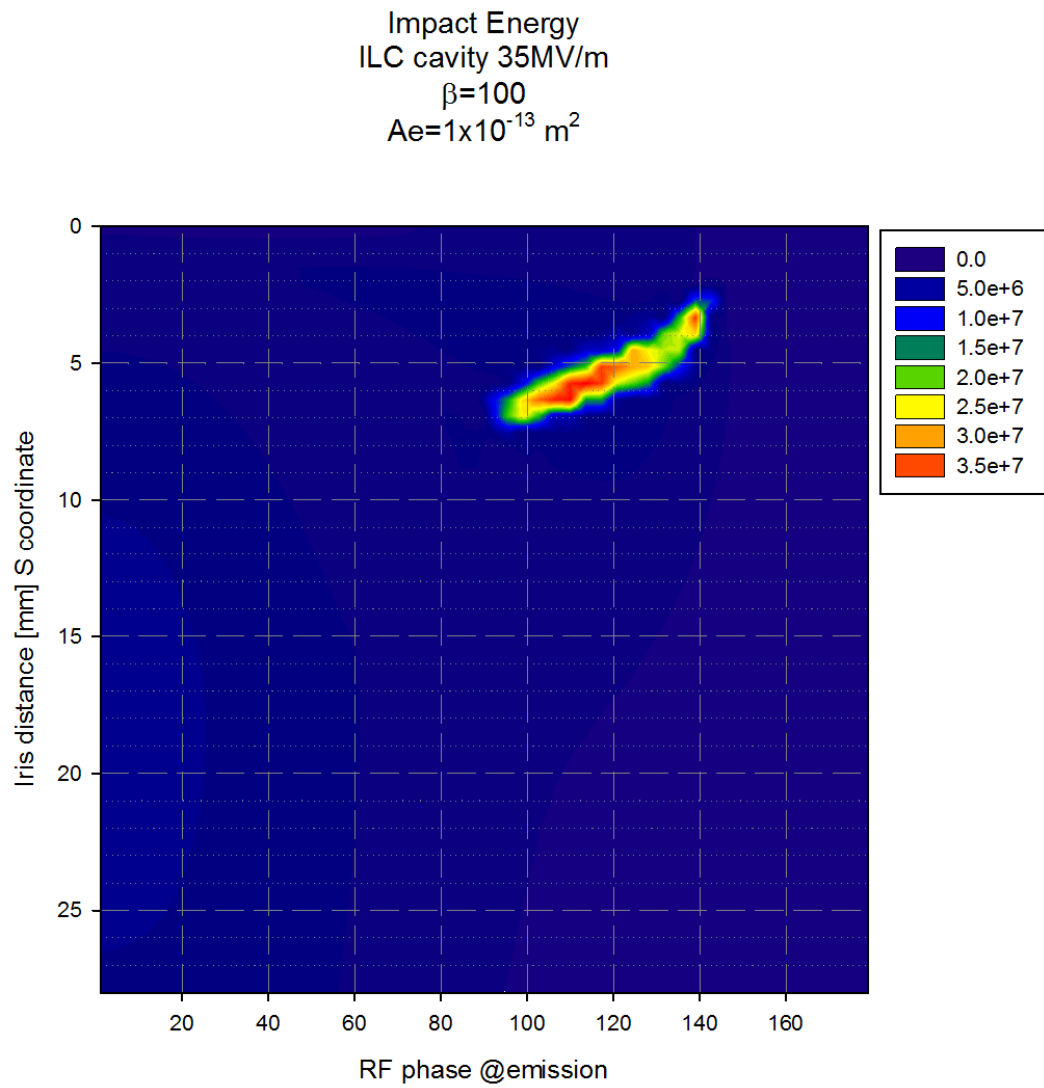


Figure 5.99 Electron impact energy, ILC cavity π mode 35MV/m.

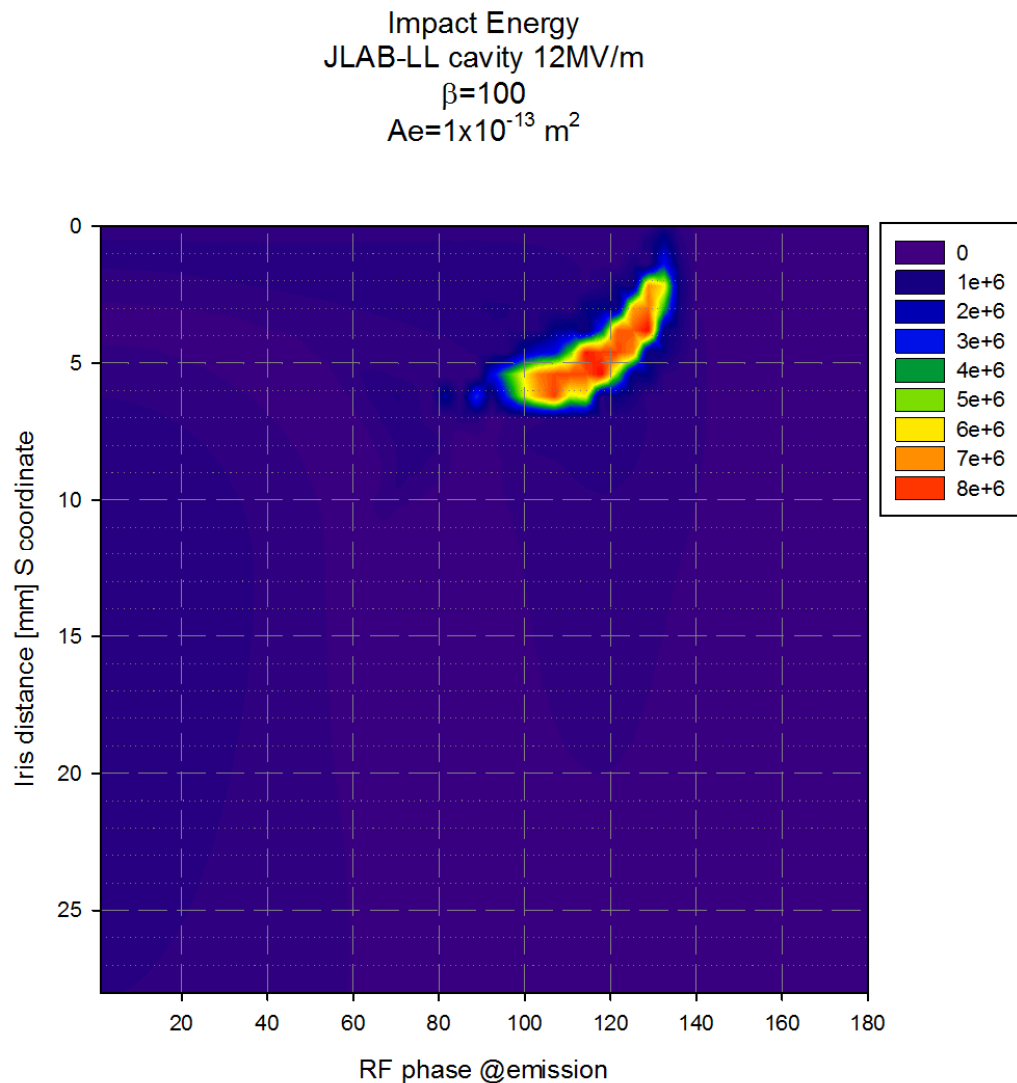


Figure 5.100 Electron impact energy, JLAB-LL cavity π mode 12MV/m.

In the three pictures above, despite some differences in the impact energy value, the high energy region has a similar shape, this area is generated by electrons that fly along the cavity axis and exit from one side. It can be noticed that this region is located near the iris (upper part of the figure) and start after around 90° RF phase and extend up to 140° approximately. Only this location in the space-phase plane has electron trajectories that can fly out of the cavity after traversing it.

Despite the difference in the iris shape, iris aperture, operating frequency and accelerating voltage this region can be found in all three cavity and has a similar shape.

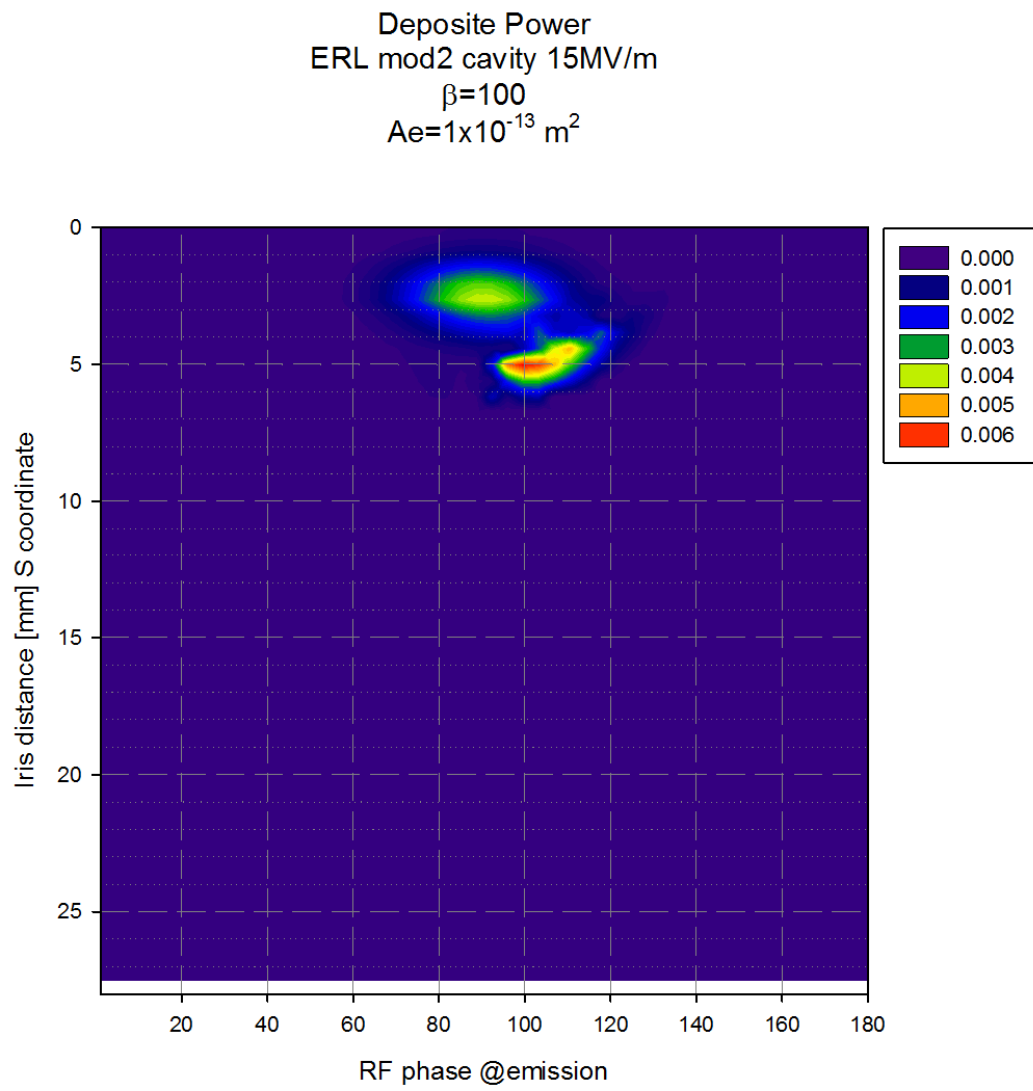


Figure 5.101 Deposited power, ERL mod2 cavity π mode 15MV/m.

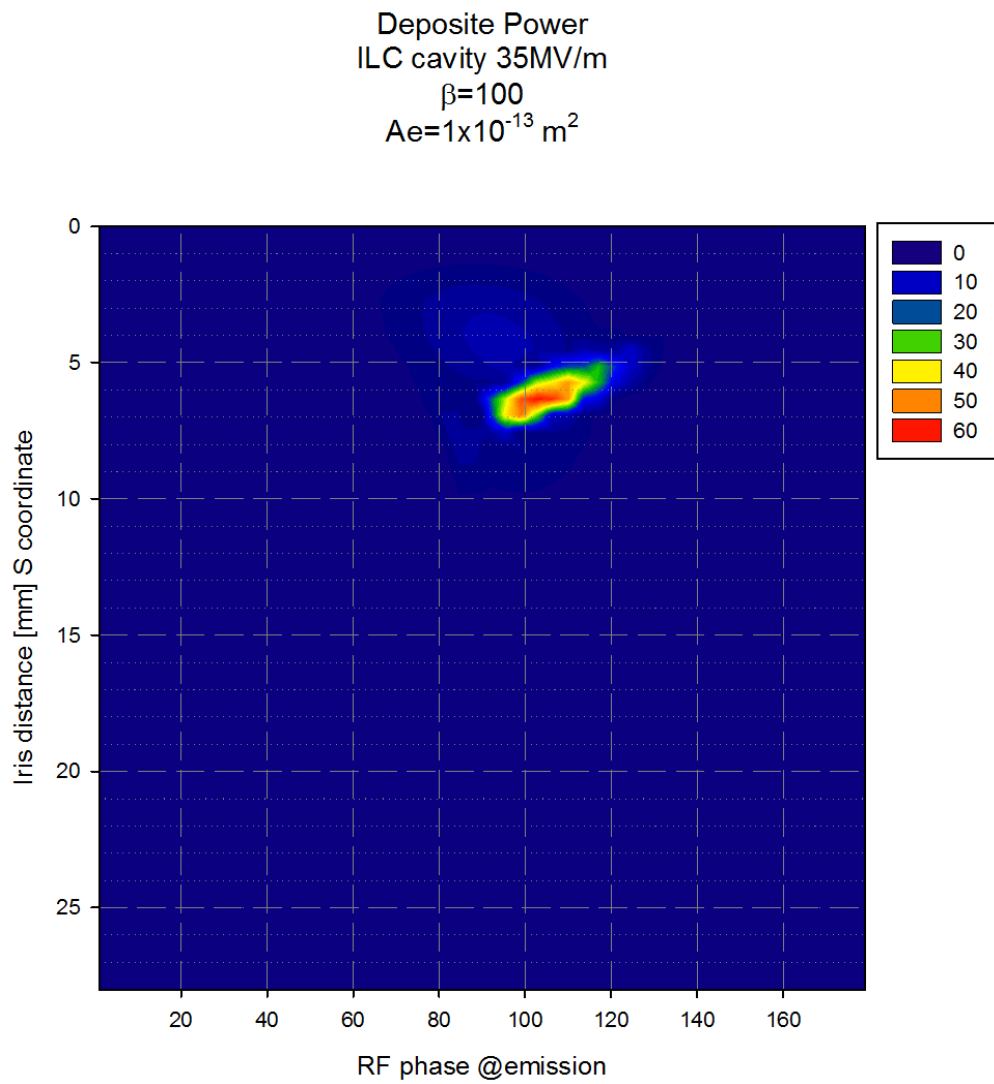


Figure 5.102 Deposited power, ILC cavity π mode 35MV/m.

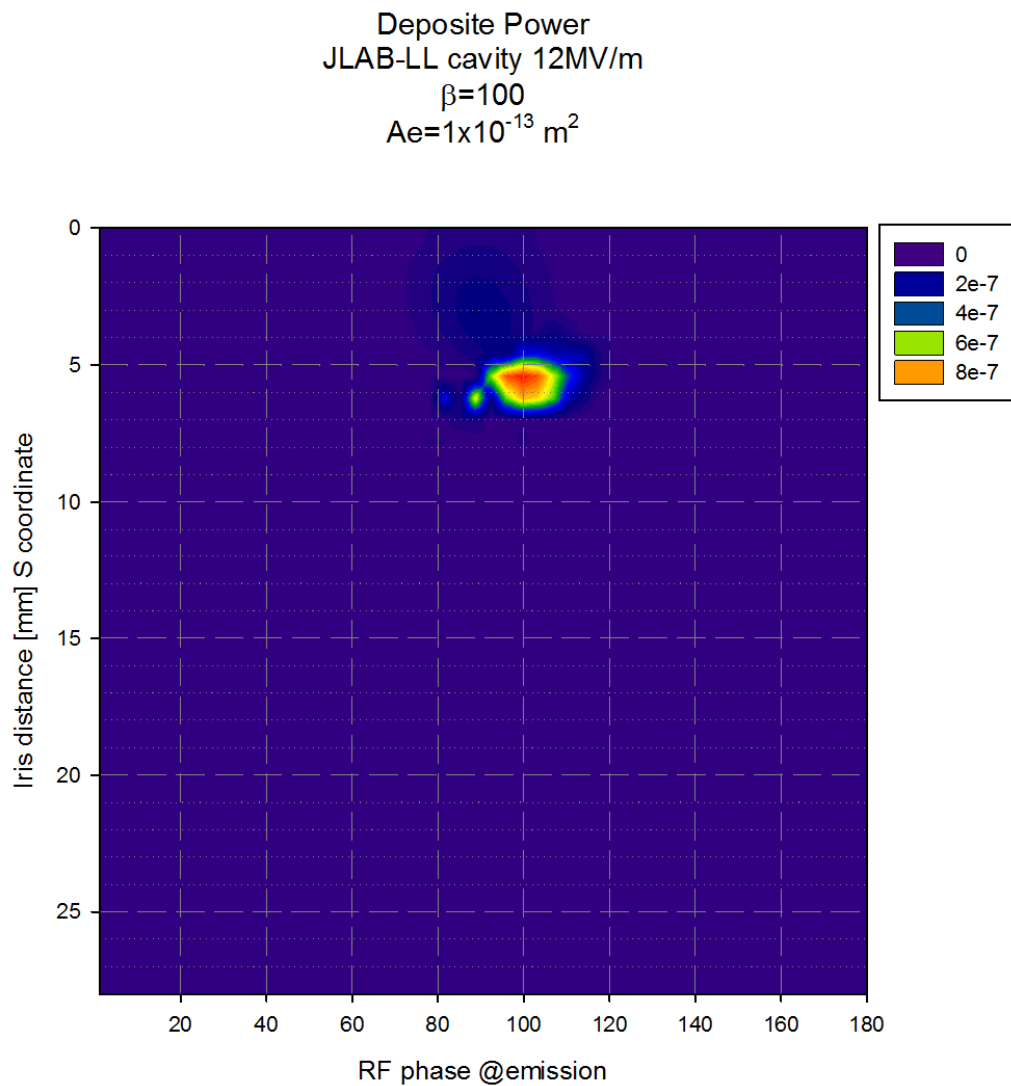


Figure 5.103 Deposited power, JLAB-LL cavity π mode 12MV/m.

5.5.2 Danger area

The picture above represents the deposited power on the cavity surface, at each point amount of power dissipated is calculated from the emitter at the specific RF phase. Also in this case, as seen before, it is possible to notice an area with similar shape and location in all the examined cavity model, despite the difference in its values it can be found in any shape.

In this area, the maximum power dissipation can be found: it is located near the 90° phase due to the fact that the emitted current reach its maximum at that value. Any emitter located in that area can strongly deteriorates the cavity performance increasing the cavity power loss.

5.5.2 Danger length

Next, it is possible to sum up the power dissipated at each phase and plot the result with respect to the emitter location, to compare the three cavity results the power is normalized respect its maximum.

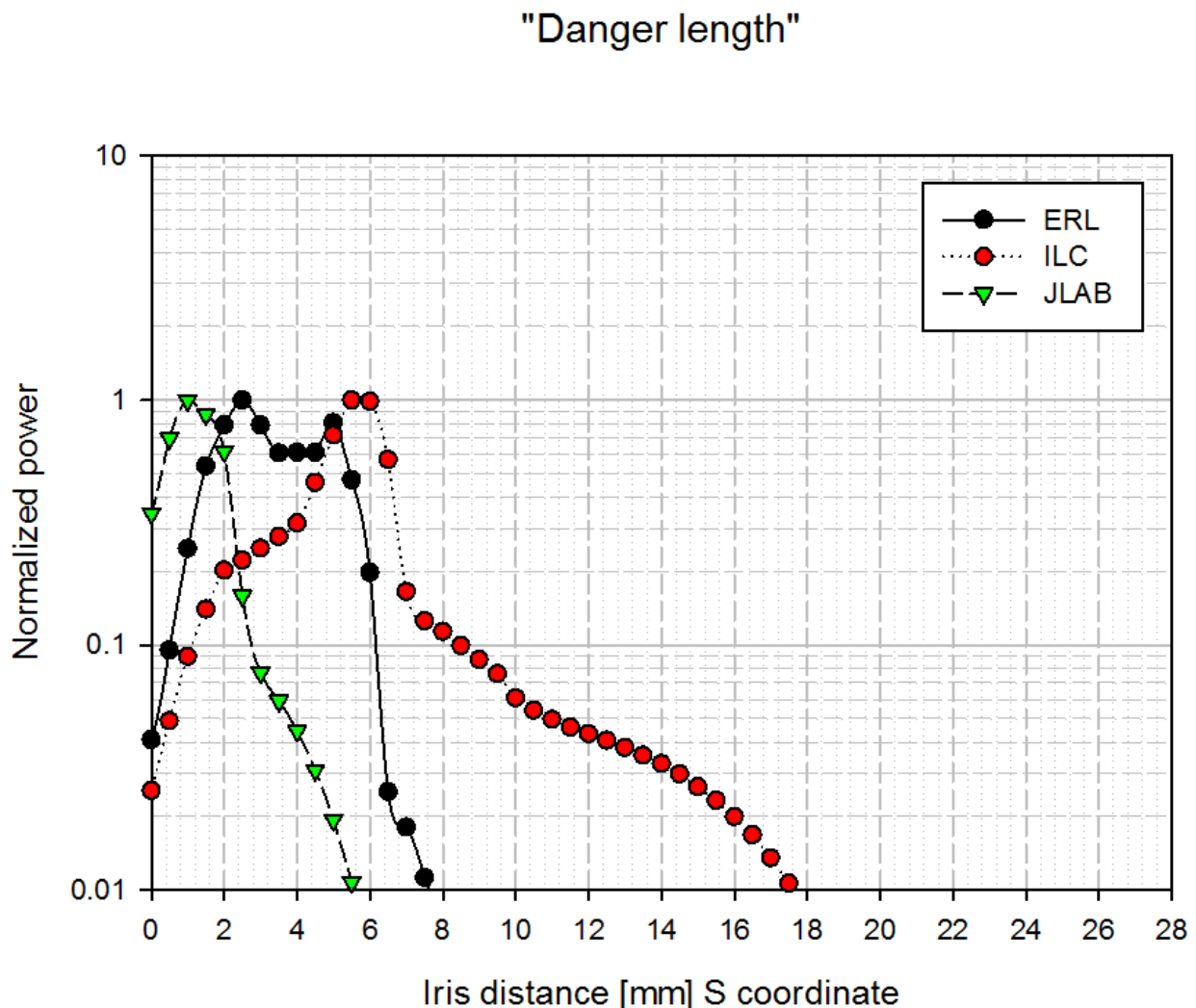


Figure 5.104 Normalized power respect to emitter location for π mode, ERL mod2 at 15MV/m, JLAB-LL at 12MV/m and ILC at 35MV/m.

The logarithmic plot is cut when the power drops to 1/100 of the maximum, so that the region between the iris (left part) and the intercept of the graph with the x-axis account for more than 90% of the total power dissipated. It has different lengths in the three cavity shapes and its dimensions are summarized in the next table.

Table 5. 10 Danger length and area for different cavity models.

| Cavity model | Danger length [mm] | Iris radius [mm] | Danger area [mm ²] |
|--------------|--------------------|------------------|--------------------------------|
| JLAB-LL | 6 | 26.5 | 159 |
| KEK ERL mod2 | 8 | 40 | 320 |
| ILC | 18 | 35 | 630 |

The “danger area” is here defined as the product between the “danger length” and to the iris radius: the bigger is the area, higher is the chance that an emitter is located in a region where it can strongly affect the cavity performance. Roughly, it can be said that respect the JLAB-LL cavity the ERL model has two times the chance that an emitter is located in a danger area while the ILC has a chance four times higher.

Chapter references

1. Furman, M. and M. Pivi, *Probabilistic model for the simulation of secondary electron emission*. Phys. Rev. ST Accel. Beams, 2002. **5**(124404): p. 124404-1.
2. Hirayama, H., et al., *The EGS5 code system*, 2005, United States. Department of Energy.
3. HamatsuPhotonics, *S1223*.
<http://www.hamamatsu.com/us/en/product/category/3100/4001/4103/S1223/index.html>.
4. Knoll, G.F., *Radiation detection and measurement*2010: Wiley. com.
5. Leo, W.R., *Techniques for nuclear and particle physics experiments: a how-to approach*1994: Springer.
6. AnalogDevices, *AD711*. http://www.analog.com/static/imported-files/data_sheets/AD711.pdf.
7. TexasInstruments, *OP07CP*. <http://www.ti.com/lit/ds/symlink/op07c.pdf>.
8. Cenni, E., T. Furuya, and H. Sakai, *Vertical test results on KEK-ERL 9-cell L-band superconducting cavity*. Proceedings of SRF2011, THPO034, Chicago, 2011.
9. Iwashita, Y., Y. Tajima, and H. Hayano, *Development of high resolution camera for observations of superconducting cavities*. Physical Review Special Topics-Accelerators and Beams, 2008. **11**(9): p. 093501.
10. Watanabe, K., et al., *Review of optical inspection methods and results*. Proc. SRF 2009 (Berlin, Germany), 2009.
11. Iwashita, Y., et al., *R&D of Nondestructive Inspection Systems for SRF Cavities*.
12. Sakai, H., et al., *Cavity diagnostics using rotating mapping system for 1.3 GHz ERL 9-cell superconducting cavity*. IPAC. **10**: p. 2950.
13. Fowler, R.H. and L. Nordheim, *Electron emission in intense electric fields*. Proceedings of the Royal Society of London. Series A, Containing Papers of a Mathematical and Physical Character, 1928. **119**(781): p. 173-181.
14. Musser, S.E., *X-ray imaging of superconducting radio frequency cavities*, 2006, Michigan State University.
15. Wang, J. and G. Loew, *Field emission and rf breakdown in high-gradient room-temperature linac structures*. Proc. Joint School RF Engineering for Accelerators, 1997.
16. Latham, R.V., *High voltage vacuum insulation: basic concepts and technological practice*1995: Academic Press.
17. Forbes, R., *Private communication*.
18. Umemori, K., et al. *Design of L-band superconducting cavity for the energy recovery linacs*. in *APAC*. 2007.
19. Phinney, N., N. Toge, and N. Walker, *ILC reference design report volume 3-accelerator*. 2007.
20. Geng, R.-L., *Review of new shapes for higher gradients*. Physica C: Superconductivity, 2006. **441**(1): p. 145-150.

21. Sekutowicz, J., et al., *Low Loss Cavity for the 12 GeV CEBAF Upgrade*. JLAB, TN-02-023, June, 2002.
22. Wiener, J. and H. Padamsee, *Thermal and statistical models for quench in superconducting cavities*. TTC-Report, 2008. **8**: p. 2008.

CHAPTER VI

Conclusion and Outlook

Conclusion

In this dissertation the field emission process inside SRF cavities and how it can affect their performance was extensively discussed. The vertical test data and the x-ray pattern detected with the rotating mapping system have proven to be a valuable asset in combination with a newly developed analysis method. Indeed, it was possible to locate and enumerate the emitters through an insight in the variegated radiation pattern detected.

The same tools developed to analyze the data were also used to understand the complex relation between field emission effect, cavity geometry and their operating conditions. They can be used during cavity design to determine how each geometry can be affected by field emission phenomena. In every analyzed geometry it was possible to identify a specific region where field emission effects can be the most severe. This is of critical importance as any improvement toward the reduction of that area can strongly enhance the performance of the cavity.

For the first time it was possible to gather and analyze valuable information about emitters number and location during high power test where the cavities were installed inside the cryomodule. At the same time it was possible to notice a drastic change in the radiation pattern and field emission onset respect to last vertical test for both cavities. Such deduction was possible by comparing the detailed information obtained from the rotating mapping system and the signal from the PIN diodes installed in the cryomodule. The most probable location was determined to be in the first two cells near the input coupler: they are located on the side of iris facing the input coupler and their region is about 2cm^2 . Excluding a radical change in cavity surface like a scratch that can occur after a vertical test, it is more likely that some dust particles landed on the iris between the two tests, during the Argon purging, during the final assembly or during the cavity evacuation. The estimated location strongly suggests that the particles are coming from outside the cavity.

Outlook

The methods and simulation described in this dissertation have proven to be able to describe field emission effect in SRF cavities quite accurately. It can be even more improved in order to calculate possible quenches location due to high field emission or calculate more precisely the interaction between the particle shower and the PIN diodes. Nevertheless, it can be used at this stage to evaluate various cavity design in order to assess the cavity performance degradation with respect to the different geometry choices.

Another important aspect that deserves more investigation is the severe degradation of cavity performance during the high power test despite the good performance during the vertical test. In this direction, it should be examined how dust particle can move inside the cavity, which is the most common dust composition and geometry at microscopic level. At the same time, the x-ray detection system around the cryomodule should be improved. Indeed, more sensitive measures can lead to a more accurate emitter localization. In this sense, designing a detection system that could be inserted in the helium jacket is a desirable feature as in other high energy physics fields quartz fiber are successfully used for radiation and particle detection due their radiation hardness [1]. This ability combined with their small dimension make them good candidates for a new detection system that can be installed during cavity operation, in order to monitor any change in the radiation pattern responsible for performance degradation.

Chapter references

1. Akchurin, N. and R. Wigmans, *Quartz fibers as active elements in detectors for particle physics*. Review of scientific instruments, 2003. **74**(6): p. 2955-2972.

Acknowledgments

This work would not have been possible without the help and guidance of several individuals to whom I am very grateful.

I would like to thank the Japan Ministry of Education, Culture, Sports, Science and Technology (MEXT) for the scholarship that allowed me to study, work and live in Japan for three years. Thank to Professor S. Kamada for his help through the application process and the invitation for interview at KEK.

I will be always in debt with all the ERL superconducting cavities group. Professor T. Furuya for his guidance and support along my Ph.D studies, I will miss our Thursday meeting. H. Sakai and K. Umemori for their patience and all the fruitful discussions that helped me to improve. M. Sawamura to introduce me to Fishpact. K. Shinoe and M. Satoh for their help during experiments preparation.

My sincere thanks to Professor Y. Namito for helping me with EGS5 code. I am grateful to Professor S. Sasaki for allowing me to use the NaI scintillator and for the useful discussions concerning the data analysis.

On personal level I am very thankful to all Fujitsu Yutenkai members for their support during my stay. Ariga sensei you will be forever with me. Nakano and Koibuchi sensei thank for your kindness and guidance. Keisuke you are my big brother, thanks to make me feel at home with my Japanese family.

Thank to my parents to be always on my side and constantly encourage me.

Thank to Nathanaelle, I would not be able to finish this dissertation without your support and help...we are a good team.

Appendix

A. SuperFish code

ERL model 2 cavity

Design beta = 1.0

Resonant frequency = 1300 MHz, Bore radius = 4.0 cm

```

&REG KPROB=1           ; Superfish problem
MAT=1                 ; Material air or empty space
FREQ=1300             ; Mode frequency
CLENGTH=103.774312   ; Normalization length
BETAD=1.000000       ; Design beta
NBSUP=1,NBSLO=0,NBSRT=1,NBSLF=1 ; Boundary conditions
LINES=1              ; Fix internal points on line regions
ICYLIN=1             ; X=>Z,Y=>R, cylindrical coordinates
NORM=1               ; Normalize to EZEROT
;EZERO=2.60066647778E+07 ; Accelerating field
EZEROT=1.0e6         ;
; SCCAV=6             ; 6-cell superconducting cavity
RMASS=-1             ; Rest mass value or indicator
EPSO=1.0E-6          ; Mesh optimization convergence parameter
IRTYPE=1             ; Rs method: Superconductor formula
TEMPK=2              ; Superconductor temperature, degrees K
TC=9.2               ; Critical temperature, degrees K
RESIDR=1.0E-08       ; Residual resistance
XDRI=51.889279       ; Drive point X coordinate
YDRI=9.330000        ; Drive point Y coordinate
; DSLOPE=-1          ; Allow convergence in 1 iteration
DX=0.1               ; Mesh spacing in X direction
; Y line-region physical locations:
; YREG=0.2828427124746,0.8485281374239,2.510050506339,3.075735931288,
; Y line-region logical locations:
; LREG=1,3,5,8,10,
; LMAX=62            ; Row number for Y = YMAX
&

; *** left beampipe ***
&po x = 0.000000 , y = 0.000000 &
&po nt = 1, x = -16.000000 , y = 0.000000 &
&po nt = 1, x = -16.000000 , y = 5.000000 &

&po nt = 1, x = -1.22 , y = 5.0 &
&po nt = 2, x0 = -1.22 , y0 = 4.516 , a = 0.484, b = 0.484, x = 0.4578378 , y = 0.156973 &
&po nt = 2, x0 = -0.1 , y0 = 4.9 , a = 0.7 , b = 0.7 , x = 0.0 , y = -0.7 &

```

&po nt = 1, x = 0.000000 , y = 4.200000 &

; *** cell number 1 ***

&po nt = 1, x = 0.100000, y = 4.200000 &

&po nt = 2, x0 = 0.100000, y0 = 5.165028, a = 0.965028, b= 0.965028, x = 0.928359, y = -0.263495 &

&po nt = 1, x = 1.723155, y = 7.349478 &

&po nt = 2, x0 = 5.667362, y0 = 6.230000, a = 4.100000, b= 4.100000, x = 0.000000, y = 4.100000 &

&po nt = 1, x = 5.767362, y = 10.330000 &

&po nt = 1, x = 5.867362, y = 10.330000 &

&po nt = 2, x0 = 5.867362, y0 = 6.130000, a = 4.683000, b= 4.200000, x = 4.634188, y = 0.604825 &

&po nt = 1, x = 10.794881, y = 4.927018 &

&po nt = 2, x0 = 11.432602, y0 = 5.340919, a = 0.670459, b= 1.340919, x = 0.000000, y = -1.340919 &

&po nt = 1, x = 11.532602, y = 4.000000 &

; *** cell number 2 ***

&po nt = 1, x = 11.632602, y = 4.000000 &

&po nt = 2, x0 = 11.632602, y0 = 5.340919, a = 0.670459, b= 1.340919, x = 0.637720, y = -0.413901 &

&po nt = 1, x = 12.563653, y = 6.734825 &

&po nt = 2, x0 = 17.197841, y0 = 6.130000, a = 4.683000, b= 4.200000, x = 0.000000, y = 4.200000 &

&po nt = 1, x = 17.297841, y = 10.330000 &

&po nt = 1, x = 17.397841, y = 10.330000 &

&po nt = 2, x0 = 17.397841, y0 = 6.130000, a = 4.683000, b= 4.200000, x = 4.634188, y = 0.604825 &

&po nt = 1, x = 22.325360, y = 4.927018 &

&po nt = 2, x0 = 22.963081, y0 = 5.340919, a = 0.670459, b= 1.340919, x = 0.000000, y = -1.340919 &

&po nt = 1, x = 23.063081, y = 4.000000 &

; *** cell number 3 ***

&po nt = 1, x = 23.163081, y = 4.000000 &

&po nt = 2, x0 = 23.163081, y0 = 5.340919, a = 0.670459, b= 1.340919, x = 0.637720, y = -0.413901 &

&po nt = 1, x = 24.094132, y = 6.734825 &

&po nt = 2, x0 = 28.728320, y0 = 6.130000, a = 4.683000, b= 4.200000, x = 0.000000, y = 4.200000 &

&po nt = 1, x = 28.828320, y = 10.330000 &

&po nt = 1, x = 28.928320, y = 10.330000 &

&po nt = 2, x0 = 28.928320, y0 = 6.130000, a = 4.683000, b= 4.200000, x = 4.634188, y = 0.604825 &

&po nt = 1, x = 33.855840, y = 4.927018 &
&po nt = 2, x0 = 34.493560, y0 = 5.340919, a = 0.670459, b= 1.340919, x = 0.000000, y = -
1.340919 &
&po nt = 1, x = 34.593560, y = 4.000000 &

; *** cell number 4 ***
&po nt = 1, x = 34.693560, y = 4.000000 &
&po nt = 2, x0 = 34.693560, y0 = 5.340919, a = 0.670459, b= 1.340919, x = 0.637720, y = -
0.413901 &
&po nt = 1, x = 35.624611, y = 6.734825 &
&po nt = 2, x0 = 40.258799, y0 = 6.130000, a = 4.683000, b= 4.200000, x = 0.000000, y = -
4.200000 &
&po nt = 1, x = 40.358799, y = 10.330000 &
&po nt = 1, x = 40.458799, y = 10.330000 &
&po nt = 2, x0 = 40.458799, y0 = 6.130000, a = 4.683000, b= 4.200000, x = 4.634188, y = -
0.604825 &
&po nt = 1, x = 45.386319, y = 4.927018 &
&po nt = 2, x0 = 46.024039, y0 = 5.340919, a = 0.670459, b= 1.340919, x = 0.000000, y = -
1.340919 &
&po nt = 1, x = 46.124039, y = 4.000000 &

; *** cell number 5 ***
&po nt = 1, x = 46.224039, y = 4.000000 &
&po nt = 2, x0 = 46.224039, y0 = 5.340919, a = 0.670459, b= 1.340919, x = 0.637720, y = -
0.413901 &
&po nt = 1, x = 47.155090, y = 6.734825 &
&po nt = 2, x0 = 51.789279, y0 = 6.130000, a = 4.683000, b= 4.200000, x = 0.000000, y = -
4.200000 &
&po nt = 1, x = 51.889279, y = 10.330000 &
&po nt = 1, x = 51.989279, y = 10.330000 &
&po nt = 2, x0 = 51.989279, y0 = 6.130000, a = 4.683000, b= 4.200000, x = 4.634188, y = -
0.604825 &
&po nt = 1, x = 56.916798, y = 4.927018 &
&po nt = 2, x0 = 57.554518, y0 = 5.340919, a = 0.670459, b= 1.340919, x = 0.000000, y = -
1.340919 &
&po nt = 1, x = 57.654518, y = 4.000000 &

; *** cell number 6 ***
&po nt = 1, x = 57.754518, y = 4.000000 &
&po nt = 2, x0 = 57.754518, y0 = 5.340919, a = 0.670459, b= 1.340919, x = 0.637720, y = -
0.413901 &
&po nt = 1, x = 58.685570, y = 6.734825 &
&po nt = 2, x0 = 63.319758, y0 = 6.130000, a = 4.683000, b= 4.200000, x = 0.000000, y = -
4.200000 &
&po nt = 1, x = 63.419758, y = 10.330000 &

&po nt = 1, x = 63.519758, y = 10.330000 &
&po nt = 2, x0 = 63.519758, y0 = 6.130000, a = 4.683000, b= 4.200000, x = 4.634188, y = 0.604825 &
&po nt = 1, x = 68.447277, y = 4.927018 &
&po nt = 2, x0 = 69.084997, y0 = 5.340919, a = 0.670459, b= 1.340919, x = 0.000000, y = -1.340919 &
&po nt = 1, x = 69.184997, y = 4.000000 &

; *** cell number 7 ***

&po nt = 1, x = 69.284997, y = 4.000000 &
&po nt = 2, x0 = 69.284997, y0 = 5.340919, a = 0.670459, b= 1.340919, x = 0.637720, y = -0.413901 &
&po nt = 1, x = 70.216049, y = 6.734825 &
&po nt = 2, x0 = 74.850237, y0 = 6.130000, a = 4.683000, b= 4.200000, x = 0.000000, y = 4.200000 &
&po nt = 1, x = 74.950237, y = 10.330000 &
&po nt = 1, x = 75.050237, y = 10.330000 &
&po nt = 2, x0 = 75.050237, y0 = 6.130000, a = 4.683000, b= 4.200000, x = 4.634188, y = 0.604825 &
&po nt = 1, x = 79.977756, y = 4.927018 &
&po nt = 2, x0 = 80.615476, y0 = 5.340919, a = 0.670459, b= 1.340919, x = 0.000000, y = -1.340919 &
&po nt = 1, x = 80.715476, y = 4.000000 &

; *** cell number 8 ***

&po nt = 1, x = 80.815476, y = 4.000000 &
&po nt = 2, x0 = 80.815476, y0 = 5.340919, a = 0.670459, b= 1.340919, x = 0.637720, y = -0.413901 &
&po nt = 1, x = 81.746528, y = 6.734825 &
&po nt = 2, x0 = 86.380716, y0 = 6.130000, a = 4.683000, b= 4.200000, x = 0.000000, y = 4.200000 &
&po nt = 1, x = 86.480716, y = 10.330000 &
&po nt = 1, x = 86.580716, y = 10.330000 &
&po nt = 2, x0 = 86.580716, y0 = 6.130000, a = 4.683000, b= 4.200000, x = 4.634188, y = 0.604825 &
&po nt = 1, x = 91.508235, y = 4.927018 &
&po nt = 2, x0 = 92.145956, y0 = 5.340919, a = 0.670459, b= 1.340919, x = 0.000000, y = -1.340919 &
&po nt = 1, x = 92.245956, y = 4.000000 &

; *** cell number 9 ***

&po nt = 1, x = 92.345956, y = 4.000000 &
&po nt = 2, x0 = 92.345956, y0 = 5.340919, a = 0.670459, b= 1.340919, x = 0.637720, y = -0.413901 &
&po nt = 1, x = 93.277007, y = 6.734825 &

&po nt = 2, x0 = 97.911195, y0 = 6.130000, a = 4.683000, b= 4.200000, x = 0.000000, y = 4.200000 &

&po nt = 1, x = 98.011195, y = 10.330000 &

&po nt = 1, x = 98.111195, y = 10.330000 &

&po nt = 2, x0 = 98.111195, y0 = 6.130000, a = 4.200000, b= 4.200000, x = 4.014476, y = 1.234496 &

&po nt = 1, x = 102.928352, y = 4.754249 &

&po nt = 2, x0 = 103.678652, y0 = 4.984974, a = 0.784974, b= 0.784974, x = 0.000000, y = -0.784974 &

&po nt = 1, x = 103.778652, y = 4.200000 &

; *** right beampipe ***

&po nt = 1, x=103.847652, y=4.2 &

&po nt=2, x0=103.847652, y0=5.1, a=0.9, b=0.9, X= 0.8685590, Y= -0.2358079 &

&po nt=2, x0=106.397652, y0=4.4076923, a=1.7423077, b=1.7423077, X=0, Y=1.7423077 &

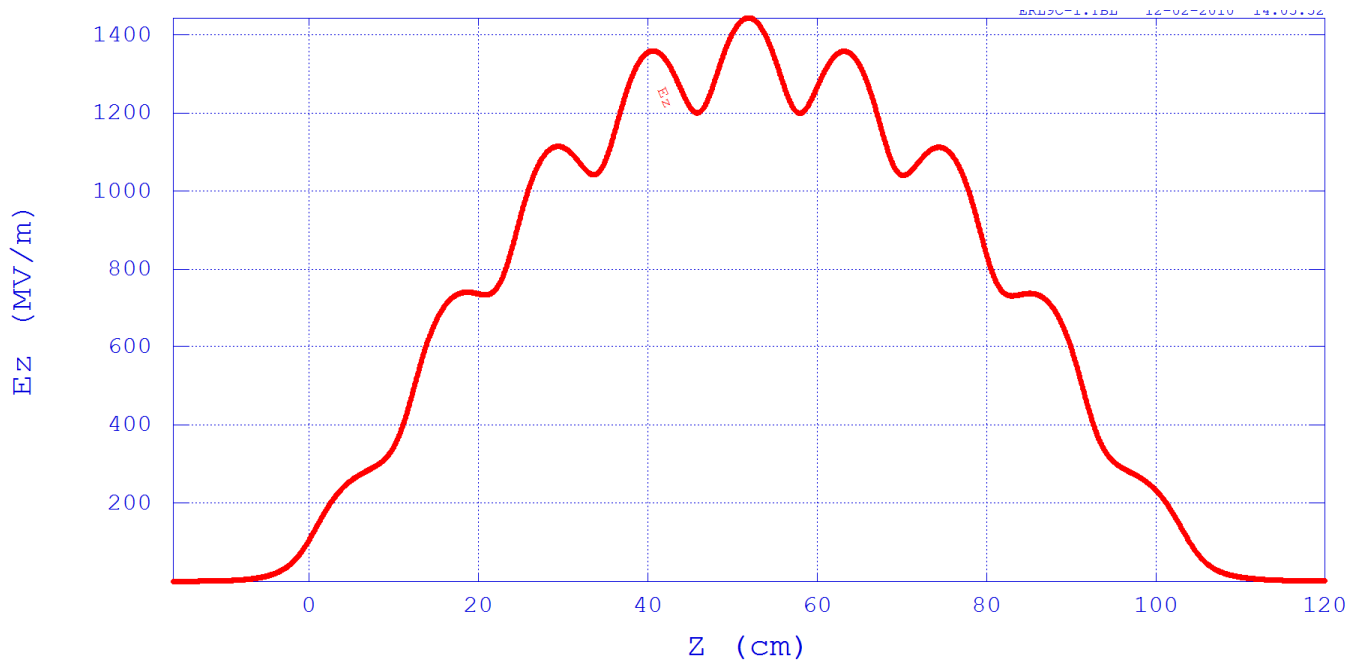
&po nt = 1, x = 120.278652 , y = 6.150000 &

&po nt = 1, x = 120.278652 , y = 0.000000 &

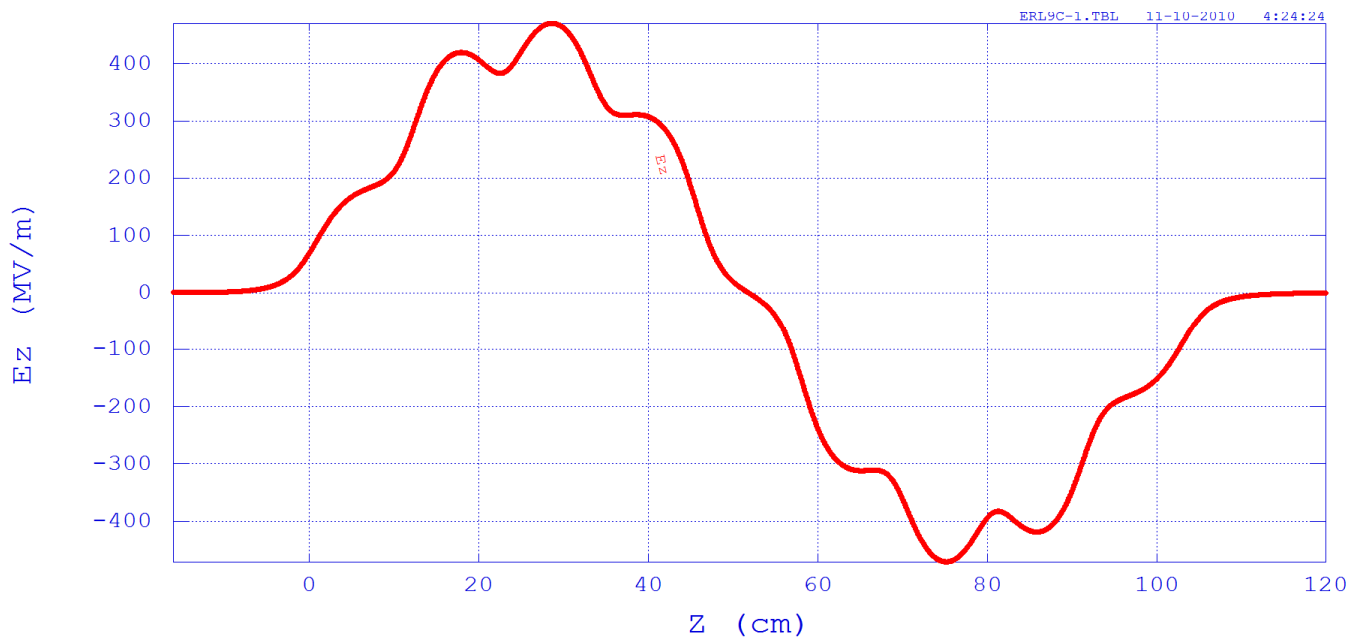
&po nt = 1, x = 0.000000 , y = 0.000000 &

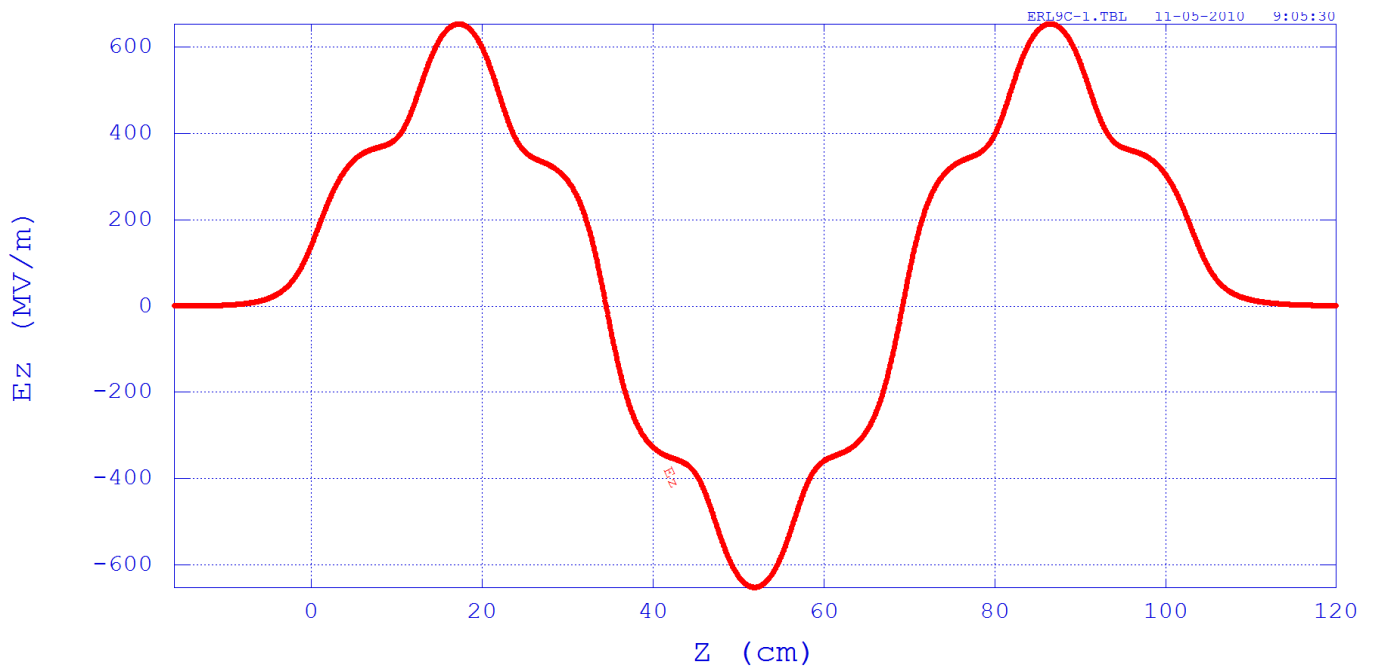
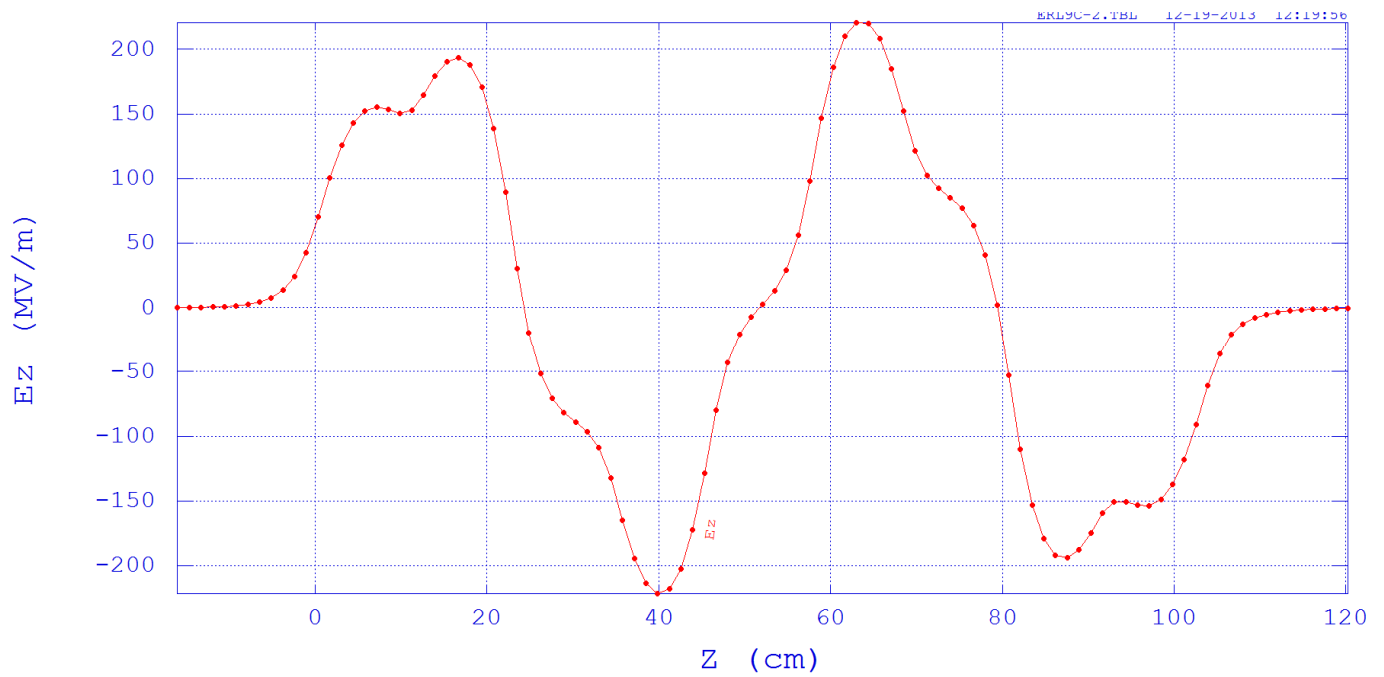
B. Passband modes

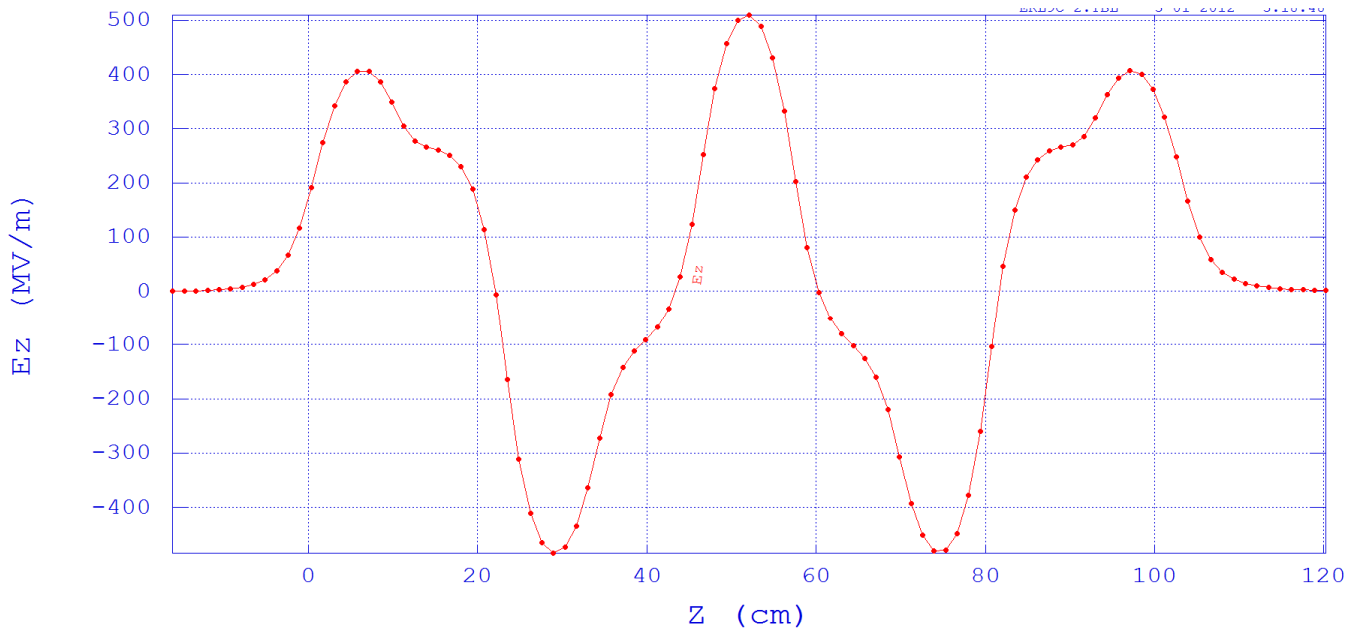
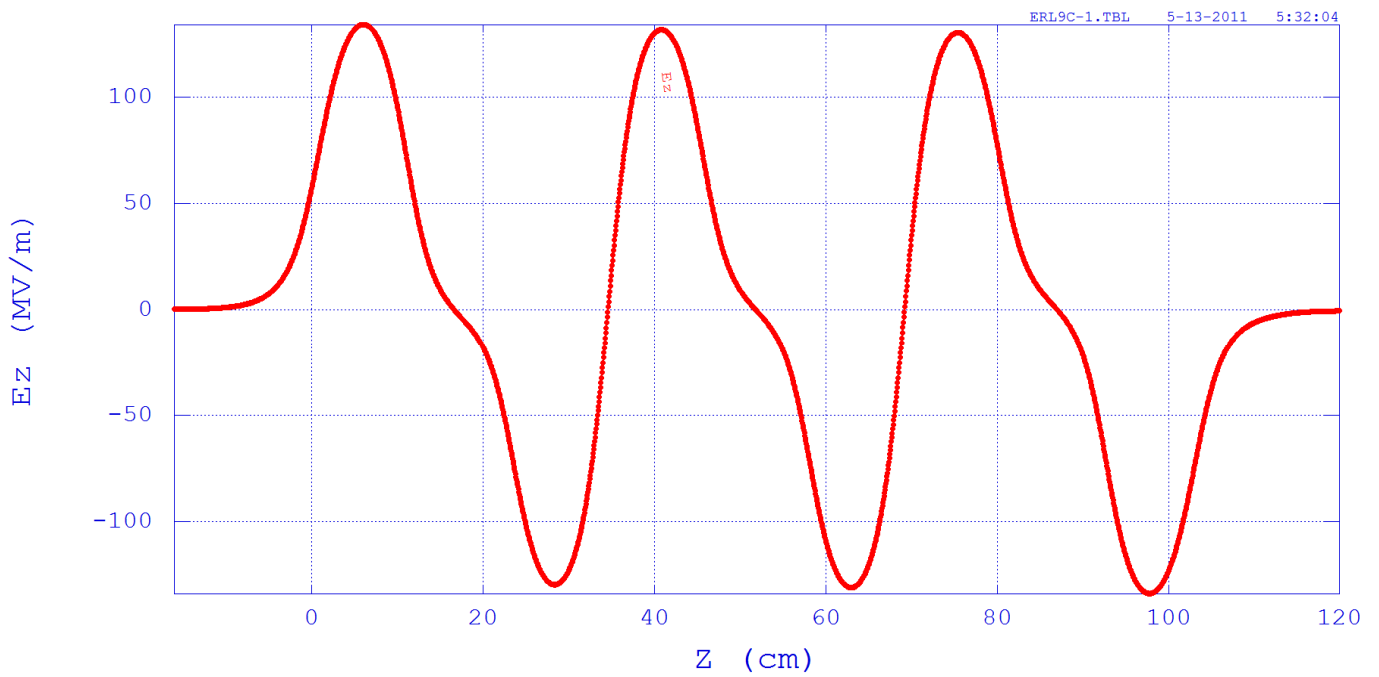
1/9 π mode

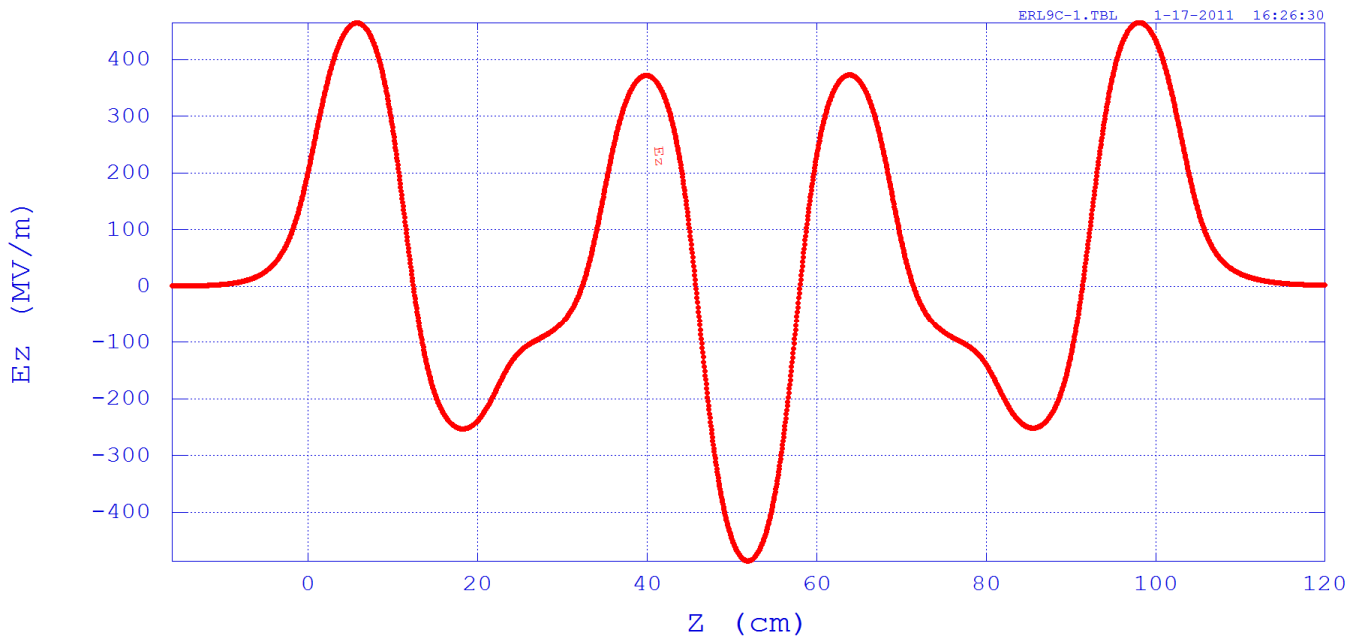
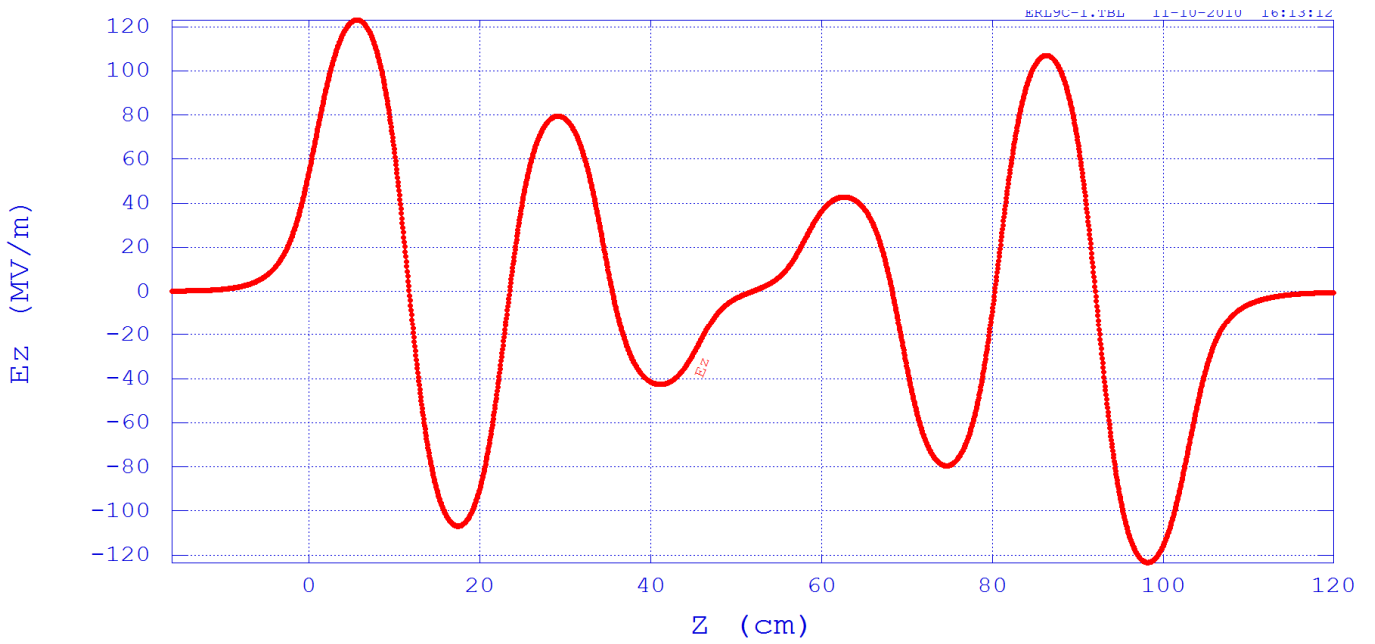


2/9 π mode



3/9 π mode4/9 π mode

5/9 π mode6/9 π mode

7/9 π mode8/9 π mode

C. FishPact Runge-Kutta implementation (p function)

```

while (!impact) /* loop through each runge-kutta until impact
happens */
{
    /*first, calculate the momentum shift */
    Pf=p_function (En,Bn,Pn,t,frequency);
    P1.x=dt*Pf.x;
    P1.y=dt*Pf.y;
    P1.z=dt*Pf.z;

    Ptemp.x=Pn.x+P1.x/2.0;Ptemp.y=Pn.y+P1.y/2.0;Ptemp.z=Pn.z+P1.z/2.0;
    Pf=p_function (En,Bn,Ptemp,t+dt/2.0,frequency);
    P2.x=dt*Pf.x;
    P2.y=dt*Pf.y;
    P2.z=dt*Pf.z;

    Ptemp.x=Pn.x+P2.x/2.0;Ptemp.y=Pn.y+P2.y/2.0;Ptemp.z=Pn.z+P2.z/2.0;
    Pf=p_function (En,Bn,Ptemp,t+dt/2.0,frequency);
    P3.x=dt*Pf.x;
    P3.y=dt*Pf.y;
    P3.z=dt*Pf.z;

    Ptemp.x=Pn.x+P3.x;Ptemp.y=Pn.y+P3.y;Ptemp.z=Pn.z+P3.z;
    Pf=p_function (En,Bn,Ptemp,t+dt,frequency);
    P4.x=dt*Pf.x;
    P4.y=dt*Pf.y;
    P4.z=dt*Pf.z;

    Pn1.x=Pn.x+P1.x/6.0+P2.x/3.0+P3.x/3.0+P4.x/6;
    Pn1.y=Pn.y+P1.y/6.0+P2.y/3.0+P3.y/3.0+P4.y/6;
    Pn1.z=Pn.z+P1.z/6.0+P2.z/3.0+P3.z/3.0+P4.z/6;

    /* compute the new velocity */
    v.x=C_light*Pn1.x/sqrt (E_mass*E_mass*C_light*C_light+
        Pn1.x*Pn1.x+Pn1.y*Pn1.y+Pn1.z*Pn1.z);
    v.y=C_light*Pn1.y/sqrt (E_mass*E_mass*C_light*C_light+
        Pn1.x*Pn1.x+Pn1.y*Pn1.y+Pn1.z*Pn1.z);
    v.z=C_light*Pn1.z/sqrt (E_mass*E_mass*C_light*C_light+
        Pn1.x*Pn1.x+Pn1.y*Pn1.y+Pn1.z*Pn1.z);
    /* compute the new location */
    Ln1.x=Ln.x+v.x*dt;
    Ln1.y=Ln.y+v.y*dt;
    Ln1.z=Ln.z+v.z*dt;
    /*check if there is an impact*/
    Bn=B (Ln1,ascale,stringSolutionName); Bn.x*=Eacc; Bn.y*=Eacc;
Bn.z*=Eacc;
    En=E (Ln1,ascale,stringSolutionName); En.x*=Eacc; En.y*=Eacc; En.z*=Eacc;

```

List of figures

Chapter I

| | |
|--|----|
| Figure 1.1 Schematic view of the c-ERL [5, 6]. | 4 |
| Figure 1.2 Schematic view of the ERL (From Energy Recovery Linac Preliminary Design Report) [5]. | 6 |
| Figure 1.3 KEK-ERL model 2 superconducting cavity. | 7 |
| Figure 1.4 Surface electric field, comparison between TESLA shape and ERL model 2. | 10 |
| Figure 1.5 Rotating mapping system details, sensors installation around a cell (left), sensors location drawing (top right), PIN diodes and carbon resistors (bottom right). | 11 |
| Figure 1.6 X-ray map during cavity vertical test (left), Q-E plot during the same test (right). | 12 |

Chapter II

| | |
|---|----|
| Figure 2.1 RLC circuit scheme. | 20 |
| Figure 2.2 Capacitor connected with “single-loop” inductance. | 22 |
| Figure 2.3 Resonator obtained from a capacitor enclosed by “single-loop” inductances. | 22 |
| Figure 2.4 Resonance curve. Circuit voltage against the feeding frequency, the natural frequency is 1000Hz and the damping factor is 200. | 24 |
| Figure 2.5 Phase shift with respect to the driving frequency (<i>from Feynman lectures on physics [2]</i>) at resonance frequency the response lag 90° respect to the feeding. | 26 |
| Figure 2.6 Pillbox cavity model. | 27 |
| Figure 2.7 First kind Bessel function $x = \omega rc$. | 29 |
| Figure 2.8 Pillbox cavity, electric field for TM_{010} mode. | 31 |
| Figure 2.9 Pillbox cavity, electric and magnetic field for TM_{010} mode. | 31 |
| Figure 2.10 Electric and magnetic field intensity with respect to radial coordinates for TM_{010} mode. | 32 |
| Figure 2.11 Electric field components along the Pillbox cavity axis for TM_{010} . | 33 |
| Figure 2.12 Transit time factor for pillbox cavity. | 36 |
| Figure 2.13 Pendulum coupled through a spring with constant k. | 44 |
| Figure 2.14 Coupled resonant circuits, the coupling is obtained through a capacitor. | 45 |
| Figure 2.15 5GeV ERL machine, green dots represent the accelerating beam and red dots represent the decelerating beam [11]. | 46 |
| Figure 2.16 Average brilliance and coherent flux for CHESS, LCLS, APS, ESRF and ERL machine [11]. | 47 |
| Figure 2.17 KEK-ERL cavity with Ferrite HOM absorber (orange) [9]. | 49 |

| | |
|--|----|
| Figure 2. 18 KEK-ERL model 2 half cell schematic. | 50 |
| Figure 2. 19 From top to bottom, ERL mod2 cavity, ILC baseline cavity and JLAB low loss cavity. Electric field for π -mode are shown with contour and arrows..... | 52 |
| Figure 2. 20 Cavities left beam pipe and end cells. | 52 |
| Figure 2. 21 Cavities right beam pipe and end cells. | 53 |
| Figure 2. 22 Comparison between dipole HOM spectrum for TESLA cavity, ERL model 1 cavity (same as TESLA but with larger beam pipe) and final ERL model 2 cavity [9]..... | 55 |
| Figure 2. 23 Spectrum of Monopole HOMs around 2.6GHz and 5.2GHz [9]..... | 56 |
| Figure 2. 24 Eccentric fluted pipe schematic drawings [9]..... | 57 |
| Figure 2. 25 Dispersion curve calculated by numerical code (SuperFish). | 57 |
| Figure 2. 26 Step potential with (right) and without (left) electric field on the metal surface. | 58 |
| Figure 2. 27 Electric surface field for KEK ERL model 2 cavity with different enhancing factors, $E_{acc}=15MV/m$ | 61 |
| Figure 2. 28 Electric surface field with enhancing factor $\beta=100$, respect to different cavity shapes, $E_{acc}=15MV/m$ | 62 |
| Figure 2. 29 Emitted current density with respect to RF phase. | 64 |
| Figure 2. 30 Emitted current density with respect to RF phase with different enhancing factor. | 65 |
| Figure 2. 31 Emitted current density with respect to electric field on the surface at different enhancing factors. | 66 |
| Figure 2. 32 Electropolishing system for multi-cell cavities. | 68 |
| Figure 2. 33 Electropolishing system control panel..... | 69 |
| Figure 2. 34 Cavity immersed in the ultrasonic cleaning system. | 70 |
| Figure 2. 35 Cavity during baking with heating jacket..... | 71 |
| Figure 2. 36 RF system block diagram for vertical test stand installed at STF in KEK..... | 73 |
| Figure 2. 37 Surface resistance with respect to cavity temperature, the obtained residual resistance is $16n\Omega$ | 78 |

Chapter III

| | |
|---|----|
| Figure 3. 1 Cavity central cell with mesh as obtained with SuperFish code. | 83 |
| Figure 3. 2 Dispersion curve from SuperFish calculation. | 86 |
| Figure 3. 3 Electric field 2D plot, from top to bottom $\pi/9, 2\pi/9, 3\pi/9, 4\pi/9, 5\pi/9, 6\pi/9, 7\pi/9, 8\pi/9$ and π mode [3]. | 87 |
| Figure 3. 4 Electric field along cavity axis for TM_{010} π mode [3]. | 88 |
| Figure 3. 5 Electric field amplitude along cavity axis for TM_{010} π mode [3]. | 89 |

| | |
|--|-----|
| Figure 3. 6 Electric field on the surface for TM_{010} π mode and $E_{acc}=1MV/m$, with respect to Z coordinate [3]. | 90 |
| Figure 3. 7 Electric field on the surface for TM_{010} π mode and $E_{acc}=1MV/m$, with respect to Z coordinate near the iris between first and second cell. | 90 |
| Figure 3. 8 Magnetic field on the surface for TM_{010} π mode and $E_{acc}=1MV/m$, with respect to Z coordinate [3]. | 91 |
| Figure 3. 9 Electric field (lines) and magnetic field (circle) in the first two cells for TM_{010} π mode. | 94 |
| Figure 3. 10 Particle tracking code block diagram. | 95 |
| Figure 3.11 Electron trajectories, each trajectory start at different RF phase during electron emission, the emitter is located between the 8 th and 9 th cell (upper part). | 98 |
| Figure 3.12 Electron trajectories, each trajectory start at different RF phase, from 0° to 180° the phase increase clockwise. | 99 |
| Figure 3. 13 Electron trajectory starting from 8-9 Iris at 135°RF phase. | 99 |
| Figure 3. 14 Electron kinetic energy during the time of flight inside the cavity. | 100 |
| Figure 3. 15 Electron kinetic energy with respect to position inside the cavity, each cell location is highlighted, the electrons move from 9 th cell to the 1 st (right to left). | 101 |
| Figure 3. 16 Region where emitters are located (red line). | 102 |
| Figure 3.17 Escaping location with respect to emitter location (Z coordinate) and emission RF phase at 15MV/m π mode. | 103 |
| Figure 3.18 Regions located in the 1 st cell that allows electrons to exit from SBP (left) or LBP (right). | 104 |
| Figure 3.19 Escaping location with respect to emitter location (S-coordinate) and emission RF phase at 15MV/m π mode. | 105 |
| Figure 3.20 Landing location with respect to emitter location (S-coordinate) and emission RF phase at 15MV/m π mode, emitters are located on iris between cell 1 and cell 2. | 106 |
| Figure 3.21 Landing location with respect to emitter location (S-coordinate) and emission RF phase at 15MV/m π mode, emitters are located on iris between cell 4 and cell 5. | 107 |
| Figure 3.22 Electrons trajectory at different RF phase during emission at 15MV/m π mode, emitters are located on iris between cell 1 and cell 2. | 108 |
| Figure 3.23 Flying direction with respect to emitter location (S-coordinate) and emission RF phase at 15MV/m π mode, the plot is generalized for any iris. | 109 |
| Figure 3.24 Impact energy with respect to emitter location (S-coordinate) and emission RF phase at 15MV/m π mode, emission region is between 1 st and 2 nd cell. | 110 |
| Figure 3.25 Impact energy with respect to emitter location (S-coordinate) and emission RF phase at 15MV/m π mode, emission region is between 4 th and 5 th cell. | 111 |
| Figure 3.26 Contour plot for E_{surf}/E_{acc} with respect to RF phase and S coordinate. | 113 |

| | |
|---|-----|
| Figure 3.27 Emitted current [μA] with respect to RF phase at $E_{\text{acc}}=15\text{MV/m}$, field enhancement factor $\beta=100$ and emitter area 10^{-13} m^2 . | 114 |
| Figure 3.28 Emitted power [mW] with respect to RF phase at $E_{\text{acc}}=15\text{MV/m}$, field enhancement factor $\beta=100$ and emitter area 10^{-13} m^2 . | 116 |
| Figure 3.29 Total emitted power [W] or each emitter, with respect to RF phase at $E_{\text{acc}}=15\text{MV/m}$, field enhancement factor $\beta=100$ and emitter area 10^{-13} m^2 . | 117 |
| Figure 3.30 EGS5 model geometry. | 120 |
| Figure 3.31 Model zones definition [10]. | 121 |
| Figure 3.32 Mass energy-absorption coefficient for Niobium as published by Hubbell and Seltzer (NIST)[12]. | 122 |
| Figure 3.33 Transmitted energy percentage, literature data (black dots) and calculated data with EGS5 (red dots). | 123 |

Chapter IV

| | |
|--|-----|
| Figure 4.1 STF map [1]. | 126 |
| Figure 4.2 Cryostat pit for vertical test in STF. | 127 |
| Figure 4.3 LLRF diagram. | 128 |
| Figure 4.4 Vertical test set up, cavity #1 and #2 (left), cavity #4 and #3 (right). | 129 |
| Figure 4.5 Mapping system details. | 130 |
| Figure 4.6 PIN diode S1223 details [5]. | 131 |
| Figure 4.7 PIN diode amplification scheme. | 132 |
| Figure 4.8 NaI scintillator connected to photomultiplier. | 133 |
| Figure 4.9 NaI scintillator setup, photomultiplier (top left), high voltage generator (top right) and analog-digital converter (bottom right). | 134 |
| Figure 4.10 Voltage adjustment knob. | 135 |
| Figure 4.11 NaI scintillator calibration curve, each channel account for 10.9eV . | 136 |

Chapter V

| | |
|---|-----|
| Figure 5.1 Electron trajectories starting at different RF phases from an emitter located between 1 st and 2 nd cell, $E_{\text{acc}}=15\text{MV/m}$. | 139 |
| Figure 5.2 Impact Energy for electron trajectories starting at different RF phases from an emitter located between 1 st and 2 nd cell, $E_{\text{acc}}=15\text{MV/m}$. | 140 |

| | |
|--|-----|
| Figure 5. 3 SEY graph for Niobium (below) [1] and metals properties respect to secondary electrons emission (above). | 141 |
| Figure 5.4 Percentage of energy transmitted, absorbed or reflected by a 2.5mm Niobium plate upon electron impact perpendicular to the surface. | 143 |
| Figure 5.5 Total amount of energy transmitted, absorbed or reflected by a 2.5mm Niobium plate upon electron impact perpendicular to the surface. | 144 |
| Figure 5.6 Impact angle for electron trajectories starting at different RF phases from an emitter located between 1 st and 2 nd cell (as shown in figure 5.1), $E_{acc}=15MV/m$ | 145 |
| Figure 5.7 Percentage of energy transmitted, absorbed or reflected by a 2.5mm Niobium plate upon electron impact with 10MeV at different incident angles. | 146 |
| Figure 5.8 PIN diode geometry model for EGS5. | 147 |
| Figure 5.9 Particle shower produces by 10MeV electrons hit the Niobium (left side), electron trajectories (red lines) and photon trajectories (yellow lines). | 148 |
| Figure 5.10 Particle shower produces by 2MeV electrons hit the Niobium (left side), electron trajectories (red lines) and photon trajectories (yellow lines). | 148 |
| Figure 5.11 Diode current with respect to electron impact energy. | 149 |
| Figure 5.12 Average deposited energy in the Silicon crystal with respect to electrons impact energy, the green line represents the energy needed to produce at least one electron-hole pair. | 150 |
| Figure 5.13 PIN diode amplification circuit schematic. | 151 |
| Figure 5. 14 Voltage response from PIN diodes circuit as calculated through EGS5 (average deposited energy) respect to electrons impact energy. | 152 |
| Figure 5.15 Cavity #1 surface resistance, the residual resistance was $14n\Omega$ | 155 |
| Figure 5.16 Cavity #1 π modes Q-E plot. | 156 |
| Figure 5.17 Cavity #1 π mode 2 power dissipation with respect to accelerating field, total power loss (dotted line), RF field loss (red line) and field emission loss (blue line). | 157 |
| Figure 5. 18 Cavity #1 π mode 2 radiation dose at cavity ends. | 158 |
| Figure 5. 19 Cavity #1 4 th vertical test π mode (2), $E_{acc}=13.9MV/m$ $Q_0=7.93 \times 10^9$, $P_{loss}=29.56W$, x-ray pattern detected by PIN diodes (rotating mapping system). | 159 |
| Figure 5. 20 Cavity #1 optical inspection result (left) after 5 th vertical test, Kyoto camera set up (right). | 160 |
| Figure 5. 21 Electron trajectories at different RF phase, π mode $E_{acc}=13.9MV/m$ | 160 |
| Figure 5. 22 Impact locations and energy at different RF phase, π mode $E_{acc}=13.9MV/m$ | 161 |
| Figure 5. 23 Electric field on the surface for TM010 π mode and $E_{acc}=1MV/m$, with respect to Z coordinate near the iris between first and second cell | 163 |
| Figure 5. 24 Numerical integration to calculate the dissipated power with respect to the accelerating field. | 165 |

| | |
|--|-----|
| Figure 5. 25 Linear fitting for field emission power loss respect to accelerating field. | 166 |
| Figure 5. 26 Power loss due to field emission during 4th and 5th vertical test. | 167 |
| Figure 5. 27 Linear fitting to calculate the emitter geometric parameters. | 168 |
| Figure 5. 28 Power dissipation as measured during the 5th vertical test π -mode(1) and calculated with simulation code. | 169 |
| Figure 5. 29 Q-E plot from 5th vertical test π -mode(1) and π -mode(2). | 170 |
| Figure 5. 30 Q-E plot comparing vertical test data and simulation result. | 171 |
| Figure 5. 31 Δ^2 contour plot, comparing 5 th vertical test π mode(1) with simulation results. | 172 |
| Figure 5. 32 Δ^2 contour plot, comparing 5 th vertical test π mode(1) with simulation results, emitter location is 0.5mm away from the observed position. | 173 |
| Figure 5. 33 Cavity #1 4 th vertical test π mode (2), $E_{acc}=13.9\text{MV/m}$ $Q_0=7.93 \times 10^9$, $P_{loss}=29.56\text{W}$, x-ray pattern detected by PIN diodes (rotating mapping system), dashed line is at 310° meridian. | 174 |
| Figure 5. 34 Cavity #1 4 th vertical test mapping system set up, PIN diodes (blue), carbon resistor (black). | 175 |
| Figure 5. 35 Cavity #1 4 th vertical test π mode (2), $E_{acc}=13.9\text{MV/m}$ $Q_0=7.93 \times 10^9$, $P_{loss}=29.56\text{W}$, x-ray pattern detected by PIN diodes (rotating mapping system) <u>without iris signal</u> (The image is reversed respect to the previous one). | 176 |
| Figure 5.36 Electron trajectories at different RF phase, π mode $E_{acc}=13.9\text{MV/m}$ | 177 |
| Figure 5. 37 Flying direction with respect to emitter location (S-coordinate) and emission RF phase at 15MV/m π mode, the plot is generalized for any iris. | 178 |
| Figure 5. 38 Power landing on the cavity surface at 13.9MV/m π mode, the two emitters are located on iris between 8 th and 9 th cell, emitter A is the location detected during optical inspection and emitter B is 0.5mm distance from A (inside the 9 th cell). | 179 |
| Figure 5. 39 Power landing on the cavity surface at 13.9MV/m π mode, the two emitters are located on iris between 8 th and 9 th cell, emitter A is the location detected during optical inspection and emitter B is 0.5mm distance from A (inside the 9 th cell) Zoom from previous image. | 180 |
| Figure 5. 40 Power transmitted through Niobium at 13.9MV/m π mode, the emitter is located on iris between 8 th and 9 th cell. | 181 |
| Figure 5. 41 PIN diodes voltage at 13.9MV/m π mode, the signal is measured inside the 8 th and 9 th cell, the signal coming from 8-9Iris is about 8 times bigger than the one detected from 7-8Iris. | 182 |
| Figure 5. 42 Impact angles from emitter B at 13.9MV/m π mode, starting from iris between 6 th and 7 th cell the impact angle start to be lower than 10° | 183 |
| Figure 5. 43 Impact kinetic energy from emitter B at 13.9MV/m π mode. | 184 |
| Figure 5. 44 EGS5 cavity model, cells are designed with torus, and iris with cylinder with the same curvature radius. | 185 |
| Figure 5. 45 EGS5 cavity model, shower produced by electron impact on iris, electrons (red lines) and photons (yellow lines). | 186 |

| | |
|---|-----|
| Figure 5. 46 EGS5 cavity model, shower electrons energy and location. | 187 |
| Figure 5. 47 Electrons impact, meridian and z coordinate location. | 188 |
| Figure 5. 48 Comparison between the observed broad peak during vertical test (left) and the simulation result (right). | 188 |
| Figure 5. 49 Summary of the spot location in the measured data and simulation set up, emitter is located at 150° meridian. | 189 |
| Figure 5. 50 Vertical test set up, cavity #1 (left),cavity #4 (right). | 191 |
| Figure 5. 51 PIN diodes installed on helium jacket cap, on SBP and LBP side. | 192 |
| Figure 5. 52 Cavity #4 surface resistance, the residual resistance was 17nΩ. | 192 |
| Figure 5. 53 Cavity #4 π modes Q-E plot. | 193 |
| Figure 5. 54 Cavity #4 π modes field emission power loss. | 194 |
| Figure 5. 55 Cavity #4 π modes field emission power loss. | 195 |
| Figure 5. 56 Cavity #4 π mode x-ray mapping from 15MV/m to 22MV/m, the field emission signal is visible from 16MV/m, the spots location remain the same. | 196 |
| Figure 5. 57 Cavity #4 π modes extrapolated β | 197 |
| Figure 5. 58 Cavity #4 π modes at 22MV/m, signal from PIN diodes in the 1 st cell, the graph represent the PIN voltage against the meridian angle. | 198 |
| Figure 5. 59 Region to test the emitter location, from this area the electron trajectories are towards the LBP side (right side of the picture) | 199 |
| Figure 5. 60 PIN diode voltage against meridian angle, the PIN diodes are located in front of iris200 | |
| Figure 5. 61 Landing location from emitters located on 1st-2nd cell iris, on the Y axis is represented the emitter number, the X axis represent the RF emission phase, the cavity is at 22MV/m π mode. | 201 |
| Figure 5. 62 Δ^2 calculated for different emitter locations, different emitter area and different β | 202 |
| Figure 5. 63 Radiation map for π mode at 22MV/m, with iris signal (top) and without iris signal (bottom). | 204 |
| Figure 5. 64 Radiation map for 8/9 π mode at 23.5MV/m, with iris signal (top) and without iris signal (bottom). | 205 |
| Figure 5. 65 PIN diode signal from LBP and SBP ring for π mode at 22MV/m (top) and 8/9 π mode at 23.5MV/m (bottom). | 206 |
| Figure 5. 66 Transmitted power along 360° meridian for π mode at 22MV/m for emitters 47, 48 and 49. | 208 |
| Figure 5. 67 Transmitted power along 360° meridian for π mode at 22MV/m for emitters 50, 51 and 52. | 209 |
| Figure 5. 68 Transmitted power along 360° meridian for 8/9 π mode at 23.5MV/m for emitters 47, 48 and 49. | 210 |

| | |
|---|-----|
| Figure 5. 69 Transmitted power along 360° meridian for 8/9 π mode at 23.5MV/m for emitters 50, 51 and 52..... | 211 |
| Figure 5. 70 Incident angle along 360° meridian for π mode at 22MV/m for emitters 47, 48 and 49. | 212 |
| Figure 5. 71 Incident angle along 360° meridian for π mode at 22MV/m for emitters 50, 51 and 52. | 213 |
| Figure 5. 72 Incident angle along 360° meridian for 8/9 π mode at 23.5MV/m for emitters 47, 48 and 49..... | 214 |
| Figure 5. 73 Incident angle along 360° meridian for 8/9 π mode at 23.5MV/m for emitters 50, 51 and 52..... | 215 |
| Figure 5.74 Q-E plot comparison between measured and simulation, cavity #4 π mode(1)..... | 217 |
| Figure 5. 75 Cavities inside the cryomodule (front view). | 218 |
| Figure 5.76 PIN diodes installed on the SBP side, around the Helium jacket cap. | 220 |
| Figure 5.77 PIN diodes installed on the LBP side, around the damper tube on a diameter about 60mm. | 221 |
| Figure 5.78 PIN diodes configuration for the profile monitor installed in front of the gate valve (LBP side). | 222 |
| Figure 5.79 Profile monitor installed during the high power test. | 222 |
| Figure 5.80 Online screen capture for the EPICS code, profile monitor (top left),SBP ring diodes (top center and right), LBP ring diodes (bottom center and right), all the quantities are volts measured in the PIN diode circuit, the meridian angles are calculated starting at 0° (top PIN diode) increasing clockwise up to 360°. | 223 |
| Figure 5.81 Cavity location inside the c-ERL and sensors location. | 225 |
| Figure 5.82 Cavity #4 at 14MV. | 226 |
| Figure 5. 83 Cavity #4 PIN diodes voltage from sensors installed on the LBP damper tube..... | 227 |
| Figure 5. 84 Cavity #4 radiation pattern after x-ray burst, the cavity voltage is about 12MV. | 228 |
| Figure 5. 85 NaI scintillator positioned in front of cavity #4 LBP side..... | 229 |
| Figure 5.86 NaI scintillator background signal taken for 120 minutes..... | 230 |
| Figure 5.87 NaI scintillator measure near field emission onset, each measure is taken at different cavity voltage for 2 minutes..... | 231 |
| Figure 5.88 Scintillator data fitting from left to right 8MV, 8.5MV, 9MV and 9.5MV spectra and linear fitting..... | 232 |
| Figure 5. 89 Comparison between energy spectrum produced by emitters on different iris and measured data for cavity #4 (upstream). | 233 |
| Figure 5. 90 Landing location with respect to emission phase and emitter location from iris between 2nd and 3rd cell at 8.5MV. Trajectories that can reach the LBP are represented as black dots. | 235 |

| | |
|---|-----|
| Figure 5.91 Possible emitters region, in the figure is represented a red line covering 30mm surface length, the estimated region is 7mm too small to be appreciated in the figure..... | 235 |
| Figure 5.92 Cavity #3 radiation pattern at 11MV cavity voltage. | 236 |
| Figure 5. 93 Cavity #3 radiation pattern at 12MV cavity voltage. | 237 |
| Figure 5. 94 NaI scintillator measure near field emission onset, each measure is taken at different cavity voltage for 2 minutes..... | 238 |
| Figure 5. 95 Comparison between energy spectrum produced by emitters on different iris and measured data for cavity #3 (black dots) and cavity #4 (purple dots). | 239 |
| Figure 5. 96 Landing location with respect to emission phase and emitter location from iris between 1 st and 2 nd cell. Trajectories that can reach the LBP are represented as black dots. | 240 |
| Figure 5. 97 Possible emitters region, in the figure is represented a red line covering 30mm surface length, the estimated region is 7mm too small to be appreciated in the figure..... | 240 |
| Figure 5. 98 Electron impact energy, ERL mod2 cavity π mode 15MV/m..... | 244 |
| Figure 5.99 Electron impact energy, ILC cavity π mode 35MV/m. | 245 |
| Figure 5.100 Electron impact energy, JLAB-LL cavity π mode 12MV/m..... | 246 |
| Figure 5.101 Deposited power, ERL mod2 cavity π mode 15MV/m. | 247 |
| Figure 5.102 Deposited power, ILC cavity π mode 35MV/m. | 248 |
| Figure 5.103 Deposited power, JLAB-LL cavity π mode 12MV/m..... | 249 |
| Figure 5.104 Normalized power respect to emitter location for π mode, ERL mod2 at 15MV/m, JLAB-LL at 12MV/m and ILC at 35MV/m..... | 250 |

Scientific publications

TALKS

The 50th ICFA Advanced Beam Dynamics Workshop on Energy Recovery Linac (ERL 2011)

- *Vertical test diagnostics and simulation studies for 9-cell cERL cavities*

Enrico Cenni (The Graduate University for Advanced Studies, KEK), Takaaki Furuya, Hiroshi Sakai, Kensei Umemori, Kenji Shinoe, Masato Sato (KEK), Masaru Sawamura (JAEA)

PAPERS

- **(SRF 2011) Vertical Test Results on KEK-ERL 9-Cell L-Band Superconducting Cavity**

Enrico Cenni (The Graduate University for Advanced Studies, KEK), Takaaki Furuya, Hiroshi Sakai, Kensei Umemori, Kenji Shinoe, Masato Sato (KEK), Masaru Sawamura (JAEA)

- **(IPAC 2012) Field emission simulation for KEK-ERL 9-Cell Superconducting Cavity**

Enrico Cenni (The Graduate University for Advanced Studies, KEK), Takaaki Furuya, Hiroshi Sakai, Kensei Umemori, Kenji Shinoe, Masato Sato (KEK), Masaru Sawamura (JAEA)

- **(SRF 2013) Field emission measure during cERL main linac cryomodule high power test in KEK**

Enrico Cenni (The Graduate University for Advanced Studies, KEK), Takaaki Furuya, Hiroshi Sakai, Kensei Umemori, Kenji Shinoe, Masato Sato (KEK), Masaru Sawamura (JAEA)

- **(Submitted to PRSTAB) Field emission studies on KEK energy recovery Linac superconducting cavities**

Coauthored papers

The 15th International Conference on RF Superconductivity (SRF 2011):

✓ *Cooling Properties of HOM Absorber Model for cERL in Japan*

M. Sawamura, JAEA, Tokai, Ibaraki 319-1195, Japan
 T. Furuya, H. Sakai, K. Umemori, KEK, Tsukuba, Ibaraki 305-0801, Japan
 K. Shinoe, ISSP, University of Tokyo, Kashiwa, Chiba 277-8581, Japan
 E. Cenni, The Graduate University for Advanced Studies, Tsukuba, Ibaraki 305-0801, Japan

✓ *High power tests of KEK-ERL input coupler for main linac under liquid nitrogen condition*

Hiroshi Sakai, Takaaki Furuya, Norio Nakamura, Kensei Umemori,
 KEK, Tsukuba, Ibaraki, 305-0801, Japan,
 Kenji Shinoe, ISSP, Univ. of Tokyo, Kashiwa, Chiba, 277-8581, Japan,
 Masaru Sawamura, JAEA, Tokai, Naka, Ibaraki, 319-1195, Japan
 E. Cenni, The Graduate University for Advanced Studies, Tsukuba, Ibaraki 305-0801, Japan

✓ *Construction of cERL cryomodules for injector and main linac*

K. Umemori, T. Furuya, E. Kako, S. Noguchi, H. Sakai, M. Satoh, T. Shishido,
 K. Watanabe, Y. Yamamoto, KEK, Tsukuba, Ibaraki, 305-0801, Japan
 K. Shinoe, ISSP, University of Tokyo, Kashiwa, Chiba, 277-8581, Japan
 M. Sawamura, JAEA-ERL, Tokai, Naka, Ibaraki, 319-1195, Japan
 E. Cenni, The Graduate University for Advanced Studies, Tsukuba, Ibaraki, 305-0801,
 Japan

The 50th ICFA Advanced Beam Dynamics Workshop on Energy Recovery Linac (ERL 2011):

✓ *Development of main linac cavity for cERL project*

Kensei Umemori, Takaaki Furuya, Hiroshi Sakai, Kenji Shinoe, Masato Sato (KEK),
 Masaru Sawamura (JAEA), Enrico Cenni (The Graduate University for Advanced Studies,
 KEK)

✓ *Development of input coupler for cERL main linac*

Hiroshi Sakai, Kensei Umemori, Takaaki Furuya, Kenji Shinoe, Masato Sato (KEK),
 Masaru Sawamura (JAEA), Enrico Cenni (The Graduate University for Advanced Studies,
 KEK)

✓ ***HOM properties of main linac for cERL in Japan***

Masaru Sawamura (JAEA), Hiroshi Sakai, Kensei Umemori, Takaaki Furuya, Kenji Shinoe, Masato Sato (KEK), Enrico Cenni (The Graduate University for Advanced Studies, KEK)

✓ ***Cryomodule of KEK-ML cavity***

Takaaki Furuya, Hiroshi Sakai, Kensei Umemori, Kenji Shinoe, Masato Sato (KEK), Masaru Sawamura (JAEA), Enrico Cenni (The Graduate University for Advanced Studies, KEK)

✓ ***Performance Evaluation of KEK Tuner***

Kazuhiro Enami, Takaaki Furuya, Hiroshi Sakai, Kensei Umemori, Kenji Shinoe, Masato Sato (KEK), Masaru Sawamura (JAEA), Enrico Cenni (The Graduate University for Advanced Studies, KEK)

International Particle Accelerator Conference (IPAC 2012):

✓ ***Status of main linac cryomodule development for compact ERL project***

K. Umemori, K. Enami, T. Furuya, H. Sakai, M. Satoh, K. Shinoe, KEK, Tsukuba, Ibaraki, Japan
M. Sawamura, JAEA, Tokai, Naka, Ibaraki, Japan
E. Cenni, The Graduate University for Advanced Studies, Tsukuba, Ibaraki, Japan

✓ ***Vertical test results for ERL 9-cell cavities for compact ERL project***

K. Umemori, T. Furuya, H. Sakai, M. Satoh, K. Shinoe, KEK, Tsukuba, Ibaraki, Japan
M. Sawamura, JAEA, Tokai, Naka, Ibaraki, Japan
E. Cenni, The Graduate University for Advanced Studies, Tsukuba, Ibaraki, Japan

ICFA Workshop on Future Light Sources (FLS2012):

✓ ***ERL Cryomodule Development in Japan -- Progress with SRF cavities for ERL project --***

Hiroshi Sakai, Eiji Kako, Shuichi Noguchi, Masato Satoh, Toshio Shishido, Ken Watanabe, Yasuchika Yamamoto, Kensei Umemori, Kenji Shinoe, KEK
Masaru Sawamura, JAEA, Tokai, Naka, Ibaraki, 319-1195, Japan
E. Cenni, The Graduate University for Advanced Studies, Tsukuba, Ibaraki 305-0801, Japan

International Particle Accelerator Conference (IPAC 2013):

- ✓ ***Progress in Construction of the 35 MeV Compact Energy Recovery Linac at KEK***
S. Sakanaka, S. Adachi, M. Akemoto, D.A. Arakawa, S. Asaoka, K. Enami, K. Endo, S. Fukuda, T. Furuya, K. Haga, K. Hara, K. Harada, T. Honda, Y. Honda, H. Honma, T. Honma, K. Hosoyama, K. Hozumi, E. Kako, Y. Kamiya, H. Katagiri, H. Kawata, Y. Kobayashi, Y. Kojima, Y. Kondou, T. Kume, T. Matsumoto, H. Matsumura, H. Matsushita, S. Michizono, T. Miura, T. Miyajima, S. Nagahashi, H. Nakai, H. Nakajima, N. Nakamura, K. Nakanishi, K. Nakao, K.N. Nigorikawa, T. Nogami, S. Noguchi, S. Nozawa, T. Obina, T. Ozaki, F. Qiu, H. Sagehashi, H. Sakai, S. Sasaki, K. Satoh, M. Satoh, T. Shidara, M. Shimada, K. Shinoe, T. Shioya, T. Shishido, M. Tadano, T. Takahashi, R. Takai, T. Takenaka, Y. Tanimoto, M. Tobiyama, K. Tsuchiya, T. Uchiyama, A. Ueda, K. Umemori, K. Watanabe, M. Yamamoto, Y. Yamamoto, Y. Yano, M. Yoshida
KEK, Ibaraki, Japan
E. Cenni, Sokendai, Ibaraki, Japan
R. Hajima, S.M. Matsuba, R. Nagai, N. Nishimori, M. Sawamura, T. Shizuma
JAEA, Ibaraki-ken, Japan
H. Takaki, ISSP/SRL, Chiba, Japan

- ✓ ***Construction of Main Linac Cryomodule for Compact ERL Project***
K. Umemori, T. Furuya, H. Sakai, M. Satoh, K.Shinoe, KEK, Tsukuba, Ibaraki, Japan
M. Sawamura, JAEA, Tokai, Naka, Ibaraki, Japan
E. Cenni, The Graduate University for Advanced Studies, Tsukuba, Ibaraki, Japan